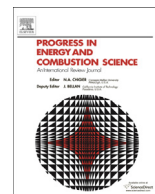




Contents lists available at ScienceDirect

# Progress in Energy and Combustion Science

journal homepage: [www.elsevier.com/locate/pecs](http://www.elsevier.com/locate/pecs)



## Review

# Recent advances in understanding of flammability characteristics of hydrogen



Antonio L. Sánchez<sup>a</sup>, Forman A. Williams<sup>b,\*</sup>

<sup>a</sup> Dept. Ingeniería Térmica y de Fluidos, Universidad Carlos III de Madrid, Leganés 28911, Spain

<sup>b</sup> Dept. of Mechanical and Aerospace Engineering, University of California San Diego, La Jolla, CA 92093-0411, USA

## ARTICLE INFO

### Article history:

Received 26 August 2013

Accepted 29 October 2013

Available online 2 December 2013

### Keywords:

Hydrogen combustion

Flammability limits

Reduced chemistry

Crossover temperature

## ABSTRACT

The current increasing interest in hydrogen utilization and increasing understanding of hydrogen combustion motivate this review of flammability characteristics of hydrogen. The intent is to present a thorough and self-contained tutorial that covers the existing fundamental knowledge in a uniform and concise manner. The presentation begins with an up-dated exposition of the elementary chemical mechanism of hydrogen oxidation, including the latest chemical-kinetic results, with evaluated selections of reaction-rate parameters. Understanding of the mechanism is emphasized through presentation of systematically reduced overall steps and their associated rates. Useful simplifications of the chemistry are thereby exposed and appraised, identifying applicable quasi-steady-state approximations. The status of our knowledge of the fundamental transport properties for hydrogen combustion is then summarized, with indication of the relevance of thermal diffusion for hydrogen. Hydrogen–oxygen autoignition processes are next analyzed, including the important differences found under conditions above and below the crossover temperature at which the rates of the branching and recombination steps are equal, with an explanation of the classical explosion diagram that exhibits three explosion limits. Time-dependent and counter-flow mixing layers are addressed in the context of ignition processes. Knowledge of hydrogen deflagrations is reviewed, including their flame structures, burning velocities, and flammability limits, with special emphasis on peculiarities and simplification that occur in the vicinity of the lean limit. Deflagration instabilities and effects of strain and curvature on deflagrations are described, resulting under appropriate circumstances in flame balls, the structures, characteristics, and importance of which are analyzed. The structures and stabilization mechanisms of hydrogen diffusion flames are reviewed, pointing out the current state of knowledge and current uncertainties in their extinction conditions. Hydrogen detonations also are considered, with explanations given of their detonation velocities, structures, and instabilities, including cellular detonations and emphasizing the importance of future studies of vibrational relaxation effects in these detonations. Finally, some comments and observations on the applications and future prospects for hydrogen usage are offered from viewpoints of safety and energy production.

© 2013 Elsevier Ltd. All rights reserved.

## Contents

1. Introduction .....	2
2. The chemistry of hydrogen oxidation .....	4
2.1. Elementary reactions .....	4
2.2. The role of the hydrogen–oxygen shuffle reactions .....	5
2.3. Rate parameters for the hydrogen–oxygen shuffle reactions .....	5
2.4. The role of the hydroperoxyl reactions and the crossover temperature .....	5
2.5. Rate parameters for the hydroperoxyl reactions .....	6
2.6. Radical–radical recombinations .....	7
2.7. Hydrogen peroxide reactions .....	8

\* Corresponding author.

E-mail address: [faw@ucsd.edu](mailto:faw@ucsd.edu) (F.A. Williams).

3.	Simplified chemistry descriptions for hydrogen oxidation	9
3.1.	A sufficiently accurate short mechanism	9
3.2.	Chemistry reduction: issues and techniques	10
3.3.	The quasi-steady-state approximation	11
3.4.	Systematically reduced chemical-kinetic mechanisms for hydrogen oxidation	12
3.4.1.	The four-step mechanism	12
3.4.2.	The two separate three-step mechanisms	13
3.4.3.	The two-step mechanism	14
4.	Transport properties related to hydrogen	14
4.1.	The computation of diffusion velocities	14
4.2.	Evaluation of diffusion coefficients	15
4.3.	Thermal diffusion effects in hydrogen combustion	17
4.4.	Evaluation of viscosity and thermal conductivity	17
5.	Autoignition processes for hydrogen	18
5.1.	Ignition above crossover: the chain-branching explosion	19
5.2.	Ignition below crossover: the thermal explosion	21
5.3.	The explosion limits of hydrogen–oxygen combustion	23
5.3.1.	The lower peninsula of the explosion diagram	24
5.3.2.	The third explosion limit	24
5.4.	Effects of flow strain and nonuniform temperature and composition fields on autoignition	25
5.4.1.	Ignition in the counterflow mixing layer	27
5.4.2.	Chain-branching explosions in unsteady unstrained mixing layers	28
6.	Premixed hydrogen combustion	29
6.1.	The burning rate	30
6.2.	The structure of planar flames	32
6.3.	Flames near the lean flammability limit	34
6.4.	Effects of stretch	37
6.5.	Stability of planar hydrogen deflagrations	38
6.6.	Hydrogen flame balls and flammability limits	39
7.	Nonpremixed combustion of hydrogen	42
7.1.	Attached and lifted hydrogen jet diffusion flames	43
7.2.	Structure and extinction of hydrogen diffusion flames	44
7.3.	Associated problems related to rocket engines	45
8.	Structure and stability of hydrogen detonations	45
8.1.	Pressure buildup under confinement	46
8.2.	Chapman–Jouguet detonation velocities	46
8.3.	Planar detonation structure	46
8.4.	Mechanisms of instability of planar detonations	48
9.	Applications, outstanding problems, and future prospects for hydrogen utilization	49
	Acknowledgments	50
	References	50

## 1. Introduction

The practical motivation for investigating the combustion of hydrogen falls into two broad categories, one concerning its utilization and the other concerning its safety. From the viewpoint of utilization, there is increasing interest in hydrogen usage for power production because of its inherent cleanliness. In addition to being well adapted to fuel cells, it tends to produce fewer pollutants in direct combustion than do other fuels. Notably absent in hydrogen combustion, for example, is the greenhouse gas carbon dioxide, which is of increasing concern for energy generation from fossil fuels. One of many marks of the attractiveness of hydrogen in this respect is the existence of the International Journal of Hydrogen Energy, devoted to publication of scientific and engineering aspects related to energy production through hydrogen. In this context, it is relevant to bear in mind that, unlike fossil or nuclear fuels, combustible hydrogen is not found in deposits on Earth but instead must be generated in energy-consuming processes, so that it is best viewed as an energy carrier. Not only is hydrogen an effective energy carrier, but it also serves as one of the most powerful propellant constituents for rocket and air-breathing engines. There are thus many varied applications for extracting energy, power, or force from hydrogen.

Along with its increasing utilization come increasing safety concerns about hydrogen. It is much easier to ignite hydrogen than most other fuels, and its range of flammability is considerably broader. In addition, transition to detonation occurs more easily for hydrogen mixtures than for the vast majority of other mixtures, thereby making it potentially more dangerous. Coupled with the facts that hydrogen flames generally are more difficult to detect and that combustible hydrogen–air mixtures can be (and have been) generated from coolants in nuclear-reactor accidents, considerable efforts are warranted in evaluating and planning mitigation of potential hydrogen fire hazards. Prevention of hydrogen fires may be deemed essential. It thus becomes of paramount importance to ascertain accurately the flammability limits of hydrogen mixtures under different circumstances. Complications arise from the fact that the limits may be appreciably different in spacecraft, for example, than on Earth. Safety aspects thus warrant extensive investigation for hydrogen.

Studies of hydrogen combustion also are of interest from the viewpoint of enhancing scientific understanding. The chemistry of hydrogen oxidation is considerably simpler than that for any other fuel, and in fact it is part of the oxidation mechanisms of carbon monoxide and all hydrocarbons, alcohols, and other biofuels. It thus should be possible, in principle, to develop a better scientific

**Nomenclature***Latin letters*

$a$	spherical-vessel radius
$A$	counterflow strain rate
$A_0, A_1, A_2$	quantities defined in Eq. (10)
$B$	constant appearing in the preexponential factor of the reaction-rate coefficient
$B_1, B_2$	quantities defined in Eq. (14)
$\bar{c}$	average molecular speed
$C$	radical-pool concentration defined in Eq. (37)
$C_i$	concentration of species $i$
$\dot{C}_i$	chemical production rate of species $i$
$C_{H_2O_2c}$	characteristic $H_2O_2$ mole fraction for ignition defined in Eq. (46)
$\tilde{C}_{H_2O_2c}$	characteristic $H_2O_2$ mole fraction for ignition defined in Eq. (53)
$C_{M_j}$	effective third-body concentration of reaction $j$
$c_p$	specific heat at constant pressure
$D_H$	effective diffusion coefficient defined in Eq. (50)
$D_{ij}$	binary diffusion coefficient of the species pair ( $ij$ )
$D_i$	binary diffusion coefficient of a dilute species $i$ into the dominant species
$\tilde{D}_i$	modified diffusion coefficient accounting for thermal diffusion, as defined below Eq. (22)
$D_i^T$	thermal diffusion coefficient of species $i$
$D_T$	thermal diffusivity
$\tilde{D}$	average radical-pool diffusivity ratio defined in Eq. (61)
$Da$	Damköhler number defined in Eq. (55)
$D_{ij}$	multicomponent diffusion coefficient of the species pair ( $ij$ )
$f$	chemical-rate function defined in Eq. (90)
$F_c$	constant for the Troe falloff factor
$G$	chemical-rate function defined in Eq. (89)
$G_0, G_1, G_2$	coefficients in the WKB expansion of Eq. (66)
$h_i$	standard molar enthalpy of formation of species $i$
$H$	chemical-rate function defined in Eq. (91)
$k_j$	rate constant of reaction $j$
$k_0$	low-pressure rate constant for three-body collisions
$k_\infty$	high-pressure rate constant for three-body collisions
$K$	equilibrium constant defined in Eq. (81)
$K_j$	equilibrium constant of reaction $j$
$L_{H_2A}$	Lewis number based on $D_{H_2A}$
$\tilde{L}_{H_2}$	effective hydrogen Lewis number defined below Eq. (106)
$L_M$	Markstein length
$m_i^+$	mass rate of production of species $i$
$m_i^-$	mass rate of consumption of species $i$
$M_i$	molecular mass of species $i$
$\dot{M}_{H_2}$	hydrogen burning rate (fuel mass burnt per unit flame surface per unit time)
$n$	temperature exponent of the preexponential factor in the reaction-rate constant
$p$	pressure
$q$	nondimensional heat of combustion defined below Eq. (46)
$Q_R$	rate of radiant heat loss defined in Eq. (100)
$r$	radial coordinate
$r_f$	flame-ball radius
$R$	radius of curvature of the curved flame

$\tilde{r}$	dimensionless radial coordinate defined above Eq. (54)
$t_B$	characteristic branching time defined in Eq. (29)
$\tilde{t}_B$	modified characteristic branching time defined in Eq. (39)
$\tilde{t}_B^*$	minimum value of the modified branching time across the mixing layer
$t_i$	characteristic initiation time defined in Eq. (30)
$t_R$	characteristic radical-recombination time
$t_i$	ignition time
$t_i^+$	characteristic chemical production time of species $i$
$t_i^-$	characteristic chemical consumption time of species $i$
$t_M$	characteristic mechanical time
$T$	temperature
$T_a$	activation temperature
$T_{af}$	adiabatic flame temperature
$T_B$	branching-layer temperature
$T_c$	crossover temperature
$T_u$	temperature of the unburnt fresh mixture
$\bar{v}$	flow velocity
$\bar{V}_i$	diffusion velocity of species $i$
$W_B$	nondimensional branching rate defined in Eq. (60)
$X_i$	mole fraction of species $i$
$X_{O_2A}$	mole fraction of oxygen in air
$Y_i$	mass fraction of species $i$
$\tilde{Y}_i$	modified mass fraction, as defined below Eq. (22)

*Greek letters*

$\alpha$	fraction of $HO_2$ radicals consumed through the chain-terminating path, defined in Eq. (75)
$\alpha_{H_2A}$	hydrogen–air thermal diffusion factor
$\alpha_i$	thermal diffusion factor of the dilute species $i$
$\beta$	nondimensional activation energy of reaction 10f defined below Eq. (45)
$\gamma$	specific-heat ratio
$\gamma_{3b}$	reaction-rate ratio defined below Eq. (91)
$\delta_B$	characteristic thickness of the branching layer
$\delta_L$	flame thickness
$\Delta$	Damköhler number defined in Eq. (59)
$\varepsilon$	fraction of H atoms destroyed on striking the catalytic wall surface
$\varepsilon$	initiation-to-branching rate ratio defined in Eq. (65)
$\zeta$	dimensionless transverse coordinate appearing in Eq. (57)
$\eta$	dimensionless transverse coordinate appearing in Eq. (62)
$\theta$	dimensionless temperature increment defined in Eq. (45)
$\kappa_{H_2O}$	Plank-mean absorption coefficient
$\lambda$	thermal conductivity
$\rho$	density
$\sigma$	Stefan–Boltzmann constant
$\tau$	dimensionless time defined above Eq. (47)
$\phi$	equivalence ratio
$\phi_1$	critical equivalence ratio at the lean flammability limit
$\varphi$	dimensionless $H_2O_2$ concentration defined above Eq. (47)
$\tilde{\varphi}$	dimensionless $H_2O_2$ concentration defined above Eq. (54)
$\omega_j$	rate of reaction $j$ (moles per unit volume per unit time)
$\omega_{jf}$	forward rate of reaction $j$
$\omega_{jb}$	backward rate of reaction $j$

understanding of hydrogen combustion than of the oxidation of other fuels, and that understanding should contribute to the understanding for those others. In a sense, then, determining the correct description of hydrogen combustion constitutes the central, most important scientific problem to be addressed in the area of fuel oxidation, with the highest susceptibility to true fundamental advances. It will be seen in this review that, while significant scientific progress has been made in describing the basic processes of hydrogen oxidation, there remains a number of important aspects in need of further investigation.

We shall begin by reviewing the chemistry and then transport for hydrogen combustion. In those reviews we shall focus especially on useful simplifications that help to increase understanding while still providing good accuracy. Next we shall present an extensive discussion of various autoignition processes for hydrogen as a vehicle for comprehension of many of its unique combustion characteristics. We shall then address hydrogen deflagrations, their stability, flame balls, and associated flammability limits. Diffusion flames will be considered next, followed by detonations, with emphasis placed on unique aspects of hydrogen detonations and their instabilities. Finally, some applications and future prospects will be discussed, along with identification of some outstanding problems.

## 2. The chemistry of hydrogen oxidation

The high-temperature elementary reactions involved in the combustion of hydrogen–oxygen mixtures have been studied for many years. The seminal investigations of Hinshelwood and Semenov in the 1920's set the basis for the study of the underlying chain-branching processes and provided the first estimates of the associated controlling rates (see Refs. [1,2] for an account of the early developments). This section presents the current level of understanding of the gas-phase chemical kinetics of hydrogen combustion, which stems largely from extensive experimental data, collected mostly in the last three decades. Since the focus of this article is on gas-phase combustion, attention is restricted to homogeneous chemical reactions. Thus, hydrogen surface reactions, which have been studied extensively and in many ways are material-specific, and their applications in catalytic combustion devices, including the passive autocatalytic recombiners presently used as mitigation tools in nuclear power plants, are not covered here. Nor will the chemistry in liquid solutions or ion or electron processes, as occur in fuel cells, be addressed.

### 2.1. Elementary reactions

Several updated chemical-kinetic mechanisms have been proposed in the last ten years for the description of hydrogen–oxygen combustion. Besides investigations specifically focused on hydrogen [3–8], studies of detailed mechanisms for the combustion of CO/H<sub>2</sub> (syngas) mixtures [9–12] include as necessary sub-mechanisms chemical-kinetic schemes for hydrogen oxidation. An example of the latter is the so-called San Diego mechanism shown in Table 1. This table incorporates a number of changes to the version published in 2006 [10], developed on the basis of new information and re-evaluations of earlier decisions.

Table 1 lists 20 reversible elementary reactions among eight reactive species, namely, H<sub>2</sub>, O<sub>2</sub>, H<sub>2</sub>O, H, O, OH, HO<sub>2</sub>, and H<sub>2</sub>O<sub>2</sub>. The reactions in Table 1 have been grouped in four different categories that reflect their main role in the combustion process, namely, hydrogen–oxygen shuffle reactions, hydroperoxyl reactions, radical–radical recombination reactions, and hydrogen–peroxide reactions. Some arbitrariness is necessarily present in assigning reactions to a given category, in that, for instance, within the hydrogen–

**Table 1**

Rate coefficients in Arrhenius form  $k = BT^n \exp(-T_a/T)$ .

		$B^a$	$n$	$T_a^a$	Ref.
<i>Shuffle reactions</i>					
$H + O_2 \rightleftharpoons OH + O$		$3.52 \times 10^{16}$	−0.7	8590	[20]
$H_2 + O \rightleftharpoons OH + H$		$5.06 \times 10^4$	2.67	3165	[24]
$H_2 + OH \rightleftharpoons H_2O + H$		$1.17 \times 10^9$	1.3	1825	[25]
$H_2O + O \rightleftharpoons OH + OH$		$7.00 \times 10^5$	2.33	7321	See text
<i>Hydroperoxyl reactions</i>					
$H + O_2 + M \rightleftharpoons HO_2 + M^b$	$k_0$	$5.75 \times 10^{19}$	−1.4	0.0	[10]
	$k_\infty$	$4.65 \times 10^{12}$	0.44	0.0	
$HO_2 + H \rightleftharpoons OH + OH$		$7.08 \times 10^{13}$	0.0	148	[32]
$HO_2 + H \rightleftharpoons H_2 + O_2$		$1.66 \times 10^{13}$	0.0	414	[32]
$HO_2 + H \rightleftharpoons H_2O + O$		$3.10 \times 10^{13}$	0.0	866	[31]
$HO_2 + O \rightleftharpoons OH + O_2$		$2.00 \times 10^{13}$	0.0	0.0	[35]
$HO_2 + OH \rightleftharpoons H_2O + O_2$		$2.89 \times 10^{13}$	0.0	−250	[31]
		$4.50 \times 10^{14}$	0.0	5500	[39]
<i>Radical–radical recombination reactions</i>					
$H + OH + M \rightleftharpoons H_2O + M^c$		$4.00 \times 10^{22}$	−2.0	0.0	[10]
$H + H + M \rightleftharpoons H_2 + M^d$		$1.30 \times 10^{18}$	−1.0	0.0	[10]
$O + O + M \rightleftharpoons O_2 + M^e$		$6.17 \times 10^{15}$	−0.5	0.0	[10]
$H + O + M \rightleftharpoons OH + M^f$		$4.71 \times 10^{18}$	−1.0	0.0	[10]
<i>Hydrogen peroxide reactions</i>					
$OH + OH + M \rightleftharpoons H_2O_2 + M^g$	$k_0$	$2.76 \times 10^{25}$	−3.2	0.0	[44]
	$k_\infty$	$9.55 \times 10^{13}$	−0.27	0.0	See text
$HO_2 + HO_2 \rightleftharpoons H_2O_2 + O_2$		$1.03 \times 10^{14}$	0.0	5556	[37]
		$1.94 \times 10^{11}$	0.0	−709	[37]
$H_2O_2 + H \rightleftharpoons HO_2 + H_2$		$2.30 \times 10^{13}$	0.0	4000	See text
$H_2O_2 + H \rightleftharpoons H_2O + OH$		$1.00 \times 10^{13}$	0.0	1804	[24]
$H_2O_2 + OH \rightleftharpoons H_2O + HO_2$		$1.74 \times 10^{12}$	0.0	160	[49]
		$7.59 \times 10^{13}$	0.0	3660	[49]
$H_2O_2 + O \rightleftharpoons HO_2 + OH$		$9.63 \times 10^6$	2.0	2009	[24]

<sup>a</sup> Units are mol, s, cm<sup>3</sup>, and K.

<sup>b</sup> Chaperon efficiencies: H<sub>2</sub> (2.5), H<sub>2</sub>O (16.0), CO (1.2), CO<sub>2</sub> (2.4), Ar and He (0.7), and 1.0 for all other species; Troe falloff with  $F_c = 0.5$ .

<sup>c</sup> Chaperon efficiencies: H<sub>2</sub> (2.5), H<sub>2</sub>O (12.0), CO (1.9), CO<sub>2</sub> (3.8), Ar and He (0.4), and 1.0 for all other species.

<sup>d</sup> Chaperon efficiencies: H<sub>2</sub> (2.5), H<sub>2</sub>O (12.0), CO (1.9), CO<sub>2</sub> (3.8), Ar and He (0.5), and 1.0 for all other species.

<sup>e</sup> Chaperon efficiencies: H<sub>2</sub> (2.5), H<sub>2</sub>O (12.0), CO (1.9), CO<sub>2</sub> (3.8), Ar and He (0.2), and 1.0 for all other species.

<sup>f</sup> Chaperon efficiencies: H<sub>2</sub> (2.5), H<sub>2</sub>O (12.0), CO (1.9), CO<sub>2</sub> (3.8), Ar and He (0.7), and 1.0 for all other species.

<sup>g</sup> Chaperon efficiencies: H<sub>2</sub> (2.5), H<sub>2</sub>O (6.0), H<sub>2</sub>O<sub>2</sub> (6.0), CO (1.5), CO<sub>2</sub> (2.0), Ar (0.7), and He (0.4), and 1.0 for all other species; Troe falloff with  $F_c = 0.43$ .

peroxide reactions we include  $OH + OH + M \rightleftharpoons H_2O_2 + M$ , which is also a radical–radical recombination reaction, along with  $HO_2 + HO_2 \rightleftharpoons H_2O_2 + O_2$ , which could equally well be listed with the hydroperoxyl reactions, as could  $H_2O_2 + H \rightleftharpoons HO_2 + H_2$ . The rationale here is that reactions involving H<sub>2</sub>O<sub>2</sub> are unimportant at sufficiently high temperatures and low pressures, so it is convenient to group them together at the end, where they can easily be omitted under such conditions. The HO<sub>2</sub> reactions that do not involve H<sub>2</sub>O<sub>2</sub> are grouped together because they often are important when H<sub>2</sub>O<sub>2</sub> is not, and when HO<sub>2</sub> is formed, its consumption by some of the five steps following its formation step often is important.

Underlying the rates in Table 1 is an implicit assumption of Boltzmann equilibration of internal degrees of freedom of all species, which begins to break down in sufficiently rapid processes such as those often encountered in detonations, to be discussed in Section 8.3. Reaction-rate adjustments are periodically proposed as more accurate experimental data become available, with many of the recent efforts placed on improvements of predictive capabilities under combustion conditions of interest for gas-turbine applications [13–15]. For most of the elementary reactions, the reaction-rate parameters listed in Table 1 are those selected in [10]. As explained below, updated values are given in the table for  $H_2O + O \rightleftharpoons OH + OH$ , which is now taken from Ref. [16], for  $HO_2 + OH \rightleftharpoons H_2O + O_2$ , which is adjusted with a bi-Arrhenius law to improve agreement with new experimental data, including

measurements of strain-induced diffusion-flame extinction at high pressure [17], and also for four of the six hydrogen-peroxide reactions, as suggested by new experimental data and recent theoretical developments.

For each elementary reaction, the table gives the parameters needed to compute the associated reaction-rate constant  $k = BT^n \exp(-T_a/T)$  in terms of the temperature  $T$ , including the activation temperature  $T_a$  and the constant  $B$  and temperature exponent  $n$  of the preexponential factor  $BT^n$ . The sum of two Arrhenius terms is employed to represent the more complex temperature dependence of the rate constants of reactions  $\text{HO}_2 + \text{OH} \rightleftharpoons \text{H}_2\text{O} + \text{O}_2$ ,  $\text{HO}_2 + \text{HO}_2 \rightleftharpoons \text{H}_2\text{O}_2 + \text{O}_2$ , and  $\text{H}_2\text{O}_2 + \text{OH} \rightleftharpoons \text{H}_2\text{O} + \text{HO}_2$ , including a minimum at an intermediate temperature for the first two coefficients. Chaperon efficiencies relative to that of nitrogen are provided in the footnotes for all three-body reactions, with temperature-averaged values utilized in some instances to avoid the introduction of different rate expressions for different third bodies. Also, the nonnegligible pressure dependences of reactions  $\text{H} + \text{O}_2 + \text{M} \rightleftharpoons \text{HO}_2 + \text{M}$  and  $\text{OH} + \text{OH} + \text{M} \rightleftharpoons \text{H}_2\text{O}_2 + \text{M}$  are accounted for in the mechanism, which employs Troe falloff. Table 1 lists a constant value of  $F_c$  (different for the two reactions) since recent investigations have indicated that, within existing uncertainties, the more complicated temperature-dependent Troe falloff is unnecessary for these two steps.

## 2.2. The role of the hydrogen–oxygen shuffle reactions

The first four reactions in Table 1 are the so-called hydrogen–oxygen shuffle reactions, which describe the rapid interconversion of radicals  $\text{H}$ ,  $\text{O}$ , and  $\text{OH}$  and the corresponding local composition of the radical pool that exists in hot flames. The temperature dependences of their rates cause these reactions to be faster in hot regions, where they are often found individually to maintain equilibrium. In those hot regions, three relationships relating the concentrations of  $\text{H}$ ,  $\text{O}$ , and  $\text{OH}$  to those of  $\text{H}_2$ ,  $\text{O}_2$ , and  $\text{H}_2\text{O}$  can be derived from these equilibrium equations. Since equilibrium of the fourth reaction is a direct consequence of equilibria of the second and third reactions, this last reaction,  $\text{H}_2\text{O} + \text{O} \rightleftharpoons \text{OH} + \text{OH}$ , becomes effectively unimportant in such cases, in that the first three shuffle reactions  $\text{H} + \text{O}_2 \rightleftharpoons \text{OH} + \text{O}$ ,  $\text{H}_2 + \text{O} \rightleftharpoons \text{OH} + \text{H}$ , and  $\text{H}_2 + \text{OH} \rightleftharpoons \text{H}_2\text{O} + \text{H}$  are sufficient to describe the radical pool [18]. As a result, computations excluding  $\text{H}_2\text{O} + \text{O} \rightleftharpoons \text{OH} + \text{OH}$  give propagation velocities of planar laminar flames and associated radical profiles in excellent agreement with those obtained when considering all four shuffle reactions [19]. These individual equilibria do not hold, however, in low-temperature regions, including reaction layers of lean deflagrations near the flammability limit, for which neglecting  $\text{H}_2\text{O} + \text{O} \rightleftharpoons \text{OH} + \text{OH}$  results in an erroneous  $\text{O}$ – $\text{OH}$  balance [19].

An overall reaction representing the global effect of the shuffle reactions on the radical-pool balance can be derived from the first three shuffle reactions by noting that, under most conditions,  $\text{H}_2 + \text{O} \rightleftharpoons \text{OH} + \text{H}$  and  $\text{H}_2 + \text{OH} \rightleftharpoons \text{H}_2\text{O} + \text{H}$  are much faster than  $\text{H} + \text{O}_2 \rightleftharpoons \text{OH} + \text{O}$ , causing the concentrations of  $\text{O}$  and  $\text{OH}$  to be smaller than that of  $\text{H}$ . This rapid  $\text{O}$  and  $\text{OH}$  removal rate can be taken into account to write the overall chain-branching reaction



representing the effect of the elementary step  $\text{H} + \text{O}_2 \rightleftharpoons \text{OH} + \text{O}$ , followed by the occurrence of  $\text{H}_2 + \text{O} \rightleftharpoons \text{OH} + \text{H}$  to eliminate the  $\text{O}$  atom and of twice  $\text{H}_2 + \text{OH} \rightleftharpoons \text{H}_2\text{O} + \text{H}$  to remove the resulting two  $\text{OH}$  molecules. Clearly, since  $\text{O}$  and  $\text{OH}$  removal is rapid, the rate of the overall chain-branching reaction given in Eq. (1) is in the first approximation that of  $\text{H} + \text{O}_2 \rightleftharpoons \text{OH} + \text{O}$ . Because of its rate-

controlling role in the overall chain-branching step shown in Eq. (1), the elementary reaction  $\text{H} + \text{O}_2 \rightleftharpoons \text{OH} + \text{O}$  is of central importance for the description of hydrogen oxidation. Its rate influences in a fundamental way the combustion of all hydrogen-containing fuels, not only  $\text{H}_2$  and syngas, but also hydrocarbons and alcohols. Consequently, much attention has been devoted to the experimental measurement of this reaction constant.

## 2.3. Rate parameters for the hydrogen–oxygen shuffle reactions

The rate parameters displayed in Table 1 for  $\text{H} + \text{O}_2 \rightleftharpoons \text{OH} + \text{O}$  are based on the shock-tube data of Masten et al. [20] corresponding to temperatures in the range 1450–3370 K. Their results, supplemented by a new set of shock-tube measurements at lower temperature, were recently employed by Hong et al. [21] in deriving the reaction-rate coefficient adopted in [7,8]. The differences between the coefficient proposed by Hong et al. [21] and that of Table 1 are small at high temperatures but differ by as much as 10% at lower temperatures, extending down to 1100 K, the lowest temperature addressed by Hong et al. [21], resulting in the coefficient in Table 1 predicting a rate that is larger than that of Hong et al. [21] by about 10% at  $T = 1000$  K. At lower temperatures, where the rates are known less well, the rate from Table 1 crosses over that of Hong et al. [21], now becoming lower (rather than higher), by as much as 30% at 500 K. Differences on the order of 10% are also found over the temperature range  $900 \text{ K} \leq T \leq 2500 \text{ K}$  when the comparison is extended to the coefficients proposed for this reaction in most of the other detailed mechanisms [3,5,9–11] and also in other specific studies [22]. A notable exception is the constant used in [4,6], derived by Pirraglia et al. [23], which gives rate predictions in reasonable agreement with the other mechanisms at low temperatures, but that at high temperatures exceed those of the other schemes by a significant amount, on the order of 30% for  $T = 2500 \text{ K}$ . The decision to retain the previous rate, instead of adopting the newer recommendation of Hong et al. [21], is based on interest in a wider temperature range than the range 1100–1530 K of the new experiments, including interest in temperatures below the range 1100–3370 K for which the new correlation was recommended. It produces reasonably good agreement over the temperature range of these experiments for this step, the most important one in all of combustion.

As with  $\text{H} + \text{O}_2 \rightleftharpoons \text{OH} + \text{O}$ , the rate constants shown in the table for the remaining shuffle reactions are those employed in [10], except that of  $\text{H}_2\text{O} + \text{O} \rightleftharpoons \text{OH} + \text{OH}$ , which has been updated, with the value given in Table 1 calculated (by use of the equilibrium constant) from the rate constant proposed by Baulch et al. [16] for the reverse reaction. This modification, which brings the constant into line with those proposed in other recent detailed mechanisms, does not change in a measurable way any of the test results performed in [10]. For most applications of interest this reaction is either too slow, as it is for autoignition, or remains in equilibrium, as occurs in hot regions of flames, so that the specific rate selected is largely inconsequential, as long as the equilibrium constant is appropriately contained in the associated combustion calculations. On the other hand, the rate constants of  $\text{H}_2 + \text{O} \rightleftharpoons \text{OH} + \text{H}$  and of  $\text{H}_2 + \text{OH} \rightleftharpoons \text{H}_2\text{O} + \text{H}$ , taken from earlier references [24,25], are in good agreement with those employed in other detailed mechanisms [3–9,11], with departures remaining below approximately 10% in the temperature range  $900 \text{ K} \leq T \leq 2500 \text{ K}$ .

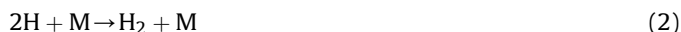
## 2.4. The role of the hydroperoxyl reactions and the crossover temperature

In the presence of a third body  $\text{M}$ , the collision of hydrogen atoms with oxygen molecules, which is involved in the rate-



controlling reaction  $\text{H} + \text{O}_2 \rightleftharpoons \text{OH} + \text{O}$ , can lead instead to the formation of hydroperoxyl through  $\text{H} + \text{O}_2 + \text{M} \rightleftharpoons \text{HO}_2 + \text{M}$ . Subsequent consumption of  $\text{HO}_2$  occurs mainly through collisions with  $\text{H}$ ,  $\text{O}$ , and  $\text{OH}$  (i.e., the five elementary reactions listed immediately below  $\text{H} + \text{O}_2 + \text{M} \rightleftharpoons \text{HO}_2 + \text{M}$  in Table 1), which are fast in high-temperature regions in flames, leading to small hydroperoxyl concentrations. In ignition processes, however, the concentrations of  $\text{H}$ ,  $\text{O}$ , and  $\text{OH}$  are so small that the consumption of  $\text{HO}_2$  proceeds initially at a negligibly slow rate, with  $\text{HO}_2$  building up as if it were a combustion product. For these ignition cases, the competition of the elementary reaction  $\text{H} + \text{O}_2 + \text{M} \rightleftharpoons \text{HO}_2 + \text{M}$ , which eliminates one radical  $\text{H}$ , with the overall chain-branching reaction given in Eq. (1), which produces two  $\text{H}$  atoms with a rate equal to that of reaction  $\text{H} + \text{O}_2 \rightleftharpoons \text{OH} + \text{O}$ , defines the so-called crossover temperature, whose value depends on the pressure through the presence of the third-body concentration in the resulting equation. Fast radical branching leading to a branched-chain explosion occurs only for temperatures above this crossover value, such that the rate of  $\text{H}$ -atom production becomes larger than that of termination. Besides being influenced by the pressure, the resulting crossover value depends also on the mixture composition through the chaperon efficiency involved in the third-body collisions. In particular, since water vapor is found to be a very efficient collider, its presence in large concentrations increases considerably the crossover temperature.

A modified crossover temperature applies to the description of flames, where the presence of radicals enables radical regeneration to occur by consumption of hydroperoxyl. When the conditions are not too fuel-lean, the removal of  $\text{HO}_2$  is mainly through the forward steps  $\text{HO}_2 + \text{H} \rightarrow \text{OH} + \text{OH}$  and  $\text{HO}_2 + \text{H} \rightarrow \text{H}_2 + \text{O}_2$ , with the former being chain-carrying and the latter being chain-terminating, thereby modulating the effective radical-removal rate associated with step  $\text{H} + \text{O}_2 + \text{M} \rightleftharpoons \text{HO}_2 + \text{M}$ . For instance, the overall recombination reaction



is obtained when the  $\text{HO}_2$  molecule produced by  $\text{H} + \text{O}_2 + \text{M} \rightleftharpoons \text{HO}_2 + \text{M}$  is consumed by  $\text{HO}_2 + \text{H} \rightarrow \text{H}_2 + \text{O}_2$ . On the other hand, when the consumption of  $\text{HO}_2$  proceeds through  $\text{HO}_2 + \text{H} \rightarrow \text{OH} + \text{OH}$  followed by rapid removal of the two  $\text{OH}$  molecules through  $\text{H}_2 + \text{OH} \rightleftharpoons \text{H}_2\text{O} + \text{H}$  to regenerate two  $\text{H}$  atoms, the resulting overall reaction  $2\text{H}_2 + \text{O}_2 \rightarrow 2\text{H}_2\text{O}$  leaves the radical population unaltered. Since the rate of  $\text{HO}_2 + \text{H} \rightarrow \text{OH} + \text{OH}$  is about five times larger than that of  $\text{HO}_2 + \text{H} \rightarrow \text{H}_2 + \text{O}_2$ , only one out of six molecules of  $\text{HO}_2$  produced by  $\text{H} + \text{O}_2 + \text{M} \rightleftharpoons \text{HO}_2 + \text{M}$  follows the  $\text{H}$ -atom recombination path through Eq. (2). For flames, therefore, the crossover temperature is determined by equating the rate of the branching reaction shown in Eq. (1), given by that of the elementary reaction  $\text{H} + \text{O}_2 \rightleftharpoons \text{OH} + \text{O}$ , to the rate of the recombination reaction  $2\text{H} + \text{M} \rightarrow \text{H}_2 + \text{M}$ , given approximately by one sixth of the rate of  $\text{H} + \text{O}_2 + \text{M} \rightleftharpoons \text{HO}_2 + \text{M}$ , yielding a value that is about 100 K smaller for flames than it is for ignition. In fuel-lean combustion, the reaction  $\text{HO}_2 + \text{OH} \rightarrow \text{H}_2\text{O} + \text{O}_2$ , which is chain-terminating, also becomes a significant  $\text{HO}_2$ -consumption step, and this needs to be taken into account in computing the resulting crossover temperature, which in turn determines the flammability limit of lean premixed flames [19,26].

The two overall reactions given in Eqs. (1) and (2) have been known for years to provide the basis for understanding hydrogen combustion. The shuffle reactions are fast at high temperature, and in hot regions they tend to produce radicals according to Eq. (1). Since this reaction is very weakly exothermic (its heat of reaction being only about a tenth of that of Eq. (2)), heat release is necessarily associated with radical recombination. As a result, both

reactions given in Eqs. (1) and (2) are interdependent, with Eq. (1) providing the radicals to be recombined through Eq. (2), and Eq. (2) releasing the heat needed to elevate the temperature sufficiently for Eq. (1) to proceed at a significant rate. In the interplay, it is noteworthy that the initial stage of  $\text{H}_2$  oxidation through Eq. (1) requires three molecules of hydrogen per molecule of oxygen, and not two as in the overall oxidation reaction  $2\text{H}_2 + \text{O}_2 \rightleftharpoons 2\text{H}_2\text{O}$ . For steady planar hydrogen–air flames, this altered stoichiometry can be conjectured to be one of the reasons behind the prominent displacement observed in the curve of burning rate as a function of the equivalence ratio  $\phi$  (the fuel–air ratio divided by the stoichiometric fuel–air ratio), with peak burning rates reached not far above the value  $\phi = 1.5$  associated with Eq. (1).

The relatively large value of the activation temperature of  $\text{H} + \text{O}_2 \rightleftharpoons \text{OH} + \text{O}$  makes branching quite sensitive to temperature changes, while the recombination rate, proportional to that of  $\text{H} + \text{O}_2 + \text{M} \rightleftharpoons \text{HO}_2 + \text{M}$ , is much less temperature-dependent. As a result, in nonhomogeneous combustion processes thin branching layers often coexist with thicker recombination regions, a prominent feature of hydrogen combustion to be discussed in the following sections. That occurs, for instance, in deflagrations far from flammability limits, with recombination extending downstream from a thin branching layer [18], and also in nonpremixed flames far from extinction [27], where rapid branching through Eq. (1) is found to occur in a thin layer separating a region with no oxygen molecules from a region with no hydrogen molecules, radical recombination occurring in a distributed manner outside the thin layer. Flammability limits for deflagrations and extinction conditions for diffusion flames are correspondingly approached when peak temperatures decrease to values not far above the crossover value, causing branching and recombination processes to compete in a single reaction region. Similarly, detonability and ignitability limits are the result of branching/recombination competition, although the associated crossover temperature is different from that of flames, as indicated above.

## 2.5. Rate parameters for the hydroperoxyl reactions

The degree of uncertainty associated with the rate constant of  $\text{H} + \text{O}_2 + \text{M} \rightleftharpoons \text{HO}_2 + \text{M}$  is still fairly large, despite the significant amount of work devoted to its determination, with open issues including mixing rules for multicomponent bath gases [8]. Most of the different reaction-rate constants currently used for this step in the different detailed mechanisms are based on the theoretical and experimental work carried out about ten years ago both in the low-pressure limit and in the falloff regime (e.g. Refs. [28–30]), giving values that agree reasonably well with one another within experimental uncertainty. The rate constant given in Table 1 is based on the rate parameters and falloff recommendations of Troe for nitrogen as the bath gas [28]. As with the radical–radical recombination reactions listed below in the table, rather than introducing the complication of having to use different rate expressions for different chaperons, approximate constant values are employed for the different chaperon efficiencies, with the high value for water being selected for agreement with measured autoignition times and diffusion-flame extinction by water addition [10].

Regarding the three reactions of  $\text{HO}_2$  with  $\text{H}$ , although significant uncertainties persist in values of the associated reaction constants, it is widely accepted that the branching channel leading to  $\text{OH} + \text{OH}$  and the radical-terminating channel leading to  $\text{H}_2 + \text{O}_2$  are dominant, while the channel leading to  $\text{H}_2\text{O} + \text{O}$  is less important, and it has been entirely ignored in some of the detailed mechanisms [3,4,8]. The rate parameters given in Table 1 for  $\text{HO}_2 + \text{H} \rightleftharpoons \text{H}_2\text{O} + \text{O}$  are those of [31], while those for  $\text{HO}_2 + \text{H} \rightleftharpoons \text{OH} + \text{OH}$  and  $\text{HO}_2 + \text{H} \rightleftharpoons \text{H}_2 + \text{O}_2$  are taken from the

work of Mueller et al. [32], also employed in Refs. [3,4]. The relative value of these two last constants largely determines the fraction of  $\text{HO}_2$  molecules formed that leads eventually to radical termination, a fraction which in turn enters as a proportionality factor in the overall rate of the recombination reaction shown in Eq. (2), the dominant heat-release process in high-temperature hydrogen oxidation. With the fairly low activation temperatures given in Table 1 for these two reactions, the branching-to-termination ratio does not change much over the entire temperature range of interest, giving a value of around five for  $1000 \text{ K} < T < 2500 \text{ K}$ . For these two reactions,  $\text{HO}_2 + \text{H} \rightleftharpoons \text{OH} + \text{OH}$  and  $\text{HO}_2 + \text{H} \rightleftharpoons \text{H}_2 + \text{O}_2$ , separate modification of one of the two rate constants without consideration of an accompanying revision of the other rate constant alters the overall recombination rate given in Eq. (2), so that it is advisable to consider both reactions jointly in proposing changes to any given mechanism.

While the rate parameters given in Mueller et al. [32] for  $\text{HO}_2 + \text{H} \rightleftharpoons \text{OH} + \text{OH}$  and  $\text{HO}_2 + \text{H} \rightleftharpoons \text{H}_2 + \text{O}_2$  were based on low-temperature measurements, later assessment [33] of the reverse rate of the second reaction,  $\text{H}_2 + \text{O}_2 \rightarrow \text{HO}_2 + \text{H}$ , which dominates radical initiation in high-temperature auto-ignition processes, showed this rate to be considerably larger at high temperature than that predicted by the expression proposed in [32], employed in Table 1. The alternative reaction rate given in Ref. [33] has been adopted by four of the detailed mechanisms discussed herein [6,7,9,11], and it is also used in deriving the rate employed in Refs. [8,12]. These last authors recommended, however, a 25% reduction and a 30% reduction, respectively, in the preexponential factor, a modification needed to maintain agreement with the low-temperature flow-reactor speciation data of Mueller et al. [32], while maintaining agreement with the high-temperature measurements of Michael et al. [33], within experimental uncertainty. With that modification, at temperatures of the order of  $T = 1000 \text{ K}$ , the reaction-rate constant proposed in [8] agrees with that shown in Table 1, but the rate is still significantly larger at higher temperatures, by a factor that exceeds 2 at  $T = 2000 \text{ K}$ , an expected difference in view of the experimental results of Michael et al. [33]. The differences in high-temperature ignition times computed by replacing the rate expression of Mueller et al. [32] for reaction  $\text{HO}_2 + \text{H} \rightleftharpoons \text{H}_2 + \text{O}_2$  with that of Burke et al. [8] are, however, much smaller, on the order of 5–10% at  $T = 1500\text{--}2500 \text{ K}$ , this being a result of the well-known weak (logarithmic) dependence of the chain-branching explosion time on the initiation constant [34]. Since the resulting improvement in ignition-time predictions is limited, consideration of the need for a modified rate of  $\text{HO}_2 + \text{H} \rightleftharpoons \text{H}_2 + \text{O}_2$ , as suggested by the results of Ref. [33], is deferred here until high-temperature experimental data are available to assess the accuracy of the rate constant employed for the accompanying branching channel  $\text{HO}_2 + \text{H} \rightleftharpoons \text{OH} + \text{OH}$ . Therefore, for these two reactions, we maintain in Table 1 the reaction parameters recommended by Mueller et al. [32]. The consequent underprediction of the high-temperature initiation rate will not have a large effect on predicted high-temperature induction times, and the importance of future clarifications of high-temperature rate parameters for  $\text{HO}_2 + \text{H} \rightleftharpoons \text{OH} + \text{OH}$  is thereby emphasized.

Although experimental measurements for the rate of  $\text{HO}_2 + \text{O} \rightleftharpoons \text{OH} + \text{O}_2$  are scarce and pertain only to low-temperature conditions, it is generally agreed that this reaction plays a negligible role under all combustion conditions of practical interest. The constant reaction-rate coefficient shown in Table 1, also used in Ref. [9], is taken from Ref. [35]. Other mechanisms [5,7,11] consider instead a negative temperature dependence for this reaction by introducing a small negative activation temperature that, over the temperature range of interest, gives values in close agreement with that of Table 1. Even for the larger reaction-

rate values adopted in [3,4,6,8], this reaction is always found to be unimportant compared with the other hydroperoxyl-consuming reactions. Further assessment of this reaction rate must wait until more accurate experimental data become available.

Under near-limit conditions, such as those found in very lean deflagrations [19,26] and in strongly stretched nonpremixed flames [17], the OH-to-H concentration ratio becomes larger, especially at elevated pressures, thereby causing the hydroperoxyl-consuming reaction  $\text{HO}_2 + \text{OH} \rightleftharpoons \text{H}_2\text{O} + \text{O}_2$  to become increasingly important, compared with those involving collisions of  $\text{HO}_2$  with H atoms. The rate constant for this reaction was originally based on low-temperature experimental data, which suggested a weak temperature dependence involving a negative activation energy [31], adopted in Refs. [3,4,6–8,10]. Later experiments at higher temperature showed this reaction rate to display an anomalous temperature dependence [36,37], in the sense that it achieved a minimum at an intermediate temperature – about  $T \approx 1100 \text{ K}$  according to Ref. [37] – and exhibited a sharp increase at higher temperatures. Recent experimental data further confirmed the emergence of a minimum [38,39], although the rate increase at higher temperatures found in these recent studies was considerably less pronounced than that predicted earlier [36,37].

The addition of as many as five Arrhenius terms has been suggested to account for the various channels that determine the anomalous temperature dependence of  $\text{HO}_2 + \text{OH} \rightleftharpoons \text{H}_2\text{O} + \text{O}_2$  [40]. Here, as in other mechanisms [5,9,11], we choose to represent the rate by a bi-Arrhenius expression, an approach also adopted in other recent investigations [39,41]. As in previous studies [5,16], the expression with a negative activation temperature proposed in [31] is retained to represent the low-temperature behavior, while the increase at high temperature is obtained by addition of a second Arrhenius term with a large positive activation energy, namely that from [39]. The value of the low-temperature term in [39] is close to that predicted by the term that we retain, although it does exhibit a somewhat stronger temperature dependence. The additional term gives a negligible contribution at low temperatures but becomes dominant for  $T \gtrsim 2100 \text{ K}$ . With the new rate parameters for this step, agreement with experiments on strain-induced extinction of hydrogen–air diffusion flames at high pressures [17] is significantly improved.

A primary objective of the San Diego mechanism is to maintain rate descriptions that are as simple as possible, to facilitate its application, and therefore in the past bi-Arrhenius descriptions have been excluded. Unfortunately, without at least two terms, reasonable fits to rates that tend to exhibit minima in the vicinity of temperatures of interest can seldom be obtained. Moreover, failure to account for the two channels for this last step substantially degrades agreements of prediction with recent measurements of pressure dependences of diffusion-flame extinction conditions in super-atmospheric experiments [17]. For these reason, the two terms in Table 1 for this step are now introduced. Having agreed to accept this (admittedly rather minor) complication for this step, the same type of revision is introduced in the table for other steps that warrant it, as indicated below.

## 2.6. Radical–radical recombinations

Although under most conditions the rate of radical recombination is mainly controlled by the elementary reaction  $\text{H} + \text{O}_2 + \text{M} \rightleftharpoons \text{HO}_2 + \text{M}$ , as discussed above, the radicals H, O, and OH can also recombine through radical–radical collisions, i.e., the four direct recombination reactions listed in Table 1. In particular, the first two reactions,  $\text{H} + \text{OH} + \text{M} \rightleftharpoons \text{H}_2\text{O} + \text{M}$  and  $\text{H} + \text{H} + \text{M} \rightleftharpoons \text{H}_2 + \text{M}$ , have a significant influence in the downstream region of stoichiometric and rich deflagrations and also on

the rich side of nonpremixed flames, so that they necessarily must be included for increased accuracy in computations of these flames. These two reactions are also essential for describing chemical equilibrium at high temperature, a key factor in accurate computations of detonations, for example. By way of contrast, the two recombination reactions  $O + O + M \rightleftharpoons O_2 + M$  and  $H + O + M \rightleftharpoons OH + M$  are of lesser importance under most conditions, the last never having been found to be significant and included here only for completeness, with rate parameters the same as those in practically all of the rest of the mechanisms. Besides, the contribution of the reverse reaction  $O_2 + M \rightarrow O + O + M$  to the initiation of the chemical reaction in the absence of radicals is found to be always negligible. Instead, autoignition processes are typically initiated by the hydroperoxyl reaction  $H_2 + O_2 \rightarrow HO_2 + H$  [33], with the hydrogen dissociation reaction  $H_2 + M \rightarrow H + H + M$  emerging as a significant additional source of radicals in hydrogen-rich atmospheres at high temperature. The rationale for the selection of the reaction-rate parameters given here for these radical–radical recombination reactions, including the introduction of temperature-averaged chaperon efficiencies to avoid consideration of different reaction rates for different third bodies, is explained in Ref. [10]. For some of them, such as  $H + OH + M \rightleftharpoons H_2O + M$ , experiments [42] show that constant chaperon efficiencies cannot accurately reproduce data for different colliders, and so errors as large as a factor of five are tolerated here to achieve the simplifications selected.

The additional radical–radical recombination step  $O + OH + M \rightleftharpoons HO_2 + M$ , included in the previous 21-step version of our mechanism [10] and also in Ref. [6], is no longer considered here because the rate parameters selected for it were based on older estimates which resulted in the rate being too large, as may clearly be seen from a recent discussion [8]. In particular, a new upper bound for the rate is an order of magnitude smaller than our original rate, which, in turn, was an order of magnitude smaller than the first published estimate. We have recently found that unless the rate of this step is at least an order of magnitude below the newly estimated upper bound, there is notable degradation in predicted burning velocities and diffusion-flame extinction conditions at elevated pressures. While the correct rate is not known, it must be small enough for the influence of this step to be negligible if computations are to provide good agreement with experiments of interest, and therefore this step is deleted here, reducing the mechanism to 20 steps.

Two other steps that are not included in Table 1 are worth mentioning here, namely  $H_2 + O_2 \rightleftharpoons OH + OH$  and  $H_2 + O_2 \rightleftharpoons H_2O + O$ . The first of these had often been included as an important initiation step, until it was shown [33] that its activation energy is so high that it is always negligible in comparison with  $H_2 + O_2 \rightleftharpoons HO_2 + H$  in initiation. For this reason it was omitted in our earlier work [10], although some mechanisms, such as Ref. [5], retain it at an appropriately revised reduced rate. The second of these steps,  $H_2 + O_2 \rightleftharpoons H_2O + O$ , could also serve as an initiation step, but it has never been included in any mechanism because it was always thought to be too slow to be of importance, as indeed has been verified in more recent work, although its rate is in fact comparable with that of  $H_2 + O_2 \rightleftharpoons OH + OH$ . In general, Table 1 does not include steps believed to be of no importance under any condition of interest, although some of the steps, such as the last two radical–radical recombinations, included for completeness, have not yet been determined to be important.

## 2.7. Hydrogen peroxide reactions

Combustion conditions including high pressures and low temperatures tend to favor the appearance of significant amounts of

hydrogen peroxide, because the associated high concentrations of  $HO_2$  promote  $H_2O_2$  production, mainly through  $HO_2 + HO_2 \rightarrow H_2O_2 + O_2$  but also to some extent through  $HO_2 + H \rightarrow H_2O_2 + H$ . In the presence of hydrogen peroxide, radical regeneration by the reverse of  $OH + OH + M \rightleftharpoons H_2O_2 + M$  opens up an alternative chain-branching path, associated with the third explosion limit (to be discussed later), that becomes essential for high-pressure deflagrations near flammability limits, for detonations near detonability limits, and for autoignition at temperatures below crossover, where the enhanced rate of  $H + O_2 + M \rightleftharpoons HO_2 + M$  precludes branching through the overall reaction shown in Eq. (1). For all of these combustion conditions, the  $H_2O_2$  consumption rate through the last four forward reactions listed in Table 1 is typically very small, as is the associated production rate through the last three reverse reactions. The reaction  $HO_2 + H_2 \rightarrow H_2O_2 + H$ , on the other hand, is found to have a significant effect on rich detonations and on auto-ignition of rich mixtures at high pressures, and therefore it needs to be retained together with  $HO_2 + HO_2 \rightarrow H_2O_2 + O_2$  and  $H_2O_2 + M \rightarrow OH + OH + M$  in describing the evolution of hydrogen peroxide.

Updated values are given in Table 1 for the rate parameters of four of the six reactions involving hydrogen peroxide, the only two exceptions being  $H_2O_2 + H \rightleftharpoons H_2O + OH$  and  $H_2O_2 + O \rightleftharpoons HO_2 + OH$ , for which the listed parameters are those selected in [10]. For  $OH + OH + M \rightleftharpoons H_2O_2 + M$ , ab-initio calculations have recently been used [43] to derive a two-term expression for the high-pressure coefficient  $k_\infty$  that is more accurate over the temperature range 60–5000 K than any results that can be deduced from the meager available experimental high-pressure data. These theoretical results were used in deriving recently [44] a simple one-term power-law expression that fits the theoretical results in the range 300–1500 K. The same fitting procedure was employed in determining the expression used in Table 1 for this high-pressure coefficient, although here the temperature range  $500\text{ K} < T < 3000\text{ K}$  was considered instead in adjusting the expression, thereby resulting in rate parameters that are slightly different from those given in Ref. [44]. In addition, the low-pressure coefficient  $k_0$  given in Ref. [44] is adopted here as an improvement over our previous selection. Troe falloff for this step is now computed with the constant value  $F_c = 0.43$  in place of the previous more complicated expression, it having clearly been shown in this cited new work that, given existing uncertainties, this constant value is preferable.

The rate constant for the reaction  $HO_2 + HO_2 \rightleftharpoons H_2O_2 + O_2$  has been known for some time to reach a minimum at an intermediate temperature of about 800 K [37,45], giving an anomalous temperature dependence that cannot be described with the simple Arrhenius law employed previously [10] but that can be fit with a bi-Arrhenius rate expression [37,45]. Having been forced to do this for  $HO_2 + OH \rightleftharpoons H_2O + O_2$ , we now accept a similar fit here. Although the rate parameters suggested in the 1990 analysis of Hippler et al. [45] have been adopted in most of the chemical-kinetic mechanisms [3,4,7–9,11], later experiments [37], further reconfirmed recently [39], seem to indicate that this rate constant tends to overpredict the reaction rate by a significant amount at temperatures above 1000 K, so that the alternative expression suggested by Kappel et al. [37], and adopted by Konnov [5], appears to be a more accurate representation of the reaction rate. This expression is therefore selected for this reaction in Table 1.

The other rate constants that have been revised since the publication of the mechanism [10] are those for the steps  $H_2O_2 + H \rightleftharpoons HO_2 + H_2$  and  $H_2O_2 + OH \rightleftharpoons H_2O + HO_2$ . Regarding the former reaction, the parameters adopted now are those determined in Ref. [46] on the basis of measurements of low-temperature



autoignition histories and comparisons with experimental data. Their analysis concluded that the rate constant originally proposed in Ref. [47], adopted for instance in Ref. [8], must be modified by reducing its preexponential factor by about a factor of two while maintaining the same value of the activation temperature, as is needed to reproduce correctly the temperature dependence observed in early experiments performed for  $713\text{ K} < T < 773\text{ K}$  [48]. A weaker temperature dependence is present in the rate coefficient recommended for this reaction in Ref. [16], used in other mechanisms [5,11], giving differences with the rate constant used here that remain smaller than 30% in the range  $700\text{ K} < T < 900\text{ K}$  but become significantly larger at both smaller and larger temperatures. Clearly, more extensive experimental measurements including higher temperatures would be needed for a more accurate assessment of the rate coefficient of this reaction, as would be desirable given the prominent role of its reverse reaction in low-temperature high-pressure combustion processes.

As for the reaction  $\text{H}_2\text{O}_2 + \text{OH} \rightleftharpoons \text{H}_2\text{O} + \text{HO}_2$ , different shock-tube studies [36,49] at temperatures on the order of and also larger than  $1000\text{ K}$  have shown its temperature sensitivity to be larger at these high temperatures than that displayed by our previous rate constant [10]. Large discrepancies are found between the two experimental studies, with the first study [36] suggesting an activation temperature about four times larger than that of the more recent study [49]. Reconciling the new high-temperature data with previous measurements near room temperature, which indicated a much weaker temperature dependence, again requires utilization of a two-term Arrhenius expression for this reaction, with different expressions needed depending on the high-temperature data used in the fit [36,49]. Here we adopt the expression suggested by Hong et al. [49], which appears to be supported by more carefully monitored measurements of hydrogen peroxide concentration histories. It is worth mentioning that, although the new expression is markedly different from that employed previously [10], in the range  $500\text{ K} < T < 1200\text{ K}$  differences are smaller than 30%.

### 3. Simplified chemistry descriptions for hydrogen oxidation

The detailed chemical-kinetic mechanism shown in Table 1 provides a sufficiently accurate description of most hydrogen–oxygen combustion processes, the only exception being the extreme conditions of temperature and pressure encountered in many detonative processes, as discussed later, for which a correct description is not currently available. Despite the relative simplicity of the resulting scheme, which contains only 20 reversible elementary reactions and 8 reactive species, combustion at high Reynolds numbers or in complex configurations excessively taxes computational capabilities, so that simplifications are needed to provide a more manageable chemistry description that still has sufficient accuracy to yield reliable computational results.

#### 3.1. A sufficiently accurate short mechanism

A first simplification follows from observing that some of the elementary reactions in Table 1 contribute negligibly to the reaction process under most conditions of interest and can therefore be discarded in the first approximation. In particular, as shown in Ref. [50], the twelve steps listed in Table 2, only six of which are reversible, describe accurately premixed and non-premixed combustion, as well as autoignition, over the whole flammability range, from low to very high pressure. This mechanism is to be used as a basis for the discussions in the remainder of the paper. To facilitate the evaluation of analytic results, for the six reversible reactions

**Table 2**

Rate coefficients in Arrhenius form  $k = BT^n \exp(-T_a/T)$  for the skeletal mechanism with rate parameters in mol, s,  $\text{cm}^3$ , kJ, and K.

	Reaction	B	n	$T_a$
1f	$\text{H} + \text{O}_2 \rightarrow \text{OH} + \text{O}$	$3.52 \times 10^{16}$	−0.7	8590
1b	$\text{OH} + \text{O} \rightarrow \text{H} + \text{O}_2$	$3.03 \times 10^4$	−0.26	72
2f	$\text{H}_2 + \text{O} \rightarrow \text{OH} + \text{H}$	$5.06 \times 10^4$	2.67	3165
2b	$\text{OH} + \text{H} \rightarrow \text{H}_2 + \text{O}$	$3.03 \times 10^4$	2.63	2433
3f	$\text{H}_2 + \text{OH} \rightarrow \text{H}_2\text{O} + \text{H}$	$1.17 \times 10^9$	1.3	1825
3b	$\text{H}_2\text{O} + \text{H} \rightarrow \text{H}_2 + \text{OH}$	$1.28 \times 10^{10}$	1.19	9412
4f	$\text{H} + \text{O}_2 + \text{M} \rightarrow \text{HO}_2 + \text{M}^a$	$k_0$	−1.4	0.0
		$k_\infty$	0.44	0.0
5f	$\text{HO}_2 + \text{H} \rightarrow \text{OH} + \text{OH}$	$7.08 \times 10^{13}$	0.0	148
6f	$\text{HO}_2 + \text{H} \rightarrow \text{H}_2 + \text{O}_2$	$1.66 \times 10^{13}$	0.0	414
6b	$\text{H}_2 + \text{O}_2 \rightarrow \text{HO}_2 + \text{H}$	$2.69 \times 10^{12}$	0.36	27,888
7f	$\text{HO}_2 + \text{OH} \rightarrow \text{H}_2\text{O} + \text{O}_2$	$2.89 \times 10^{13}$	0.0	−250
		$4.50 \times 10^{14}$	0.0	5500
8f	$\text{H} + \text{OH} + \text{M} \rightarrow \text{H}_2\text{O} + \text{M}^b$	$4.00 \times 10^{22}$	−2.0	0.0
8b	$\text{H}_2\text{O} + \text{M} \rightarrow \text{H} + \text{OH} + \text{M}^b$	$1.03 \times 10^{23}$	−1.75	59,675
9f	$\text{H} + \text{H} + \text{M} \rightarrow \text{H}_2 + \text{M}^c$	$1.30 \times 10^{18}$	−1.0	0.0
9b	$\text{H}_2 + \text{M} \rightarrow \text{H} + \text{H} + \text{M}^c$	$3.04 \times 10^{17}$	−0.65	52,092
10f	$\text{H}_2\text{O}_2 + \text{M} \rightarrow \text{OH} + \text{OH} + \text{M}^d$	$k_0$	−4.20	25,703
		$k_\infty$	−1.27	25,703
11f	$\text{HO}_2 + \text{HO}_2 \rightarrow \text{H}_2\text{O}_2 + \text{O}_2$	$1.03 \times 10^{14}$	0.0	5556
		$1.94 \times 10^{11}$	0.0	−709
12f	$\text{HO}_2 + \text{H}_2 \rightarrow \text{H}_2\text{O}_2 + \text{H}$	$7.80 \times 10^{10}$	0.61	12,045

<sup>a</sup> Chaperon efficiencies:  $\text{H}_2$  (2.5),  $\text{H}_2\text{O}$  (16.0),  $\text{CO}$  (1.2),  $\text{CO}_2$  (2.4), Ar and He (0.7), and 1.0 for all other species; Troe falloff with  $F_c = 0.5$ .

<sup>b</sup> Chaperon efficiencies:  $\text{H}_2$  (2.5),  $\text{H}_2\text{O}$  (12.0),  $\text{CO}$  (1.9),  $\text{CO}_2$  (3.8), Ar and He (0.4), and 1.0 for all other species.

<sup>c</sup> Chaperon efficiencies:  $\text{H}_2$  (2.5),  $\text{H}_2\text{O}$  (12.0),  $\text{CO}$  (1.9),  $\text{CO}_2$  (3.8), Ar and He (0.5), and 1.0 for all other species.

<sup>d</sup> Chaperon efficiencies:  $\text{H}_2$  (2.5),  $\text{H}_2\text{O}$  (6.0),  $\text{H}_2\text{O}_2$  (6.0),  $\text{CO}$  (1.5),  $\text{CO}_2$  (2.0), Ar (0.7), and He (0.4), and 1.0 for all other species; Troe falloff with  $F_c = 0.43$ .

explicit expressions are given for both the forward and backward coefficients.

The accuracy with which this skeletal scheme describes premixed and nonpremixed flames and autoignition is illustrated in Figs. 1–3, which show results of sample numerical integrations employing the detailed and skeletal mechanisms (also included in Figs. 1 and 2 are results of reduced chemistry, represented by the dot-dashed curves, to be discussed later). In particular, Fig. 1 shows the variation with equivalence ratio of the laminar propagation velocity of a steady, planar, hydrogen–air deflagration for three different pressures. As can be seen, the agreement is excellent, with significant departures emerging only for rich flames at  $p = 50\text{ atm}$ , while for all other conditions typical errors remain below approximately 5% over the whole range of compositions explored in the

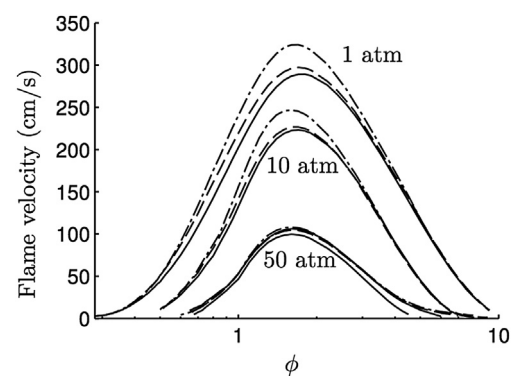


**Fig. 1.** The variation with equivalence ratio,  $\phi$ , of the laminar propagation velocity of hydrogen–air planar deflagrations with initial temperature  $T_u = 300\text{ K}$  and three different pressures as obtained with the detailed chemistry of Table 1 (solid curves), with the skeletal mechanism of Table 2 (dashed curves), and with the 2-step reduced mechanism shown in Eq. (15) (dot-dashed curves); based on Ref. [51].

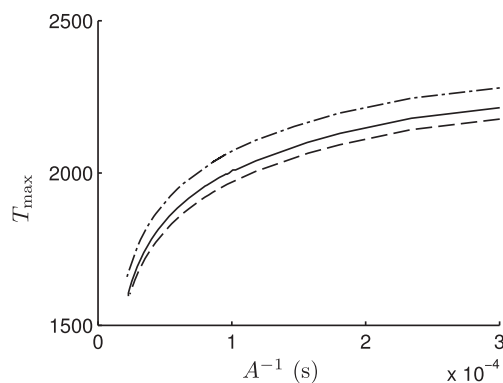


**Fig. 2.** The variation with strain rate,  $A$ , of the maximum temperature in a hydrogen–air planar counterflow at atmospheric pressure with feed-stream temperatures  $T = 300$  K as obtained with the detailed chemistry of Table 1 (solid curves), with the skeletal mechanism of Table 2 (dashed curves), and with the 2-step reduced mechanism shown in Eq. (15) (dot–dashed curves); based on Ref. [51].

figure. Hydrogen–air diffusion flames in planar counterflow configurations were also computed with the detailed and skeletal mechanisms, with resulting peak temperatures plotted in Fig. 2 as a function of the reciprocal of the strain rate of the air stream. The results indicate that the skeletal mechanism also performs well in nonpremixed environments. Not only do the differences in the predicted peak temperature remain typically below 30 K for conditions ranging from moderately strained flames to near extinction but also the skeletal mechanism reproduces accurately the critical strain rate at extinction. Ignition times computed with the temperature-inflection criterion for a stoichiometric hydrogen–air mixture in a homogeneous reactor are shown in Fig. 3. The degree of agreement between the results of the detailed and skeletal mechanism is such that the resulting curves are almost indistinguishable in the logarithmic scale of the plot, with noticeable differences appearing only for the atmospheric results at low temperature.

Skeletal mechanisms that contain even fewer reactions can be used for specific combustion conditions. For instance, the sub-mechanism formed by selecting the three shuffle reactions 1–3, the recombination reaction 4f, and the  $\text{HO}_2$ -consuming reactions 5f, 6f, and 7f, has been shown recently to describe lean deflagrations accurately [19,26]. The direct recombination reactions 8f and 9f need to be added if accuracy is required for stoichiometric and rich

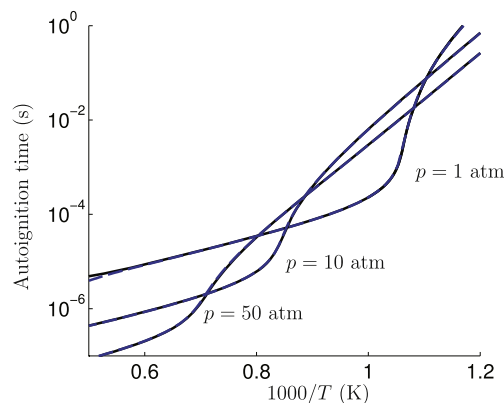


**Fig. 3.** The variation with initial temperature,  $T$ , of the induction time obtained with the inflection-point criterion in isobaric homogeneous combustion for a stoichiometric hydrogen–air mixture as obtained for three different pressures detailed chemistry of Table 1 (solid curves) and with the skeletal mechanism of Table 2 (dashed curves); based on Ref. [50].

deflagrations, as well as for non-premixed flames [51]. Another submechanism, formed by selecting the chain reactions 1f, 2f, and 3f, the recombination reaction 4f, and the initiation step 6b, describes accurately high-temperature autoignition [34], whereas description of low-temperature autoignition requires the addition of steps 10f–12f [52]. A skeletal mechanism containing 11 steps (all of those in Table 2 except for  $\text{H} + \text{H} + \text{M} \rightleftharpoons \text{H}_2 + \text{M}$ ) has been proposed for lean hydrogen combustion under conditions typical of gas-turbine operation [53].

### 3.2. Chemistry reduction: issues and techniques

Additional simplifications follow from application of systematic reduction techniques aimed at lowering the order of the system of differential conservation equations to be integrated by reducing the effective number of chemical species to be considered in the simulation. The number of species is, indeed, one of the main contributions to the cost of the chemistry integration in a reactive flow simulation. Even in the case of hydrogen oxidation the potential savings associated with the reduction of the number of species are substantial.

A number of additional factors influence the resulting computational costs. For instance, the number of chemical reactions considered also is of importance, because computing each Arrhenius rate has a non-negligible cost, since evaluating its exponential term requires many more CPU cycles than a simple addition or multiplication. The expressions for the rates of the overall chemical reactions of the reduced chemistry, typically more complicated than a simple Arrhenius term, may increase somewhat the associated computational times, so in reducing the chemistry it is important to keep these expressions as simple as possible, avoiding implicit representations. Care should also be exerted in connection with numerical stiffness. Depending on the specific reduction development, the resulting reduced system, although involving a smaller number of equations, may actually be stiffer than the complete one, and therefore less computationally efficient than the original system. It is also important to keep a certain level of simplicity in the model, in order for it to be easily accessible by the user, whether for analytical or numerical work.

There are a number of strategies for chemistry reduction [54,55], each one responding differently to the challenges listed above. Tabulated chemistry [56–58], for instance, consists of storing the chemical source terms in tables to avoid repeated calculations. There are numerous variants; some require computations prior to the simulation for the conditions expected to be encountered, while others evaluate chemical terms in run time. Common to all tabulated chemistry techniques is the need for a very optimized algorithm for storing and searching out data in the table in order to be efficient.

An alternative reduction strategy stems from identifying automatically the fast and slow time scales of the chemical system in order to decouple them. Fast time scales in chemistry are typically much shorter than the transport time scales. It is then possible to avoid having to compute them, thus reducing the order of the system by the number of fast time scales in the species conservation equations. This idea is the foundation of methods such as Computational Singular Perturbation [59–61] and Intrinsic Low-Dimensional Manifolds [62]. A different family of models stem from application of the so-called Rate-Controlled Constrained Equilibrium [63], which also exploits the disparity of the chemical time scales present in the system while making use of the second law of thermodynamics in the development. Although the conceptual derivation of these methods originated over forty years ago [64], applications to flame computations have been scarce because of issues regarding its formulation and its numerical solution [65].

The methods cited so far were developed specifically for use in numerical simulations. Their success relies on the fact that they are not fuel-specific, and the degree of reduction required is entered as a parameter, enabling the automatic reduction of the chemistry to be performed for complex fuels, including hundreds of species. However, the implementation of these methods is complex, and it is to be done at the root of the solver, hindering implementation in commercial codes. Although they can be quite effective, their automatic character obscures physical understanding of the chemical interactions occurring in the flow field and detracts from their utility in analytic studies. For these reasons, analytic methods for chemistry reduction employing rigorous approximations based on time disparities, such as the quasi-steady-state approximation for intermediates and the partial-equilibrium approximation for reversible elementary reactions [66], are more appropriate for many purposes, in particular when the starting detailed fuel chemistry is of moderate size. This occurs for hydrogen, leading to reduced descriptions with a small number of overall reactions that can be implemented readily in existing numerical codes.

### 3.3. The quasi-steady-state approximation

Although the partial-equilibrium approximation has been used in the past with some success to simplify the description of hydrogen combustion, for instance in deriving simplified formulations for numerical modeling of diffusion flames maintaining equilibria of the shuffle reactions [27,67], most of the recent reduced-chemistry developments have been based on the steady-state approximation. This approximation is applicable to the description of reaction intermediaries when their effective production and consumption rates are much larger than the corresponding accumulation and transport rates (by convection or diffusion). The term “quasi-steady-state” or, more simply, “steady-state” was coined in the original developments, dealing with transportless homogeneous systems, for which the steady-state approximation amounts to neglecting the time derivative of the given intermediate species, thereby reducing the conservation equation for this species to a balance between its production and consumption rates. In the more general case, the conservation equation for a given intermediate species includes not only the rate of accumulation but also the rates of convection and diffusion according to [66]

$$\underbrace{\frac{\partial Y_i}{\partial t} + \bar{v} \cdot \nabla Y_i + \frac{1}{\rho} \nabla \cdot (\rho Y_i \bar{V}_i)}_{1/t_M} = \frac{M_i \dot{C}_i}{\rho} = \underbrace{\frac{\dot{m}_i^+}{\rho}}_{1/t_i^+} - \underbrace{\frac{\dot{m}_i^-}{\rho}}_{1/t_i^-} \quad (3)$$

Here  $\rho$  and  $\bar{v}$  denote the density and flow velocity and  $Y_i$ ,  $\bar{V}_i$ ,  $M_i$ , and  $\dot{C}_i$  are the mass fraction, diffusion velocity, molecular mass, and chemical production rate (moles per unit volume per unit time) of the species considered. For the discussion, the chemical production term has been expressed by grouping together the elementary reactions that contribute to the production and consumption of the intermediate, with  $\dot{m}_i^+$  and  $\dot{m}_i^-$  denoting, respectively, the mass rate of production and consumption.

The conservation balance given in Eq. (3) has been conveniently divided by the local density, so that the dimension of the different terms is simply the inverse of a time, enabling the discussion of the orders of magnitude to be based on characteristic times. Thus, for a given combustion problem, a characteristic chemical production (consumption) time  $t_i^+$  ( $t_i^-$ ), measuring the order of magnitude of the production (consumption) rate of the given intermediary, can be obtained by evaluating the rate of appropriately selected key elementary reactions at representative values of the pressure and

temperature. These times are written below the corresponding chemical terms on the right-hand side of Eq. (3) to indicate their orders of magnitude. Also, the residence time, defined as the ratio of the characteristic length of the flow field to the characteristic flow velocity, serves to measure the order of magnitude of the rate of convection  $\bar{v} \cdot \nabla Y_i$ , and, similarly, there exist characteristic times for accumulation and diffusion, with values depending on the specific scales and time history of the problem at hand. The smallest of these three fluid-mechanical times, denoted by  $t_M$  in Eq. (3), identifies the dominant mechanical process.

The steady-state approximation arises when the conditions are such that  $t_M$  is much larger than the chemical times  $t_i^+$  and  $t_i^-$ . This condition guarantees that the accumulation, convection, and diffusion terms in Eq. (3) are much smaller than the chemical terms, and can consequently be neglected in the first approximation, thereby reducing the governing equation of the steady-state radical to a balance between chemical production and consumption. This algebraic equation replaces the corresponding differential equation in the flow-field description, thereby reducing by one the order of the system of differential equations to be integrated. In many instances, the chemical-balance equation  $\dot{C}_i = 0$  can be solved explicitly for the concentration of the steady-state species. The resulting values are often much smaller than those of the other intermediaries and also than those of the reactants, a property that can be taken into account in the systematic derivation of reduced mechanisms, as is done below for hydrogen oxidation.

Reduced chemical-kinetic mechanisms based on steady-state approximations are easier to develop for hydrogen–oxygen chemistry than for the oxidation of other fuels because fewer species and fewer elementary steps are involved for hydrogen. Note that, from a global-reaction viewpoint, the hydrogen oxidation chemistry is no more than a six-step mechanism, there being two atom (or element) conservation equations for the eight chemical species. In other words, although there are many more elementary chemical-kinetic reactions, there are only six independent differential equations for species conservation with nonzero chemical source terms.

Various mechanisms that are reduced to fewer than six steps have been proposed and tested in the literature. For example, a two-step mechanism has been derived for laminar deflagrations [18,68,69] and a one-step overall mechanism, systematically derived for sufficiently lean deflagrations, is accurate for many purposes [19,26], including the description of flame-ball structures and flammability limits [70,71]. There are also specific reductions for autoignition, which are markedly different depending on whether the initial temperature is above or below crossover [72]. Reductions for laminar diffusion flames [73–75] are much more similar to those for deflagrations than to those for autoignition, although even the reductions for these flames exhibit differences in detail. Reduced chemistry for detonations, used for instance in [76], resemble that for autoignition more closely than that for flames, because the solution in the induction zone right behind the shock is essentially determined by a high-temperature branched-chain explosion. Besides mechanisms targeting specific combustion conditions, there have been recent efforts to derive a systematically reduced description of hydrogen–oxygen chemistry that can be applied to a wide range of combustion processes with acceptable accuracy [50,51], as is needed for general computational approaches when it is not known in advance, at the start of a calculation, in exactly what manner the combustion will develop.

Many of these specific reduced descriptions are to be introduced below in the course of the discussion for application to the analysis of different combustion problems. Having defined a sufficiently accurate skeletal mechanism, shown in Table 2, it is of interest in this introductory section to complete the definition of the general chemical-kinetic framework by deriving the corresponding

reduced mechanisms that arise through the systematic introduction of steady-state assumptions for the different radicals, a development that largely follows that presented in Ref. [50].

#### 3.4. Systematically reduced chemical-kinetic mechanisms for hydrogen oxidation

The accuracy of the steady-state approximation and the number of intermediates that can be assumed to be in steady state without excessive loss of accuracy depend on the combustion conditions. Thus, in deflagrations, steady-state approximations can be assumed for OH, O, and HO<sub>2</sub> [19], while the same approximation for H atoms would be very poor except for conditions such that the peak temperature is not far above the crossover value, as occurs for instance near the lean flammability limit [19,26]. In diffusion flames, the steady state assumption for OH is more accurate than that for O for the purpose of calculating critical ignition and extinction strain rates in counterflow configurations, but even imposing both of these steady states leads to errors in critical strain rates only of about 20% [75]. Thus errors approaching 20% for certain results must be accepted in imposing the O and OH steady states to achieve the reduced chemistry. In autoignition processes at temperatures above crossover, on the other hand, a steady state assumption for HO<sub>2</sub> results in a poor approximation [34] and a steady state approximation for H would apply only under extremely fuel-lean conditions, beyond normal flammability limits, while for O and OH it is accurate in fuel-rich systems [77]. As for the molecule H<sub>2</sub>O<sub>2</sub>, its concentration is always sufficiently small for the steady-state approximation to be a very accurate representation under most conditions, the only exceptions being high-pressure deflagrations near flammability conditions and autoignition below crossover.

The above considerations indicate that the first step in seeking a reduced description for hydrogen oxidation involves introduction of steady-state assumptions for O and OH because these assumptions are reasonably accurate for flames and also during autoignition events, although larger errors are to be expected in ignition at temperatures above crossover, especially as the mixture becomes leaner [77]. Simpler reduced mechanism can be derived for flames, for which steady-state assumptions for both HO<sub>2</sub> and H<sub>2</sub>O<sub>2</sub> apply also with good accuracy. Simplifications to the four-step description also arise for autoignition away from the second explosion limit, although different approaches are needed depending on the existing conditions, in that for ignition at temperatures above crossover H<sub>2</sub>O<sub>2</sub> may be assumed to be in steady state but HO<sub>2</sub> may not, while the opposite is found for ignition below crossover. Consideration of either O, OH, and HO<sub>2</sub> or O, OH, and H<sub>2</sub>O<sub>2</sub> as steady-state species lead to two different three-step descriptions for ignition, which are given below, along with the two-step mechanism that can be derived for flame calculations by assuming all four species O, OH, HO<sub>2</sub>, and H<sub>2</sub>O<sub>2</sub> to be in steady state.

##### 3.4.1. The four-step mechanism

The development begins by writing the equations expressing the production rates of the different chemical species  $\dot{C}_i$  in terms of the rates of the different elementary steps of Table 2 to give

$$\begin{aligned}\dot{C}_{H_2} &= -\omega_2 - \omega_3 + \omega_6 + \omega_9 - \omega_{12f} \\ \dot{C}_{O_2} &= -\omega_1 - \omega_{4f} + \omega_6 + \omega_{7f} + \omega_{11f} \\ \dot{C}_{H_2O} &= \omega_3 + \omega_{7f} + \omega_8 \\ \dot{C}_H &= -\omega_1 + \omega_2 + \omega_3 - \omega_{4f} - \omega_{5f} - \omega_6 - \omega_8 - 2\omega_9 + \omega_{12} \\ \dot{C}_{HO_2} &= \omega_{4f} - \omega_{5f} - \omega_6 - \omega_{7f} - 2\omega_{11f} - \omega_{12f} \\ \dot{C}_{H_2O_2} &= -\omega_{10f} + \omega_{11f} + \omega_{12f} \\ \dot{C}_{OH} &= \omega_1 + \omega_2 - \omega_3 + 2\omega_{5f} - \omega_{7f} - \omega_8 + 2\omega_{10f} \\ \dot{C}_O &= \omega_1 - \omega_2\end{aligned}\quad (4)$$

Here  $\omega_{jf}$  and  $\omega_{jb}$  represent the forward and backward rates of the  $j$ -th reaction in the skeletal mechanism. When neither  $f$  nor  $b$  is present as a subscript, the corresponding rate  $\omega_j = \omega_{jf} - \omega_{jb}$  denotes the difference between the forward and backward rates.

The steady states for O and OH are largely a result of their fast consumption through the elementary reactions 2 and 3. Eliminating these fast rates in the equations for  $\dot{C}_{H_2}$ ,  $\dot{C}_{H_2O}$ , and  $\dot{C}_H$  by linear combinations with the equations for  $\dot{C}_{OH}$  and  $\dot{C}_O$ , and introducing the global rates

$$\begin{aligned}\omega_I &= \omega_1 + \omega_{5f} + \omega_{10f} \\ \omega_{II} &= \omega_{4f} + \omega_8 + \omega_9 - \omega_{11f} - \omega_{12f} \\ \omega_{III} &= \omega_{4f} - \omega_{5f} - \omega_6 - \omega_{7f} - 2\omega_{11f} - \omega_{12f} \\ \omega_{IV} &= -\omega_{10f} + \omega_{11f} + \omega_{12f}\end{aligned}\quad (5)$$

enables the first six equations in Eq. (4) to be rewritten in the alternative form

$$\begin{aligned}\dot{C}_{H_2} - \dot{C}_{OH} - 2\dot{C}_O &= -3\omega_I + \omega_{II} - \omega_{III} - \omega_{IV} \\ \dot{C}_{O_2} &= -\omega_I - \omega_{III} - \omega_{IV} \\ \dot{C}_{H_2O} + \dot{C}_O + \dot{C}_{OH} &= 2\omega_I \\ \dot{C}_H + \dot{C}_{OH} + 2\dot{C}_O &= 2\omega_I - 2\omega_{II} + \omega_{III} \\ \dot{C}_{HO_2} &= \omega_{III} \\ \dot{C}_{H_2O_2} &= \omega_{IV},\end{aligned}\quad (6)$$

which facilitates the identification of the reduced mechanism, as shown below.

In the steady-state approximation for O and OH, their transport and accumulation rates can be neglected in Eq. (3), so that their associated conservation equations reduce to  $\dot{C}_{OH} = \dot{C}_O = 0$ , thereby providing from Eq. (4) the two algebraic equations

$$\omega_1 + \omega_2 - \omega_3 + 2\omega_{5f} - \omega_{7f} - \omega_8 + 2\omega_{10f} = \omega_1 - \omega_2 = 0. \quad (7)$$

The concentrations of the steady-state species O and OH are very small compared with those of H<sub>2</sub>, H<sub>2</sub>O, or H and can be consequently neglected in the production-rate expressions of Eq. (6). It can be easily verified by inspection that the resulting simplified equations correspond to the four overall reactions



with rates given in Eq. (5), hence defining the reduced chemical-kinetic mechanism arising through introduction of the steady-state approximations for O and OH. Although the reduced chemistry could be expressed in terms of different alternative sets of overall reactions, the resulting formulations are all equivalent. The one selected here is written in an intuitive form that serves to identify the main chemical processes involved in hydrogen combustion. In particular, reactions I and II, which were anticipated earlier in Eqs. (1) and (2), represent the overall processes of chain branching and chain termination governing the dynamics of high-temperature hydrogen oxidation. The other two reactions, representing the production of HO<sub>2</sub> and H<sub>2</sub>O<sub>2</sub>, respectively, are most important for ignition applications.

The computation of the rates  $\omega_{1b}$ ,  $\omega_{7f}$ , and  $\omega_{8f}$  appearing in Eq. (5) requires knowledge of the concentrations of O and OH, which can be obtained in explicit form by solving their steady-state equations shown in Eq. (7) to give



$$C_{OH} = \left[ \left( A_1^2 + 4A_0A_2 \right)^{1/2} - A_1 \right] / (2A_2), \quad (9)$$

where

$$\begin{aligned} A_0 &= C_{H_2} k_{2f} \left( 2k_{1f} C_H C_{O_2} + k_{3b} C_H C_{H_2O} + 2k_{5f} C_H C_{HO_2} + 2k_{10f} C_{H_2O_2} C_{M_{10}} + k_{8b} C_{M_8} C_{H_2O} \right) \\ A_1 &= +C_{H_2} k_{2f} \left( k_{8f} C_{M_8} C_H + k_{7f} C_{HO_2} + k_{3f} C_{H_2} \right) - k_{1b} \left( k_{3b} C_H C_{H_2O} + 2k_{5f} C_H C_{HO_2} + 2k_{10f} C_{H_2O_2} C_{M_{10}} + k_{8b} C_{M_8} C_{H_2O} \right) \\ A_2 &= k_{1b} \left( 2k_{2b} C_H + k_{3f} C_{H_2} + k_{7f} C_{HO_2} + k_{8f} C_{M_8} C_H \right), \end{aligned} \quad (10)$$

and

$$C_O = \frac{k_{1f} C_H C_{O_2} + k_{2b} C_{OH} C_H}{k_{1b} C_{OH} + k_{2f} C_{H_2}}. \quad (11)$$

Here  $C_{M_j}$  represents the effective third-body concentration of reaction  $j$ , which accounts for the chaperon efficiencies indicated in Table 1. The four-step description defined in Eqs. (5) and (8), and Eqs. (9)–(11) provides sufficient accuracy for computations of hydrogen combustion under most conditions, reducing by two the number of differential equations that need to be integrated.

#### 3.4.2. The two separate three-step mechanisms

According to the discussions given in Refs. [50,72], simplified versions of the four-step reduced mechanism apply for ignition conditions away from the second explosion limit. Thus, for ignition above crossover,  $H_2O_2$  may be assumed to be in steady state, leading to the three-step reduced chemistry



derived in Ref. [51], with corresponding rates given in Eq. (5).

On the other hand, for conditions sufficiently below the second explosion limit, the results presented in Ref. [52] suggest that the  $HO_2$  steady-state assumption is a reasonable approximation, whereas that of  $H_2O_2$  is not. Introducing a steady-state approximation for  $HO_2$  reduces the four-step chemistry to



The evaluation of the associated rates, given in Eq. (5), requires knowledge of the  $HO_2$  concentration, to be evaluated from the steady-state expression

$$\begin{aligned} C_{HO_2} &= \left( B_2^2 + B_1 \right)^{1/2} - B_2, \\ B_1 &= \left( k_{6b} C_{H_2} C_{O_2} + k_{4f} C_H C_{O_2} C_{M_4} \right) / \left( 2k_{11f} \right), \\ B_2 &= \left( k_{5f} C_H + k_{6f} C_H + k_{7f} C_{OH} + k_{12f} C_{H_2} \right) / \left( 4k_{11f} \right), \end{aligned} \quad (14)$$

while the corresponding concentrations of OH and O are to be computed from Eqs. (9) and (11). Although Eqs. (9) and (14) are coupled, the additional computational cost involved in their

simultaneous solution is limited [50], with no more than five iterations needed for convergence when an iterative procedure similar to that proposed in Ref. [68] is established. It may be noted that other proposals for reduced chemistry descriptions [68] use truncated

expressions for  $C_{OH}$ , instead of Eq. (9). This however can result in significant errors, for instance in the computation of flame speeds. It is also worth pointing out that inclusion of reactions 11f and 12f in the rate expressions improves predictive capabilities at high pressure beyond those of previous mechanisms [68,69].

The adequacy of the four-step and three-step reduced mechanisms for calculating autoignition events is illustrated in Fig. 4, which shows results of isobaric temperature-inflection ignition times at atmospheric pressure for a rich  $H_2$ –air mixture with  $\phi = 3$ . As can be seen by comparison with the detailed-chemistry results, while the four-step mechanism including both  $HO_2$  and  $H_2O_2$  gives accurate predictions for ignition times regardless of the initial temperature, the two separate three-step descriptions derived by considering either H and  $HO_2$  or H and  $H_2O_2$  to be out of steady state, the dashed curve and the dot-dashed curve, give reasonable accuracy in their expected ranges of validity, but are much less accurate otherwise. The selection of one or the other three-step mechanism depends therefore on whether or not the temperature is above crossover. It is worth mentioning here that, for all three reduced mechanisms tested in the figure, larger errors emerge at temperatures above crossover when smaller equivalence ratios are considered, that being a result of the progressive loss of accuracy of the steady-state assumptions for O and OH, as explained later in Section 5.1.

As can be inferred from Fig. 4, the two species  $HO_2$  and  $H_2O_2$  are hardly ever simultaneously far out of steady state, the only exception being ignition events at temperatures close to crossover, while for all other combustion situations the steady-state assumption is

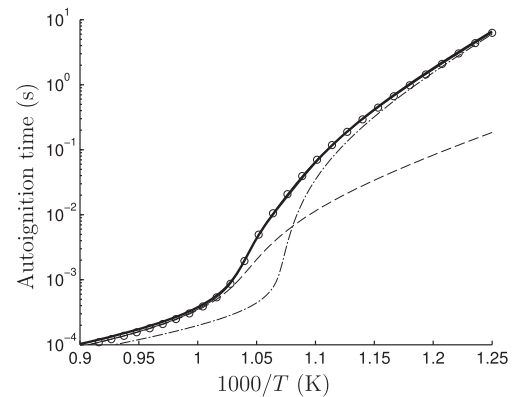


**Fig. 4.** The isobaric temperature-inflection ignition time at atmospheric pressure as obtained for a  $H_2$ –air mixture with  $\phi = 3$  by numerical integration of the conservation equations with the detailed 20-step chemistry (solid curve), with the 4-step reduced chemistry including both  $HO_2$  and  $H_2O_2$  (circles), with the 3-step reduced mechanism shown in Eq. (12) (dashed curve), and with the 3-step mechanism shown in Eq. (13) (dot-dashed curve); based on Ref. [50].

accurate for at least one of these two species. This observation has motivated a recent investigation [50], in which a three-step mechanism is proposed as the minimum description able to encompass all combustion processes. Besides H atoms, a second species out of steady state, a surrogate intermediate X, is introduced to represent the role of either HO<sub>2</sub> or H<sub>2</sub>O<sub>2</sub>, depending on the local conditions. An additional refinement of the chemistry description presented in Ref. [50], which was introduced in earlier work [51], involves the rescaling of key reaction rates to improve autoignition-time agreements under fuel-lean and stoichiometric conditions, for which the hypothesized O and OH steady states is less accurate, to be described later in discussing autoignition processes.

### 3.4.3. The two-step mechanism

For flames, where both HO<sub>2</sub> and H<sub>2</sub>O<sub>2</sub> may be assumed to be in steady state [19,26,68,69], the two three-step descriptions presented above naturally reduce to a single two-step reduced mechanism



with rates

$$\begin{aligned} \omega_{\text{I}} &= \omega_1 + \omega_{5\text{f}} + \omega_{11\text{f}} + \omega_{12\text{f}} \\ \omega_{\text{II}} &= \omega_{4\text{f}} + \omega_8 + \omega_9 - \omega_{11\text{f}} - \omega_{12\text{f}}. \end{aligned} \quad (16)$$

The steady-state equation for H<sub>2</sub>O<sub>2</sub>,  $\omega_{10\text{f}} = \omega_{11\text{f}} + \omega_{12\text{f}}$ , has been employed in writing the first expression in Eq. (16), so that the evaluation of the overall rates becomes independent of the concentration of H<sub>2</sub>O<sub>2</sub>.

The resulting two-step mechanism, defined by Eqs. (15) and (16) supplemented by Eqs. (9)–(11) and (14), is an extension of that introduced in Refs. [68,69] (in particular including reaction 11f, 12f, and implicitly 10f, important for high-pressure conditions) that provides sufficient accuracy for laminar burning velocities and strained diffusion flames. This is shown in the comparisons of Figs. 1 and 2. The departures observed, similar to those arising in the comparisons shown in early investigations of premixed flames [68] and of nonpremixed flames [73], are mainly a consequence of the steady-state approximations introduced for O and OH, while the corresponding approximations for HO<sub>2</sub> and H<sub>2</sub>O<sub>2</sub> are found to be quite accurate for flames. Since O and OH are also assumed to be in steady state in the four-step and also in the two three-step reduced mechanisms derived above, results of these reduced descriptions for flames are almost indistinguishable from those shown in Figs. 1 and 2 for the two-step mechanism. If there is interest in autoignition, however, then the two-step mechanism is not sufficient, and either HO<sub>2</sub> or H<sub>2</sub>O<sub>2</sub> needs to be incorporated in the reduced chemistry as an additional chemical species out of steady state, as explained above.

## 4. Transport properties related to hydrogen

Interactions at a molecular level are responsible for the intimate mixing of chemical species and for the transfer of heat at small scales. As a result, an accurate description of molecular transport processes is a necessary requirement for the computation of most reactive flows, including diffusion flames and deflagrations. The extent to which uncertainties in transport coefficients limit predictive capabilities of reactive flows can be expected to be comparable with that stemming from uncertainties in chemical-kinetic rate parameters [78]. This is especially true for hydrogen combustion, for which the high diffusivity of its molecules and atoms and

the associated preferential-diffusion effects cause predictions to be very sensitive to changes in the diffusion rates of these two species.

The description of transport properties for combustion modeling is a challenging topic in its own right [79]. Experimental measurements are scarce, especially at the high temperatures typical of combustion. Improvements are needed in calculation procedures for transport properties in multicomponent mixtures, both to increase accuracy and to reduce associated computational times. For hydrogen combustion, specific challenges arise in connection with the description of diffusion velocities. For instance, approximate mixture-average methods that are often successful for predicting diffusion velocities in hydrocarbon flames fail to provide sufficient accuracy in computations of hydrogen flames. For these flames, uncertainties in diffusion coefficients at elevated temperature have a profound effect on the overall flow response. Furthermore, thermal diffusion of H<sub>2</sub> and H, also called the Soret effect or the Ludwig–Soret effect, which plays a secondary role in combustion of many hydrocarbons, is nonnegligible under most combustion conditions pertaining to hydrogen and hydrogen-containing fuel blends.

The theory of dilute gases [66,80] is known to provide a realistic description of the molecular interactions occurring under conditions of temperature and pressure of interest for most combustion applications, including in particular pressures ranging from sub-atmospheric values to roughly one hundred atmospheres. The dilute-gas assumption is not applicable, however, under the extreme conditions encountered in H<sub>2</sub>–O<sub>2</sub> rocket-engine combustion chambers, where the pressure may reach hundreds of atmospheres. As a result, real-gas effects must be considered in computing the associated diffusion flames, including modified expressions for the equation of state and for transport properties (see, e.g. Refs. [81–83]). For all other hydrogen combustion situations of practical interest, the theory of dilute gases can be employed in evaluating molecular transport phenomena, as described below.

### 4.1. The computation of diffusion velocities

The computation of diffusion velocities follows from the rigorous solution of the multicomponent diffusion equation derived from the complete kinetic theory of dilute gases [66,80]. Diffusion velocities may arise from gradients of composition (Fickian diffusion), gradients of temperature (thermal diffusion), and gradients of pressure (barodiffusion), and they may also be induced by body forces, when the resultant force per unit mass is different for different species (body-force diffusion). This last effect appears, for example, when an electric field acts upon chemical species that have different electric charges, but it is irrelevant in most combustion flows, because the predominant external forces (gravity and inertial forces) act equally on all important participating species. The participation of ionized species in the chemical kinetics of combustion, which has been addressed in the literature (e.g. Ref. [84]), seldom is significant for hydrogen, and the electric wind [85] is typically associated with charged soot particles, which are not present for pure hydrogen fuels. Barodiffusion is also usually found to be negligible in applications, a result of the prevailing low-Mach-number flow conditions under which diffusion processes are most important.

When both barodiffusion and body-force diffusion are absent, to leading order in a Sonine-polynomial expansion the set of equations to be solved in a mixture of  $N$  different species reduce to [66]

$$\nabla X_i = \sum_{j=1}^N \left( \frac{X_i X_j}{D_{ij}} \right) (\bar{V}_j - \bar{V}_i) + \sum_{j=1}^N \left[ \left( \frac{X_i X_j}{\rho D_{ij}} \right) \left( \frac{D_j^T}{Y_j} - \frac{D_i^T}{Y_i} \right) \right] \frac{\nabla T}{T}. \quad (17)$$

Here  $\bar{V}_i$ ,  $X_i$ , and  $Y_i$  denote the diffusion velocity, mole fraction, and mass fraction of species  $i$ . The above expressions involve two different types of transport coefficients, the binary diffusion coefficient of the species pair  $(i, j)$ ,  $D_{ij}$ , and the thermal diffusion coefficient of species  $i$ ,  $D_i^T$ . An alternative formulation, often utilized in numerical computations [86,87], employs the multicomponent diffusion coefficients  $\mathcal{D}_{ij}$  in place of the binary diffusion coefficients to write the diffusion velocities in the explicit form [80,88]

$$\bar{V}_i = \sum_{j=1}^N \frac{Y_j \mathcal{D}_{ij}}{X_i X_j} \nabla X_j - \frac{D_i^T}{\rho Y_i} \frac{\nabla T}{T}. \quad (18)$$

Note that this last expression is written with a different notation in the work of Ern and Giovangigli [89,90], who employed a different definition for the multicomponent diffusion coefficients following the formalism of Waldmann and Trübenbacher [91]. Irrespective of that choice, unlike the binary diffusion coefficients  $D_{ij}$ , the multicomponent diffusion coefficients  $\mathcal{D}_{ij}$  (or their equivalent) and the thermal diffusion coefficients  $D_i^T$  are complicated functions of the local composition, whose calculation involves the solution of a linear system of equations, a computationally challenging task that requires consideration of specific numerical techniques [92,93].

Thermal diffusion, the last term in Eqs. (17) and (18), can also be formulated in terms of alternative coefficients, including thermal diffusion ratios [80,94] and thermal diffusion factors [95,96], the latter showing a weaker dependence on composition and temperature that makes them more suitable for investigations of analytical nature and also in engineering approximations. It is worth mentioning that, whereas thermal diffusion has been found to be quantitatively important in hydrogen combustion, its Onsager inverse, the so-called Dufour effect, by which an energy flux is generated by species concentrations, always has been found to have a negligibly small effect, although its inclusion in computations is needed if a correct entropy production budget is to be met [97].

To circumvent the difficulties inherent in the multicomponent formulation, approximate explicit Fickian expressions are often used in numerical integrations, with the diffusion velocity of a given species computed as the product of the gradient of either its mole or mass fraction and an effective diffusion coefficient, which is calculated explicitly in terms of the composition and the different binary diffusion coefficients. These mixture-average models provide sufficient accuracy for many hydrocarbon flames [98], with somewhat larger errors often emerging in computations of non-premixed flames [99]. The success of mixture-average methods in describing hydrogen flames is much more limited, with significant inaccuracies encountered, for example, in predictions of extinction conditions for hydrogen–air lean deflagrations [100] and of propagation velocities for planar flames in rich hydrogen–oxygen mixtures [101]. For this reason, use of the multicomponent description must be considered in general for increased accuracy.

The computation of diffusion velocities can be simplified with good accuracy in a number of situations of practical interest. In particular, the expression

$$Y_1 \bar{V}_1 = -Y_2 \bar{V}_2 = -D_{12} \left[ \nabla Y_1 + \left( \frac{D_1^T}{\rho D_{12}} \right) \frac{\nabla T}{T} \right], \quad (19)$$

obtained by solving Eq. (17) exactly for a binary mixture [66] (in which case  $D_{12} = D_{21}$  and  $D_1^T = -D_2^T$ ), can be applied accurately in some hydrogen combustion problems. For example, in ignition of  $H_2$ –air diffusion flames the main components of the mixture are hydrogen, nitrogen, and oxygen, while all other species appear in negligibly low concentrations. Since nitrogen and oxygen are very

similar, they can be treated in a good approximation as a single species, enabling Eq. (19) to be used to give

$$Y_{H_2} \bar{V}_{H_2} = -(1 - Y_{H_2}) \bar{V}_A = -D_{H_2A} [\nabla Y_{H_2} + \alpha_{H_2A} Y_{H_2} (1 - Y_{H_2}) \nabla T / T] \quad (20)$$

for the diffusion velocities of hydrogen and air,  $\bar{V}_{H_2}$  and  $\bar{V}_A$ . Here  $\alpha_{H_2A}$  is the so-called thermal diffusion factor, defined such that  $Y_{H_2} (1 - Y_{H_2}) \alpha_{H_2A} = D_{H_2}^T / (\rho D_{H_2A})$ , a negative quantity that depends only weakly on the composition and temperature of the mixture [95]. In these ignition analyses, once the concentration of the main components is determined with use made of Eq. (20), the diffusion velocities of all minor species into the effectively binary mixture can be determined by solving approximately Eq. (17), as has been done previously [102,103]. The resulting expression is particularly simple when the binary mixture is nearly uniform and nearly isothermal. For instance, in the experiments on hydrogen–oxygen explosion limits in closed vessels reported in [104], the solution of Eq. (17) for the minor species  $i$  reduces to the Fickian expression

$$Y_i \bar{V}_i = - \left( \frac{X_{H_2}}{D_{iH_2}} + \frac{1 - X_{H_2}}{D_{iO_2}} \right)^{-1} \nabla Y_i \quad (21)$$

in terms of the binary diffusion coefficients  $D_{iH_2}$  and  $D_{iO_2}$ .

Another situation of interest in which Eq. (19) finds application is in dilute environments where all chemical species but one appear in small concentrations, so that the diffusion of these minor species is described by the binary law

$$Y_i \bar{V}_i = -D_i \left( \nabla Y_i + \alpha_i Y_i \frac{\nabla T}{T} \right), \quad (22)$$

where  $D_i$  is the binary diffusion coefficient of species  $i$  into the dominant species, and  $\alpha_i$  is the associated thermal diffusion factor. This expression can be used, for instance, in computing  $H_2$ –air premixed combustion in extremely lean mixtures [70,71], with  $N_2$  in that case being the dominant species, differences between  $N_2$  and  $O_2$  again being neglected in this approximation. In analytical studies employing Eq. (22), it is sometimes convenient to introduce the modified mass fraction  $\tilde{Y}_i = T^{\alpha_i} Y_i$  and the modified diffusion coefficient  $\tilde{D}_i = D_i / T^{\alpha_i}$  to write the diffusion flux in Eq. (22) in the compact form  $Y_i \bar{V}_i = -\tilde{D}_i \nabla \tilde{Y}_i$ , providing a one-term Fickian-Soret description.

#### 4.2. Evaluation of diffusion coefficients

Inaccuracies in molecular transport coefficients may affect predictions of hydrogen combustion severely, particularly in connection with the diffusion coefficients of H and  $H_2$ . For instance, in computations of flame speeds in  $H_2$ – $O_2$  mixtures with different diluents, the sensitivities to changes of binary diffusion coefficients of these two species have been verified to be comparable to and even larger than that associated with the rate coefficient of the main chain-branching reaction  $H + O_2 \rightarrow OH + O$  [105–107]. Furthermore, numerical computations of strain-induced extinction of lean  $H_2$ –air flames have revealed that the results are strongly dependent on the diffusion coefficient of  $H_2$ , with a 10% difference in  $D_{H_2N_2}$  leading to 30% differences in extinction strain rates [100]. Also, a large sensitivity of the ignition temperature to the  $H_2$  diffusivity has been observed in counterflow  $H_2$ –air flames with dilute fuel feed [108]. In calculating critical strain rates for extinction of  $H_2/O_2/N_2$  nonpremixed flames, sensitivity indices of  $D_{H_2N_2}$  and  $D_{HN_2}$  are also found to be nonnegligible [109]. All of these high sensitivities, affecting the computation of different hydrogen

reactive flows, justify recent efforts to try to improve predictions of the diffusion coefficients of hydrogen atoms and molecules.

Since experimental measurements for molecular transport properties are only available over limited temperature ranges and for specific mixture compositions, existing software packages [86,87,90] employ in the evaluations of the transport coefficients the formulas derived from the exact kinetic theory of dilute gases [80]. The theory provides leading-order results for the different coefficients as well as higher-order corrections derived by introducing expansions in terms of Sonine polynomials [80]. The different expressions include certain quantities called collision integrals, which must be evaluated for each pair of colliding molecules in terms of the potential associated with their interacting force [66,80]. If the different potentials for all species pairs are known, then the theory provides in principle accurate values for the different transport coefficients, including in particular the diffusion coefficients appearing above in Eqs. 17–22. Unfortunately, potential functions are difficult to compute, so that in reactive-flow calculations the standard evaluation procedure for transport coefficients presently used in existing software packages [86,87,90] requires the introduction of a reasonable functional form for the potential, with adjustable constants that are selected to fit the available experimental data. Clearly, the computation procedure suffers from uncertainties in the form of the potential and in the values of the parameters, which limit the resulting accuracy.

larger number of parameters for defining the potential function of each species. The transport model of Paul and Warnatz [87,112] includes also a number of additional improvements, such as new combination rules for pairs of different species and a simplified formula for evaluating thermal-diffusion properties. All of these changes prevent the proposed calculation procedure from being readily implemented in existing transport codes [86,90]. Despite the increased complexity, the new evaluation has been shown to improve predictive capabilities considerably by providing a better description of H-atom diffusivities [106].

A more direct approach to the calculation of diffusion coefficients of H and H<sub>2</sub>, albeit considerably more costly, is that taken by Wang and coworkers [100,105,106], who extended a first-principle methodology reported previously by Partridge and coworkers (see, e.g. Refs. [113,114]). Their development starts by computing directly the potential functions of collisions involving either H or H<sub>2</sub> by high-level quantum-chemistry calculations, then is followed by direct numerical integrations of the resulting potentials to determine the collision integrals. The final results are expressed in a parametrized form that is fully compatible with widely-used transport codes [86], thereby facilitating its implementation in flame computations. For instance, the new binary diffusion coefficients of H and N<sub>2</sub> and of H<sub>2</sub> and N<sub>2</sub> at atmospheric pressure, computed in [113,114], are expressed in Ref. [100] in the standard 4-term polynomial form

$$\begin{aligned} \ln(D_{\text{HN}_2}) &= -13.2703 + 3.1507 \ln T - 0.296649(\ln T)^2 + 1.64314 \times 10^{-2}(\ln T)^3 \\ \ln(D_{\text{H}_2\text{N}_2}) &= -10.9994 + 2.2026 \ln T - 8.1155 \times 10^{-2}(\ln T)^2 + 4.4061 \times 10^{-3}(\ln T)^3, \end{aligned} \quad (23)$$

For non-polar molecules, the Lennard-Jones 12-6 potential function (twelfth-power repulsion, sixth-power attraction) has been employed widely in computations [86,90]. It contains two adjustable parameters, the depth of the potential well (the maximum energy of attraction) and the collision diameter for low energy collisions (the value of the inter-molecule distance for which the potential vanishes). Values of these two parameters can be obtained by fitting the temperature dependence of transport properties measured experimentally. For instance, for collisions between identical molecules, the fitting may involve making use of the viscosity of the corresponding pure gas [79], as was done in Ref. [110] for H<sub>2</sub>. For collisions of two non-identical species, when experimental measurements of transport properties are not available, the depth and diameter are computed by combining the corresponding values of the two separate species, with the simplest combination rule consisting of taking the geometric mean of the depths and the arithmetic mean of the diameters [88].

Despite the widespread use of the Lennard-Jones potential in transport modeling for reactive flows, it has been known for some time that the twelfth-power of its repulsive part is too stiff for describing collisions involving light species [111], with the result that the standard procedure described above tends to give diffusion coefficients of H and H<sub>2</sub> that are too small, especially at high temperatures [87,112]. To remedy this shortcoming, Paul and Warnatz [87,112] proposed the use of hybrid potentials including an effective Lennard-Jones 12-6 function for reduced temperatures below 10 (the reduced temperature being the temperature scaled with the ratio of the well depth to the Boltzmann constant [80]) and a softer, exponential repulsive potential for higher temperatures. Compared with the standard procedure, the proposed development includes a

with  $D_{ij}$  in cm<sup>2</sup>/s and  $T$  in K, as required for compatibility with [86].

Although a thorough comparative study with the results obtained by Paul and Warnatz is not available, the comparison shown in [106] for the binary diffusion coefficients of H and Ar seems to indicate that there exists good agreement between the two evaluation procedures. Larger differences are observed when the new expressions in Eq. (23) are compared with those obtained with the standard Lennard-Jones 12-6 potential function utilized in existing software packages [86], with differences exceeding 10% at temperatures typical of combustion [100]. As previously mentioned, these seemingly small differences may have a large impact on the flame response under near-limit conditions [100], thereby justifying interest in these improved quantifications of H and H<sub>2</sub> diffusivities. More extensive comparisons of different transport models should be undertaken in future work to assess effects on predictions of other flames. For instance, results for strained premixed flames shown in Ref. [100] indicate that use of multicomponent diffusion coefficients combined with collision integrals evaluated with the improved potentials, as opposed to either multicomponent descriptions without the improved potentials or mixture-average descriptions with the improved potentials, will reduce significantly the values of extinction strain rates of hydrogen–air flames. This helps to resolve recently identified high-pressure discrepancies between computations and experimental measurements [17].

While significant recent progress has been made in improving calculation procedures for binary and multicomponent diffusion coefficients for hydrogen combustion, as just described, considerably less attention has been given to the evaluation of thermal-diffusion parameters, whose uncertainties are larger than those of



Fickian-diffusion parameters, although results similar to those in Eq. (23) based on improved intermolecular potentials are available for the parameters needed in calculations of thermal diffusion [100]. According to the kinetic theory of dilute gases [66,80], thermal diffusion is a second-order effect, such that the leading-order representation for the thermal diffusion coefficient emerges from the second term in the Sonine expansion, the first term being identically zero for this transport coefficient. The error associated with the resulting expression is known to be greater than that of any other transport coefficient [80] and its computation is more dependent on the specific shape of the intermolecular potential. Besides, the experimental measurement of this transport coefficient is subject to considerable uncertainties. For all these reasons, improvements in experimental and computational techniques are warranted to reduce uncertainties in evaluations of  $D_i^T$ , enabling improved assessments of thermal diffusion effects in hydrogen combustion processes to be made. The current understanding of this topic will now be reviewed.

#### 4.3. Thermal diffusion effects in hydrogen combustion

Thermal diffusion tends to drive small and light species towards hotter regions and large and heavy species away from them. Correspondingly, thermal diffusion coefficients (and thermal diffusion ratios and factors) are negative (positive) for small, light (large, heavy) species. The nondimensional thermal diffusion factors appearing in Eqs. (20) and (22) provide an effective quantitative measure of the relative contribution of thermal diffusion to the diffusion velocity of a given species. For instance, when  $N_2$  appears as the dominant carrier in the gas mixture, the approximate values  $\alpha_{H_2} = -0.29$ ,  $\alpha_H = -0.23$ ,  $\alpha_{H_2O} = -0.02$ , and  $\alpha_{O_2} = +0.02$  apply at sufficiently high temperature [95], clearly indicating the comparatively larger influence of thermal diffusion on hydrogen atoms and molecules.

Concerning premixed hydrogen combustion, effects of thermal diffusion were assessed in the numerical computations of planar deflagrations reported in the seminal work of Dixon-Lewis [115], who found that exclusion of thermal diffusion of H atoms increases the value of the burning rate of a stoichiometric planar flame by about 6%. These early investigations of planar flames with realistic chemistry were complemented by more general numerical [116] and theoretical [117,118] studies using a one-step Arrhenius model. In particular, for large values of the activation energy, it was found that, for strictly planar flames, thermal diffusion enters only in the second-order correction to the flame propagation velocity, but that it enters however at leading order when determining the flame response to curvature [117,118].

More extensive numerical evaluations of thermal diffusion effects in premixed hydrogen–air combustion with multicomponent transport were carried by Ern and Giovangigli [97,119]. Their computations clearly showed that the structure of both rich and lean Bunsen flames is strongly influenced by thermal diffusion [97]. For steady planar deflagrations [119], inclusion of thermal diffusion was found to decrease the propagation velocity for most equivalence ratios, in accordance with the early results of Dixon-Lewis [115] and also with subsequent numerical computations [19,101]. The only exception to that tendency was found for very fuel-rich conditions, for which a slight increase in burning rate was observed when thermal diffusion was included [119]. Soret diffusion was also found to be significant in strained premixed flames, especially for near-extinction conditions [119], with general trends of effects of diffusion fluxes explained in light of earlier theoretical predictions [120,121].

For freely propagating planar flames, the effects H and  $H_2$  thermal diffusion were evaluated separately by Yang et al. [122]. In particular,

it was found that Soret diffusion of H atoms is always irrelevant for near-limit fuel-lean combustion, an effect that can be explained by noting that, under those conditions, H remains in steady state [19,26], so that its diffusive rate does not influence the flame propagation velocity. For those fuel-lean conditions, molecular hydrogen also appears in small concentrations in the thin reaction layer, where the effect of thermal diffusion is correspondingly negligible according to Eq. (22). Thermal diffusion can, however, be appreciable in the preheat region. For unstrained planar flames, this effect has no consequences on the burning rate, because it does not modify the diffusive flux of fuel into the thin reaction zone, whose value remains equal to the upstream convective flux, as can be seen by straightforward integration of the convection-diffusion conservation equation of  $H_2$  across the planar preheat region. As a consequence, the value of the propagation velocity computed for near-limit fuel-lean unstrained planar deflagrations is independent of whether or not thermal diffusion of  $H_2$  is considered in the integration. This result, verified in all previous numerical studies [19,101,119,122], agrees with the large-activation-energy predictions for one-step Arrhenius chemistry [117,118].

By way of contrast, when the flame is stretched or curved, the effect of thermal diffusion of  $H_2$  in the preheat region can lead to significant changes in the amount of fuel that reaches the reaction layer. Consequently, computations of fuel-lean hydrogen deflagrations subject to either strain, as in opposed-jet configurations [119,122], or curvature, arising for instance from thermodiffusive instabilities of freely propagating flames [123], show a non-negligible dependence on the thermal diffusion of  $H_2$  that does not vanish as flammability limits are approached. Therefore, for fuel-lean hydrogen–air mixtures, predictions of strain rates for extinction [119,122], burning rates of corrugated flames [123], and critical radii for existence of flame balls [70,71] all need to account for Soret effects if reasonable accuracy is desired.

Thermal diffusion also has a significant effect on ignition of high-velocity hydrogen–air streams by hot walls, as was ascertained in boundary-layer analyses with realistic chemistry descriptions [124–126]. It was found that, in this specific problem, the thermal diffusion fluxes of  $H_2$  and H have counteracting effects, with the former facilitating the ignition of lean flames by enriching locally the mixture near the wall and the latter delaying ignition by increasing the evacuation rate of H atoms away from the reaction zone. The second effect appears to be dominant in the process under most conditions, causing the ignition length to be considerably larger than that computed with thermal diffusion neglected [124–126]. These previous analyses suggest that thermal diffusion might also play a nonnegligible role in forced ignition of hydrogen mixtures by localized energy release, an issue remaining to be clarified in future work. In particular, consideration of Soret effects may lead to improvements in accuracy of predictions of minimum ignition energies [127].

Thermal diffusion has also been shown to be important for nonpremixed flames [128]. Counterflow configurations have been used to assess effects of Soret diffusion on peak temperatures and flame locations [129] and also on extinction strain rates [122], the latter study showing that, for  $H_2$ –air diffusion flames, H and  $H_2$  thermal diffusion have a comparable effect. The counterflow has also been the configuration selected to investigate numerically partially premixed  $H_2$ –air flames at atmospheric and elevated pressures [130], with results indicating that thermal diffusion has a significant influence on the resulting two-reaction-zone structure.

#### 4.4. Evaluation of viscosity and thermal conductivity

Uncertainties in values of shear viscosity of gaseous mixtures are smaller than those for other coefficients. Experimental data are

available for many gases with accuracies better than 5% [79]. Besides, since viscous stresses affect the temperature and species concentrations in an indirect way (i.e., through associated changes in the velocity and pressure field), flame predictions tend to be less sensitive to uncertainties in viscosity coefficients than they are to those of other transport coefficients. Although the value of the coefficient of bulk viscosity (which vanishes for monoatomic dilute gases) can be comparable to or larger than that of shear viscosity, for many combustion processes its effect is negligible. It is, however, noteworthy that, unlike diatomics such as  $N_2$  and  $O_2$ , for which the ratio of bulk to shear viscosity is near unity, for  $H_2$  the ratio is about 30, motivating simulations indicating that it produces measurable effects in some circumstances [131,132]. In evaluating the bulk viscosity, these recent simulations make use of approximate explicit formulas derived for this coefficient in dilute polyatomic gas mixtures [133].

For a multicomponent mixture, at leading order in the Sonine polynomial expansion the value of the shear viscosity can be obtained as a ratio of two determinants with coefficients written in terms of collision integrals for the different species pairs present in the mixture [80]. Simpler mixture-average approximations are preferred for the computation of this coefficient in most numerical codes [86,87], a notable example being the semi-empirical Wilke formula [134] employed in Ref. [86]. Although the multicomponent formalism of Ern and Giovangigli [92] involves in principle the solution of a system of linear equations to determine the shear viscosity, an analytical expression for this coefficient follows from the first iteration in the associated conjugate gradient solution. This simpler expression is reasoned to be more accurate and also more cost-effective than the widely used Wilke formula [92]. Future work should assess the accuracy of the different approximations currently employed, in particular in connection with mixtures of  $H_2$ ,  $N_2$ ,  $O_2$ , and  $H_2O$ , the dominant chemical species in hydrogen combustion, as well as quantitative influences of minor species.

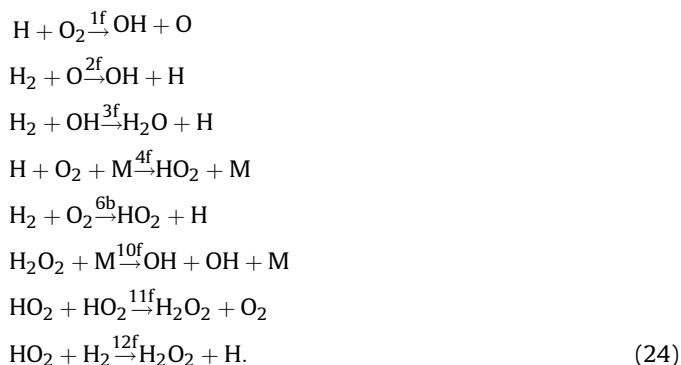
Although the kinetic theory [80] also provides expressions for the thermal conductivity, involving complicated formulas derived with two terms retained in the Sonine polynomial expansion, the computation of this quantity for mixtures of polyatomic species is more complex, because of the contribution of the internal degrees of freedom, with different approximations adopted in different numerical codes [86,87,90]. All of the evaluation procedures assume that the thermal conductivity can be obtained by adding the separate contributions of the different degrees of freedom. Although in some of the codes [86,90] the computational scheme requires the solution of a large system of linear equations, the simpler Eucken–Hirschfelder approach [135] has been argued in recent work [87,112] to provide accuracies comparable to those of more complicated procedures. Clearly, also in this case more work is desirable to assess the accuracy and computational advantages of the different evaluation procedures, especially with regard to mixture compositions typical of hydrogen combustion.

## 5. Autoignition processes for hydrogen

The occurrence of self-ignition in hydrogen–air systems is of interest for safety issues associated with planning of a future hydrogen economy and also in technological applications, including designs of hypersonic air-breathing propulsion devices and reliable mixing systems for hydrogen-fired gas turbines. A common measure of the ignitability of the mixture is the so-called ignition (or induction) time,  $t_i$ , defined in a homogeneous mixture as the delay time required to reach a state of vigorous reaction from given initial conditions of composition, temperature, and pressure. This quantity can be measured experimentally in shock tubes, rapid-compression machines, and flow reactors, and it can also be

computed by integrating numerically the time-dependent conservation equations for homogeneous adiabatic systems, with characteristic results shown for instance in Fig. 4.

Because of the low radical concentrations that exist prior to ignition, many of the elementary reactions in Table 2 become negligibly slow and consequently can be neglected in the computation of  $t_i$ , including the backward shuffle reactions 1b, 2b, and 3b, the elementary reactions describing  $HO_2$  attack by H and OH (5f, 6f, and 7f), and the direct recombination reactions 8f and 9f. Besides, the dissociation of  $H_2$  and  $H_2O$  through 8b and 9b is always much too slow to be consequential in ignition processes, thereby reducing the ignition chemistry to the subset of elementary reactions



Although the rate coefficient of the initiation reaction 6b is extremely small compared with that of the other steps (e.g.,  $k_{6b}/k_{1f} = 4.81 \times 10^{-10}$  at  $T = 1000$  K), this reaction necessarily must be retained in the mechanism for describing the initial production of radicals when their initial concentrations are identically zero.

The character of the ignition event that emerges and the resulting ignition time depends strongly on the initial temperature and pressure [72]. Thus, when the initial temperature is sufficiently high, ignition occurs through a fast chain-branching explosion started by the initiation reaction 6b and supported by the shuffle reactions 1f–3f in competition with 4f, giving ignition times that, for the atmospheric stoichiometric conditions of Fig. 4, are of the order of  $t_i \sim 100$   $\mu s$  for  $T \approx 1100$  K, reducing to  $t_i \sim 5$   $\mu s$  at  $T \approx 2000$  K. The ignition time increases rapidly as the so-called crossover temperature is approached, at which the effective rate of radical production through the shuffle reactions becomes equal to the rate of the recombination step  $H + O_2 + M \xrightarrow{4f} HO_2 + M$ . For initial temperatures below crossover, step 4f maintains the H-atom concentration at very low values, effectively preventing the chain-branching explosion from taking place and causing ignition to occur instead through an alternative slow reaction path involving a thermal explosion controlled by the last three steps in Eq. (24).

At temperatures above crossover, good agreement is generally observed between theoretical predictions and experimental measurements of induction times (see, e.g. Ref. [34], and references therein). Below crossover, however, the associated homogeneous ignition time becomes very large, and its experimental determination encounters numerous difficulties associated with the presence of localized perturbations that result in measured induction times being consistently smaller than the values predicted theoretically for homogeneous adiabatic systems [136,137]. It has been reasoned [138] that the prevailing mode of ignition in shock-tube experiments at temperatures below crossover involves flame propagation from hot spots near walls [138], so that what is being measured in experiments is actually not the homogeneous ignition delay time but rather the ratio of the tube radius to the flame propagation speed. Clearly, for this regime of low-temperature homogeneous ignition, more work is required to improve designs of experiments free from these complicating effects.

The ignition crossover temperature, to be defined precisely in Eq. (31), is of the order of  $T_c \approx 950$  K at  $p = 1$  atm, as can be inferred from the results of Fig. 4, but it increases to values of the order of  $T_c \approx 1250$  K at  $p = 20$  atm. Therefore, the chain-branching explosion occurring above crossover is of interest for applications such as supersonic combustion in scramjet systems, with typical operation conditions at the combustor inlet including temperatures above 1200 K and near atmospheric pressures. The low-temperature ignition regime, on the other hand, is relevant for the conditions typically found in gas-turbine mixing systems, with pressures in the range  $10 \text{ atm} < p < 30 \text{ atm}$  and temperatures not exceeding  $T \approx 1000$  K. Both regimes are to be considered below. Besides computation of ignition times in homogeneous systems, the discussion will address explosion limits in closed vessels, determined by the competition of the ignition chemistry with the transport of chemical species and heat. Effects of flow strain and of gradients of temperature and reactant concentration are also to be discussed, because of their importance for autoignition in practical applications.

### 5.1. Ignition above crossover: the chain-branching explosion

The numerical computation of homogeneous autoignition in isobaric adiabatic systems requires the integration of the unsteady conservation equations for energy and chemical species. For illustrative purposes, a typical time history obtained above crossover with the detailed mechanism of Table 1 is plotted in Fig. 5 for a stoichiometric  $\text{H}_2$ –air mixture. In this case of high-temperature ignition, the reaction history exhibits an induction stage of exponential radical growth with negligible reactant consumption and negligible heat release, followed by a stage of radical recombination with progressive temperature increase. The resulting curves also indicate that the application of different criteria to identify ignition, such as the temperature-inflection criterion, the occurrence of a maximum in the radical concentration, or the decrease of the relative fuel content by some fixed significant amount, leads to values of the induction time in close agreement with one another.

For the conditions of high temperature considered in Fig. 5, the associated concentrations of  $\text{HO}_2$  and  $\text{H}_2\text{O}_2$  are so small than the last three reactions in Eq. (24) become negligibly slow, so that the first five elementary steps provide a sufficiently accurate chemistry description of the branched-chain explosion [34] and its associated ignition time. The accuracy of this simplified description is verified

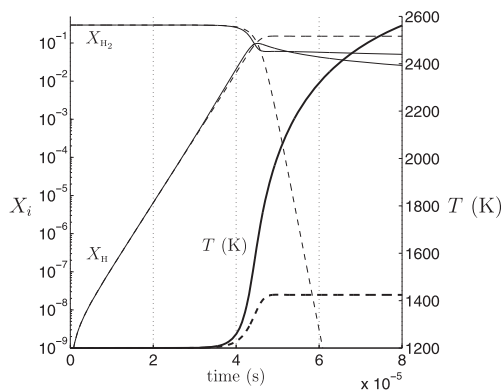


**Fig. 5.** The temporal evolution of  $X_{\text{H}_2}$ ,  $X_{\text{H}}$ , and  $T$  for a stoichiometric hydrogen–air mixture in a homogeneous adiabatic reactor at constant atmospheric pressure and initial temperature  $T = 1200$  K as obtained from numerical integrations with the 20-step mechanism of Table 1 (solid curves) and with the five elementary reactions 1f, 2f, 3f, 4f, and 6b (dashed curves); adapted from Ref. [142].

in the comparisons of Fig. 5, with the dashed curve of H-atom mass fraction obtained with the five elementary reactions 1f, 2f, 3f, 4f, and 6b following closely that computed with detailed chemistry up to the ignition instant. With reactant consumption neglected along with the variation of the rate coefficients resulting from temperature increase, as is appropriate during the chain-branching stage of the ignition process, the computation of the temporal evolution of the radical pool is reduced to the integration of the system of homogeneous balance equations

$$\frac{dC_{\text{H}}}{dt} = -k_{1f}C_{\text{O}_2}C_{\text{H}} + k_{2f}C_{\text{H}_2}C_{\text{O}} + k_{3f}C_{\text{H}_2}C_{\text{OH}} - k_{4f}C_{\text{M4}}C_{\text{O}_2}C_{\text{H}} + k_{6b}C_{\text{O}_2}C_{\text{H}_2} \quad (25)$$

$$\frac{dC_{\text{O}}}{dt} = k_{1f}C_{\text{O}_2}C_{\text{H}} - k_{2f}C_{\text{H}_2}C_{\text{O}} \quad (26)$$

$$\frac{dC_{\text{OH}}}{dt} = k_{1f}C_{\text{O}_2}C_{\text{H}} + k_{2f}C_{\text{H}_2}C_{\text{O}} - k_{3f}C_{\text{H}_2}C_{\text{OH}}, \quad (27)$$

with initial conditions  $C_{\text{H}} = C_{\text{O}} = C_{\text{OH}} = 0$ . Here  $C_i = \rho Y_i/M_i$  is the concentration of species  $i$  and  $C_{\text{M4}}$  is the effective third-body concentration of reaction 4f, which must account for the chaperon efficiencies indicated in Table 1.

The simple problem formulated above, which admits an exact analytic solution (see Ref. [34] and references therein), can be used as an illustrative example to show how disparities of reaction rates lead to steady-state approximations for chemical intermediaries, a simplification that arises in this case because the rate constants for reactions 2f and 3f are significantly larger than that for reaction 1f (e.g.,  $k_{1f}/k_{2f} = 0.318$  and  $k_{1f}/k_{3f} = 0.0746$  at  $T = 1200$  K). To identify more clearly the role of the different reactions in the problem at hand, it is instructive to begin the development by combining linearly Eqs. 25–27 to eliminate the terms involving the fast reactions 2f and 3f, yielding a conservation equation for the radical-pool concentration  $C_{\text{H}} + 2C_{\text{O}} + C_{\text{OH}}$  in the form

$$\frac{d}{dt}(C_{\text{H}} + 2C_{\text{O}} + C_{\text{OH}}) = (2k_{1f} - k_{4f}C_{\text{M4}})C_{\text{O}_2}C_{\text{H}} + k_{6b}C_{\text{O}_2}C_{\text{H}_2}. \quad (28)$$

Inspection of this equation reveals the autocatalytic character of the chain-branching explosion, with the radical growth rate being proportional to the concentration of H atoms. The characteristic branching time

$$t_{\text{B}} = \frac{1}{(2k_{1f} - k_{4f}C_{\text{M4}})C_{\text{O}_2}} \quad (29)$$

defines the time scale for the exponential radical growth, while the initiation term, with characteristic time

$$t_{\text{I}} = \frac{1}{k_{6b}C_{\text{O}_2}}, \quad (30)$$

is important only to create the first radicals, but becomes negligible at later stages in the ignition process, because its associated rate constant is such that  $t_{\text{B}}/t_{\text{I}} \sim k_{6b}/k_{1f} \ll 1$ . Equation (28) also indicates that an exponential radical growth takes place only if the condition  $2k_{1f} > k_{4f}C_{\text{M4}}$  is satisfied, which occurs as long as the temperature is above a crossover temperature  $T_c$ , defined for ignition by the equation

$$2k_{1f} = k_{4f}C_{M4}, \quad (31)$$

identified three quarters of a century ago in the seminal work of Von Elbe and Lewis [139]. As previously anticipated, the precise value of the crossover temperature depends on the composition through the third-body efficiencies present in  $C_{M4}$ .

Having shown from Eq. (28) that the radical evolution time is of order  $t_B \sim (k_{1f}C_{O_2})^{-1}$ , it is now possible to seek simplifications associated with chemical-time disparities by attempting an order-of-magnitude analysis of Eqs. (26) and (27) with  $k_{2f} \gg k_{1f}$  and  $k_{3f} \gg k_{1f}$ . Analysis of Eq. (26) indicates that the accumulation rate of oxygen atoms, proportional to  $t_B^{-1}$ , is negligible compared with its consumption rate through reaction 2f, proportional to the inverse characteristic time  $k_{2f}C_{H_2}$ , so long as the condition  $k_{2f}C_{H_2} \gg k_{1f}C_{O_2}$  is satisfied, as is always the case in mixtures that are sufficiently fuel rich. Similarly, under those fuel rich conditions the accumulation rate of OH in Eq. (27) is also negligible compared with its consumption rate through 3f, because  $k_{3f}C_{H_2} \gg k_{1f}C_{O_2}$ . If both accumulation rates are neglected, then Eqs. (26) and (27) reduce to algebraic equations that can be solved to give the steady-state expressions

$$C_O = \frac{k_{1f}C_{O_2}}{k_{2f}C_{H_2}} C_H \quad (32)$$

and

$$C_{OH} = \frac{2k_{1f}C_{O_2}}{k_{3f}C_{H_2}} C_H. \quad (33)$$

These expressions can be substituted into Eq. (25) to give

$$\frac{d}{dt}(C_H) = (2k_{1f} - k_{4f}C_{M4})C_{O_2}C_H + k_{6b}C_{O_2}C_{H_2} \quad (34)$$

for the evolution of the H concentration, the only chain-branching radical out of steady state, yielding

$$\begin{aligned} \frac{C_H}{C_{H_2}} &= \frac{t_B}{t_i} (e^{t/t_B} - 1) \\ &= \frac{k_{6b}}{2k_{1f} - k_{4f}C_{M4}} \left\{ \exp\left[(2k_{1f} - k_{4f}C_{M4})C_{O_2}t\right] - 1 \right\} \end{aligned} \quad (35)$$

upon integration with initial condition  $C_H(0) = 0$ . This condition should be modified when radicals are present at the outset, yielding corrections to the ignition time that can be significant when the initial H-atom concentration is comparable to or larger than  $(t_B/t_i)C_{H_2}$ . These departures must be accounted for in addressing influences of residual radical impurities on experimentally measured ignition times in shock-tube experiments [140].

The expression shown in Eq. (35) indicates that for  $t \sim t_B$  the H-atom concentration reaches very small values of order  $C_H = (t_B/t_i)C_{H_2}$ . The results in Fig. 5 indicate that ignition is associated with radical concentrations becoming comparable to, although somewhat smaller than, the initial reactant concentrations, and therefore ignition requires much larger times, which can be computed by using the approximate ignition criterion  $C_H = C_{H_2}$  in Eq. (35) to yield in the first approximation

$$t_i = t_B \ln\left(\frac{t_i}{t_B}\right) = \frac{\ln\left[(2k_{1f} - k_{4f}C_{M4})/k_{6b}\right]}{(2k_{1f} - k_{4f}C_{M4})C_{O_2}} \quad (36)$$

for the ignition time. This last expression clearly shows that the slow initiation rate has a noticeable retarding effect on the chain-branching explosion, causing the ignition time to be larger than

the branching time by a logarithmic factor that is of the order of  $\ln(t_i/t_B) \sim 15\text{--}20$  at temperatures of practical interest. The evolution with time of  $X_{H_2}$  and  $X_H$  shown in Fig. 5 seems to indicate that the condition  $C_H = C_{H_2}$ , used in deriving Eq. (36), may result in predictions of ignition times that are slightly larger than those obtained with the temperature-inflection criterion.

The above introduction of the steady-state assumptions for O and OH simplifies the problem by removing the need to integrate their associated differential conservation equations, which are replaced by the algebraic expressions in Eqs. (32) and (33). The physical interpretation of this result is that in the limit  $k_{2f}C_{H_2} \gg k_{1f}C_{O_2}$ , the consumption rate of O through  $H_2 + O \xrightarrow{2f} OH + H$  is so rapid that this intermediate is consumed as soon as it is created by  $H + O_2 \xrightarrow{1f} OH + O$ , in an instantaneous balance that determines the O concentration as indicated in Eq. (32). The combined effect of 1f followed rapidly by 2f leads to the overall reaction  $H_2 + O_2 \rightarrow 2OH$ , with a rate equal to that of the elementary step 1f. Because of the additional condition  $k_{3f}C_{H_2} \gg k_{1f}C_{O_2}$ , the two OH produced are rapidly eliminated by the occurrence of twice  $H_2 + OH \xrightarrow{3f} H_2O + H$ , to give finally the overall branching reaction  $3H_2 + O_2 \rightarrow 2H_2O + 2H$ , anticipated earlier in Eq. (1), with a rate that for ignition is equal to that of the elementary reaction  $H + O_2 \xrightarrow{1f} OH + O$ . This overall reaction replaces the three shuffle reactions 1f, 2f, and 3f in the reduced description, giving as a result the H-atom expression appearing in Eq. (34) which accounts for the additional effects of the elementary reactions  $H + O_2 + M \xrightarrow{4f} HO_2 + M$  and  $H_2 + O_2 \xrightarrow{6b} HO_2 + H$ . It is worth mentioning that, although a steady-state approximation for H atoms instead of O and OH would hold in principle for ignition in the opposite limit of extremely lean mixtures, such that  $k_{2f}C_{H_2} \ll k_{1f}C_{O_2}$  and  $k_{3f}C_{H_2} \ll k_{1f}C_{O_2}$ , such mixtures are beyond normal flammability boundaries [34].

According to Eqs. (32) and (33), in the limits  $k_{2f}C_{H_2} \gg k_{1f}C_{O_2}$  and  $k_{3f}C_{H_2} \gg k_{1f}C_{O_2}$  the concentrations of O and OH are much smaller than that of H. This condition can be used in deriving directly Eq. (34) from Eq. (28) by neglecting the presence of O and OH in the radical pool. Correspondingly, the relative error of the steady-state approximation is measured by the terms  $(k_{1f}C_{O_2})/(k_{2f}C_{H_2})$  and  $(k_{1f}C_{O_2})/(k_{3f}C_{H_2})$  in Eq. (28), which become larger as the mixture becomes leaner. This is clearly seen in the comparisons shown in Fig. 6, where the prediction given in Eq. (36) is compared with detailed-chemistry integrations using the temperature-inflection criterion. As can be seen, for rich mixtures, the agreement is satisfactory, with Eq. (36) slightly overpredicting the ignition time, as is to be expected as a result of the criterion  $C_H = C_{H_2}$  used in deriving Eq. (36) from Eq. (35). However, the accuracy of the analytic prediction deteriorates as the mixture becomes leaner, leading to significant underpredictions of values of  $t_i$ .

In principle, the exact original chain-branching problem defined in Eqs. 25–27 should be considered to determine accurately the ignition time for stoichiometric and lean mixtures. The time evolution of the radical concentrations can be expressed in terms of exponentials with frequency factors that can be determined by solving the characteristic equation associated with the linear problem shown in Eqs. 25–27 [34], which possesses a single positive eigenvalue that dominates the solution for large times. The resulting modified branching rate, which reduces to that displayed in Eq. (35) for very rich mixtures, has been incorporated in multi-purpose reduced-chemistry descriptions [50,51] to improve predictive capabilities of autoignition problems, including computations of liftoff distances of hydrogen–air flames in supersonic mixing layers [141].

The comparison of Eq. (28), which is exact, with the steady-state Eq. (34), suggests that the errors of the steady-state approximation



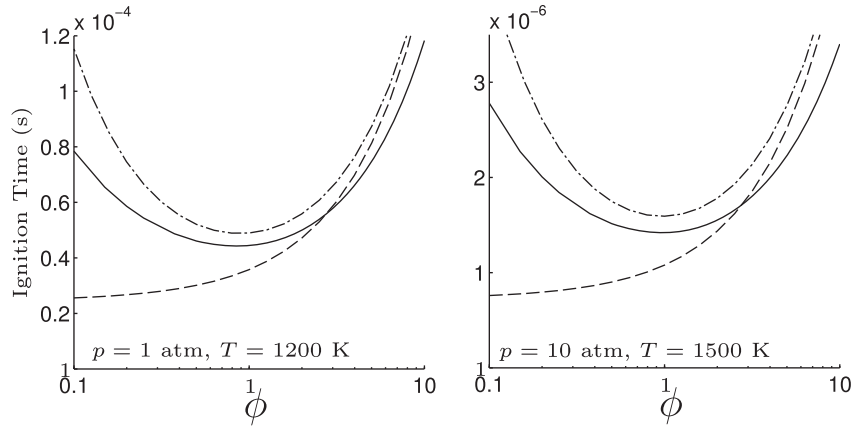


**Fig. 6.** The dependence on equivalence ratio  $\phi$  of the ignition time of a hydrogen–air mixture as obtained in a homogeneous adiabatic reactor at constant pressure from numerical integrations with the detailed mechanism of Table 1 using the temperature-inflection criterion (solid curves) and from evaluations of Eq. (36) (dashed curves) and of the corrected expression  $t_i = \tilde{t}_B \ln(t_i/\tilde{t}_B)$  (dot–dashed curves); adapted from Ref. [142].

can be attributed to a deficit in the actual overall concentration of the radical pool, compared to that calculated. Similar ideas, based on deficits of element mass fractions, were explored in the early analyses of reduced chemistry for hydrogen deflagrations [68]. As explained in Ref. [142], for ignition problems the errors associated with Eq. (34) can be reduced by introducing a modified radical-pool variable  $C = C_H + 2C_O + C_{OH}$ , which can be expressed in terms of the H-atom concentration through

$$C = C_H + 2C_O + C_{OH} = \left(1 + \frac{2k_{1f}C_{O_2}}{k_{2f}C_{H_2}} + \frac{2k_{1f}C_{O_2}}{k_{3f}C_{H_2}}\right)C_H \quad (37)$$

with use made of Eqs. (32) and (33). The procedure, which effectively includes first-order corrections in the steady-state asymptotic limits  $(k_{1f}C_{O_2})/(k_{2f}C_{H_2}) \ll 1$  and  $(k_{1f}C_{O_2})/(k_{3f}C_{H_2}) \ll 1$ , proceeds by using the new variable  $C$  to rewrite Eq. (28) in the form

$$\frac{dC}{dt} = \frac{C}{\tilde{t}_B} + \frac{C_{H_2}}{t_i} = \frac{(2k_{1f} - k_{4f}C_{M4})C_{O_2}C_{H_2}}{C_{H_2} + 2(k_{1f}/k_{2f} + k_{1f}/k_{3f})C_{O_2}}C + k_{6b}C_{O_2}C_{H_2} \quad (38)$$

similar to Eq. (34) but involving a branching time

$$\tilde{t}_B = \frac{C_{H_2} + 2(k_{1f}/k_{2f} + k_{1f}/k_{3f})C_{O_2}}{(2k_{1f} - k_{4f}C_{M4})C_{O_2}C_{H_2}} \quad (39)$$

that depends on the  $H_2$  concentration and shows a minimum value for a mixture composition close to stoichiometric conditions. Integrating Eq. (38) with initial condition  $C(0) = 0$  gives

$$\frac{C}{C_{H_2}} = \frac{\tilde{t}_B}{t_i} (e^{t/\tilde{t}_B} - 1), \quad (40)$$

which can be employed, together with the ignition condition  $C = C_{H_2}$ , to derive the expression  $t_i = \tilde{t}_B \ln(t_i/\tilde{t}_B)$  for the ignition time, with  $t_i$  and  $\tilde{t}_B$  given, respectively, in Eqs. (30) and (39) in terms of the composition and temperature. This last equation is shown in Fig. 6 to give reasonably accurate predictions of ignition times over the whole range of compositions, with overpredictions that are of the order of 10% for the most reactive conditions, found near stoichiometry. The results indicate that the introduction of the radical-pool variable effectively corrects for deviations from steady-state approximations of O and OH in stoichiometric and even lean

mixtures, as is needed, for instance, in studies of nonpremixed autoignition in mixing layers [142,143].

### 5.2. Ignition below crossover: the thermal explosion

The relative importance of H-atom recombination through  $H + O_2 + M \xrightarrow{4f} HO_2 + M$  increases as the temperature decreases towards the crossover value, as is noticeable in the ignition-time expression in Eq. (36), which includes in the denominator the factor  $(2k_{1f} - k_{4f}C_{M4})$ . As crossover is approached, this factor becomes smaller, causing the predicted ignition time to diverge as the analysis fails when  $2k_{1f} = k_{4f}C_{M4}$ . Below crossover, i.e., when  $2k_{1f} < k_{4f}C_{M4}$ , the chain-branching path supported by the shuffle reactions is precluded by the recombination step 4f and, according to the previous description leading to Eq. (35), the system would reach a weakly reactive state with negligibly small radical concentrations proportional to  $k_{6b}$ , seen from Eq. (34) by setting the time derivative equal to zero. In reality, under these conditions ignition proceeds instead through an alternative route involving  $HO_2$  and  $H_2O_2$  [72], with production and consumption rates controlled by reactions 10f, 11f, and 12f, whose effect above crossover is, however, inappreciable because of their extremely slow associated rates.

During the ignition process at temperatures below crossover, fast radical consumption through 2f, 3f, and 4f maintains H, O, and OH in steady state with extremely small concentrations [72]. As noted in an early analysis of ignition by a hot plate [144] (see also the discussion in Ref. [52]), the ignition history includes a short initial stage of  $HO_2$  buildup, followed by a longer period leading to a thermal runaway during which hydroperoxyl maintains steady state as a result of its fast consumption through  $2HO_2 \xrightarrow{11f} H_2O_2 + O_2$ . With all four radicals in steady state, the chemistry reduces to two overall reactions involving  $H_2$ ,  $O_2$ ,  $HO_2$ , and  $H_2O_2$ , to be derived below. To focus more directly on the essential chemical interactions that determine the reduced chemistry, attention will be restricted in the following to temperatures sufficiently below crossover for the rate of H-atom consumption through 1f to be negligibly slow. As an additional simplification, the initiation reaction 6b will not be considered, because its effect on the resulting ignition time has been shown to be entirely negligible [52], thereby reducing the starting chemistry description to the five elementary reactions 3f, 4f, 10f, 11f, and 12f. Effects associated with 1f and 6b could be incorporated readily in the description, as shown in Ref. [52], leading to modified rates for the two overall reactions that would be needed to improve descriptions of near-crossover ignition events and to address radical growth during the initial initiation stages.

The reduction of the chemistry begins by noting that the two OH molecules created by the hydrogen-peroxide dissociation reaction  $\text{H}_2\text{O}_2 + \text{M} \xrightarrow{10f} 2\text{OH} + \text{M}$  are rapidly destroyed by the occurrence of twice  $\text{OH} + \text{H}_2 \xrightarrow{3f} \text{H}_2\text{O} + \text{H}$  followed by twice  $\text{H} + \text{O}_2 + \text{M} \xrightarrow{4f} \text{HO}_2 + \text{M}$  to eliminate the two H atoms produced, leading in a first stage to the overall reaction  $\text{H}_2\text{O}_2 + 2\text{H}_2 + 2\text{O}_2 \rightarrow 2\text{H}_2\text{O} + 2\text{HO}_2$  with a rate that is simply equal to that the elementary reaction  $\text{H}_2\text{O}_2 + \text{M} \xrightarrow{10f} 2\text{OH} + \text{M}$ . As previously mentioned, it has been shown [52] that ignition involves values of the hydroperoxyl concentration large enough for the elementary reaction  $2\text{HO}_2 \xrightarrow{11f} \text{H}_2\text{O}_2 + \text{O}_2$  to proceed at a fast rate, such that the two  $\text{HO}_2$  molecules created by  $\text{H}_2\text{O}_2 + 2\text{H}_2 + 2\text{O}_2 \rightarrow 2\text{H}_2\text{O} + 2\text{HO}_2$  at a given location are immediately converted to  $\text{H}_2\text{O}_2$  and  $\text{O}_2$  at that same location, with the consequence that the transport and accumulation rates of  $\text{HO}_2$  become entirely negligible. The resulting  $\text{HO}_2$  concentration attains the local steady-state value

$$C_{\text{HO}_2} = \left(k_{10f}/k_{11f}\right)^{1/2} C_{\text{M10}}^{1/2} C_{\text{H}_2\text{O}_2}^{1/2}, \quad (41)$$

obtained by equating the rates of  $\text{HO}_2$  production and consumption, i.e.,  $2\omega_{10f} = 2\omega_{11f}$ , where  $C_{\text{M10}}$  is the effective third-body concentration for the elementary reaction 10f. Since  $\text{HO}_2$  recombination through  $2\text{HO}_2 \xrightarrow{11f} \text{H}_2\text{O}_2 + \text{O}_2$  regenerates the hydrogen peroxide molecule that was originally used in initiating the reaction sequence, the final overall step associated with the steady state of  $\text{HO}_2$ ,



derived by addition of  $\text{H}_2\text{O}_2 + 2\text{H}_2 + 2\text{O}_2 \rightarrow 2\text{H}_2\text{O} + 2\text{HO}_2$  and  $2\text{HO}_2 \xrightarrow{11f} \text{H}_2\text{O}_2 + \text{O}_2$ , neither produces nor destroys  $\text{H}_2\text{O}_2$ . Nevertheless its rate is proportional to the concentration of this species according to

$$\omega_{\text{I}'} = \omega_{10f} = k_{10f} C_{\text{M10}} C_{\text{H}_2\text{O}_2}. \quad (42)$$

It is of interest that the fast elementary reaction  $2\text{HO}_2 \xrightarrow{11f} \text{H}_2\text{O}_2 + \text{O}_2$  in the gas phase, responsible for the  $\text{HO}_2$  rapid consumption, was not present in the early theoretical analyses of reactions below crossover [145,146], leading these investigators to conclude erroneously that the radical  $\text{HO}_2$  remains out of steady state during the ignition process. It may be noted that this same erroneous conclusion continues to arise today [147].

Since the preceding path neither produces nor destroys  $\text{H}_2\text{O}_2$ , production of hydrogen peroxide relies instead on the elementary reaction  $\text{HO}_2 + \text{H}_2 \xrightarrow{12f} \text{H}_2\text{O}_2 + \text{H}$ . This does not alter, however, the concentration of  $\text{HO}_2$ , because subsequent removal of the H atom through  $\text{H} + \text{O}_2 + \text{M} \xrightarrow{4f} \text{HO}_2 + \text{M}$  leads by straightforward addition of these two elementary steps to the overall reaction



with corresponding rate  $\omega_{\text{II}'} = \omega_{12f}$ . This last step is autocatalytic, in that it produces  $\text{H}_2\text{O}_2$  with a rate that is proportional to the square root of its concentration, as can be seen by using the steady-state expression for  $\text{HO}_2$ , given in Eq. (41), to write

$$\omega_{\text{II}'} = \omega_{12f} = k_{12f} \left(k_{10f}/k_{11f}\right)^{1/2} C_{\text{M10}}^{1/2} C_{\text{H}_2} C_{\text{H}_2\text{O}_2}^{1/2}. \quad (43)$$

It is interesting to note in passing that the autocatalytic character of  $\text{H}_2\text{O}_2$  also arises in reduced autoignition chemistry of hydrocarbons [148,149].

The two overall steps I' and II', together with their associated rates, given, respectively, in Eqs. (42) and (43), provide the chemistry description needed to study ignition of hydrogen–oxygen mixtures below crossover. Unlike the high-temperature ignition events discussed in the previous section, ignition below crossover is seen to take place as a thermal explosion [72] as a result of the strong temperature sensitivity of both overall reactions, with corresponding activation temperatures, associated with the coefficients  $k_{10f}$  and  $k_{12f}(k_{10f}/k_{11f})^{1/2}$ , that can be seen to be almost identical [52]. Both steps have distinct necessary roles in the explosion development. Thus, because the heat of reaction associated with I' is about four times larger than that of II', the enthalpy of formation of  $\text{H}_2\text{O}$  being about twice that of  $\text{H}_2\text{O}_2$ , heat release relies predominantly on the first global step, whereas the second step contributes to the ignition process by creating in an autocatalytic fashion the  $\text{H}_2\text{O}_2$  needed to enable both reactions to proceed, as dictated by Eqs. (42) and (43).

With reactant consumption neglected, as is appropriate during the induction period leading to the thermal runaway in thermal explosions, the computation of the homogeneous ignition time reduces to the integration of the reduced conservation equations for energy and  $\text{H}_2\text{O}_2$  concentration,

$$\begin{aligned} \rho c_p \frac{dT}{dt} &= -2h_{\text{H}_2\text{O}} \omega_{\text{I}'}, \\ \frac{dC_{\text{H}_2\text{O}_2}}{dt} &= \omega_{\text{II}'}, \end{aligned} \quad (44)$$

with initial conditions  $T - T_0 = C_{\text{H}_2\text{O}_2} = 0$ , where  $T_0$  is the initial temperature and  $h_{\text{H}_2\text{O}} = -241.8$  kJ/mol is the value of the standard enthalpy of formation of water vapor. Variations of density  $\rho$  and specific heat  $c_p$  are negligibly small during the ignition process, and may correspondingly be ignored in Eq. (44), where heat release by  $\text{H}_2\text{O}_2$  formation has also been neglected in the energy balance.

If differences between the activation temperatures of the two overall rates are neglected, then the same dimensionless activation energy  $\beta$  can be employed in defining the dimensionless temperature increment

$$\theta = \beta \frac{T - T_0}{T_0}, \quad (45)$$

to be introduced in the Frank-Kamenetskii linearization of the reaction rates. The value,  $\beta = 25,703/T_0 - 4.2$ , corresponding to the low-pressure limit of the reaction coefficient  $k_{10f}$  controlling the rate  $\omega_{\text{I}'}$ , will be used below in the evaluations of the results. The scales needed to write the problem in dimensionless form follow from straightforward order-of-magnitude balances in Eq. (44), yielding the characteristic concentration of hydrogen peroxide

$$C_{\text{H}_2\text{O}_{2c}} = \frac{k_{12f}^{2/3}}{(k_{10f} k_{11f})^{1/3}} \frac{C_{\text{M10}}^{1/3} C_{\text{H}_2}^{2/3}}{(q\beta)^{2/3}} \quad (46)$$

and the accompanying characteristic time  $(q\beta k_{10f} C_{\text{H}_2\text{O}_{2c}})^{-1}$  required to reach a temperature increment of order  $T_0/\beta$ , as needed for ignition. Here  $q = -2h_{\text{H}_2\text{O}} C_{\text{M10}}/(\rho c_p T_0)$  represents an appropriate dimensionless heat of combustion. Introducing the dimensionless variables  $\varphi = C_{\text{H}_2\text{O}_2}/C_{\text{H}_2\text{O}_{2c}}$  and  $\tau = q\beta k_{10f} C_{\text{H}_2\text{O}_{2c}} t$  reduces Eq. (44) to

$$\frac{d\theta}{d\tau} = \frac{2}{3} \frac{d\varphi^{3/2}}{d\tau} = \varphi e^\theta; \quad \theta(0) = \varphi(0) = 0. \quad (47)$$

Integrating the first equation gives  $\theta = 2/3 \varphi^{3/2}$ , which can be substituted back into Eq. (47) to give

$$\tau_i = \left(\frac{2}{3}\right)^{2/3} \int_0^\infty \frac{d\theta}{\theta^{2/3} e^\theta} = \left(\frac{2}{3}\right)^{2/3} \Gamma(1/3) \approx 2.0444 \quad (48)$$

for the dimensionless ignition time, where  $\Gamma$  is the gamma function. The corresponding dimensional expression  $t_i = 2.0444/(q\beta k_{10f} C_{H_2O_2})$  has been shown to provide accurate predictions for homogeneous ignition times of  $H_2$ –air and  $H_2$ – $O_2$  mixtures under a wide range of conditions [52], including in particular those shown in Fig. 7. It is noteworthy that, since the overall rates given in Eqs. (42) and (43) are independent of the oxygen concentration, the predicted ignition time continuously decreases with increasing equivalence ratio, in agreement with the results obtained with detailed chemistry, also shown in the figure, consistent with recent experimental measurements [12]. Clearly, this trend must change for sufficiently large values of  $\phi$ , because in the absence of oxygen H-atom consumption through  $H + O_2 + M \xrightarrow{Af} HO_2 + M$  would no longer be operative, but the integrations suggest that this would occur for very rich mixtures, beyond the flammability limit, of little interest in applications.

### 5.3. The explosion limits of hydrogen–oxygen combustion

The ignitability of hydrogen–oxygen mixtures by elevated temperatures in closed chambers is known to possess a complex dependence on pressure [1,2] that exhibits three different limits separating self-ignitable and non-self-ignitable states [104]. The existence of these so-called explosion limits, emerging as a consequence of the competition of chemical kinetics with species transport, was unveiled in early experiments on the ignition of hydrogen–oxygen mixtures in spherical vessels coated with KCl (see, e.g. Refs. [150–152]), the gas-phase chemical kinetics competing with diffusive transport of species and their catalytic destruction at the wall surface. These explosion limits, which refer to spontaneous ignition, should not be confused with flammability limits, which are limiting conditions for deflagration propagation, possibly initiated by energy deposition.

For a given mixture composition and a given vessel radius, identification of self-ignition conditions in a pressure–temperature

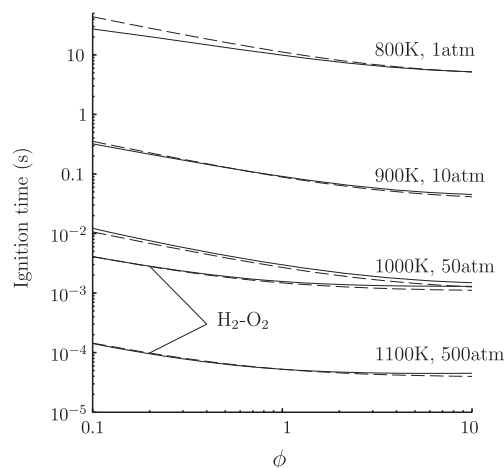


**Fig. 7.** The variation with equivalence ratio of the ignition time as obtained with the temperature-inflation criterion by numerical integration of the conservation equations with the 20-step detailed chemistry description of Table 1 (solid curves) and by evaluation of  $t_i = 2.0444/(q\beta k_{10f} C_{H_2O_2})$  (dashed curves) for  $H_2$ –air mixtures at different conditions of pressure and initial temperature and also for a  $H_2$ – $O_2$  mixture at  $p = 50$  atm and  $T = 1000$  K and at  $p = 500$  atm and  $T = 1100$  K; adapted from Ref. [52].

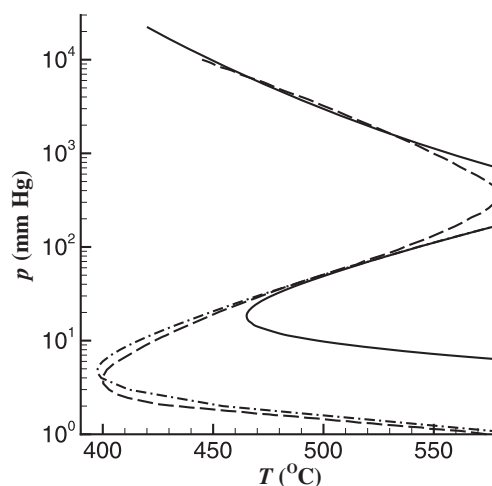


**Fig. 8.** The dashed curve corresponds to the experimental explosion limits of a stoichiometric hydrogen–oxygen mixture in a spherical KCl-coated vessels of 7.4 cm diameter as shown by Lewis and Von Elbe (p. 8 of Ref. [104]), with the solid curves being the analytic predictions obtained for a perfectly catalytic wall by evaluation of Eq. (51) (first and second explosion limits) and of Eq. (56) (third explosion limit) with  $a = 3.7$  cm and  $X_{H_2} = 0.66$ . The dot–dashed curve corresponds to the prediction obtained for the lower explosion peninsula by evaluating Eq. (51) with  $\pi^2$  replaced by 0.285, as corresponds to a wall surface with H-atom catalytic efficiency  $\epsilon = 0.72\sqrt{D_H/t_B/c}$ .

plot produces a reverse S curve. This is the classical explosion diagram shown in the first figure of the book by Lewis and Von Elbe [104], which is reproduced here in Fig. 8. The figure represents a collection of experimental measurements obtained in a spherical vessel of radius  $a = 3.7$  cm. The lower and upper branches of the curve involve extrapolation of the experimental measurements to lower and upper pressures, respectively. While the first limit is known to be “subject to erratic changes” [104], the third limit is reported to be quite reproducible, giving identical results for different salt-coated surfaces when a sufficiently thick coating layer is applied [145], that being the case for the experiments along the upper branch in Fig. 8.

Ignition in the lower peninsula of the diagram takes place as a branched-chain explosion controlled by the radical–production reaction  $3H_2 + O_2 \rightarrow 2H_2O + 2H$  described above. At low pressure, H-atom production by this chain-branching reaction competes with radical diffusion to the walls, where radicals are destroyed by surface reactions. Since the molecular diffusivity is inversely proportional to the pressure, while the rate of radical production is proportional to the pressure squared, for sufficiently low pressures radical diffusion dominates, and a non-explosive behavior is found below the so-called first explosion limit. On the other hand, the upper bound of the lower peninsula is a purely chemical-kinetic limit that arises because of the competition of radical production through  $3H_2 + O_2 \rightarrow 2H_2O + 2H$  with the three-body radical termination step  $H + O_2 + M \xrightarrow{Af} HO_2 + M$  [139], leading to the so-called second explosion limit defined by the crossover expression of Eq. (31).

For temperatures below crossover, that is, for pressures above the second explosion limit, the resulting chemical reactions are very slow, with homogeneous ignition times that are many orders of magnitude larger than those found above crossover, as is apparent by comparing the results in Fig. 6 with the two upper curves in Fig. 7. Consequently, for pressures exceeding the second explosion limit ignition is neutralized by diffusive transport of active species (mainly  $H_2O_2$ , all other radicals being in steady state) and subsequent destruction by surface reactions, leading to the

appearance of a non-explosive region above the explosion peninsula. Even though the chemistry is extremely slow, consideration of the reaction-diffusion balance indicates that, because of the increase of gas-phase chemical reaction rates with pressure and the accompanying reduction in species diffusivity, ignition may eventually take place provided that the pressure is increased to a sufficiently high value, thereby delineating a third explosion limit in the diagram.

The explosion limits of hydrogen–air mixtures have been investigated numerically in the past by integration of transient reaction-diffusion equations in spherically symmetric containers with detailed chemistry [153]. An alternative approach, providing analogous results for ignition boundaries, involves investigation of weakly reactive steady solutions with negligible reactant consumption, that being the classical approach postulated by Frank-Kamenetskii in his theory of thermal explosions [154]. For the hydrogen explosion problem, application of the Frank-Kamenetskii theory in combination with the reduced-chemistry descriptions presented in the two preceding sections provides simple analytic expressions for the explosion limits, given below in Eqs. (51) and (56). We begin by analyzing the boundary of the lower peninsula, determined by the solution of a linear eigenvalue problem, and address subsequently the nonlinear thermal-runaway problem that determines the third explosion limit, a presentation that largely follows our recent work [155].

### 5.3.1. The lower peninsula of the explosion diagram

One classical approach to the quantification of the lower explosion limit is based on the investigation of existence of solutions in spherical symmetry to the branching-diffusion equations with radical destruction at the wall. This problem was addressed over 80 years ago by Bursian and Sorokin, as discussed by Kassel and Storch [156]. According to the chain-branching chemistry described above, the equations that should be written to determine the quasisteady radial distributions of H, O, and OH would be identical to Eqs. 25–27, with the accumulation terms on the left-hand side replaced by the spherically symmetrical diffusion operator, written with the simple Fickian description of Eq. (21) for the diffusion velocities, as corresponds to the nearly uniform conditions envisioned here. If the small initiation reaction is neglected, then the linear combination leading to Eq. (28) would provide in this case

$$-\frac{D_H}{r^2} \frac{d}{dr} \left[ r^2 \frac{d}{dr} \left( C_H + \frac{2D_O}{D_H} C_O + \frac{D_{OH}}{D_H} C_{OH} \right) \right] = (2k_{1f} - k_{4f} C_{M4}) C_{O_2} C_H. \quad (49)$$

The different mixture-average diffusion coefficients are defined in terms of binary diffusion coefficients in Eq. (21), giving, for instance,

$$D_H = \left( \frac{X_{H_2}}{D_{H H_2}} + \frac{1 - X_{H_2}}{D_{H O_2}} \right)^{-1} \quad (50)$$

for the H-atom diffusivity, with recently updated values reported in [100] for  $D_{H H_2}$  and  $D_{H O_2}$ . Since the diffusion-coefficient ratios emerging in Eq. (49) are fairly small, i.e.,  $D_O/D_H \approx D_{OH}/D_H \approx 0.30$ , it is apparent that neglecting the presence of the steady-state species O and OH in the radical pool in this case introduces errors in the description that are significantly smaller than those involved in writing Eq. (34) from Eq. (28). The same conclusion can be expected in general to apply in other combustion problems dominated by diffusion, including reaction layers in premixed flames, for which the steady-state assumptions for O and OH are much more accurate

than they are in homogeneous ignition processes, as indicated by the results of flame propagation velocities shown in Fig. 1.

The simplified equation obtained when the terms involving  $C_O$  and  $C_{OH}$  are neglected in Eq. (49) can be integrated with the condition  $dC_H/dr = 0$  at  $r = 0$ , excluding a singularity and enforcing symmetry, to give the general solution  $C_H = (\mathcal{A}/r) \sin(r/\sqrt{D_H t_B})$ , where  $\mathcal{A}$  is an undetermined constant, and  $t_B$  is the characteristic branching time defined in Eq. (29). A second boundary condition must be applied at the vessel wall associated with the occurrence of catalytic reactions on its surface. For perfectly catalytic walls the condition  $C_H = 0$  of complete radical destruction may be applied at  $r = a$ , resulting in  $(\mathcal{A}/a) \sin(a/\sqrt{D_H t_B}) = 0$ . The equation  $a/\sqrt{D_H t_B} = \pi$  then emerges as a necessary condition for non-negative, nontrivial solutions to exist, thereby providing the criticality condition

$$\pi^2 = a^2 (2k_{1f} - k_{4f} C_{M4}) C_{O_2} / D_H \quad (51)$$

for the explosion limit. When the right-hand side of Eq. (51) is less than  $\pi^2$  the time dependent system evolves to a slowly reacting state, while for larger values radical concentrations experience an exponential growth in time. For given values of the vessel radius  $a$  and the mixture composition, this last expression can be used to relate the pressure and temperature along the lower peninsula of the explosion diagram. There is a low-pressure branch  $\pi^2 \approx 2a^2 k_{1f} C_{O_2} / D_H$  defining the first explosion limit and a high-pressure branch  $2k_{1f} \approx k_{4f} C_{M4}$  defining the second.

The  $p$ – $T$  curve obtained by evaluating Eq. (51) with  $a = 3.7$  cm and  $X_{H_2} = 0.66$  is plotted in Fig. 8, showing that while the second explosion limit is described adequately, the solution (51) clearly overpredicts the experimental measurements along the lower branch, suggesting that in the experiments the walls are not perfectly catalytic for H-atom removal, so that a more complicated boundary condition needs to be applied. Equating the diffusive flux  $-D_H dC_H/dr$  at  $r = a$  to the rate of catalytic reaction  $\varepsilon(\bar{c}/4)C_H(a)$  (i.e., number of moles destroyed per unit time per unit wall surface), where  $\varepsilon$  is the fraction of H atoms destroyed on striking the wall surface and  $\bar{c}$  is the average molecular speed [157], yields

$$\frac{\varepsilon}{4\sqrt{D_H/t_B}/\bar{c}} = \frac{\sin(a/\sqrt{D_H t_B}) / (a/\sqrt{D_H t_B}) - \cos(a/\sqrt{D_H t_B})}{\sin(a/\sqrt{D_H t_B})}. \quad (52)$$

The previous result  $a/\sqrt{D_H t_B} = \pi$  emerges from Eq. (52) for highly catalytic walls with  $\varepsilon \gg 4\sqrt{D_H/t_B}/\bar{c}$ . The experimental data suggests however a much smaller radical-recombination efficiency. For instance, the dot-dashed curve in Fig. 8 follows from replacing  $\pi^2$  on the left-hand side of Eq. (51) with 0.285, which corresponds to the result  $a/\sqrt{D_H t_B} = 0.534$  obtained for  $\varepsilon = 0.72\sqrt{D_H/t_B}/\bar{c}$ , a value between 0.002 and 0.006 in this range of temperatures. Figure 8 demonstrates that the prediction obtained from the simple theory with additional account of the reduced catalytic efficiency is in excellent agreement with the experimental measurements.

### 5.3.2. The third explosion limit

The classical explanation for the third explosion limit relies on the competition of the gas-phase chemistry with the diffusion of  $HO_2$  to the container walls [145,146], where it is destroyed by catalytic reactions. These classical analyses, and also similar more recent investigations [147], do not account for the effect of  $HO_2$  consumption through  $2HO_2 \xrightarrow{11f} H_2O_2 + O_2$ . When this essential reaction is removed from the chemistry description, the problem at the third limit can be reduced to a linear eigenvalue problem representative of an apparent



chain-branching explosion, with  $\text{HO}_2$  as the predominant chain carrier. However, ignition at the third limit is not a chain-branching explosion, but rather a thermal explosion, as was demonstrated twenty five years ago in numerical integrations with detailed chemistry [153]. The description of the process must account for the rapid removal of  $\text{HO}_2$  radicals through  $2\text{HO}_2 \xrightarrow{11f} \text{H}_2\text{O}_2 + \text{O}_2$ , because this reaction becomes dominant at the radical levels associated with the thermal runaway, deactivating the chain-branching explosion by keeping  $\text{HO}_2$  in steady state [52], with a local concentration that corresponds to the instantaneous production–consumption balance. As a result, hydroperoxyl transport towards the catalytic walls becomes irrelevant for the determination of the third explosion limit [155]. Instead, ignition develops as a thermal explosion driven by the cooperative action of heat release and  $\text{H}_2\text{O}_2$  production by gas-phase reactions, in the presence of heat conduction and  $\text{H}_2\text{O}_2$  diffusion towards the vessel walls. The solution of the associated Frank-Kamenetskii problem for the thermal explosion in the spherical vessel, given in [155], yields a simple analytical expression for the third explosion limit that compares favorably with the upper curve of the experimental diagram of Fig. 8.

To formulate the Frank-Kamenetskii problem for the quasi-steady weakly reactive solution in the spherical vessel, the conservation equations for energy and for hydrogen peroxide were written in Ref. [155] with variations of density and transport properties neglected along with reactant consumption and heat release by  $\text{H}_2\text{O}_2$  formation. Correspondingly, the resulting equations are simply those of the homogeneous-explosion problem defined in Eq. (44) with the accumulation terms replaced by the differential operators for heat conduction and  $\text{H}_2\text{O}_2$  diffusion, and the simple Fickian description of Eq. (21) is used for the diffusion velocity. The problem is subject to the conditions  $dT/dr = dC_{\text{H}_2\text{O}_2}/dr = 0$  at the center  $r = 0$  and the boundary conditions  $T - T_0 = C_{\text{H}_2\text{O}_2} = 0$  at  $r = a$ , the latter imposing a fixed temperature  $T_0$  at the wall (maintained with a thermostat in experiments), where it is assumed that hydrogen peroxide is rapidly destroyed by the fast surface reaction  $\text{H}_2\text{O}_2 \rightarrow \text{H}_2 + \text{O}_2$ . Consideration of the balance between  $\text{H}_2\text{O}_2$  diffusion and its gas-phase production through reaction II' gives in this case

$$\tilde{C}_{\text{H}_2\text{O}_{2c}} = \frac{\lambda T_0 / \beta}{(-2h_{\text{H}_2\text{O}})k_{10f}C_{\text{M}10}a^2} \quad (53)$$

for the characteristic hydrogen peroxide concentration required to increase the temperature by an amount of the order of the Frank-Kamenetskii increment  $T_0/\beta$ , where  $\lambda$  is the thermal conductivity of the gas mixture. Introducing the dimensionless temperature  $\theta$  defined in Eq. (45) and the accompanying  $\text{H}_2\text{O}_2$  concentration  $\tilde{\varphi} = C_{\text{H}_2\text{O}_2}/\tilde{C}_{\text{H}_2\text{O}_{2c}}$ , along with the dimensionless radial coordinate  $\tilde{r} = r/a$ , reduces the problem to that of integrating

$$\left. \begin{aligned} \frac{1}{\tilde{r}^2} \frac{d}{d\tilde{r}} \left( \tilde{r}^2 \frac{d\theta}{d\tilde{r}} \right) &= -\tilde{\varphi} e^\theta; & \theta(1) &= \frac{d\theta}{d\tilde{r}}(0) = 0 \\ \frac{1}{\tilde{r}^2} \frac{d}{d\tilde{r}} \left( \tilde{r}^2 \frac{d\tilde{\varphi}}{d\tilde{r}} \right) &= -Da \tilde{\varphi}^{1/2} e^\theta; & \tilde{\varphi}(1) &= \frac{d\tilde{\varphi}}{d\tilde{r}}(0) = 0 \end{aligned} \right\} \quad (54)$$

The only controlling parameter in Eq. (54) is the Damköhler number

$$Da = k_{12f} \left( k_{10f}/k_{11f} \right)^{1/2} \frac{C_{\text{M}10}^{1/2} C_{\text{H}_2}}{\tilde{C}_{\text{H}_2\text{O}_{2c}}^{1/2}} \left( a^2/D_{\text{H}_2\text{O}_2} \right) \quad (55)$$

defined as the ratio of the diffusion time across the vessel,  $a^2/D_{\text{H}_2\text{O}_2}$ , to the characteristic chemical time required to increase the  $\text{H}_2\text{O}_2$  concentration to a value of the order of  $\tilde{C}_{\text{H}_2\text{O}_{2c}}$ .

As occurs in the classical Frank-Kamenetskii analysis of thermal explosions for one-step Arrhenius kinetics [154], the problem defined in Eq. (54) possesses two different nontrivial solutions for any given value of  $Da$  smaller than a critical value, and no weakly reacting solution exists for  $Da > Da_c$ , indicating that this critical value identifies ignition conditions. Numerical integration provides  $Da_c = 10.25$ , a value that can be substituted into Eq. (55) to produce the equation

$$a = \left[ \frac{10.25 D_{\text{H}_2\text{O}_2} \left( \lambda T_0 k_{11f} \right)^{1/2}}{k_{10f} k_{12f} C_{\text{M}10} C_{\text{H}_2} \left( -2\beta h_{\text{H}_2\text{O}} \right)^{1/2}} \right]^{1/3} \quad (56)$$

for the critical conditions corresponding to the third explosion limit [155]. In principle, an implicit calculation is required to determine the variation of the pressure as a function of the temperature for given values of  $a$  and  $X_{\text{H}_2}$  from Eq. (56). The results obtained in [155] for  $a = 3.7$  cm and  $X_{\text{H}_2} = 0.66$  are included in Fig. 8, where it can be seen that, away from the upper nose of the explosion diagram, the temperature dependence of the critical explosion pressure is predicted remarkably well by the analytical expression in Eq. (56). The accuracy of the agreement displayed in the figure seems to indicate that, despite the many uncertainties present in the problem (see the detailed discussion in Ref. [155]), the simplified model developed captures well the essential physical phenomena underlying the explosion in this limit, thereby providing the answer to a long-standing problem that in early work was characterized as being “hopelessly difficult” [152]. The comparisons in Fig. 8 also suggest that the catalytic efficiencies of the coated walls are much higher for  $\text{H}_2\text{O}_2$  removal than for H-atom removal.

#### 5.4. Effects of flow strain and nonuniform temperature and composition fields on autoignition

The fundamental problems reviewed above – homogeneous ignition and critical explosion conditions resulting from diffusion-reaction balances in closed vessels – have been studied at length in the past because they provide valuable insight into the specific chemistry interactions occurring in hydrogen–oxygen systems and their dependences on pressure, temperature, and composition. However, the associated convection-free uniform (or nearly uniform) conditions postulated in these simplified configurations are hardly ever encountered in practical applications. Instead, auto-ignition of hydrogen often occurs in turbulent flows within ignition kernels having nonuniform temperature and composition fields [158,159], that being the case in scramjet combustors, gas-turbine mixing systems, and also in many of the accidental scenarios pertaining to hydrogen storage and transport. In all of these practical applications, influences of strain rate,  $A$ , and of local gradients of temperature and reactants on the ignition process need to be incorporated in the description for an accurate quantification of autoignition times and distances.

Much of our present understanding of the local chemistry-mixing interactions occurring in turbulent reacting flows stems from analyses of simple laminar-flow problems [160], the counterflow mixing layer and the unstrained unsteady mixing layer being two prominent examples. As indicated in Fig. 9, the former may be thought to be representative of local flow conditions in vortex-braid regions along unstable shear layers, while the latter describes approximately mixing and reaction at the low-strain interfaces wrapped around the vortices. These laminar configurations have been employed in the last twenty years to investigate hydrogen ignition, mostly in systems with boundary temperatures above crossover. Autoignition solutions in steady counterflow nonpremixed configurations have been computed with detailed

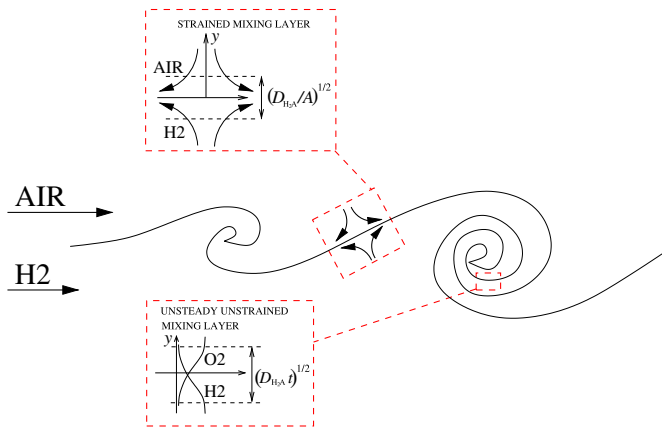


Fig. 9. Schematic view of the downstream evolution of a hydrogen–air mixing layer.

and reduced chemistry [75,102,161–167] and critical conditions for ignition have been measured experimentally for this configuration [168,169]. Effects of strain-rate fluctuations on autoignition of counterflow hydrogen–air flames have been addressed analytically [143], computationally [170–172], and experimentally [173]. The problem of the unstrained unsteady mixing layer, recently addressed in investigations of hydrogen autoignition [103,142], is known to be similar to that of the steady coflow mixing layer, extensive work on which has been motivated by interest in supersonic combustion. While most of the previous studies of hydrogen–air ignition for this last configuration are either numerical or theoretical [174–181], a few experimental studies are also available (see, e.g. Refs. [182–184]).

The early analyses of ignition in mixing layers employed a one-step Arrhenius reaction with large activation energy for the chemistry description [185,186]. The variation of the peak temperature with strain time in steady counterflow mixing layers was found to display a characteristic S-shape curve [185], with the lower turning point identifying critical ignition conditions above which a weakly reactive solution is no longer attainable. On the other hand, ignition in unsteady mixing layers was found to proceed as a thermal explosion with a well-defined thermal-runaway time [186], after which the flame develops, often with a tribrachial structure that evolves to leave for large times a central diffusion flame. For one-step Arrhenius chemistry, both the strain time in the counterflow and the ignition time in the unsteady mixing layer were found to be of the order of the homogeneous ignition time for the stoichiometric fuel–oxidizer mixture, although significant quantitative corrections were seen to arise from the nonuniform character of the flow [185,186].

Many of the qualitative results obtained in previous mixing-layer analyses with model one-step Arrhenius chemistry can be expected to apply to hydrogen combustion when ignition occurs as a thermal explosion, i.e., for boundary temperatures below crossover. For instance, our recent analysis of hydrogen ignition in unstrained mixing layers [103] has shown that, just as in the early general theory [186], when the temperatures of the two sides are very close, the reaction is distributed all across the mixing layer, whereas for hot-air ignition the reaction zone is thin and sits next to the hot boundary. The corresponding analytical treatments, based on activation-energy asymptotics and involving either parabolic partial differential equations for describing the evolution with time of the distributed reaction or a two-point boundary-value problem for hot-side ignition, are also mathematically similar to those encountered previously with one-step Arrhenius chemistry. It can be expected that, as in Ref. [185], the solution for ignition

in steady counterflow mixing layers at temperatures below crossover will be determined by the lower turning point in an S-shape diagram, with values of the critical strain rate of the order of the reciprocal of the homogeneous thermal-runaway time  $t_i = 2.0444/(q\beta k_{10f}C_{H_2O_{2c}})$  obtained in Eq. (48), but such an analysis has not been attempted yet.

Because of fundamental differences in the chemistry, for the chain-branching explosion found above crossover interesting new features arise that cannot be predicted with one-step Arrhenius chemistry. For example, the early numerical integrations of Darabiha and Candel [161] showed that the S-shape curve in counterflow diffusion flames is replaced by solutions involving a sharp transition from the frozen state, representative of a transcritical bifurcation [102], with a reactive branch that may exhibit a positive or negative slope depending on the conditions, degenerating to give an unconnected C-shape curve when the boundary temperatures fall below crossover [162], as shown in the schematic representation on Fig. 10. Differences with the results of one-step Arrhenius chemistry also emerge in unsteady unstrained mixing layers (and also in spatially developing, coflow mixing layers). Since the chain-branching explosion requires large times  $t_i = t_B \ln(t_i/t_B) \gg t_B$  as in Eq. (36), the solution develops a distinct structure dominated by transverse radical diffusion and including a localized kernel of radical production located around the transverse location where the local branching time of the mixture, defined in Eq. (39), reaches its minimum value [142].

To close this section on autoignition, we shall present below a brief description of the solutions corresponding to ignition above crossover in both counterflow and unsteady unstrained mixing layers with hot oxidizer streams. Nonpremixed hydrogen–air systems will be considered, although the associated mathematical treatments and most of the conclusions drawn also apply to premixed autoignition (e.g., in boundary layers [144,187] and counterflow configurations [188,189]). Since the temperature sensitivity of the chain-branching explosion characterizing hydrogen ignition at high temperature is modest (because the activation temperature of the controlling reaction 1f is only moderately large), the accuracy of analytical approaches based on activation-energy asymptotics [163] is necessarily limited. Alternative mathematical techniques, exploiting the disparity of time scales  $t_i \gg t_B$ , are better suited for the treatment of hydrogen-ignition problems at high temperature, including bifurcation methods for counterflow ignition [102,162] and WKB methods for radical growth in mixing layers [179,180,190].

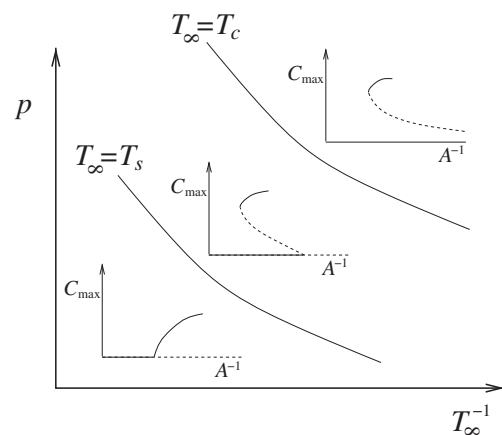


Fig. 10. Ignition behaviors present in high-temperature hydrogen–air counterflow flames (adapted from Ref. [162]). Dashed lines are employed to denote unstable solutions.

#### 5.4.1. Ignition in the counterflow mixing layer

The solution in the steady counterflow mixing layer depends fundamentally on the strain rate of the outer streams, whose reciprocal defines the characteristic residence time of the flow. The solution is self-similar, with the profiles of temperature and composition being a function of the distance  $y$  to the stagnation plane. As indicated in Fig. 9, in the problem considered below air flows from  $y = \infty$  and hydrogen flows from  $y = -\infty$ , the subscripts  $\infty$  and  $-\infty$  being correspondingly used to denote properties in the feed streams. To simplify the presentation here, the density and transport properties will be assumed to be constant, so that the transverse velocity reduces to  $v = -Ay$  in terms of the strain rate  $A$ , which can be used to define a dimensionless transverse coordinate  $\zeta = y/(D_{H_2A}/A)^{1/2}$ . Here  $D_{H_2A}$  denotes the binary diffusion coefficient of hydrogen and air, with corresponding diffusion velocities computed from Eq. (20) with thermal diffusion neglected, while a simple Fickian description with constant diffusivity is adopted for the radicals. If at least one of the boundary temperatures lies above crossover, then the predominant chemical reactions are those described above in Section 5.1. With convection included in the description, the linear combination leading to Eq. (49) provides in this case

$$-\zeta \frac{d}{d\zeta} (C_H + 2C_O + C_{OH}) - \frac{d^2}{d\zeta^2} \left( \frac{D_H}{D_{H_2A}} C_H + \frac{2D_O}{D_{H_2A}} C_O + \frac{D_{OH}}{D_{H_2A}} C_{OH} \right) = A^{-1} (2k_{1f} - k_{4f}C_{M4}) C_{O_2} C_H. \quad (57)$$

for the steady distributions of radical concentration in the planar counterflow mixing layer. Since the small initiation term has been neglected in Eq. (57), when the air and hydrogen streams are free of radicals, the problem admits the trivial solution  $C_H = C_O = C_{OH} = 0$  corresponding to frozen flow for all values of the strain rate, with associated frozen reactant and temperature profiles determined by the convection–diffusion balances in their respective conservation equations. Besides the frozen solution, there exists a branch of reactive solutions bifurcating from the frozen solution at a critical value of the strain rate, as is schematically represented in Fig. 10 by plotting the maximum concentration of radicals as a function of the strain time  $A^{-1}$ .

The solution for the bifurcation, first obtained in Ref. [162], requires consideration of expansions for the different variables around the frozen solution. If steady-state assumptions are introduced for the radicals O and OH, then the solution at leading order, determining the critical strain rate at ignition, can be obtained by solving

$$-\zeta \frac{dC}{d\zeta} - \frac{d^2}{d\zeta^2} [\tilde{D}(\zeta)C] = \Delta W_B(\zeta)C; \quad C(\pm\infty) = 0, \quad (58)$$

derived by writing Eq. (57) in terms of the radical pool variable  $C = C_H + 2C_O + C_{OH}$ . The ignition Damköhler number,

$$\Delta = \frac{1}{At_{B_\infty}} = \frac{[(2k_{1f} - k_{4f}C_{M4})C_{O_2}]_\infty}{A}, \quad (59)$$

has been defined with the characteristic branching time evaluated on the oxidizer side on the mixing layer, as is appropriate when the air side is hotter than the hydrogen side, the case most commonly encountered in applications. The nondimensional branching rate

$$W_B = \frac{(2k_{1f} - k_{4f}C_{M4})}{(2k_{1f} - k_{4f}C_{M4})_\infty} \frac{(X_{O_2}/X_{O_{2A}})X_{H_2}}{X_{H_2} + 2(k_{1f}/k_{2f} + k_{1f}/k_{3f})X_{O_2}} \quad (60)$$

and the average radical-pool diffusivity ratio

$$\tilde{D} = \frac{\frac{D_H}{D_{H_2A}}X_{H_2} + 2\left(\frac{k_{1f}}{k_{2f}}\frac{D_O}{D_{H_2A}} + \frac{k_{1f}}{k_{3f}}\frac{D_{OH}}{D_{H_2A}}\right)X_{O_2}}{X_{H_2} + 2\left(\frac{k_{1f}}{k_{2f}} + \frac{k_{1f}}{k_{3f}}\right)X_{O_2}} \quad (61)$$

are to be evaluated with use made of the frozen reactant and temperature profiles  $X_{H_2} = 1 - X_{O_2}/X_{O_{2A}} = 1/2\text{erfc}(\zeta/\sqrt{2})$  and  $(T - T_\infty)/(T_{-\infty} - T_\infty) = 1/2\text{erfc}(\zeta/\sqrt{2L_{H_2A}})$ . Here  $\text{erfc}$  is the complementary error function,  $X_{O_{2A}} \approx 0.21$  is the mole fraction of oxygen in air,  $L_{H_2A}$  is the Lewis number based on  $D_{H_2A}$ , and  $T_\infty$  and  $T_{-\infty}$  are the air and hydrogen free-stream temperatures, respectively.

A nontrivial, non-negative solution to the linear problem defined in Eq. (58) exists for a single value of  $\Delta = \Delta_i$  of order unity, which determines from Eq. (59) the critical ignition strain rate  $A_i \sim t_{B_\infty}^{-1}$  at which the reactive branch bifurcates from the frozen solution. As expected, when  $T_\infty$  approaches the crossover value  $T_c$ , the critical strain time  $A_i^{-1}$  increases, becoming infinity when  $T_\infty = T_c$  (i.e., when  $(2k_{1f} - k_{4f}C_{M4})_\infty = 0$ ). Consequently, for  $T_\infty < T_c$  the present description predicts the reactive branch to be a C-shape curve unconnected to the frozen solution. Consideration of the low-temperature chemistry described in Section 5.2 would be needed to describe the connection between both branches, which would appear for very large strain times  $A^{-1}$  of the order of the characteristic homogeneous ignition time  $(q\beta k_{10f}C_{H_2O_{2c}})^{-1}$ .

The sign of the slope of the resulting igniting branch in the plot of peak radical concentration versus strain time  $A^{-1}$  depends on the variation of the associated reaction rate occurring as ignition develops, which is determined by the counteracting effects of chemical heat release and reactant consumption, as is clearly apparent in the time ratio  $A^{-1}(2k_{1f} - k_{4f}C_{M4})C_{O_2}$  emerging on the right-hand side of Eq. (57). Along the igniting branch, the changes in the strain time  $A^{-1}$  must compensate the changes in branching time  $1/[(2k_{1f} - k_{4f}C_{M4})C_{O_2}]$ . As the chemical reaction proceeds away from the bifurcation point, the effective branching coefficient  $(2k_{1f} - k_{4f}C_{M4})$  increases because of the associated temperature increase, but the oxygen concentration decreases, so that the product  $(2k_{1f} - k_{4f}C_{M4})C_{O_2}$  may increase or decrease, depending on the existing conditions. It was found [162] that for low values of the boundary temperature, the sensitivity of reaction 1f, measured by the dimensionless activation temperature  $T_{a1f}/T_\infty$ , is sufficiently high for the effect of heat release to be dominant, causing the product  $(2k_{1f} - k_{4f}C_{M4})C_{O_2}$  to increase as ignition develops and forcing the compensating strain time  $A^{-1}$  to have to decrease. The bifurcation diagram of these solutions, including a negative slope, is represented in the intermediate plot of Fig. 10, giving a curve that, except for the sharp turning point, resembles the S-shape curve obtained in the early activation-energy analyses [185]. As the boundary temperature further increases, the dimensionless activation temperature  $T_{a1f}/T_\infty$  becomes smaller, and the slope of the curve  $C_{\max}A^{-1}$  becomes larger. A limiting temperature  $T_\infty = T_s$  is reached above which reactant consumption becomes dominant, causing the product  $(2k_{1f} - k_{4f}C_{M4})C_{O_2}$  to decrease – and the accompanying value of  $A^{-1}$  to increase – as ignition proceeds. With a positive slope, the resulting bifurcating branch for  $T_\infty > T_s$  provides a smooth transition from the frozen state to the diffusion flame appearing for much larger values of  $A^{-1}$ , as described in the lower plot of Fig. 10, giving a physical picture that is fundamentally different from that envisioned in the classical S-shape curve.

The different ignition behaviors shown in Fig. 10, first identified in numerical integrations with detailed chemistry [161], were

described by bifurcation methods in Ref. [162], with effects of detailed transport and variable density being addressed in a later study [102]. Although stability analyses of the resulting solutions have not been attempted, it is expected that the frozen solution loses stability at the bifurcation point. For high boundary temperatures  $T_\infty > T_s$ , the igniting branch corresponds to stable solutions, but for  $T_\infty < T_s$ , the solutions along the igniting branch below a point very close to the upper turning point are probably unstable, in agreement with the stability characteristics of the S-shape curve for one-step Arrhenius chemistry [191].

#### 5.4.2. Chain-branching explosions in unsteady unstrained mixing layers

For steady elliptic problems, just as in the weakly reactive reaction-diffusion solutions that determine the lower explosion peninsula for closed vessels or the counterflow ignition problem described in the previous section, the slow initiation reaction has a minor effect on the branched-chain explosion. This situation arises because, in each of these two cases, the characteristic initiation time  $t_i$ , given in Eq. (30), is much larger than the corresponding controlling time.<sup>1</sup> For instance, as discussed in [102], consideration of initiation would only modify slightly the ignition behavior shown Fig. 10, with the transcritical bifurcation becoming an imperfect bifurcation. By way of contrast, it was shown in Section 5.1 that initiation reactions are needed to describe the initial development of the chain-branching homogeneous explosion when no radicals are present at the start. In a similar manner, initiation reactions are also found to be important in parabolic problems with radical-free initial conditions, an example being the unsteady unstrained mixing layer now to be analyzed.

Consider the temporal evolution of two stagnant spaces of  $H_2$  and air that begin to mix and react at time  $t = 0$ , with the air occupying initially the semispace  $y > 0$ . In the weakly reactive solution observed prior to ignition, the reactants mix without appreciable chemical reaction, giving a nearly self-similar evolution for the reactant and temperature profiles. As in the previous section, we simplify the presentation by assuming constant density and constant transport properties. To describe the ignition process, including the self-similar mixing occurring in the absence of chemical reaction, it is convenient to formulate the problem in terms of the dimensionless coordinate  $\eta = y/(D_{H_2A}t)^{1/2}$ . If the temperature of at least one of the two reactants is above crossover, then ignition proceeds as a chain-branching explosion, with the elementary reactions considered in Section 5.1. Elimination of the fast rates  $\omega_{2f}$  and  $\omega_{3f}$  by linear combination of the radical conservation equations and introduction of the radical-pool concentration and the diffusivity ratio given in Eqs. (37) and (61) leads in this case to the evolution problem

$$\frac{\partial C}{\partial t} - \frac{1}{t} \left[ \frac{\eta}{2} \frac{\partial C}{\partial \eta} + \frac{\partial^2}{\partial \eta^2} (\tilde{D}C) \right] = \frac{C}{\tilde{t}_B} + \frac{C_{H_2}}{t_i} \quad (62)$$

subject to the initial and boundary conditions

$$\begin{aligned} t = 0: & \quad C = 0 \text{ for } -\infty < \eta < +\infty \\ t > 0: & \quad C = 0 \text{ as } \eta \rightarrow \pm\infty. \end{aligned} \quad (63)$$

As in Eq. (38), the chemical times  $t_i$  and  $\tilde{t}_B$  are those defined in Eqs. (30) and (39), which now are functions of  $\eta$ , to be calculated across the mixing layer from the chemically frozen profiles  $X_{H_2} = 1 - X_{O_2}/X_{O_{2A}} = 1/2\text{erfc}(\eta/2)$  and  $(T - T_\infty)/(T_- - T_\infty) = 1/2\text{erfc}(\eta/\sqrt{L_{H_2A}})$ . In particular, the

presence of the product  $C_{O_2}C_{H_2}$  in the denominator of Eq. (39) guarantees that the branching time  $\tilde{t}_B$  diverges in the free streams, as it should because of the absence of one of the two reactants, and that a minimum value  $\tilde{t}_B^*$  is reached at the intermediate location  $\eta = \eta^*$  where the most reactive conditions are achieved.

According to the homogeneous-explosion result in Eq. (40), if the effect of radical transport were entirely negligible, then the radical pool at each transverse location would follow an exponential increase, with the branching rate corresponding to the local conditions of composition and temperature, giving a maximum growth rate at an intermediate location dependent on the distributions of both  $\tilde{t}_B(\eta)$  and  $t_i(\eta)$ . This simple transportless description is, however, fundamentally incorrect because, since values of  $t/\tilde{t}_B \sim \ln(t_i/t_B) \gg 1$  are required to reach the ignition conditions corresponding to  $C \sim C_{H_2}$ , the radical profile given in Eq. (40) would develop a pronounced peak, clearly incompatible with the assumption of negligible radical diffusion. In fact, rather than being negligible, radical diffusion becomes dominant for large values of  $t/\tilde{t}_B$ , causing radical growth to proceed at a uniform rate at leading order all across the mixing layer, with a value everywhere associated with the minimum branching time  $\tilde{t}_B^*$ , found at  $\eta = \eta^*$ . The necessary mathematical description, based on  $\ln(t_i/t_B) \gg 1$  as an asymptotically large quantity, was first developed for spatially evolving mixing layers [179,180,190]. The following presentation of the approach parallels our recent application of the methodology to transient ignition in unstrained mixing layers [142]. The results can find application, in particular, in assessing the accidental ignition of hydrogen jets suddenly issuing from pressurized containers, for which the shock wave produced by the jet discharge preheats the surrounding air and enables ignition to occur in the mixing layer formed at the jet front [192,193]. The methodology could be extended in principle to treat other high-temperature hydrogen-ignition problems, such as boundary-layer ignition over a hot plate [144,187] and diffusion-flame ignition in the presence of a vortex [194,195].

The development begins by writing Eq. (62) in terms of the dimensionless time  $\tau = [(2k_{1f} - k_{4f}C_{M4})C_{O_2}]_\infty t$  and the normalized radical concentration  $Y = C/C_{H_2-\infty}$  to give

$$\frac{\partial C}{\partial \tau} - \frac{1}{\tau} \left[ \frac{\eta}{2} C_\eta + (\tilde{D}C)_{\eta\eta} \right] = W_B(\eta)Y + \varepsilon W_I(\eta), \quad (64)$$

where

$$\varepsilon = (t_B/t_i)_\infty = [k_{6b}/(2k_{1f} - k_{4f}C_{M4})]_\infty \ll 1 \quad (65)$$

is the initiation-to-branching rate ratio evaluated on the air side. The subscript  $\eta$  is employed in Eq. (64) to denote differentiation

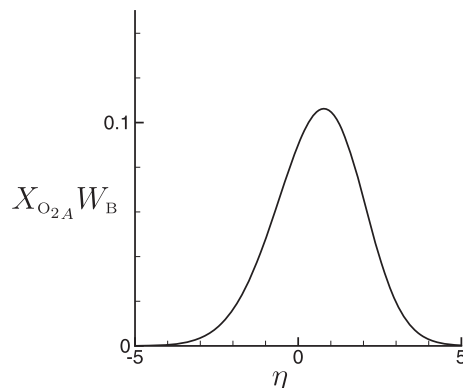


Fig. 11. The reduced branching rate  $X_{O_{2A}} W_B$  evaluated from Eq. (60) for an isothermal mixing layer with  $T = 1200$  K; adapted from Ref. [142].

<sup>1</sup> The diffusion time  $a^2/D_H$  across the spherical vessel and the strain time  $A^{-1}$  of the coflow are both of order  $t_B \ll t_i$  at ignition, as can be seen in Eqs. (51) and (59).



with respect to this variable. The branching rate  $W_B$ , defined above in Eq. (60), and the accompanying initiation rate  $W_I = (k_{6b}/k_{6b\infty})(X_{O_2}/X_{O_{2A}})X_{H_2}$  are dimensionless functions of order unity, to be evaluated from the frozen profiles of temperature and reactants. For illustrative purposes, the distribution of  $X_{O_{2A}}W_B = X_{O_2}X_{H_2}/(X_{H_2} + 2.13X_{O_2})$  corresponding to an isothermal mixing layer at  $T = 1200$  K is shown in Fig. 11. The associated branching rate  $W_B$  exhibits a maximum value  $W_B^* \approx 0.504$  at  $\eta = \eta^* \approx 0.787$ , corresponding to the minimum of the branching time given in Eq. (39).

The effect of initiation is only important for  $t \sim t_B$ , i.e.,  $\tau \sim O(1)$ , when the value of  $Y$  is of order  $\varepsilon$ , and it is negligible for larger times. Ignition occurs when  $Y = C/C_{H_2-\infty} \sim O(1)$ , corresponding to  $\tau \sim \ln(\varepsilon^{-1}) \gg 1$ . In analyzing ignition, one may therefore neglect the initial stage in which initiation is important and focus on the long-time evolution for  $\tau \gg 1$ , with initiation neglected in Eq. (64) and the radical pool taking the form

$$Y/\varepsilon = \exp[G_0(\eta)\tau + G_1(\eta)\tau^{1/2} + G_2(\eta) + \dots]. \quad (66)$$

Introducing this expansion into Eq. (64), and collecting the terms multiplied by the same power of  $\tau \gg 1$ , yields, at leading order,  $(G_0)_\eta^2 = 0$ , which can be integrated to give a constant value

$$G_0 = G_0^*, \quad (67)$$

revealing that, as anticipated above, because of the dominant effect of radical diffusion, the growth rate is uniform at leading order all across the mixing layer. The next nontrivial equation in the asymptotic development follows from the balance

$$G_0^* - \tilde{D}G_{1\eta}^2 = W_B \quad (68)$$

between accumulation, diffusion, and branching, which can be solved to give

$$G_{1\eta} = \pm \sqrt{\frac{G_0^* - W_B}{\tilde{D}}}. \quad (69)$$

This equation indicates that  $G_0^*$  must be equal to the maximum branching rate  $G_0^* = W_B^*$ , because if  $G_0^*$  were larger than  $W_B^*$ , then Eq. (69) would include a monotonically increasing solution and a monotonically decreasing solution, neither of them being valid, since they would lead to a radical-pool distribution diverging on one side of the mixing layer or on the other, and if  $G_0^*$  were smaller than  $W_B^*$ , then there would exist a central region where  $G_0^* < W_B$ , giving imaginary values of  $G_1$ , corresponding to unrealistic oscillatory radical profiles.

The solution for  $G_1$  is obtained by integrating Eq. (69) with  $G_0^* = W_B^*$  to give

$$G_1 = G_1^* + \begin{cases} -\int_{\eta^*}^{\eta} \frac{(W_B^* - W_B)^{1/2}}{\tilde{D}^{1/2}} d\eta & \text{for } \eta > \eta^* \\ +\int_{\eta}^{\eta^*} \frac{(W_B^* - W_B)^{1/2}}{\tilde{D}^{1/2}} d\eta & \text{for } \eta < \eta^* \end{cases}, \quad (70)$$

where the minus and plus branches are selected for  $\eta > \eta^*$  and for  $\eta < \eta^*$  to ensure a non-diverging behavior. Inspection of the equation found at the following order leads to the selection  $G_1^* = -(-2\tilde{D}^*W_{B\eta\eta}^*)^{1/2}$  for the peak value of  $G_1$ , as needed to avoid a singular behavior of  $G_2$  at  $\eta = \eta^*$ . Although the development can be extended to a higher order [190], the radical pool distribution

$$Y/\varepsilon = \exp\left[W_B^*\tau - \left(-2\tilde{D}^*W_{B\eta\eta}^*\right)^{1/2}\tau^{1/2}\right] \times \exp\left[\pm \tau^{1/2} \int_{\eta^*}^{\eta} \frac{(W_B^* - W_B)^{1/2}}{\tilde{D}^{1/2}} d\eta\right], \quad (71)$$

obtained by retaining the first two terms in the asymptotic expansion, suffices to provide satisfactory accuracy, as demonstrated by the comparisons with numerical integrations shown in the right-hand-side plot of Fig. 12, taken from Ref. [142].

At the order considered here, the WKB analysis gives

$$Y_{\max} = \varepsilon \exp\left[W_B^*\tau - \left(-2\tilde{D}^*W_{B\eta\eta}^*\right)^{1/2}\tau^{1/2}\right] \quad (72)$$

for the peak of the radical-pool concentration, reached at  $\eta = \eta^*$ . According to Eq. (71), the radical growth is uniform at leading order, with a branching rate equal to its peak value at  $\eta = \eta^*$ . The first-order correction, associated with diffusive radical loss, involves the square root of the radical diffusivity times the curvature of the branching-rate distribution evaluated at  $\eta = \eta^*$ . The comparison of this prediction with numerical results and with the leading-order result  $Y_{\max} = \varepsilon \exp(W_B^*\tau)$  is shown in the left-hand-side plot of Fig. 12. A prediction for the ignition time is obtained by setting  $Y_{\max} = 1$  in Eq. (72), corresponding to the criterion  $C_H = C_{H_2}$ , previously used for homogeneous explosions. At leading order, the explicit solution  $\tau_i = \ln(\varepsilon^{-1})/W_B^*$  follows, which can be written in the approximate dimensional form

$$t_i = \tilde{t}_B^* \ln[t_i^*/\tilde{t}_B^*], \quad (73)$$

where  $\tilde{t}_B^*$  is the minimum of the branching time across the mixing layer. This time can be computed from Eq. (39) by evaluating the chemically frozen profiles of temperature and of oxygen and hydrogen mole fractions, and  $t_i^*$  is the corresponding initiation time, evaluated from Eq. (30) at  $\eta = \eta^*$ . At the next order, Eq. (72) must be used, and there is not an explicit expression for  $t_i$ , but the prescription involves the same determinations of  $\tilde{t}_B^*$  and  $t_i^*$ . This prescription, which follows from the analysis, differs from merely evaluating the minimum  $t$  in Eq. (40) for which its left-hand side is unity, since, in general, that minimum occurs at a value of  $\eta$  dependent on both functions  $\tilde{t}_B$  and  $t_i$ , which may be different from  $\eta^*$ .

Estimates of autoignition distances in practical nonpremixed combustion devices can be obtained by multiplying the ignition time given in Eq. (73) by an appropriately selected average velocity. This straightforward computation procedure, neglecting the effect of flow strain on the mixing and reaction in the mixing layer, has been shown recently [142] to provide results in reasonable agreement with experimentally measured liftoff distances of supersonic hydrogen jets [196]. The agreement is acceptable because the accuracies of such measurements are not great. It may be inferred from the upper limits of the curves on the left-hand plot of Fig. 12 that the ignition time predicted by the more accurate two-term expansion of Eq. (72) exceeds that of Eq. (73) by more than 30%. Accurate predictions therefore require the additional complications of employing the two-term results.

## 6. Premixed hydrogen combustion

In most applications, premixed combustion relies on the propagation of quasi-isobaric reaction-diffusion waves called deflagrations or premixed flames. These deflagrations often propagate in

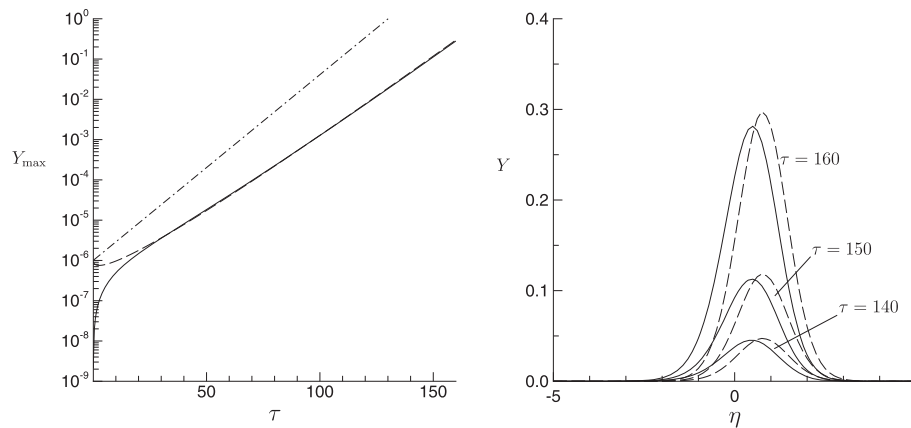


**Fig. 12.** Radical-pool profiles and associated peak values obtained from numerical integrations (solid lines) and corresponding predictions obtained from Eqs. (71) and (72) (dashed curves), and also from the leading-order result  $Y_{\max} = \varepsilon \exp(W_b^* \tau)$  (dot-dashed curves) for an isothermal mixing layer at 1200 K [142].

highly turbulent flows and are affected by curvature and flow strain. Different combustion regimes result from the competition of the turbulent flow with molecular transport and chemical reaction. A regime classification follows from introduction of appropriately defined dimensionless parameters [197], notably a Reynolds number and a Damköhler number based on the integral flow scales, with the latter involving a chemical time that depends on the fuel and on the combustion conditions. The resulting diagram, shown in Fig. 13, serves to identify the combustion mode that predominantly appears in a particular application. This figure, which may be extended in the future by adding additional coordinates to represent other nondimensional parameters relevant to other applications, is equivalent to the Borghi diagram [160] for premixed systems but also can be applied to nonpremixed systems.

Despite the significant progress achieved in understanding the complexities of premixed turbulent combustion, many outstanding issues remain to be clarified [160]. The distinct character of the hydrogen molecule (i.e., high reactivity and high diffusivity) influences its combustion characteristics in turbulent environments. In that respect, the investigation of steadily propagating, planar laminar flames emerges as an essential preliminary step to provide the basic knowledge required to address the complex dynamical behavior found in practical systems [66,198], especially for the

flamelet regimes of Fig. 13. Therefore, planar hydrogen deflagrations will be reviewed first in this section, including their propagation velocity, inner structure, and limit solutions near the lean flammability limit, with emphasis on the understanding gained on the basis of reduced-chemistry descriptions. Effects of curvature and flow strain will be addressed next, followed by flame stability and flame balls, a unique combustion phenomenon closely related to the cellular flames characterizing combustion of lean hydrogen mixtures. Although a specific section is not dedicated to reviewing turbulent premixed combustion, all of the issues discussed below clearly have a bearing on the distinct characteristics of hydrogen turbulent deflagrations.

### 6.1. The burning rate

The laminar burning velocity, defined as the velocity at which the steady planar deflagration travels through a quiescent fuel–oxidizer mixture, is a fundamental measure of the reactivity of a premixed system for given conditions of composition, pressure, and initial temperature. Experimental measurements of this quantity can be affected by effects of flame stretch associated with either front curvature or flow strain, which explain the large discrepancies observed among the different sets of experimental data that were available 30 years ago [199]. To reduce experimental errors associated with the early measuring techniques, methods were proposed in subsequent work to infer stretch-free values of burning rates from visualizations of outwardly propagating, spherical flames [200] and also from measurements of flow structures in counterflow twin-flame configurations [201,202]. Variants of the former method have been used extensively over the past two decades to determine hydrogen burning rates [203–214]. Alternative experimental techniques employed by different groups in that same period include schlieren visualizations of approaching flame fronts in double-kernel combustion setups [215], particle-tracking velocimetry applied to inclined steady flames [216,217], measurements of pressure history in windowless closed explosion chambers [218], heat-flux measurements in flames stabilized near a perforated flat plate [219], and measurements of flame inclination angles in slot-nozzle burners [220].

Reasonably good agreement is found between the results of the different recent studies, especially when effects of stretch are minimized or appropriately accounted for in handling the resulting data, as can be seen in the results shown in Fig. 14 for hydrogen–air flames at normal atmospheric conditions. The experimental data used for the plot are selected to minimize the resulting scatter, so that results of visualizations of spherical flames that either underpredict [203] or

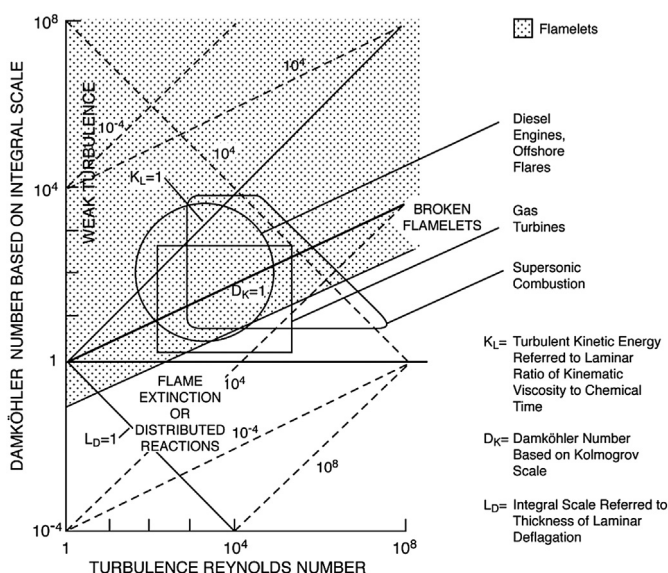


**Fig. 13.** Regimes of turbulent combustion.

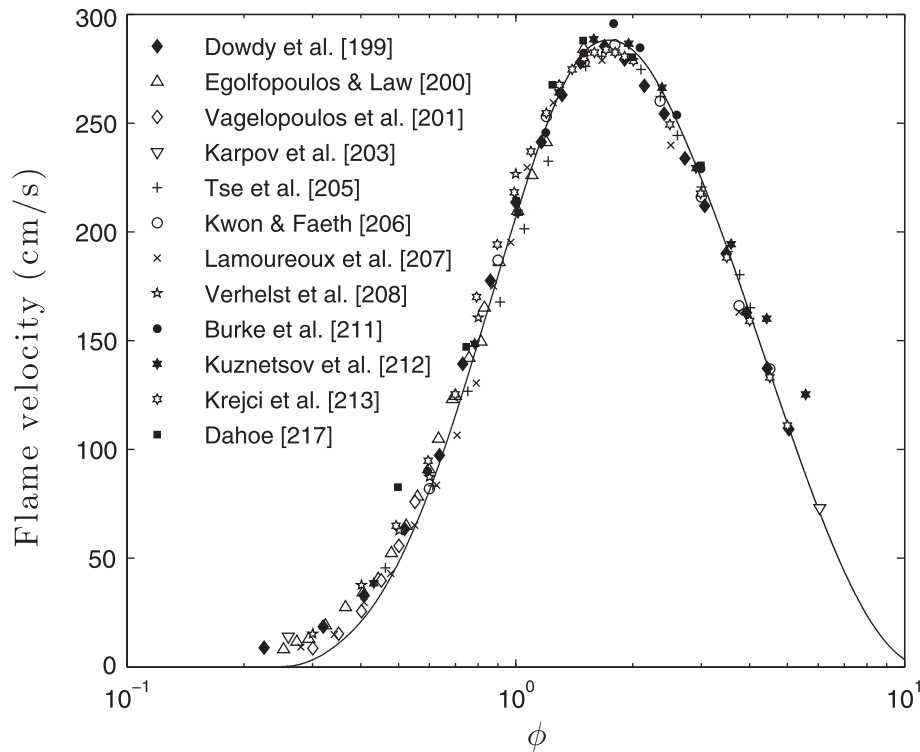


**Fig. 14.** The variation with equivalence ratio of the laminar propagation velocity of hydrogen–air planar deflagrations at normal atmospheric conditions as obtained from experimental measurements (symbols) and from numerical integrations with the detailed chemistry of Table 1 (solid curve).

overpredict [211] significantly maximum burning rates are not shown in the figure, and neither are results of measurements in Bunsen flames [216,217,220] or those obtained by the double-kernel technique [215], which tend to give burning rates that are consistently larger than those determined with the other techniques. Besides results for hydrogen–air flames at normal atmospheric conditions, measurements of burning rates are now available at reduced and elevated pressure [201,205–207,209–211,213,214,216,218,220], elevated initial temperatures [209,211,214,218], and for different degrees of dilution with  $N_2$ , Ar, He, and  $CO_2$  [107,205,207,208,219,221].

The burning rate of a given reactive mixture can also be determined by solving numerically the steady one-dimensional conservation equations for energy and chemical species [98]. While the associated computation was a challenging task a few years ago, dedicated numerical codes running in desktop computers can now calculate in seconds burning rates with detailed transport and chemistry descriptions. The accuracy of the result depends fundamentally on three different types of data, namely, thermochemical properties, chemical-kinetic rate parameters, and transport properties [222], the burning velocity being roughly proportional to the square root of the ratio of a diffusivity (thermal under most conditions) to a characteristic time for the overall rate of chemical heat release. For hydrogen–air mixtures, possibly including as diluents  $N_2$ , He,  $CO_2$ , and Ar, there exists now sufficiently accurate information regarding thermochemical properties, although improvements continue to arise as a result of refined experimental measurements [223]. As discussed earlier in Sections 2 and 4, despite the appreciable recent progress achieved, existing uncertainties in chemical-kinetic rate parameters and transport properties are somewhat larger than those of thermochemical properties. Nevertheless, with the knowledge presently available, computations of hydrogen burning rates with multicomponent transport and detailed chemistry provide results with accuracies that are better than 10% under most conditions. Sample numerical results obtained with the detailed chemistry of Table 1 are included in Fig. 14 as an illustration

of the present degree of agreement between the numerical and experimental determinations of the burning rate of hydrogen–air mixtures. It may be noted in general that the experimental and computational burning velocities peak at fuel-rich conditions, because of the high contribution to the thermal diffusivity from  $H_2$  and the fuel-rich stoichiometry of step I in Eq. (15).

The relative differences between the experimental measurements and the computational predictions are larger for very lean mixtures, as is apparent in the comparison shown in Fig. 15, corresponding to a blowup of the results in Fig. 14 for  $0.2 \leq \phi \leq 0.4$  (the dashed curve represents results with simplified chemical kinetics, to be discussed later). The experimental results include measurements of spherically expanding flames and of twin-flame counterflow

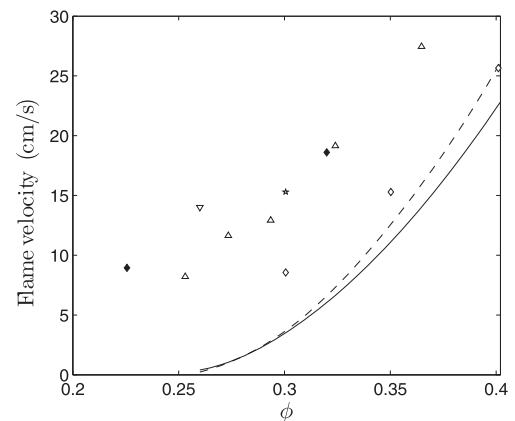


**Fig. 15.** The variation with equivalence ratio of the laminar propagation velocity of lean hydrogen–air planar deflagrations at normal atmospheric conditions as obtained from experimental measurements ([200]: solid diamonds [201]: empty triangles [202]: empty diamonds [204]: inverted triangle [209]: five-point empty star) and from numerical integrations with the detailed chemistry of Table 1 (solid curve) and with the seven elementary elementary reactions 1, 2, 3, 4f, 5f, 6f, and 7f (dashed curve).

configurations, both experimental methodologies including corrections for effects of stretch through a linear extrapolation. The results inferred from measurements of expanding flames consistently lie well above the computational predictions, suggesting that for these ultra-lean conditions the spherical flames develop cellular structures through diffusive-thermal instabilities that result in higher burning rates, thereby explaining the larger propagation speeds measured in the experiments. It is also possible that the differences observed are partly due to deficiencies in the method used to extract the burning rate from the measurements, in that nonlinear effects affecting the dependence of the stretched flame speed on the stretch rate, which have been shown to be important in experiments of *n*-butane–air spherical flames [224], may be significant for these weakly reactive mixtures. For the counterflow experiments, these nonlinear effects have been successfully minimized in the past by consideration of larger separation distances between the opposing nozzles [202], resulting in values of burning rates (represented by empty diamonds in the figure) that are much closer to the numerical predictions than those obtained in the early counterflow experiments using smaller inter-nozzle distances [201] (represented by empty triangles).

## 6.2. The structure of planar flames

Experimental measurements of flame structures of hydrogen deflagrations are scarce. The typical arrangement involves a flat flame stabilized near a porous or perforated plate. Conditions of low pressure and/or high dilution are always employed, resulting in thick flames that facilitate measurements with sufficient spatial resolution

[225–234]. Except for one study [230], all of the investigations utilized intrusive measuring techniques, with molecular beam mass spectrometry being the preferred method to determine concentration profiles in the more recent studies [231–234].

While experimental measurements of flame structures are intrinsically difficult, with the continuing increase in computer speed, flame calculations with detailed chemistry, which used to be arduous tasks 25 years ago, have become common place, providing simultaneously the burning rate and the profiles of temperature and chemical species for given conditions of temperature, pressure, and composition. Sample results obtained for atmospheric  $\text{H}_2$ –air flames at normal temperature are shown in Fig. 16 for  $\phi = 0.8$  and  $\phi = 4.0$ . In both cases a thin layer of fast radical production exists at an intermediate location where the H-atom concentration peaks and the reactant profiles show a large curvature, indicative of the rapid branching. Radical recombination occurs in a distributed manner both upstream and downstream from this branching layer, in regions of thickness comparable to that of the flame, where recombination, convection and diffusion all occur simultaneously.

A similar multilayer flame structure was envisioned by Zel'dovich fifty years ago [235] (see the discussion on pp. 397–401 of Ref. [154]). His analysis employed a chemistry model including an autocatalytic, energetically neutral branching reaction  $\text{A} + \text{B} \rightarrow 3\text{B}$  between the reactant A and the radical B and an exothermic recombination reaction  $\text{B} + \text{B} + \text{M} \rightarrow \text{C} + \text{M}$  with a constant rate coefficient, C representing a chemically inert product. Variants of this simple chemistry have been used in a number of deflagration analyses [236–241]. The Zel'dovich chemistry is, in many respects, similar to the two-step reduced chemistry derived in Section 3.4.3 by

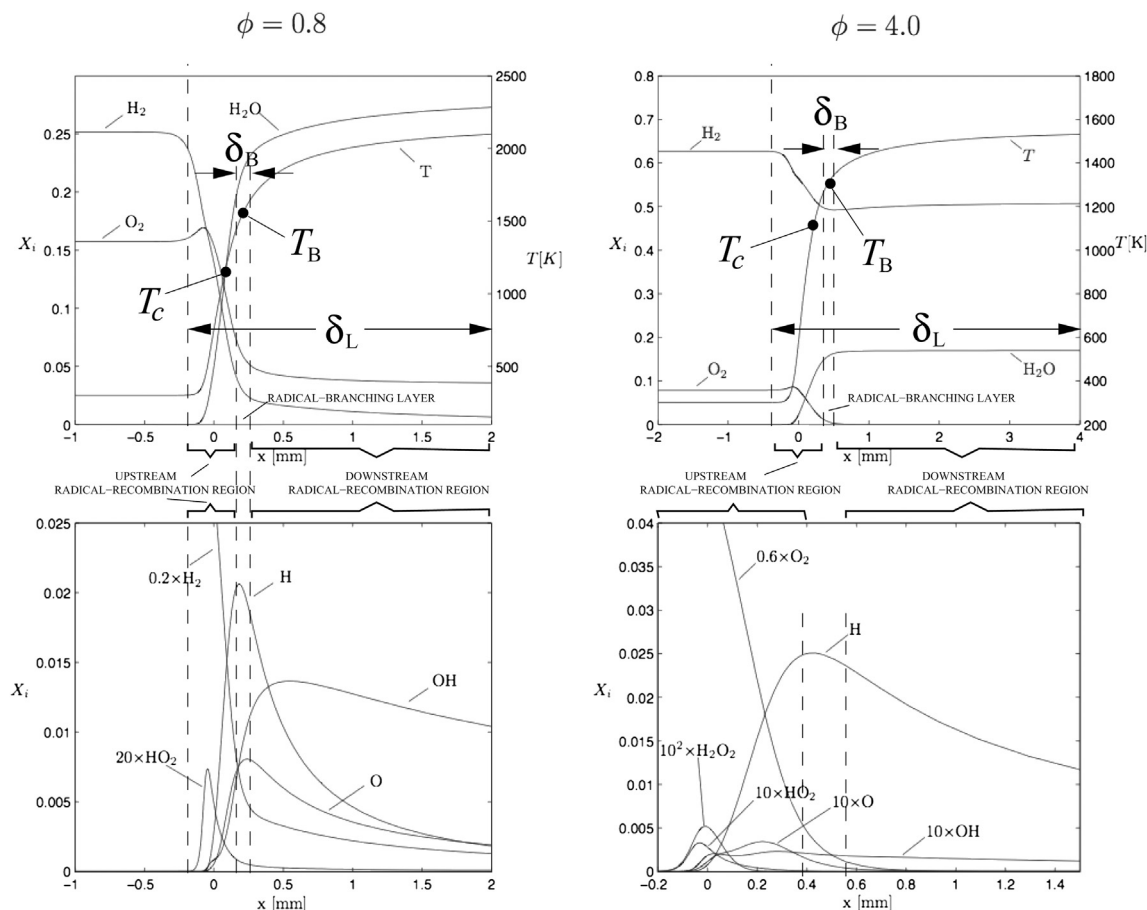


**Fig. 16.** Profiles of mole fractions and temperature across hydrogen–air flames as obtained from detailed-chemistry computations at normal atmospheric conditions for  $\phi = 0.8$  (left-hand-side plots) and for  $\phi = 4.0$  (right-hand-side plots).



introduction of steady-state assumptions for all intermediaries other than H [68,69]. For instance, the condition of thermally neutral chain branching, present in the Zel'dovich chemistry model, is approximately satisfied by the two-step reduced description, since the heat released by the global branching reaction

$3\text{H}_2 + \text{O}_2 \xrightarrow{\text{I}} 2\text{H}_2\text{O} + 2\text{H}$ , given by  $-2(h_{\text{H}_2\text{O}} + h_{\text{H}}) \approx 48$  kJ/mol, is only a small fraction of that released by the radical-recombination step

$\text{H} + \text{H} + \text{M} \xrightarrow{\text{II}} \text{H}_2 + \text{M}$ , given by  $2h_{\text{H}} \approx 436$  kJ/mol. In addition, the temperature dependence assumed by Zel'dovich for the reaction-rate constants, i.e., temperature-independent recombination and temperature-sensitive branching through a large activation energy, is also reproduced by the two-step reduced chemistry, since the rate constants of the three-body reactions, which largely determine  $\omega_{\text{II}}$ , have only a weak algebraic dependence on temperature, while the activation temperature  $T_{\text{air}} = 8590$  K of the main rate-controlling reaction  $\omega_{\text{I}}$  for step I is relatively large.

Despite these similarities, significant differences exist between the model chemistry and the reduced chemistry. Notably, contrary to the Zel'dovich model, the recombination step  $\text{H} + \text{H} + \text{M} \xrightarrow{\text{II}} \text{H}_2 + \text{M}$  regenerates one of the reactants, which affects fundamentally the downstream high-temperature region of lean flames. Also, unlike the branching reaction  $\text{A} + \text{B} \rightarrow 3\text{B}$ , the overall step  $3\text{H}_2 + \text{O}_2 \xrightarrow{\text{I}} 2\text{H}_2\text{O} + 2\text{H}$  in the reduced chemistry is reversible, and the backward rate enters to determine the downstream concentration of the deficient reactant, as explained below. Because of these fundamental differences, although analyses based on the Zel'dovich model chemistry can serve to provide qualitative understanding of some flame phenomena involving branching and recombination kinetics, direct use of rigorously derived reduced chemistry should always be preferred in theoretical analyses of hydrogen combustion to ensure a correct description of the underlying chemistry, as has been done earlier for hydrogen flames [18,69]. The remaining discussion in this section therefore uses the reduced two-step mechanism,  $3\text{H}_2 + \text{O}_2 \xrightleftharpoons{\text{I}} 2\text{H}_2\text{O} + 2\text{H}$  and  $\text{H} + \text{H} + \text{M} \xrightleftharpoons{\text{II}} \text{H}_2 + \text{M}$ , of Eq. (15) as a basis to elucidate the flame structures shown in Fig. 16.

Under most conditions, the global rates  $\omega_{\text{I}}$  and  $\omega_{\text{II}}$ , defined in Eq. (16) supplemented by Eqs. (9)–(11) and (14), can be simplified by neglecting the hydrogen-peroxide reactions 10f, 11f, and 12f along with the backward elementary reactions 6b, 8b, and 9b. Consideration of these additional reactions is only needed for increased accuracy, either in computations of high-pressure flames, when the hydrogen-peroxide chemistry becomes important, or at elevated initial temperatures  $T_{\text{u}}$  such that the final adiabatic flame temperature exceeds approximately 2500 K, when 6b, 8b, and 9b must be included to determine the final equilibrium solution. With reactions 6b, 11f, and 12f neglected in Eq. (14), the steady-state expression for the hydroperoxyl concentration becomes  $C_{\text{HO}_2} = k_{4f}C_{\text{O}_2}C_{\text{M}_4}/(k_{5f} + k_{6f} + k_{7f}C_{\text{OH}}/C_{\text{H}})$ , which can be used to rewrite Eq. (16) in the form

$$\begin{aligned}\omega_{\text{I}} &= k_{1f}C_{\text{O}_2}C_{\text{H}} - k_{1b}C_{\text{O}}C_{\text{OH}} + (1 - \alpha)k_{4f}C_{\text{M}_4}C_{\text{O}_2}C_{\text{H}} \\ \omega_{\text{II}} &= k_{4f}C_{\text{M}_4}C_{\text{O}_2}C_{\text{H}} + k_{8f}C_{\text{M}_8}C_{\text{OH}}C_{\text{H}} + k_{9f}C_{\text{M}_9}C_{\text{H}}^2,\end{aligned}\quad (74)$$

where

$$\alpha = \frac{k_{6f} + k_{7f}C_{\text{OH}}/C_{\text{H}}}{k_{5f} + k_{6f} + k_{7f}C_{\text{OH}}/C_{\text{H}}}\quad (75)$$

is the fraction of  $\text{HO}_2$  radicals consumed through the chain-terminating path. The value of  $\alpha$  varies across the flame, as

dictated by the temperature and by the relative OH-to-H content of the mixture. Evaluations of Eq. (75) using results of detailed-chemistry computations reveal that for moderately lean flames a value in the range  $0.3 < \alpha < 0.5$  is found in the intermediate region where radical concentrations peak and that  $\alpha$  approaches the limiting value  $\alpha = k_{6f}/(k_{5f} + k_{6f}) \approx 1/6$  in rich flames with small values of  $C_{\text{OH}}/C_{\text{H}}$ . It is noteworthy that, with 11f and 12f neglected in writing  $\omega_{\text{II}}$ , the recombination reaction becomes effectively irreversible, i.e.,  $\text{H} + \text{H} + \text{M} \xrightarrow{\text{II}} \text{H}_2 + \text{M}$ . Also of interest is that the H-atom production rate associated with Eq. (74)

$$\begin{aligned}\dot{C}_{\text{H}} &= 2 \left[ (k_{1f} - \alpha k_{4f}C_{\text{M}_4})C_{\text{O}_2}C_{\text{H}} - k_{1b}C_{\text{O}}C_{\text{OH}} - k_{8f}C_{\text{M}_8}C_{\text{OH}}C_{\text{H}} \right. \\ &\quad \left. - k_{9f}C_{\text{M}_9}C_{\text{H}}^2 \right]\end{aligned}\quad (76)$$

exhibits a crossover temperature,  $T_{\text{c}}$ , defined by the condition

$$k_{1f} = \alpha k_{4f}C_{\text{M}_4},\quad (77)$$

that is different from the crossover temperature defined in Eq. (31) for ignition processes.

Although Eqs. 9–11 are needed in general to compute the concentrations of O and OH, for the sake of clarity in the presentation we shall express the backward rate  $\omega_{1b} = k_{1b}C_{\text{O}}C_{\text{OH}}$  with use made of the approximate steady-state expressions

$$C_{\text{O}} = \frac{C_{\text{H}_2\text{O}}C_{\text{H}}^2}{K_2K_3C_{\text{H}_2}^2} \quad \text{and} \quad C_{\text{OH}} = \frac{C_{\text{H}_2\text{O}}C_{\text{H}}}{K_3C_{\text{H}_2}},\quad (78)$$

obtained by assuming that the elementary reactions 2 and 3 are in equilibrium, an excellent approximation on the hot side of the flame. Here  $K_j = k_{jf}/k_{jb}$  represents the equilibrium constant of the elementary step  $j$ . The compact expressions

$$\omega_{\text{I}} = k_{1f}C_{\text{O}_2}C_{\text{H}} \left( 1 - \frac{C_{\text{H}_2\text{O}}^2C_{\text{H}}^2}{KC_{\text{H}_2}^3C_{\text{O}_2}} \right) + (1 - \alpha)k_{4f}C_{\text{M}_4}C_{\text{O}_2}C_{\text{H}}\quad (79)$$

and

$$\begin{aligned}\dot{C}_{\text{H}}/2 &= \left[ k_{1f} \left( 1 - \frac{C_{\text{H}_2\text{O}}^2C_{\text{H}}^2}{KC_{\text{H}_2}^3C_{\text{O}_2}} \right) - \alpha k_{4f}C_{\text{M}_4} \right] C_{\text{O}_2}C_{\text{H}} \\ &\quad - k_{8f}C_{\text{M}_8}C_{\text{OH}}C_{\text{H}} - k_{9f}C_{\text{M}_9}C_{\text{H}}^2\end{aligned}\quad (80)$$

follow from straightforward substitution of Eq. (78) into Eqs. (74) and (76), where the equilibrium constant

$$K = K_1K_2K_3^2\quad (81)$$

is related to those of the shuffle reactions 1–3. Evaluation of the expression for  $K$  indicates that this quantity takes fairly large values at temperatures of interest for  $\text{H}_2$ –air deflagrations, giving, for instance,  $K \approx 400$  at  $T \approx 1100$  K and  $K \approx 100$  at  $T \approx 1500$  K.

The flame structure emerging in Fig. 16 can now be explained on the basis of the two-step reduced chemistry with account taken of the relatively high temperature sensitivity of  $k_{1f}$  and the large value of  $K \gg 1$ . Most of the heat released is associated with the recombination reaction  $\text{H} + \text{H} + \text{M} \xrightarrow{\text{II}} \text{H}_2 + \text{M}$ , and its rate is only weakly dependent on the temperature. Therefore heat release occurs all across the flame, with the balance between diffusion, convection, and radical recombination providing the estimates  $(D_{\text{T}}/t_{\text{R}})^{1/2}$  and  $\delta_{\text{L}} = (D_{\text{T}}t_{\text{R}})^{1/2}$  for the flame propagation velocity and the accompanying flame thickness  $\delta_{\text{L}}$  in terms of the characteristic values of the thermal diffusivity  $D_{\text{T}} = \lambda/(\rho c_{\text{p}})$  and radical-recombination time  $t_{\text{R}} = (k_{4f}C_{\text{M}_4}C_{\text{O}_2})^{-1}$  (to be evaluated at some intermediate location).

Because of the large temperature sensitivity of  $k_{1f}$ , in the upstream region where the temperature lies below the crossover temperature  $T_c$  defined by Eq. (77), the rate of the elementary branching reaction  $H + O_2 \xrightarrow{1} OH + O$  is effectively frozen, and the branching rate in Eq. (79) reduces to  $\omega_I = (1 - \alpha)k_{4f}C_{M_4}C_{O_2}C_H$ , so that Eq. (80) yields  $\dot{C}_H = -2(\alpha k_{4f}C_{M_4}C_{O_2}C_H + k_{8f}C_{M_8}C_{OH}C_H + k_{9f}C_{M_9}C_H^2)$  for the distributed H-atom destruction rate in this upstream region. Conversely, in the downstream region where the temperature lies significantly above  $T_c$ , the branching reaction  $H + O_2 \xrightarrow{1} OH + O$  (as well as the other two shuffle reactions  $H_2 + O \xrightarrow{2} OH + H$  and  $H_2 + OH \xrightarrow{3} H_2O + H$ ) becomes very rapid and reaches equilibrium, as can be seen by considering the limit  $k_{1f} \gg \alpha k_{4f}C_{M_4}$  in Eq. (80), to yield the equilibrium condition

$$KC_{H_2}^3C_{O_2} = C_{H_2O}^2C_H^2. \quad (82)$$

Since  $K \gg 1$ , this last equation indicates that, in the downstream radical-recombination region, either  $H_2$  or  $O_2$  must appear in very small concentrations, leading to two different solutions depending on the excess reactant.

For lean flames, where  $O_2$  is in excess, the equilibrium condition in Eq. (82) corresponding to rapid branching gives

$$C_{H_2} = K^{-1/3}C_{H_2O}^{2/3}C_H^{2/3}/C_{O_2}^{1/3} \quad (83)$$

for the small  $H_2$  concentration in the downstream radical-recombination region. There, the molecular hydrogen regenerated by  $H + H + M \xrightarrow{II} H_2 + M$  is rapidly consumed by  $3H_2 + O_2 \xrightarrow{1} 2H_2O + 2H$  according to  $\omega_{II} = 3\omega_I$ , placing the  $H_2$  molecules in steady state and providing the overall recombination reaction



with a rate equal to  $\omega_{II}$ . Correspondingly, H-atom recombination leading to temperature increase in the downstream region of lean flames results in  $O_2$  consumption and water-vapor production, as is clearly seen in the profiles for  $\phi = 0.8$  in Fig. 16.

For rich flames, on the other hand, the equilibrium condition in Eq. (82) gives

$$C_{O_2} = K^{-1}C_{H_2O}^2C_H^3/C_{H_2}^3, \quad (85)$$

indicating that, as a consequence of the equilibria of the shuffle reactions, the oxygen concentration is kept at very small values of order  $K^{-1}$  in this downstream region. With the rate of the elementary reaction  $H + O_2 + M \xrightarrow{4f} HO_2 + M$  being negligible in the absence of  $O_2$ , the overall rate of the H-atom recombination reaction II in this region reduces to  $\omega_{II} = k_{8f}C_{M_8}C_{OH}C_H + k_{9f}C_{M_9}C_H^2$ , where the OH concentration is to be evaluated from Eq. (78). As seen in the profiles for  $\phi = 4.0$  in Fig. 16, in the downstream region of rich flames, the  $H_2$  concentration increases slightly while the resulting  $H_2O$  concentration remains flat, because it is not affected by the overall recombination reaction  $H + H + M \xrightarrow{II} H_2 + M$ .

As indicated schematically in Fig. 16, the transition between the two radical-recombination regions discussed above occurs at a thin radical-branching layer, located where the temperature takes a value  $T_B$  slightly above the crossover temperature  $T_c$ . An estimate for  $T_B$  can be obtained by noting that the changes in the rate of the elementary reaction  $H + O_2 \xrightarrow{1} OH + O$  across the branching layer are associated with small temperature changes of order

$(T - T_B)/T_B \sim (T_{aif}/T_B)^{-1} \ll 1$ , so that the characteristic thickness of the branching layer  $\delta_B$  must satisfy

$$\delta_B/\delta_L = \left( \frac{T_{aif}}{T_B} \frac{(T_{af} - T_u)}{T_B} \right)^{-1}, \quad (86)$$

where  $T_{af}$  is the adiabatic flame temperature found downstream. On the other hand, the radicals produced in the thin branching layer must recombine across the flame, yielding the additional condition  $k_{1f}C_{O_2}C_H\delta_B \sim \alpha k_{4f}C_{M_4}C_{O_2}C_H\delta_L$ , with  $k_{1f}$  evaluated at  $T = T_B$ , which can be combined with Eq. (86) and with the crossover definition in Eq. (77) to finally yield in the first approximation

$$\frac{T_B - T_c}{T_c} \sim \frac{\ln(T_{aif}/T_c)}{T_{aif}/T_c}. \quad (87)$$

As can be seen in Fig. 16, since the value of  $T_{aif} = 8590$  K is only moderately large, the departures  $T_B - T_c$  can be as large as a few hundred Kelvin for typical conditions.

Quantitative analyses based on the types of approximations introduced here have met moderate success in the past. The solution obtained in the limit of large activation temperature  $T_{aif}/T_c \gg 1$  requires integration of the convection–diffusion–reaction equations in the outer recombination regions with appropriate jumps of gradients of concentrations at the branching layer, whose inner structure must be resolved in a coupled calculation to determine the branching temperature  $T_B$  and the flame propagation velocity [242]. An early theoretical analysis employing rate-ratio asymptotics for moderately lean and stoichiometric hydrogen–air flames revealed a flame structure fundamentally similar to that discussed above, with the upstream recombination layer and the branching layer merging to give a single branching-recombination inner layer that was assumed to be preceded by an inert preheat zone [18]. The corresponding analysis has not been done for rich flames. For conditions near the flammability limits, such that the final adiabatic flame temperature differs by a small relative amount from the crossover temperature, radical production can only occur in a thin layer near the hot side of the flame where the factor  $(k_{1f} - \alpha k_{4f}C_{M_4})$  in Eq. (76) remains positive, resulting in very small concentrations of radicals. Under these near-limit conditions, chemical reactions are confined to a single thin layer, where radicals are generated and consumed, preceded by a radical-free preheat zone. For hydrogen–oxygen flames near the rich limit, the resulting reaction layer was analyzed on the basis of the two-step chemistry description by He and Clavin [69]. Additional simplifications arise for flames near the lean limit, where the H atoms are found to follow closely a steady state [19,26], thereby simplifying the description of the reduced chemistry to a single overall step. This reduced hydrogen-oxidation chemistry, to be developed below, applies in general for combustion conditions such that the peak temperature remains close to the crossover temperature. Besides ultra-lean deflagrations, therefore, these near-crossover conditions are found, regardless of the equivalence ratio, in premixed combustion for sufficiently large dilution and also in the presence of pronounced heat losses, the latter being the case of flame balls, to be addressed later in Section 6.6.

### 6.3. Flames near the lean flammability limit

It has long been believed that a one-step systematically reduced mechanism would be too inaccurate for any realistic hydrogen-combustion application. However, recently it has been shown [19,26] that for hydrogen–air deflagrations over a range of

equivalence ratios adjacent to the lean flammability limit the concentrations of all chemical intermediates are small enough for them to follow accurately a steady-state approximation, while the main reactants obey the overall irreversible reaction  $2\text{H}_2 + \text{O}_2 \rightarrow 2\text{H}_2\text{O}$ , with a global hydrogen-oxidation non-Arrhenius rate determined by those of the elementary reactions of the starting detailed mechanism. This one-step reduced mechanism is seen to provide reasonable predictions of limits for lean deflagrations as well as good results for deflagration velocities for conditions near the lean flammability limit, of interest for gas-turbine applications seeking reduced pollutant emissions and also in hazard contexts, where release of low concentrations of hydrogen may lead to continued flame spread.

For mixtures that are very fuel-lean, radical concentrations take on very small values, causing the direct recombination reactions

$\text{H} + \text{OH} + \text{M} \xrightarrow{8f} \text{H}_2\text{O} + \text{M}$  and  $2\text{H} + \text{M} \xrightarrow{9f} \text{H}_2 + \text{M}$ , which require three-body collisions involving two radicals, to become very slow

compared with the reaction  $\text{H} + \text{O}_2 + \text{M} \xrightarrow{4f} \text{HO}_2 + \text{M}$ . Consequently, for atmospheric and moderately high pressures, a reasonably accurate flame description follows from considering only the three shuffle reactions 1–3, the irreversible recombination reaction 4f, and the three irreversible  $\text{HO}_2$ -consuming reactions 5f–7f [19]. Results of hydrogen–air flame computations employing these seven elementary reactions are represented by the dashed curve in Fig. 15. As can be seen, the 7-step mechanism tends to overpredict flame propagation velocities, with relative errors that for normal atmospheric conditions increase to values of the order of 20% when  $\phi = 0.6$  [19] but that become negligibly small as the equivalence ratio decreases below  $\phi = 0.35$ .

As previously mentioned, for conditions near the flammability limit radicals are confined to a thin layer near the hot boundary, where they appear in concentrations that are much smaller than that of  $\text{H}_2$ , as seen for H atoms in the computations shown in Fig. 17. Under those conditions, all four radicals H, O, OH, and  $\text{HO}_2$  follow a good steady-state approximation. The associated steady-state expressions can be obtained from the results of the two-step reduced description by using the steady-state equations for OH, O, and  $\text{HO}_2$ , given in Eqs. (9)–(11) and (14), together with the additional condition  $\dot{C}_\text{H} = 0$ , with  $\dot{C}_\text{H}$  given in Eq. (76). If one retains only the terms associated with the elementary reactions 1, 2, 3, 4f, 5f, 6f, and 7f, then this system of equations can be solved exactly to give the explicit expressions

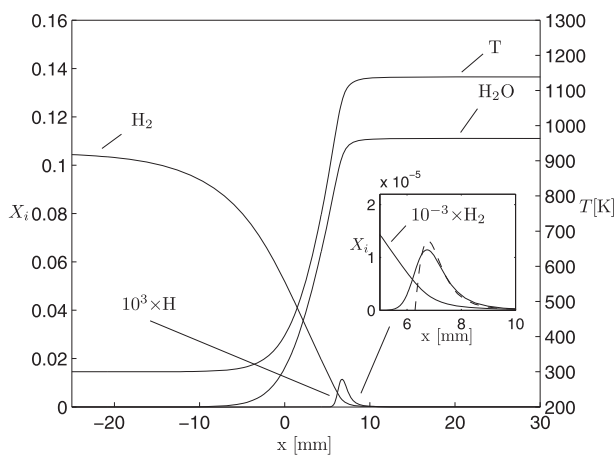


**Fig. 17.** The temperature and mole fractions across a premixed hydrogen–air mixture for  $p = 1$  atm,  $T_u = 300$  K, and  $\phi = 0.28$  as calculated with seven elementary reactions 1, 2, 3, 4f, 5f, 6f, and 7f; the inset compares the H-atom mole fraction computed numerically with that predicted by the steady-state expression in Eq. (88) with use made of the profiles of reactant and water-vapor mol fractions and of temperature obtained numerically with the 7-step mechanism [26].

$$k_{4f}C_{\text{M}_4}C_{\text{O}_2}C_{\text{H}} = \frac{k_{3f}C_{\text{H}_2}C_{\text{OH}}}{G} = \frac{k_{2f}C_{\text{H}_2}C_{\text{O}}}{\alpha H} = \frac{k_{2f}k_{3f}C_{\text{H}_2}^2}{GHk_{1b}} \left( \frac{k_{1f}}{\alpha k_{4f}C_{\text{M}_4}} - 1 \right) \quad (88)$$

and  $C_{\text{HO}_2} = (k_{3f}C_{\text{H}_2})/[(f + G)k_{7f}]$ , where

$$G = \frac{1 + \gamma_{3b}}{2} + \frac{f}{2} \left\{ \left[ 1 + \frac{2(3 + \gamma_{3b})}{f} + \frac{(1 + \gamma_{3b})^2}{f^2} \right]^{1/2} - 1 \right\}, \quad (89)$$

$$f = \frac{k_{5f} + k_{6f}}{k_{7f}} \frac{k_{3f}}{k_{4f}C_{\text{M}_4}C_{\text{O}_2}} C_{\text{H}_2}, \quad (90)$$

and

$$H = \frac{1}{2} + \frac{1}{2} \left[ 1 + \frac{4k_{7f}}{k_{5f} + k_{6f}} \frac{k_{2b}k_{2f}}{k_{1b}k_{3f}} \frac{f}{\alpha} \left( \frac{k_{1f}}{\alpha k_{4f}C_{\text{M}_4}} - 1 \right) \right]^{1/2}, \quad (91)$$

with  $\gamma_{3b} = (k_{3b}C_{\text{H}_2\text{O}})/(k_{4f}C_{\text{M}_4}C_{\text{O}_2})$ . In the steady-state approximation shown in Eq. (88), the concentrations of H, OH, and O vanish as the temperature approaches the crossover value given in Eq. (77), where the fraction of  $\text{HO}_2$  radicals consumed through the chain-terminating path  $\alpha$ , defined in Eq. (75), reduces in this case to

$$\alpha = \frac{k_{6f}/(k_{5f} + k_{6f}) + G/f}{1 + G/f}. \quad (92)$$

The accuracy of the explicit steady-state expression given in Eq. (88) is demonstrated in the inset of Fig. 17, which includes the comparison of the H-atom profile determined numerically on the basis of the 7-step mechanism with that determined from evaluating Eq. (88). It can be seen that the accuracy of the steady-state expression is excellent across the reaction layer, except at crossover, where the steady state predicts H atoms to disappear abruptly, thereby giving a profile with a discontinuous slope. Diffusive transport enters to remove this discontinuity, so that a smooth corner-layer profile replaces the abrupt change of the steady-state prediction when the 7-step mechanism is employed in the computations.

The steady state of H atoms implies that the two H atoms created by  $3\text{H}_2 + \text{O}_2 \xrightarrow{1} 2\text{H}_2\text{O} + 2\text{H}$  are rapidly consumed by  $\text{H} + \text{H} + \text{M} \xrightarrow{11} \text{H}_2 + \text{M}$ , thereby giving as a result the single overall reaction



The rate of this reaction  $\omega = \omega_1 = \omega_{11}$  can be evaluated with use made of Eq. (88) to give

$$\omega = \omega_{4f} = \frac{1}{GH} \left( \frac{k_{1f}}{\alpha k_{4f}C_{\text{M}_4}} - 1 \right) \frac{k_{2f}k_{3f}C_{\text{H}_2}^2}{k_{1b}} \quad (94)$$

if  $k_{1f} > \alpha k_{4f}C_{\text{M}_4}$  and  $\omega = 0$  otherwise, with  $\alpha$ ,  $G$ , and  $H$  evaluated from Eqs. 89–92. The accuracy with which this one-step description describes flame propagation velocities is tested in Fig. 18. The agreement of the one-step description with the results obtained for detailed and 7-step chemistry is seen to be quite satisfactory, with departures being slightly larger at elevated pressures. In general, decreasing pressure improves the burning-velocity agreement of the one-step and 7-step mechanisms (and also improves the agreement of the 7-step mechanism with detailed chemistry), and at subatmospheric pressures the one-step mechanism is quite good

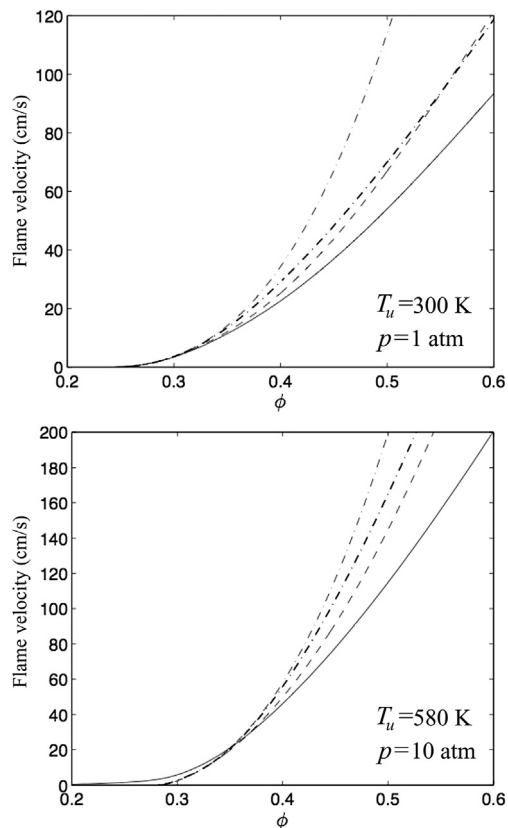


**Fig. 18.** The variation with equivalence ratio of the propagation velocity of a premixed hydrogen–air flame for  $p = 1$  atm and  $T_u = 300$  K (upper plot) and for  $p = 10$  atm and  $T_u = 580$  K (lower plot) as obtained from numerical integrations with detailed chemistry (solid curve), with the seven elementary elementary reactions 1, 2, 3, 4f, 5f, 6f, and 7f (dashed curve), with the one-step reduced mechanism (thick dot–dashed curve), and with the one-step reduced mechanism with the additional simplification  $H = 1$  (thin dot–dashed curve); based on Ref. [19].

for lean flames, as was verified in additional computations [26]. The figure also indicates that the simpler description that follows from taking  $H = 1$  in Eq. (94) produces burning velocities that agree with the 7-step results only at very lean conditions and tends to overpredict burning velocities as the mixture becomes richer.

The computations shown in Fig. 18 reveal that the simplified 7-step chemical-kinetic mechanism and also the associated one-step reduced description lead to a flame velocity that tends to zero as a kinetically determined lean flammability limit is approached. This flammability limit is, however, not observed in computations of planar adiabatic flames if the  $\text{H}_2\text{O}_2$  chemistry is included. Instead, a slow deflagration is obtained for very lean mixtures beyond the kinetically determined lean flammability limit of the 7-step mechanism, as can be seen clearly in the plot for  $p = 10$  atm. Such slow flames would readily extinguish in the presence of the slightest heat loss, so that their relevance for practical purposes is limited, especially for atmospheric and subatmospheric conditions, under which the associated velocities are only a few mm/s.

The kinetically determined lean flammability limit of the planar flame is associated with the existence of the cutoff factor  $[k_{1f}/(\alpha k_{4f} C_{M_4}) - 1]$  in Eqs. (88) and (94). According to the steady-state description, hydrogen atoms can only exist in the thin layer where the temperature lies in the range  $T_c < T < T_{af}$ , where  $T_{af}$  is the final adiabatic flame temperature, indicating that the flammability limit corresponds to conditions such that  $T_{af} = T_c$ . To compute from Eq. (77) the value of  $T_c$  at the flammability limit,  $(T_c)_l$ , one may use  $\alpha = 1$ , because for near-limit flames the  $\text{H}_2$  concentration in the

reaction layer is very small, causing the concentration of OH to become much larger than that of H in Eq. (75), as dictated by the first equation in Eq. (88). Therefore, the simplified crossover equation  $k_{1f} = k_{4f} C_{M_4}$ , different from Eq. (31) by a factor of 2, can be used to determine the variation of  $(T_c)_l$  with  $\phi$  for a given pressure, with the burnt-gas water-vapor mole fraction  $X_{\text{H}_2\text{O}} = 2\phi/(4.76 + \phi)$  used to evaluate  $C_{M_4}$ . Equating the resulting value to the adiabatic flame temperature  $T_{af}$  provides the prediction for the flammability limit of the planar flame, giving the results shown by the solid curves in Fig. 19. In the computation, the value of  $T_{af}$  can be obtained from a chemical-equilibrium calculation or, more simply, by evaluating the approximate expression

$$T_{af} = T_u + \frac{(-h_{\text{H}_2\text{O}}/M_{\text{H}_2})Y_{\text{H}_{2u}}}{c_p}, \quad (95)$$

resulting from adiabatic isobaric combustion, where  $(-h_{\text{H}_2\text{O}}/M_{\text{H}_2})$  is the amount of heat released per unit mass of hydrogen burnt according to the overall reaction shown in Eq. (93),  $c_p$  is an average specific heat, and  $Y_{\text{H}_{2u}}$  is the mass fraction of  $\text{H}_2$  in the unburnt gas (i.e.,  $Y_{\text{H}_{2u}} \approx \phi/(\phi + 35.32)$  for hydrogen–air mixtures). Also shown (by dashed curves) in Fig. 19 are the calculated flame temperatures at the limit for the two extreme cases. The results illustrate the increase of  $\phi_l$  and  $(T_c)_l$  with  $p$ , which arises from the associated increase in  $C_{M_4}$ , the three-body recombination becoming relatively faster than the two-body branching with increasing pressure; the strength of this dependence is seen to increase with  $p$ .

The calculations shown in Fig. 17 indicate that near the lean flammability limit the structure of planar steady hydrogen deflagrations involves two layers, a frozen upstream preheat region and a much thinner diffusive-reactive layer with negligible effects of convection. In comparison with the structures away from the limit, illustrated in Fig. 16, the branching layer seen there merges with the recombination layers, and an upstream inert preheat zone develops. In the presence of flame perturbations, unsteady effects, as well as curvature and strain effects, will enter first to modify the thicker preheat region, while the reactive-diffusive layer behaves as if it were steady and planar in the first approximation, giving a burning rate (fuel burnt per unit flame surface per unit time) that is mainly a function of the perturbed burnt-gas temperature. This burning rate has been computed recently [26]. At leading order, a first quadrature of the reaction-diffusion balance across the reaction layer provides

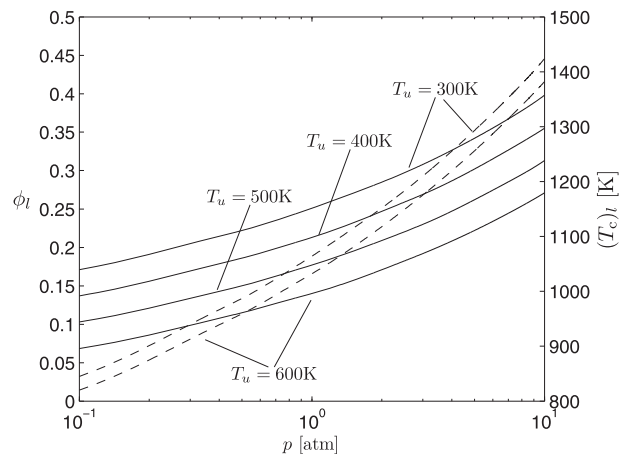


**Fig. 19.** The calculated variation of the equivalence ratio  $\phi_l$  (solid curves) and flame temperature  $(T_c)_l$  (dashed curves) with pressure at the lean flammability limit of planar flames for four different values of the initial temperature  $T_u$  [19].



$$\dot{M}_{H_2} = 2M_{H_2} \left( D_{H_2A} \int_0^{C_{H_2c}} \omega dC_{H_2} \right)^{1/2}, \quad (96)$$

where  $C_{H_2c}$  is the hydrogen concentration at the upstream boundary of the reaction layer, where the temperature equals  $T_c$ . As shown in [26], this burning-rate prediction can be improved by including a correction associated with the failure of the H-atom steady state at crossover (i.e., accounting for the presence of the small corner-layer region shown in the inset of Fig. 17). The simplified expression given in Eq. (96) for  $\dot{M}_{H_2}$  could be used for investigating the diffusive-thermal instabilities that lead to cellular structures in hydrogen flames and for studies of the dynamics of these flames under perturbations, discussed in the following sections. In such investigations, it is important to work with the resulting mass-burning-rate interface condition rather than with a burning velocity, the value of which would depend upon the structure of the preheat zone, which is being perturbed.

For steady planar flames, the condition that the convective flux of hydrogen into the flame must equal the burning rate provides  $\dot{M}_{H_2}/(\rho_u Y_{H_{2u}})$  as a prediction for the laminar burning velocity of lean hydrogen flames, with  $\rho_u$  representing the unburnt density. It is curious that the unique flame structure in this limit, with the crossover temperature determined by the kinetics and the heat release occurring in a narrow zone following that, requires modification of certain classical deflagration concepts that are based on one-step, Arrhenius chemistry with a high activation energy. In that case, the burning velocity is proportional to the square root of the thermal diffusivity because the size of the reaction zone is proportional to the size of the preheat zone, which is controlled by the thermal diffusivity, and the rate of heat release per unit area, proportional to the burning velocity, involves the integral of the heat-release rate over the reaction zone, which is proportional to its size. A further result is that increasing the diffusion coefficient of the deficient reactant (hydrogen for these lean flames) decreases the burning velocity by decreasing the reactant concentration in the reaction zone [243], it being incorrect to assume that increases in reactant as well as thermal diffusivities increase burning velocities. With this modified chemistry, however, the size of the reaction zone no longer depends significantly on the thermal diffusivity, so that the dependence of the burning velocity on the thermal diffusivity disappears and is replaced by the dependence on fuel diffusivity, derived above. The fuel Lewis number thus effectively appears in the denominator rather than in the numerator of the burning-velocity expression for these near-limit lean flames. Corresponding revisions in established ideas about characteristics of instabilities may be expected to arise, motivating future stability studies of very lean flames, which in certain respects may behave differently from the general instability processes described below.

It may be of interest to mention that Eq. (96) could also be employed to determine burning rates of lean deuterium combustion. If the chemistry involved in  $D_2$  combustion is assumed to be the same as that of  $H_2$  combustion (a reasonable assumption in view of the fact that  $D$  differs from  $H$  only through the additional neutron present in the  $D$  nucleus), then according to the prediction of Eq. (96) the ratio of the burning rate of hydrogen to that of deuterium should equal  $(D_{H_2A}/D_{D_2A})^{1/2}$ . If the approximate result

$$\frac{D_{H_2A}}{D_{D_2A}} \approx \left( \frac{M_{D_2}}{M_{H_2}} \right)^{1/2} \quad (97)$$

arising from kinetic theory is employed to evaluate the diffusion-coefficient ratio, then it follows that  $\dot{M}_{H_2}/\dot{M}_{D_2} = 2^{1/4} \approx 1.19$ , an

estimate in reasonable agreement with early experimental measurements for mixtures of these two fuels with  $O_2$  (see the lean-flame portion of the results in Fig. 1 of Ref. [244]).

#### 6.4. Effects of stretch

Premixed flames in practical combustion systems are subject to stretch, which may appear associated with aerodynamic straining or flame-front curvature [66,198]. Flame stretch modifies the internal flame structure and the resulting burning rate. The stretch rate, measured by the strain rate  $A$  in counterflow or stagnation-flow configurations, or by the ratio of the burning velocity to the radius of curvature in curved flames, this radius taken to be positive for flames convex towards the fresh mixture, is to be compared with the reciprocal of the residence time across the flame, which in turn is of the order of the recombination rate  $t_R^{-1} = (k_{4f} C_{M_4} C_{O_2})$  as was indicated when Fig. 16 was first introduced. For weakly stretched flames with stretch rates much smaller than  $t_R^{-1}$  the burning velocity varies linearly with the stretch rate, the linear dependence involving as a factor the so-called Markstein length  $L_M$ , which has been measured experimentally and also computed numerically for hydrogen–air flames [200,203–205,207,209–211,245,246].

Different definitions of  $L_M$  exist depending on whether the upstream or the downstream side of the flame is used in defining the flame speed. For hydrogen, it has been shown that the Markstein length corresponding to curvature in expanding spherical flames and that of flow strain in counterflow flames are nearly identical over the whole range of flammability conditions, provided that the burnt-gas side of the flame is employed in the definition [246]. Specifically, if the burning velocity and  $A$  are measured on the burnt-gas side of the flame, then the difference between the burning velocity under stretch and curvature from that of the planar unstretched flame is  $-L_M[A + (2/R)(dR/dt)]$ , where  $R$  is the flame radius of the spherical flame. This finding is supported by comparisons of numerical computations with experimental measurements. It is of interest that, when measured in the fresh mixture, the values of the Markstein lengths for curvature and for strain are different in general [239,247].

Figure 20 shows values of Markstein lengths extracted from experiments of expanding hydrogen–air spherical flames [200]. These experimental results lie close to other experimental results [203,209] and computations [246]. The value of  $L_M$  is found to be

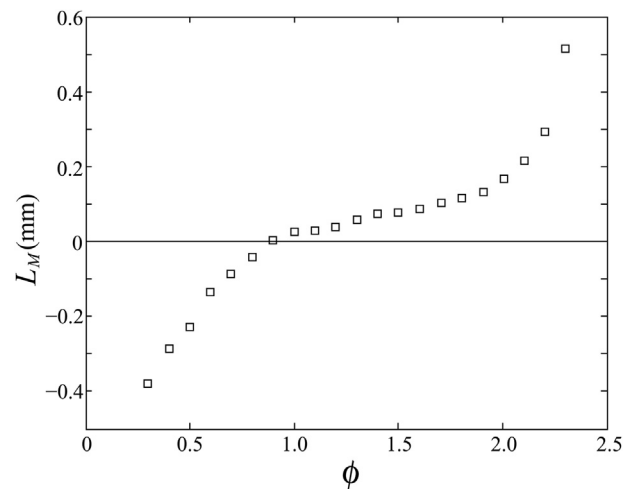


Fig. 20. The variation with equivalence ratio of the Markstein length for hydrogen–air combustion at normal atmospheric conditions as obtained experimentally from measurements of expanding spherical flames [200].

negative in lean hydrogen mixtures (for  $\phi < 0.8$  at the normal ambient conditions considered in the figure), so that the flame stretch increases the burning velocity. The reason for this characteristic behavior lies in the relatively large value of the diffusivity of  $H_2$ . Thus, for weakly stretched flames, differential diffusion of hydrogen in the preheat region increases the  $H_2$  flux into the reaction zone, resulting in a value of the local reaction-zone temperature that lies above the adiabatic flame temperature of the fresh mixture, thereby yielding values of the burning rate larger than those of the planar flame. Because of this invigorating effect, weakly stretched flames may exist for equivalence ratios below the kinetically controlled lean flammability limit of planar freely propagating flames.

The linear relationship between flame stretch and burning rate ceases to apply as the stretch rate increases to values of the order of  $t_R^{-1}$ , so that radical recombination begins to be affected, causing a significant decrease in the heat-release rate. If the flame is subject to sufficiently high stretch, conditions are reached for which the competition between stretch and heat release through radical recombination brings the temperature down to a value for which the flame no longer can exist, thereby leading to extinction. Both experiments and detailed numerical computations have been employed to determine extinction strain rates in lean hydrogen/air jets counterflowing against air at normal temperature [100]. In that particular configuration, as the strain rate increases, the reaction zone moves closer to the cold boundary, promoting downstream heat loss from the reaction zone and thereby further facilitating strain-induced extinction. Additional analyses in other configurations and for different flow conditions would be worthwhile to further characterize effects of stretch on hydrogen premixed combustion, including testing of the possible emergence of separate roles of strain and curvature. Such studies could benefit from theoretical work employing reduced chemical-kinetic descriptions of the type discussed earlier.

### 6.5. Stability of planar hydrogen deflagrations

Instabilities of planar deflagrations are associated intimately with molecular transport processes. This is in stark contrast with instabilities of planar detonations (to be discussed later), which are insensitive to molecular transport but instead involve the propagation of gas-dynamic waves. Detonation instabilities also will be seen generally to be sensitive to the chemical kinetics, while for deflagrations the instabilities are less dependent on details of the chemical kinetics, relying only on the finite rate of heat release which, along with diffusivities, gives rise to the laminar burning velocity. Hydrodynamic (Darrieus–Landau) deflagration instabilities result from the density decrease across the flame, in the presence of the existence of the laminar burning velocity that leads to the propagation of the flame into the fresh mixture at a velocity that is constant in the absence of perturbations. This hydrodynamic effect, which always is destabilizing, can be stabilized at small wavelengths by the diffusive-thermal effects of molecular transport and at large wavelengths (in favorable configurations, for example with hot products above cold reactants) by buoyancy or acceleration phenomena. In unfavorable configurations, on the other hand, the last phenomenon can be destabilizing, giving rise to Rayleigh–Taylor instability. Similarly, the molecular transport effects can be destabilizing, leading to diffusive-thermal instability.

Diffusive-thermal instabilities are understood best through comparisons of the thermal diffusivity with the diffusion coefficient of the deficient reactant (the reactant, fuel or oxidizer, that is consumed completely in the planar flame, that is, fuel for equivalence ratios less than unity and oxidizer for equivalence ratios greater than unity). The ratio of the first of these coefficients to the

second defines an effective Lewis number (for equivalence ratios different from unity). For hydrogen–air premixed combustion, the resulting value is very low in fuel-lean mixtures (i.e.,  $\approx 0.3$  near the lean flammability limit), because of the high hydrogen diffusion coefficient, and very large in fuel-rich mixtures (i.e.,  $\approx 2.0$  near the rich flammability limit), because the hydrogen content there causes the thermal diffusivity to be significantly higher than the oxygen diffusion coefficient. This effective Lewis number is related to the Markstein length shown in Fig. 20, with Lewis numbers sufficiently less than unity resulting in negative Markstein lengths, and those sufficiently greater than unity giving relatively large positive Markstein lengths. Diffusive-thermal instabilities arise in both of these limits, the molecular transport effects being stabilizing only at intermediate positive Markstein lengths. Negative Markstein lengths, associated with the low Lewis numbers of sufficiently fuel-lean hydrogen–air mixtures, result in cellular instabilities of the deflagrations, whereas sufficiently large positive Markstein lengths, corresponding to the high Lewis numbers of fuel-rich conditions, result in pulsating instabilities of the deflagrations. Hydrogen deflagrations thus exhibit a comparatively rich range of diffusive-thermal instabilities, from pronounced cellular fuel-lean flames to irregularly pulsating fuel-rich flames, because of the wide variation of the effective Lewis number with the equivalence ratio.

Cellular structures of lean hydrogen deflagrations arose in early experiments of spherical flames in a constant-volume bomb [248] and also in experiments of downwardly propagating flames in tubes [249,250]. An illustration of the mechanism underlying the associated diffusive-thermal instability is shown in Fig. 21. In this figure, the curved line represents the reaction zone, which lies towards the hot side of the flame, and the upstream diffusive-convective zone of the flame is on its left. This reaction sheet is a source for heat and a sink for reactants, so that reactants diffuse into it while heat is conducted out. For the normally diffusing reactants indicated in the figure their diffusion coefficient equals the thermal diffusivity, so that their path is essentially the same as that indicated for the heat (although in the opposite direction, of course).

General shapes of paths for strongly diffusing reactants (i.e.,  $H_2$  in fuel-lean hydrogen–air mixtures) and for weakly diffusing

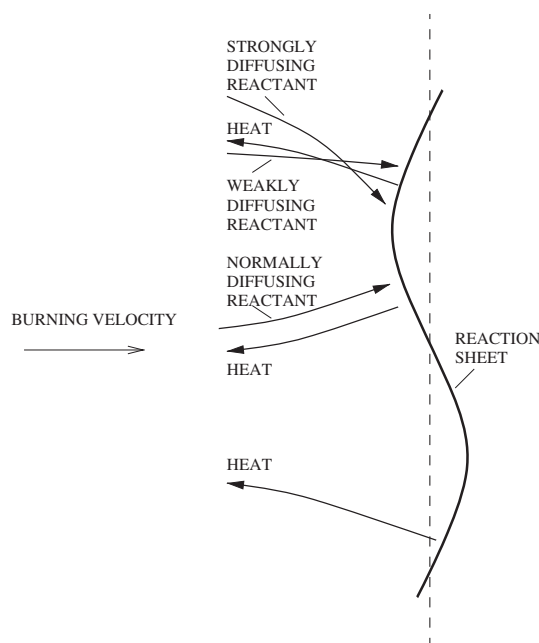


Fig. 21. A schematic illustration of the mechanism of diffusive-thermal instability.

reactants (i.e.,  $O_2$  in sufficiently fuel-rich hydrogen–air mixtures) also are indicated. It is seen that strongly diffusing reactants migrate more readily to the sink at the nearer upstream-pointing bulge, thereby releasing more heat there, and increasing the temperature in the reaction zone correspondingly. That, in turn, will increase the reaction rate and cause the reaction sheet to tend to move farther upstream. The opposite effect occurs for weakly diffusing reactants. The high diffusivity of  $H_2$  thereby favors the development of this diffusive-thermal instability of planar deflagrations in lean mixtures, while in rich mixtures the smaller  $O_2$  diffusivity tends to stabilize the planar flame by reducing any wrinkle.

Early mathematical descriptions of the diffusive-thermal instability were based on a one-step Arrhenius reaction [251,252], giving results that were subsequently reproduced in numerical computations using the same model chemistry [253]. The cellular instability was seen to appear for values of the Lewis number of the deficient reactant smaller than unity by an amount larger than twice the reciprocal of the relevant Zel'dovich number (defined as the product of the activation temperature and the temperature increment resulting from heat release, divided by the square of the adiabatic flame temperature). In principle, by estimating appropriately the Zel'dovich number, the theoretical results generated with the Arrhenius chemistry could be employed to obtain quantitative predictions for stability boundaries and cell sizes of lean hydrogen flames, and an evaluation of the latter was attempted in Ref. [250]. Approximate quantitative predictions could also be extracted from the stability results derived recently with the two-step Zel'dovich chemistry [237], although the evaluation would then involve estimated values of a larger number of quantities. A more direct quantification could be obtained by use of realistic chemistry as a basis for the stability analysis, but such theoretical descriptions are not yet available.

Direct numerical simulations of diffusive-thermal instability of dilute  $H_2$ – $O_2$ – $N_2$  deflagrations employing detailed chemistry have been available for quite some time [254]. These seminal computations considered the temporal evolution of an initially perturbed flame front. Although the integrations could not be extended to very large times because of the existing limitations in computer power, the numerical results were seen to reproduce some of the previous experimental observations [250]. Thus, as in the experiments, for moderately rich conditions ( $\phi = 1.5$ ) the flame was found to be stable to the initial perturbations, while for lean conditions ( $\phi = 0.66$ ) the perturbation was seen to grow, causing the perturbed planar front to develop a pattern resembling the cellular structure observed in the flame visualizations [249,250]. More recent computations of lean flames [255], also employing detailed kinetics, have served to investigate the combined effects of the diffusive-thermal and hydrodynamic instabilities, including the long-time evolution of the flame.

Besides the cellular diffusive-thermal instability emerging in sufficiently lean hydrogen–air deflagrations and the stable region corresponding to compositions ranging from moderately lean to moderately rich mixtures (i.e., for Lewis numbers near and somewhat above unity), pulsating instabilities are found for sufficiently rich hydrogen flames. The mechanism of the pulsating diffusive-thermal instability can be understood as a consequence of the oxygen diffusivity being significantly smaller than the thermal diffusivity, which allows the planar flame to sit nearly in one place for an appreciable time, slowly heating the material ahead of it until the flame believes it is propagating in much hotter reactants and so moves ahead very rapidly, until it again encounters cold reactants and stops.

Pulsating reaction fronts were first encountered in numerical calculations of gasless reaction fronts propagating in condensed materials [256]. Its relevance for gaseous deflagrations was

anticipated in the early stability analyses employing Arrhenius chemistry [251,257], where the pulsating instability was predicted to appear for a critical value of the Lewis number exceeding unity by an amount equal to  $4(1 + \sqrt{3})$  over the Zel'dovich number. Subsequent detailed-chemistry numerical simulations of hydrogen–oxygen [258] and hydrogen–air [259,260] planar flames found a pulsating mode of flame propagation for a narrow range of equivalence ratios adjacent to the kinetically controlled rich flammability limit. As the hydrogen content increases, the solution evolves from single-period to double-period oscillations, eventually leading to propagating cycles exhibiting a long stage of slow propagation, during which heat losses by radiation enter to promote flame extinction [261].

The altered critical value of the equivalence ratio at the rich flammability limit, accounting for both radiative heat losses and unsteady flame dynamics, has been computed as a function of the pressure [262]. Increasing the pressure is seen to shift the onset of the pulsating instability to smaller equivalence ratios, widening the range of conditions for which pulsating fronts may be observed. Additionally, effects of stretch on the instability threshold have been investigated [263], positive stretch (as in outwardly propagating spherical flames) promoting pulsation and negative stretch (as in inwardly propagating spherical flames) retarding it. For these spherical hydrogen flames, the onset of the pulsating instability has been shown in high-pressure experiments to produce interesting spiral patterns on the flame surface [264,265].

#### 6.6. Hydrogen flame balls and flammability limits

The existence of nonpropagating steady spherical flame balls was first predicted theoretically by Zel'dovich [266]. His seminal analysis envisioned a spherical reaction layer bounding a uniform hot core of reaction products, with heat conduction to and reactant diffusion from the surrounding atmosphere occurring through a steady, chemically frozen diffusion region. These diffusion-reaction structures are, however, unstable. As suggested by Zel'dovich [266] (see, also p. 331 of [154]), radiative heat losses may enter to provide the needed stabilizing mechanism. Together with the branch of unstable solutions corresponding to small radiation-free flame balls, when heat losses by radiation are included in the energy balance, the steady conservation equations are seen to possess a second branch of flame-ball solutions, with characteristic radii many times larger than the thickness of the corresponding premixed flame. The existence of these solutions was verified experimentally under microgravity conditions by Ronney and coworkers [267–270]. The observed hydrogen–air flame balls were generated in extremely lean mixtures, including values of  $\phi$  as low as  $\phi = 0.0825$  [268], well below the kinetically controlled flammability limit of planar flames ( $\phi \approx 0.251$  for normal atmospheric conditions, according to Fig. 18).

Besides the intrinsic scientific interest in the phenomenon, involving the necessary cooperation of preferential diffusion, curvature, and radiation for the existence of stable solutions [270], flame balls are relevant in general for combustion applications when hydrogen is used as a fuel. As discussed in the previous section, diffusive-thermal instabilities are known to influence deflagration propagation in very lean hydrogen–air mixtures [104]. Combustion is enhanced by effects of preferential diffusion, which produce superadiabatic flame temperatures and enable cellular flames to propagate in mixtures with hydrogen content well below the flammability limit computed theoretically for steady planar deflagrations, shown in Fig. 19. For sufficiently lean mixtures, the cellular flame breaks up into separate cells, which propagate as an array, leaving behind a finite amount of unburnt fuel. In near-limit situations, the cells close upon themselves to

form flame balls with a nearly spherical shape [271]. Interactions between neighboring flame balls become weak because of the large separating distance. Under those conditions, the flame can be envisioned as an ensemble of isolated flame balls, which propagates with a velocity that can be determined by adding the individual flame-ball burning rates, with an additional assumption introduced for the average inter-flame-ball spacing [272]. This limiting mode of cellular-flame propagation clearly fails when the conditions are too lean to support isolated self-sustained flame-ball combustion. For this reason, analyses of structures of isolated flame balls are relevant in computations of burning rates as well as of limiting flammability conditions for fuel-lean mixtures of hydrogen and oxygen that may or may not include inert species such as nitrogen.

The structure of a steady, spherically symmetrical flame ball is determined by integration of the convection-free energy and species conservation equations, including detailed descriptions for the transport, chemistry, and radiation, with symmetry conditions at the center and ambient values  $T = T_u$  and  $Y_i = Y_{i,u}$  in the far field, the subscript  $u$  denoting conditions in the ambient unburnt mixture. Early theoretical analyses of flame-ball structures were based on a one-step Arrhenius reaction [273,274], although numerical studies, including detailed-chemistry mechanisms and different models for radiation, were performed subsequently [275–277]. The computation requires taking appropriate account of  $H_2O$  radiation, with different levels of complexity being employed in previous studies. The most elaborate radiation model includes both emission and absorption, with radiative transport computed by a Statistical Narrow Band (SNB) – Discrete Ordinate method [278,279], while the simplest model assumes an optically thin medium, an approximation used, for instance, in [275–277]. As explained by Ronney [279], larger errors emerge for mixtures diluted with  $CO_2$ ; for such cases an optically thin model is never a good approximation.

Results of numerical integrations including detailed chemistry and an SNB model for radiation are shown in Fig. 22 [71]. The plots exhibit the variation with equivalence ratio of the flame-ball radius  $r_f$ , defined as the location where the rate of hydrogen consumption reaches a maximum, along with the variation of the peak temperature  $T_{max}$ , which is always reached close to  $r = r_f$ . The computations are for a hydrogen–air mixture at pressure  $p = 1$  atm and normal ambient temperature  $T_u = 300$  K, and they also include test cases with water-vapor dilution associated with ambient mass fractions  $Y_{H_2O,u} = 0.1$  and  $Y_{H_2O,u} = 0.2$ . As expected, no solution exists for values of  $\phi$  below a critical value  $\phi_1$ , and two different solutions are found for  $\phi > \phi_1$ , with the upper branch in the  $r_f$ – $\phi$  plot corresponding to the lower branch in the  $T_{max}$ – $\phi$  plot. In the range of equivalence ratio considered, the branch of larger radii corresponds to values of  $r_f$  on the order of although smaller than 1 cm, in agreement with the experimental observations [267–270].

The solutions along the branch of small flame-ball radii, with almost negligible radiation, are known to be unstable to one-dimensional disturbances [273,274], whereas radiation helps stabilize the solutions along the other branch, which correspond to the large flame balls found in the microgravity experiments [267–270]. Previous numerical computations [277] and theoretical analyses [274] indicate that the critical solution at the turning point is unstable, with the first stable solution appearing in the upper branch for an equivalence ratio slightly larger than  $\phi_1$ . This stability characteristic was further verified recently [71] by performing a number of transient computations, with the steady solution used as initial condition. The results indicated, in particular, that the instability for the solution along the upper branch occurs as a subcritical Hopf bifurcation. For the computations with a dry ambient atmosphere shown in the figure, the bifurcation occurs for  $\phi = 0.0753$ . This value

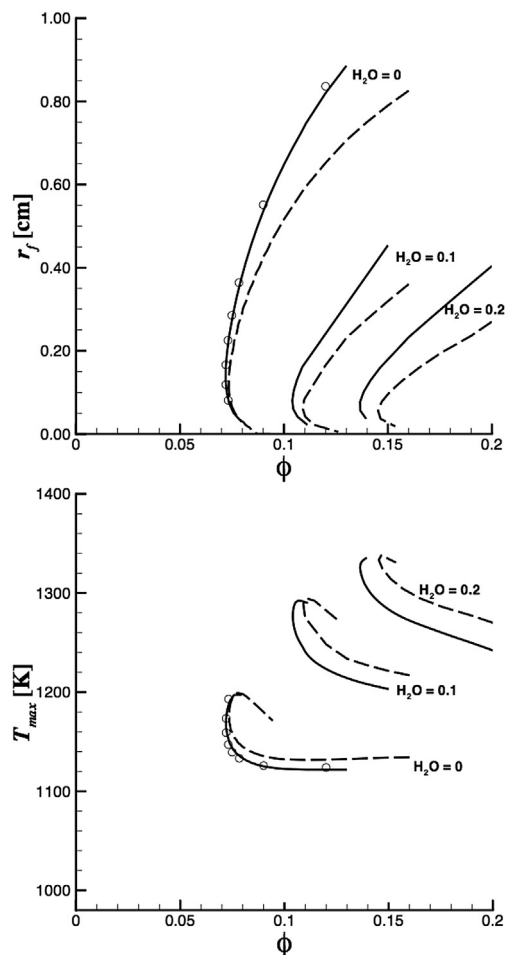


Fig. 22. The variation with the equivalence ratio of the flame-ball radius  $r_f$  and its peak temperature  $T_{max}$  as obtained from numerical integrations with the SNB radiation model and detailed chemistry (solid curves), with the SNB radiation model and the one-step reduced mechanism (circles), and with the optically thin approximation and the one-step reduced mechanism (dashed curves); for three different values of the mass fraction of water vapor in the ambient atmosphere [71].

is in fact very close to the turning-point value  $\phi_1 = 0.0735$ , so that, for practical purposes, one may in principle neglect unsteady effects in defining the critical conditions for flame-ball existence, which therefore can be associated with the turning point of the steady solution. It is worth mentioning that the prediction  $\phi_1 = 0.0735$  corresponds to a limiting hydrogen content of 3%, very close to the minimum flammable value achieved in microgravity experiments [268],  $\% H_2 = 3.35$ , which in turn is close to the flammability limit at Earth gravity, generally accepted to be  $\% H_2 \approx 4.0$ . This quantitative agreement further demonstrates the relevance of flame balls in ultra-lean combustion applications.

The computations shown in Fig. 22 reveal that the resulting peak temperature is not too far above the crossover value. As emphasized recently [70,71], under those near-crossover conditions, the one-step reduced mechanism defined in Eqs. (93) and (94), derived originally for ultra-lean planar flames [19], can be employed to describe with excellent accuracy hydrogen–air flame balls, including the solution near the turning point as well as the whole branch of stable solutions. This is demonstrated in the comparisons shown in Fig. 22, where the circles represent results for  $H_2$ –air flame balls computed with the reduced chemistry. The plots also test the accuracy of the well-known optically thin approximation used to evaluate radiation heat losses in previous studies [70,71,275–277]. The results obtained with the one-step



approximation for the chemistry combined with the optically thin approximation for radiation are shown as dashed curves in Fig. 22. As can be seen, in the range of  $\phi$  considered, the optically thin approximation yields moderate errors in flame-ball radii, on the order of 20%, in agreement with previous numerical investigations [279]. The accuracy is much better for the computation of the critical value  $\phi_1$  associated with the turning point, especially for dry hydrogen–air mixtures.

When the one-step approximation is used in the description [70,71], only three chemical species ( $H_2$ ,  $O_2$ , and  $H_2O$ ) need to be considered. In fuel-lean hydrogen–air flame balls, the molecular transport is dominated by the abundant presence of nitrogen and oxygen, so that the simple diffusion-velocity description in Eq. (22) applies, with Soret diffusion of  $H_2$  incorporated in a compact Fickian description by introducing the modified fuel mass fraction  $\tilde{Y}_{H_2} = (T/T_u)^{\alpha_{H_2}} Y_{H_2}$  and modified diffusivity  $\tilde{D}_{H_2} = (T/T_u)^{-\alpha_{H_2}} D_{H_2}$ . Note that, since the thermal diffusion factor  $\alpha_{H_2} = -0.29$  is negative, the effective diffusivity  $\tilde{D}_{H_2}$  is larger as a result of thermal diffusion. For the stoichiometry of the global reaction  $2H_2 + O_2 \rightarrow 2H_2O$ , the species conservation equations reduce to

$$\begin{aligned} \frac{1}{r^2} \frac{d}{dr} \left( \frac{\rho D_{O_2}}{M_{O_2}} r^2 \frac{dY_{O_2}}{dr} \right) &= -\frac{1}{r^2} \frac{d}{dr} \left( \frac{\rho \tilde{D}_{H_2}}{2M_{H_2O}} r^2 \frac{dY_{H_2O}}{dr} \right) \\ &= \frac{1}{r^2} \frac{d}{dr} \left( \frac{\rho \tilde{D}_{H_2}}{2M_{H_2}} r^2 \frac{d\tilde{Y}_{H_2}}{dr} \right) = \omega, \end{aligned} \quad (98)$$

while the corresponding energy equation is given by

$$\frac{1}{r^2} \frac{d}{dr} \left( \lambda r^2 \frac{dT}{dr} \right) = Q_R + 2h_{H_2O}\omega, \quad (99)$$

where the reaction rate  $\omega$  is defined in Eq. (94), and  $Q_R$  represents the rate of radiant heat loss per unit volume. The optically thin approximation, adopted here for simplicity, results in the familiar law

$$Q_R = 4\kappa_{H_2O}\sigma p(M/M_{H_2O})Y_{H_2O}(T^4 - T_u^4), \quad (100)$$

where  $M$  represents the mean molecular mass of the gas mixture, and  $\sigma$  and  $\kappa_{H_2O}$  denote the Stefan–Boltzmann constant and the Plank-mean absorption coefficient, respectively, the latter being a function of the local temperature [280]. Integrating Eqs. (98) and (99) subject to  $dT/dr = dY_i/dr = 0$  at  $r = 0$  and  $T - T_u = \tilde{Y}_{H_2} - Y_{H_{2u}} = Y_{O_2} - Y_{O_{2u}} = Y_{H_2O} - Y_{H_{2O}u} = 0$  as  $r \rightarrow \infty$  gives the results represented by the dashed curves in Fig. 22. Sample profiles corresponding to the solution with larger flame-ball radius for  $\phi = 0.15$  and  $Y_{H_{2O}u} = 0$  are shown in Fig. 23. As expected, the solution includes a fairly thin reaction layer, where  $H_2$  is depleted, separating an equilibrium hot core of uniform composition from the surrounding chemically frozen gas mixture.

Some distinct characteristics of flame-ball combustion arising from differential diffusion can be readily extracted from the above equations. For instance, if constant values of  $D_{O_2}/D_{H_2O}$  and of  $\tilde{D}_{H_2}/D_{H_2O}$  are assumed, then the first two equations in Eq. (98) can easily be integrated to yield the two simple relations

$$\begin{aligned} Y_{H_2O} - Y_{H_{2O}u} &= 2 \frac{M_{H_2O}}{M_{O_2}} \frac{D_{O_2}}{D_{H_2O}} (Y_{O_{2u}} - Y_{O_2}) \\ &= \frac{M_{H_2O}}{M_{H_2}} \frac{\tilde{D}_{H_2}}{D_{H_2O}} (Y_{H_{2u}} - \tilde{Y}_{H_2}) \end{aligned} \quad (101)$$

giving the mass fractions of water vapor and oxygen in terms of the modified fuel mass fraction  $\tilde{Y}_{H_2}$ . In the reaction layer, where  $\tilde{Y}_{H_2} \approx 0$ , these expressions can be evaluated to give

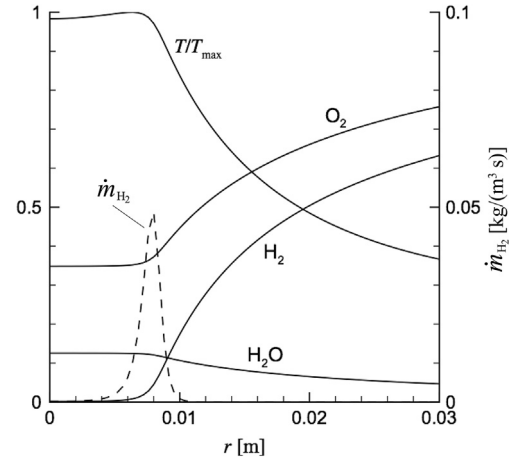


Fig. 23. Radial distributions of  $T/T_{max}$ ,  $Y_{H_2}/Y_{H_{2u}}$ ,  $Y_{O_2}/Y_{O_{2u}}$  and  $Y_{H_2O}$  as obtained from numerical integrations of Eqs. (98) and (99) for  $\phi = 0.15$ ,  $T_u = 300$  K and  $p = 1$  atm (solid curves); adapted from Ref. [70]. The dashed line shows the radial variation of the fuel mass consumption rate  $\dot{m}_{H_2} = 2M_{H_2}\omega$ .

$$\frac{Y_{H_2O_r} - Y_{H_2O_u}}{Y_{H_{2u}}} = \frac{M_{H_2O}}{M_{H_2}} \frac{\tilde{D}_{H_2}}{D_{H_2O}} = 28.73 \quad (102)$$

and

$$\frac{Y_{O_{2r}}}{Y_{O_{2u}}} = 1 - \frac{1}{2} \frac{M_{O_2}}{M_{H_2}} \frac{\tilde{D}_{H_2}}{D_{O_2}} \frac{Y_{H_{2u}}}{Y_{O_{2u}}} = 1 - \phi/0.234, \quad (103)$$

for the water vapor and oxygen mass fractions in the reaction zone, in which an averaged increased diffusivity  $\tilde{D}_{H_2}/D_{H_2} = 1.154$  has been employed in the numerical evaluation, as suggested by computations [70]. In view of this last equation, it is clear that in hydrogen–air mixtures the regime of lean flame balls is restricted to configurations with  $\phi < D_{O_2}/\tilde{D}_{H_2} \approx 0.234$ , such that  $Y_{O_{2r}} > 0$ , a result of the differential diffusion first pointed out by Joulin [281]. Note that this limiting equivalence ratio, corresponding to the effective stoichiometric conditions for which both reactants are simultaneously depleted in the reaction sheet, is clearly affected by thermal diffusion, which, according to the approximation  $\tilde{D}_{H_2}/D_{H_2} = 1.154$  employed in evaluating the concentrations of water vapor and oxygen at the flame, increases the transport rate of hydrogen by approximately 15%.

Also of interest is the pronounced effect of differential diffusion on the peak temperature  $T_{max}$  at the reaction layer. The quantification of this effect is straightforward for the solutions along the unstable branch, because the associated flame-ball radii are so small that radiation has a negligible effect, so that the heat released by combustion is removed solely by conduction, that being the solution first postulated by Zel'dovich [266]. Eliminating the reaction term by a linear combination of Eq. (99) with the last equation in Eq. (98) and integrating twice, with  $\rho\tilde{D}_{H_2}/\lambda$  assumed to be constant, gives

$$T - T_u = \frac{\rho\tilde{D}_{H_2}}{\lambda} \frac{(-h_{H_2O})}{M_{H_2}} (Y_{H_{2u}} - \tilde{Y}_{H_2}), \quad (104)$$

thereby yielding

$$T_{max} = T_u + \frac{(-h_{H_2O}/M_{H_2})Y_{H_{2u}}}{\lambda/(\rho\tilde{D}_{H_2})} \quad (105)$$

for the peak temperature at the reaction layer, where  $\tilde{Y}_{H_2} \approx 0$ . This peak value is to be compared with the adiabatic flame temperature

for the same unburnt mixture composition, given in Eq. (95). The result of the comparison can be expressed in the form

$$\frac{T_{\max} - T_u}{T_{\text{af}} - T_u} = \frac{1}{\tilde{L}_{\text{H}_2}}, \quad (106)$$

clearly reflecting the pronounced effect of differential diffusion through the effective Lewis number  $\tilde{L}_{\text{H}_2} = \lambda/(\rho c_p \tilde{D}_{\text{H}_2}) \approx 0.26$ , which includes the influence of thermal diffusion through the augmented  $\text{H}_2$  diffusivity  $\tilde{D}_{\text{H}_2}$ . The simple expression given in Eq. (106) states that burning a premixed mixture in a spherical flame produces a temperature increase that is about four times larger than that resulting from planar-flame combustion, a remarkable feature of flame balls that explains their survival in extremely lean atmospheres.

As the mixture becomes leaner along the unsteady branch, the peak temperature given in Eq. (105) decreases, thereby reducing the reaction rate shown in Eq. (94). This decreasing reaction rate requires a larger flame-ball radius to ensure an adequate conduction-reaction balance in Eq. (99). Limiting conditions are reached as the peak temperature  $T_{\max}$  approaches the crossover value  $T_c$ , defined in Eq. (77), at which the rate given in Eq. (94) vanishes, causing the flame-ball radius of the conduction-reaction solution to increase rapidly. The expression shown in Eq. (105) can therefore be used to determine in the first approximation the kinetically controlled flammability limit of lean flame-ball combustion according to

$$(Y_{\text{H}_{2\text{u}}})_1 = \left[ \lambda / (\rho \tilde{D}_{\text{H}_2}) \right] (T_c - T_u) / (-h_{\text{H}_2\text{O}}/M_{\text{H}_2}), \quad (107)$$

where  $T_c$  is obtained from Eq. (77) with  $\alpha = 1$ , as corresponds to the vanishing  $\text{H}_2$  concentration found in the reaction layer at the flammability limit. The water-vapor mass fraction  $Y_{\text{H}_2\text{O}}$ , given in Eq. (102) is used here to evaluate the effective third-body concentration. Because of the large diffusivity of hydrogen, the resulting limiting hydrogen content obtained from Eq. (107) is about one fourth that shown for planar flames in Fig. 19. For instance, for a hydrogen–air mixture at  $p = 1$  and  $T_u = 300$  K, evaluation of Eq. (107) leads to  $\phi_1 \approx 0.06$  [71], to be compared with the value  $\phi_1 \approx 0.251$  corresponding to planar-flame propagation.

It is worth mentioning that the development leading to Eq. (107) could also be used to derive an expression for the lean flammability limit of  $\text{D}_2$ –air and  $\text{D}_2$ – $\text{O}_2$  combustion [282]. In particular, if the crossover temperature corresponding to  $\text{D}_2$  oxidation is close to that for hydrogen oxidation (as would be expected if their chemical rate parameters were nearly the same), then the prediction for the limiting deuterium mass fraction would be given by Eq. (107), with the diffusion coefficient of  $\text{D}_2$  replacing  $\tilde{D}_{\text{H}_2}$ . According to Eq. (97), the resulting limiting deuterium content for lean combustion would be about 40% larger than the corresponding limiting hydrogen content. This theoretical result seems to be in reasonably good agreement with early experimental observations. Thus, although some variability exists in the experimentally measured lean flammability limits reported in the literature for  $\text{D}_2$ –air and  $\text{D}_2$ – $\text{O}_2$  flames [283–285], an approximate value of 1.35, close to this prediction, has been quoted [286] for the ratio of the percentage of hydrogen to the percentage of deuterium in their respective lean-limit mixtures.

The leading-order prediction given in Eq. (107) neglects entirely effects of radiation, and therefore it leads to values of  $\phi_1$  that are slightly smaller than those corresponding to the turning points in Fig. 22 (e.g.,  $\phi_1 = 0.0735$  for hydrogen–air). In reality, as the radius of the flame-ball solution along the unsteady branch increases on approaching  $\phi = \phi_1$ , the effect of radiant energy loss takes over. As a

result, instead of a diverging value of  $r_f$ , the solution shows a smooth transition to the branch of stable solutions through the turning point shown in Fig. 22. As seen in the figure, along the branch of stable solutions away from the turning point the radius  $r_f$  increases for increasing  $Y_{\text{H}_{2\text{u}}}$ , while the temperature remains almost constant. This behavior is a result of the relatively large temperature sensitivity of  $k_{1f}$ , which forces the peak temperature  $T_{\max}$  of the resulting solutions to remain always very close to the crossover value, because if  $T_{\max}$  were significantly above  $T_c$  then the associated increase in chemical reaction rate would be so large that it could not be balanced by radiation losses. Therefore, for increasing equivalence ratios, the resulting flame-ball radius for the branch of stable solutions increases in such a way that radiant energy losses can balance the chemical heat release while keeping the flame temperature at a value not far from  $T_c$ , a condition that can be used to determine accurately the value of  $r_f$  away from the turning point [70].

In the solution that appears, radiation is seen to be negligible in the near-field region corresponding to radial distances of order  $r_f$  [70,71], where the volumetric heat losses by conduction, given in order of magnitude by  $O(\nabla \cdot [\lambda \nabla T]) = \lambda(T_c - T_u)/r_f^2$ , are about twenty times larger than those associated with radiation, which can be evaluated from Eq. (100) with  $T = T_c$  and  $Y_{\text{H}_2\text{O}} = Y_{\text{H}_2\text{O}_f}$ . Radiation enters only in the far field, affecting the final decay of the temperature towards the ambient value  $T_u$ . This characteristic flame-ball structure has been analyzed recently, with account taken of finite-rate-chemistry effects [71], to obtain accurate analytic expressions for the critical value of  $\phi_1$  at the turning point, thereby providing corrections to the leading-order result shown in Eq. (107). These simplifications make flame-ball structures much easier to understand for hydrogen.

The one-step kinetics defined in Eqs. (93) and (94), which describes steady structures of flame balls along the stable branch with remarkable accuracy, as demonstrated in the comparisons of Fig. 22, can find application in many other near-limit combustion conditions. For example, it could be used in numerical and theoretical investigations of flame stability as well as dynamics of cellular fronts, thereby facilitating the numerical investigation of the intermediate range of flame structures encountered for decreasing values of the equivalence ratio, from steady planar flames to highly cellular flames involving an ensemble of flame balls [272]. An example of such applications includes direct numerical simulation of propagating flame cells, which becomes computationally expensive when detailed chemistry is used [287]. A limiting related problem that could also be studied with the simplified kinetics is the appearance of self-drifting flame balls as a bifurcation of the associated stationary spherical solution, a phenomenon previously investigated on the basis of a generic Arrhenius-chemistry model [288,289]. In addition, numerical simulations of three-dimensional instabilities of spherically propagating flames [290,291] could make use of the one-step  $\text{H}_2$ – $\text{O}_2$  reduced mechanism for a more realistic description, enabling the flame response to be linked directly to the ambient conditions.

## 7. Nonpremixed combustion of hydrogen

Nonpremixed combustion of hydrogen is of interest for technological applications including gas turbines and scramjets and also in accidental scenarios, e.g., jet diffusion flames formed in nuclear reactor containments during severe accidents or after the accidental discharge of hydrogen in storage facilities. Diffusion flames are also the predominant form of combustion in cryogenic hydrogen–oxygen rocket engines. In all of these configurations the reactants are initially separated. Since they need to mix at a molecular level before the chemical reaction can occur, transport by

convection and diffusion becomes essential in determining the resulting burning rate. As a consequence, while the steady, planar, unstrained, adiabatic deflagration is a self-contained entity with a well-defined burning rate, the burning rate of diffusion flames depends on the configuration and external conditions [222].

A configuration of practical interest, often considered in experimental and numerical investigations, is the jet flame sketched in Fig. 24, formed as a hydrogen jet discharges into a quiescent air atmosphere. Although recent interest in microscale combustion has motivated studies of hydrogen diffusion flames at moderately small Reynolds numbers [292], in most applications the jet Reynolds number is very large, that being the case considered in Fig. 24, which serves to highlight some of the phenomena that are encountered in diffusion flames under such conditions.

At high Reynolds numbers mixing of hydrogen with the oxygen of the air occurs in thin mixing layers distorted and strained by the flow. Chemical reactions may occur within these mixing layers, leading to the establishment of a diffusion flame that appears in the first approximation as a surface separating an inner region without oxygen from an outer region without hydrogen, as shown in Fig. 24. Because of the small value of the hydrogen-to-air mass ratio needed for stoichiometric combustion (1 g of hydrogen being needed for the combustion of 34 g of air according to the overall oxidation reaction  $2\text{H}_2 + \text{O}_2 \rightarrow 2\text{H}_2\text{O}$ ), the flame tends to sit far on the air side of the strained mixing layer. The flow strain affects the resulting burning rate and may cause flame extinction at highly strained locations, creating holes on the flame surface [293], bounded by edge flames [294] that act as extinction or re-ignition fronts [295–297]. Depending on the injection conditions, jet diffusion flames may be attached to the injector rim or may be lifted off at a given distance, the latter solution exhibiting a tri-bachial structure with lean and rich side deflagrations preceding the trailing diffusion flame [298], the case considered in the schematic view of Fig. 24.

### 7.1. Attached and lifted hydrogen jet diffusion flames

For large jet Reynolds numbers, the anchoring of the hydrogen diffusion flame depends on the structure of the small region near the injector rim where upstream heat conduction and diffusion are important. The characteristic scales of this near-edge Navier–Stokes region are determined by the wall value of the velocity gradient of the fuel stream, which must be smaller than a critical value for the diffusion flame to remain attached [299]. The generally accepted criterion is that critical conditions for flame anchoring are reached when the size of the Navier–Stokes region, given by the

square root of the ratio of the thermal diffusivity to the boundary-layer velocity gradient, decreases to a value on the order of the thickness of the stoichiometric hydrogen–air premixed-flame. For hydrogen, nozzle-attached flames have been observed for very large values of the jet velocity (and associated wall velocity gradient), well beyond those reported for hydrocarbon flames [298,300,301]. Although qualitative explanations of this phenomenon based on the high diffusivity of hydrogen have been provided [298,300], more work on this topic is required, including detailed numerical and experimental characterizations of the attachment region, which are available for instance for methane flames [302], but are however lacking for hydrogen flames. Calculations with detailed transport and chemistry descriptions, appropriately accounting for perturbations in the boundary conditions as indicated in Ref. [299], are clearly viable with the present computer power, and they could readily provide reliable values of critical anchoring conditions. Parametric results accounting for variations of feed-stream composition and temperature and also for effects of injector thickness and air coflow would be clearly of interest in applications.

Even when conditions for near-injector flame attachment are not met, the hydrogen jet flame may still exist as a lifted flame extending downstream from a given lift-off location. Detailed experimental characterizations of lifted hydrogen jet flames at elevated Reynolds numbers are available in different configurations [196,303,304], and direct numerical simulations of these flames with detailed chemistry descriptions have provided additional quantitative information of interest [305–308]. Upstream from the lifted flame, the flow is chemically frozen. Hydrogen and air interdiffuse in slender mixing layers that develop downstream from the injector rim, creating the conditions for the chemical reaction to occur. When the air temperature is above the crossover value, as occurs in supersonic combustion applications, auto-ignition of the mixture leads to combustion stabilization at a given downstream distance, the case studied in [196,304,307,308]. By way of contrast, when the air temperature is below crossover, the liftoff mechanism relies on the upstream propagation of edge flames along the turbulent mixing layers, at a location where their velocity equals that of the flow [298]. For the experimental configuration investigated in [303], including a quiescent air atmosphere at normal temperature and a fast hydrogen jet at 680 m/s, direct numerical simulations [305] indicate that the flame stabilization occurs through a laminar triple flame of ring shape that sits outside the turbulent jet.

Triple flames are known to propagate at a velocity that is of the order of, although larger than, the propagation velocity of the planar stoichiometric deflagration, the augmentation factor being related to the flow redirection ahead of the flame resulting from thermal expansion [309]. Propagation velocities of hydrogen triple flames have been calculated with detailed chemistry [310], including influences of flow strain [311,312], giving values on the order of several meters per second. Although these values are two orders of magnitude smaller than the injection velocity present in many systems (e.g., 680 m/s for the experiments in Ref. [303]), stabilization of hydrogen flames is possible because the triple flame sits outside the jet, in the slow-flow region where the velocity is determined by the jet entrainment. The high diffusivity of hydrogen together with the small value of the hydrogen-to-air stoichiometric mass ratio clearly facilitate the existence of flammable conditions in this outer region. It is of interest that, while arguments based on boundary-layer descriptions of jets and mixing layers serve to explain the lift-off characteristics of jet hydrocarbon flames [298,313,314], for hydrogen flames stabilized in high-speed jet configurations the necessary analysis is more complicated and requires consideration of the composition and velocity field in the

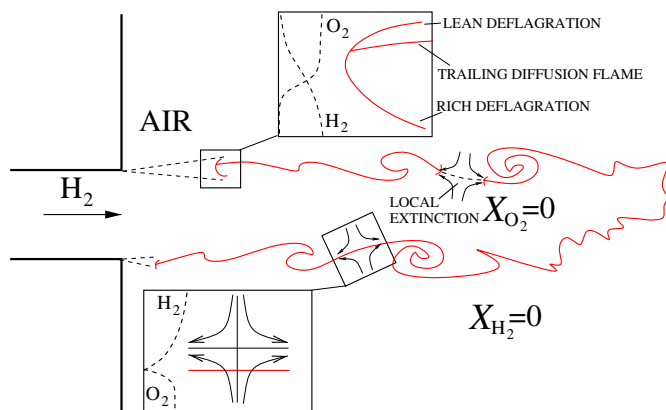


Fig. 24. Schematic view of a hydrogen–air jet diffusion flame.

entrainment region outside the jet. A relevant contribution in this respect is that of Savaş and Gollahalli [315], who used the composition associated with the Landau-Squire jet solution to investigate the conditions for existence and stability of lifted flames.

## 7.2. Structure and extinction of hydrogen diffusion flames

For the high Reynolds numbers characterizing the flow in most applications, the diffusion flames appear embedded in thin mixing layers that are locally strained by the turbulent motion [316]. The resulting flame structure, given in the first approximation by a local diffusion-reaction balance, depends fundamentally on the strain rate induced by the outer flow, as was clarified for one-step Arrhenius processes by the classical work of Liñán [185]. The counterflow configuration has been used extensively in experimental and numerical works to characterize effects of flow strain on diffusion flames, with different experimental setups and different boundary conditions for numerical integration of the associated one-dimensional solutions being considered by different groups [222]. For hydrogen, the variation of the peak radical-pool concentration of the steady solution with strain time (the inverse of the strain rate) gives the curves schematically represented in the insets of Fig. 10, the two upper insets including a distinct upper branch corresponding to the diffusion-flame solutions, whose turning point identifies extinction conditions. As previously mentioned,  $H_2$ –air counterflows with elevated air-side boundary temperature above  $T_s$ , the case shown in the bottom inset of Fig. 10, exhibit a continuous transition from the frozen state to the reactive state, without turning points, so that critical conditions for ignition or extinction do not exist for these high-temperature flows.

Numerous experimental and numerical investigations of hydrogen counterflow diffusion flames have served to clarify many different aspects of the problem. The early work was purely numerical [317], with experimental investigations following soon afterwards [318–320]. Effects of strain on flame structures and extinction limits have been investigated [75,321,322], along with those of fuel dilution [323,324]. Numerical and experimental investigations have explored influences of departures from one-dimensional flow [325–327] as well as effects of pressure [17,328], the latter studies revealing an intriguing non-monotonic variation of the extinction strain rate. The nonnegligible differences found recently [17] between experimental measurements and numerical computations of hydrogen–air counterflow flames at elevated pressure warrant further investigation with revised consideration of the chemistry and transport models.

The variation with strain rate of the peak flame temperature and peak H mole fraction is shown in Fig. 25, which corresponds to numerical computations of an axisymmetric  $H_2$ –air counterflow flame at atmospheric pressure for boundary temperatures equal to 300 K, with  $A$  representing the free-stream value of the strain rate on the air side of the mixing layer. Solutions with detailed chemistry are shown in the plots along with those obtained with the two-step reduced chemistry defined in Section 3.4.3. The two-step reduced chemistry can be seen to provide reasonably good accuracy over the whole range of strain rates explored [75]. The slight overprediction of peak temperatures (on the order of 50 K) is a result of the steady-state assumptions introduced for O and OH, which affects the associated energy balance by overpredicting the amount of chemical energy released.

As a result of the disparity of time scales of the controlling chemical reactions, nonpremixed hydrogen–air flames possess a general multilayer structure including a thin branching layer embedded in thick recombination regions. This is illustrated in Fig. 26, which shows profiles of species mole fractions and temperature computed with detailed chemistry for an intermediate

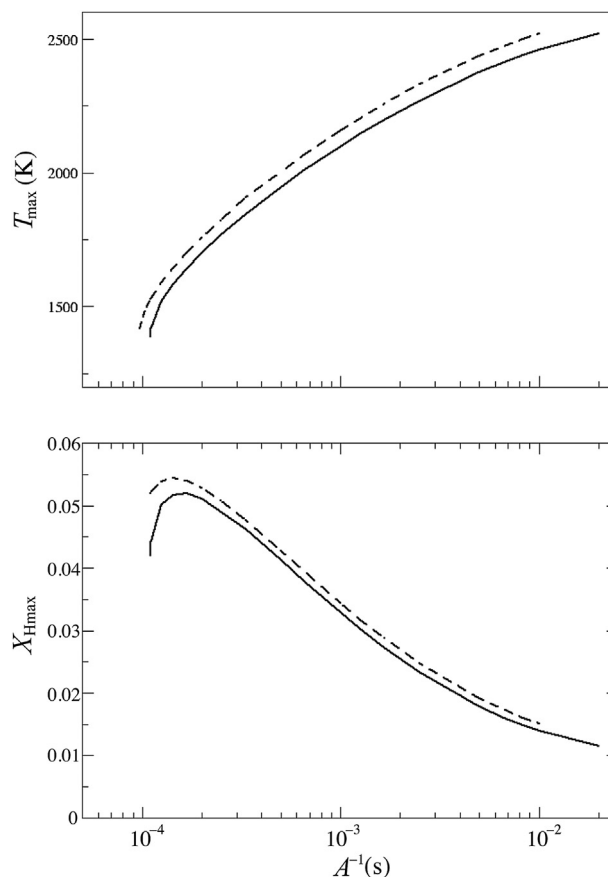


Fig. 25. The variation with the reciprocal of the air-side strain rate of the maximum temperature and of the maximum H mole fraction as obtained from computations of the axisymmetric  $H_2$ –air counterflow flame at atmospheric pressure for boundary temperatures equal to 300 K. The solid and dashed curves represent, respectively, results with the detailed chemistry of Table 1 and with the two-step reduced chemistry defined in Section 3.4.3 [329].

strain rate  $A = 4000 \text{ s}^{-1}$ . The emerging structure as well as the trends observed in the plots of Fig. 25 can be explained on the basis of the two-step reduced mechanism  $3H_2 + O_2 \xrightarrow{I} 2H_2O + 2H$  and  $H + H + M \xrightarrow{II} H_2 + M$ , used also earlier in Section 6.2 to discuss the structure of hydrogen–air deflagrations.

As can be inferred from the plot of peak temperature shown in Fig. 25, in diffusion flames away from extinction there exists an

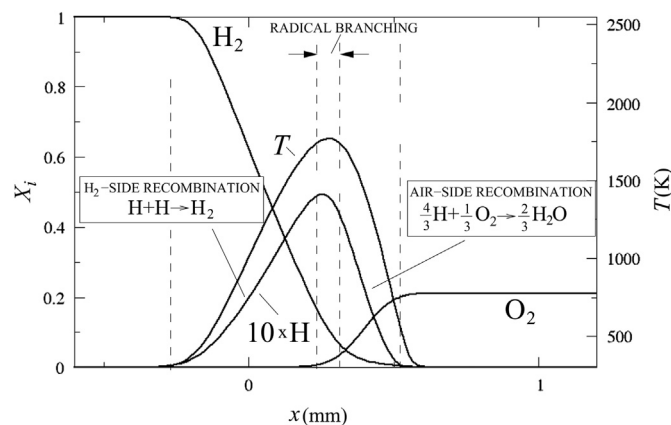


Fig. 26. Profiles of temperature and species mole fractions across an axisymmetric  $H_2$ –air counterflow flame at atmospheric pressure for boundary temperatures equal to 300 K and  $A = 4000 \text{ s}^{-1}$  [329].



intermediate hot region where the temperature is far above crossover, causing the shuffle reactions to maintain equilibrium there. The associated equilibrium expression given in Eq. (82) includes as a factor the equilibrium constant  $K$ , which takes very large values, as indicated in the evaluations given just after Eq. (81). Consideration of the limit  $K \gg 1$  provides in the first approximation the Burke–Schumann condition  $\text{C}_\text{H}_2\text{C}_\text{O}_2 = 0$ , associated with the radical chain-branching reaction  $3\text{H}_2 + \text{O}_2 \xrightarrow{\text{I}} 2\text{H}_2\text{O} + 2\text{H}$  being infinitely fast in this limit. A more careful observation of Eq. (82) reveals that the reactants can actually coexist in a thin branching layer, where they appear in small concentrations that are proportional to  $K^{-1/4}$ , while outside this thin layer the  $\text{H}_2$  concentration is of order  $K^{-1/3}$  on the air side and the  $\text{O}_2$  concentration is of order  $K^{-1}$  on the hydrogen side, as dictated by Eqs. (83) and (85), respectively. Radical recombination, providing most of the heat release, proceeds in a distributed manner outside the thin branching layer in relatively thick regions. On the hydrogen side, the  $\text{O}_2$  concentration is so small that the rate of the overall recombination reaction  $\text{H} + \text{H} + \text{M} \xrightarrow{\text{II}} \text{H}_2 + \text{M}$  reduces in Eq. (74) to  $\omega_{\text{II}} = k_{8\text{f}}\text{C}_\text{M}_8\text{C}_\text{OH}\text{C}_\text{H} + k_{9\text{f}}\text{C}_\text{M}_9\text{C}_\text{H}^2$ , which is significantly smaller than that found on the air side, where radical recombination is controlled instead by the rate of the elementary step  $\text{H} + \text{O}_2 + \text{M} \xrightarrow{4\text{f}} \text{HO}_2 + \text{M}$ . On the air side, the molecular hydrogen regenerated by  $\text{H} + \text{H} + \text{M} \xrightarrow{\text{II}} \text{H}_2 + \text{M}$  is rapidly consumed by  $3\text{H}_2 + \text{O}_2 \xrightarrow{\text{I}} 2\text{H}_2\text{O} + 2\text{H}$ , leading to the overall reaction displayed in Eq. (84).

In the two-step reduced description, most of the heat is released by the recombination reaction  $\text{H} + \text{H} + \text{M} \xrightarrow{\text{II}} \text{H}_2 + \text{M}$ , so that in assessing the effects of the flow field on the diffusion flame the strain time  $A^{-1}$ , which is a measure of the characteristic residence time in the counterflow, must be compared with the characteristic recombination time  $t_\text{R} = (k_{4\text{f}}\text{C}_\text{M}_4\text{C}_\text{O}_2)^{-1}$ , a fraction of a millisecond for the conditions typically encountered in the flame. For weakly strained flames with  $A^{-1} \gg t_\text{R}$  radical recombination is very rapid and occurs in radical recombination layers of thickness much smaller than the mixing-layer thickness  $(D_\text{T}/A)^{1/2}$ . Correspondingly, radicals appear in concentrations that are much smaller than those of the reactants or water vapor, because for these vigorously burning flames the radicals created by the overall reaction  $3\text{H}_2 + \text{O}_2 \xrightarrow{\text{I}} 2\text{H}_2\text{O} + 2\text{H}$  are immediately eliminated by the recombination reaction  $\text{H} + \text{H} + \text{M} \xrightarrow{\text{II}} \text{H}_2 + \text{M}$  to give the overall one-step description  $2\text{H}_2 + \text{O} \rightarrow 2\text{H}_2\text{O}$ . Although the associated limit of infinitely fast combustion applies with good accuracy only for strain times larger than those considered in Fig. 25, the plots in that figure clearly show how the peak H-atom concentration decreases with increasing residence time as the peak temperature increases. Note that, because of the large hydrogen diffusivity, the peak temperature in weakly strained flames exceeds the adiabatic flame temperature of stoichiometric hydrogen–air mixtures, given approximately by  $T_\text{af} \approx 2400$  K. As shown in [330], these effects of preferential diffusion can be effectively incorporated in computations of hydrogen–air diffusion flames in the limit of infinitely fast fuel oxidation by introducing coupling functions that account for species diffusivities different from the thermal diffusivity.

Significant interaction of the flow field with the diffusion flame occurs as the strain time  $A^{-1}$  becomes on the order of  $t_\text{R}$ , corresponding to the range the conditions explored in Fig. 25. The flame in this regime  $A^{-1} \sim t_\text{R}$  includes thick recombination regions that extend all across the mixing layer, as shown in Fig. 26. The resulting peak H-atom mole fraction is comparable, although somewhat

smaller than, the mole fractions of the main species. As the strain rate increases, the H-atom population increases, and the peak temperature decreases, because the smaller residence time limits the extent of radical recombination and the associated amount of heat released. Formulations of the conservation equations assuming infinitely fast chain-branching while accounting for finite rates of three-body recombination reactions are available for the numerical description of hydrogen nonpremixed combustion [27,67].

The multilayer flame structure of Fig. 26 continues to hold as long as the peak temperature remains sufficiently above crossover for the chain-branching reaction  $3\text{H}_2 + \text{O}_2 \xrightarrow{\text{I}} 2\text{H}_2\text{O} + 2\text{H}$  to be much faster than the recombination reaction  $\text{H} + \text{H} + \text{M} \xrightarrow{\text{II}} \text{H}_2 + \text{M}$ . Observation of the plots in Fig. 25 suggests that a noticeable reduction in radical production occurs already as the peak temperature decreases to values of order  $T_\text{max} \approx 1600$  K for  $A \approx 8000$  s<sup>−1</sup>. It is seen in the lower plot that, as the strain rate increases further, the resulting H-atom mole fraction reaches a maximum and eventually decreases, leading to a precipitous temperature decrease as the turning point associated with flame extinction is approached. Although studies of flame structures accounting for the competition of branching and recombination through rate-ratio asymptotics have met with some success [74,331,332], more work is necessary to improve the accuracy of the associated predictions of critical conditions at extinction.

### 7.3. Associated problems related to rocket engines

Hydrogen–oxygen diffusion-flame applications to combustion in cryogenic liquid-propellant rocket engines raise additional problems. One consideration is that often pressures inside the rocket chambers are comparable with or greater than the critical pressures of the chemical constituents, although this appears to be a quantitative complication without important qualitative effects [333]. Since liquid hydrogen is more volatile than liquid oxygen, a model sub-problem that has been investigated is the burning of a liquid oxygen droplet in a gaseous hydrogen atmosphere [334–339]. A novel potential complexity of this problem is the possible condensation and freezing of the combustion product  $\text{H}_2\text{O}$  to form ice in the diffusion flame, but this has not been encountered under practical conditions.

Acoustic combustion instability, a significant concern in the development of liquid-propellant rocket engines, is complex in that it relies on phase relations between pressure oscillations and oscillations of rates of heat release, which are modified as the acoustic perturbations propagate through the diffusion layers of the diffusion flames. Studies suggest that these phase modifications are unlikely to lead to acoustic amplification for droplet burning [340], but strained diffusion flames, as may be encountered around propellant injectors in rocket chambers, have a greater tendency to amplify the acoustic waves rather than to attenuate them [341], and thus may dominate the occurrence of acoustic instability, as supported by an empirical comparison of stable and unstable engines [342]. Rocket-motivated experiments on injection processes in hydrogen–oxygen systems [343,344] are helpful and revealing. More such experiments would be worthwhile, as would extension of the previous [341] amplification analysis, which employed one-step activation-energy asymptotics, to include more realistic hydrogen–oxygen chemistry, such as the two-step description discussed above.

## 8. Structure and stability of hydrogen detonations

Our presentation thus far has focused mainly on low-speed, hydrogen-combustion processes occurring under conditions that

are nearly isobaric spatially. The Mach number of the fluid in the region experiencing combustion, with respect to the rest of the fluid nearby, must be small under such conditions. This does not preclude all applications to supersonic flow; for example, in scramjet propulsion, the flow itself may be supersonic, while diffusion flames, such as those addressed in the previous section, may be moving with the fluid at very low relative Mach numbers. There are, however, many important hydrogen combustion processes in which this approximation of nearly isobaric conditions does not apply. For example, it is well known that slow laminar deflagrations, initiated in long tubes, become turbulent, experience flame acceleration, and eventually undergo transition to a supersonic mode of propagation in which a strong shock heats the combustible mixture to temperatures at which the chemical heat release occurs rapidly. These supersonic combustion fronts, detonations, with end states on the upper rather than the lower branch of the Hugoniot curve, represent the most destructive mode of propagation, although they also have long been investigated as possibly being employed for propulsion through standing-detonation, rotating-detonation, or pulsed-detonation engines (but never with great ultimate success).

The fluid mechanics of the process of transition from deflagration to detonation has been studied extensively, largely because of safety concerns, but it is quite complicated and remains poorly understood in many respects. Even the low-speed turbulent-combustion processes that precede any rapid flame acceleration are complex and exhibit different characteristics under different sets of conditions that define different regimes of turbulent flame propagation. Although, as in Section 5.4, we address some aspects of combustion phenomena relevant to turbulent flow, our aim in this article is not to review the complicated turbulent reacting flows that accompany transition from deflagration to detonation but rather to address the topics (in a sense more fundamental) of structures of the elementary deflagrations and detonations, for instance, including what is known today of their chemical kinetics and molecular transport processes – information basic to studies of turbulent combustion and transition to detonation.

### 8.1. Pressure buildup under confinement

Information relevant to flame acceleration and transition to detonation specifically for hydrogen–air mixtures, especially in complex geometries involving confinement with the presence of obstacles, may be found in [345–348], for example, the last summarizing results of an extensive program studying hydrogen risks in nuclear power plants. In a broader review of flame acceleration and transition to detonation [349], much of the information pertains to hydrogen. Other sources such as these must be consulted for descriptions of such interesting combustion phenomena as fast deflagrations and slow detonations, which develop during propagation processes when there are obstacles in the flow, or in porous media [350,351]. A great deal of experimental information on this may be found in the book [352], which also covers associated demolition loads.

### 8.2. Chapman–Jouguet detonation velocities

Propagation velocities of steady, planar detonations, unlike those of deflagrations, depend not on their structure but rather on their environment, which determines whether they are strong, weak, or Chapman–Jouguet waves [66,353]. The last of these, the slowest, occurs under most conditions and is shown in Fig. 27 as a function of equivalence ratio for hydrogen–air and hydrogen–oxygen mixtures initially at 1 atm and 300 K. These curves, which may be obtained by employing the latest NASA

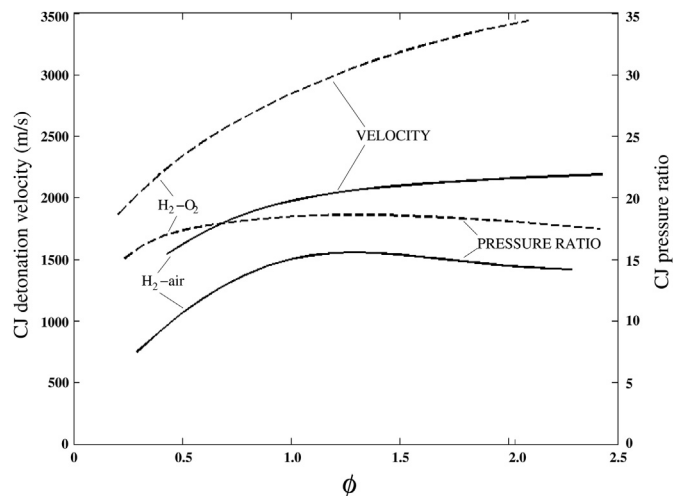


Fig. 27. The propagation velocity of and the pressure ratio across a Chapman–Jouguet detonation as a function of the equivalence ratio for  $\text{H}_2$ –air and  $\text{H}_2$ – $\text{O}_2$  mixtures initially at 1 atm and 300 K (obtained from results in [349,353]).

thermochemical data [354], are calculated on the basis of chemical equilibrium of the final mixture by using the Rankine–Hugoniot jump conditions relating the initial and final states across the detonation, along with the Chapman–Jouguet tangency condition (resulting in a Mach number of unity at the final state).

It may seem strange that, unlike, for example, the pressure ratio across these detonations (also shown in the figure), the propagation velocity does not peak near stoichiometric conditions but instead continues to increase with increasing equivalence ratio. The ultimate reason for this initially unexpected behavior is the continual decrease of the average molecular weight of the final equilibrium mixture with increasing equivalence ratio. It can be shown [353] that while pressure, temperature, and density ratios peak near stoichiometric conditions, as is expected from the net heat release per unit mass of the mixture being a maximum there, when the initial and final mixtures are approximated as ideal gas mixtures with constant but different specific-heat ratios  $\gamma$  the Chapman–Jouguet detonation velocity becomes the sound speed  $\sqrt{\gamma RT}$  of the final burnt gas times the ratio of the final to initial gas density. This is a simple consequence of mass conservation when the final Mach number is unity. It is the increase of the gas constant per unit mass  $R$  of the final mixture with increasing equivalence ratio that causes the burnt-gas sound speed and therefore the propagation velocity to continue to increase, since  $\gamma$  remains nearly constant, and  $T$  decreases only slowly, the density ratio changing only slightly.

### 8.3. Planar detonation structure

The chemical-kinetic description of hydrogen oxidation enables the structures of steady, planar ZND detonations to be calculated by forward integration along the Rayleigh line from the lead shock [66]. Mach numbers are everywhere high enough that molecular transport effects are sufficiently small to be negligible, so that reactive Euler equations are sufficient for describing these planar (as well as multidimensional) detonation structures, and the more complicated Navier–Stokes equations need not be used behind the shock. Representative results from such computations are shown in Fig. 28 [50]. The figure illustrates clearly the generally prevalent existence of an induction region, in this case extending slightly beyond 0.1 mm, where reactant concentrations remain essentially

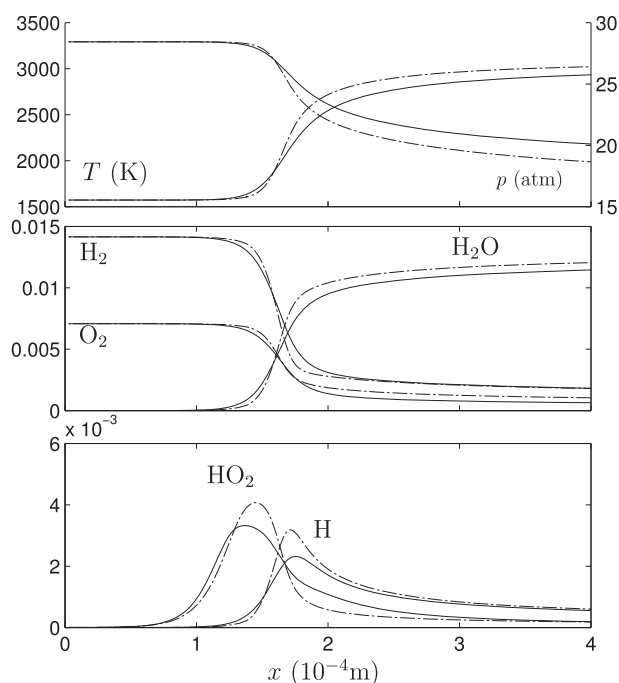


**Fig. 28.** The variation with the distance from the shock  $x$  of the pressure, temperature and species mole fractions in a Chapman–Jouguet detonation propagating in a stoichiometric  $\text{H}_2$ –air mixture initially at  $p = 1$  atm and  $T = 300$  K as obtained with the detailed chemistry of Table 1 (solid curves) and with a 3-step reduced mechanism (dash–dotted curves) [50].

constant as radicals buildup, followed by a region of heat release, of comparable or slightly less thickness, tailing off with decreasing rates of radical recombination over appreciable distances.

The solid curves in Fig. 28, obtained from the detailed mechanism of Table 1, differ very little from predictions obtained using the 12-step mechanism of Table 2. The dash–dot curves are the predictions of the three-step reduced mechanism shown in Eq. (12), including a correction for the branching rate [50]. This reduced chemistry is seen here to provide the induction length quite accurately and radical concentrations within about 20 percent. These last differences are due to the introduction of the steady-state approximations for O and OH. Also, since O and OH are present at equilibrium in non-negligible amounts, errors on the order of 5% appear in the final values of the temperature and pressure when these two species are not taken into account in the overall energy balance, as occurs when the reduced chemistry is used. This is a drawback of explicitly reduced chemistry; the selected subset of radicals has an impact in the evaluation of enthalpies, and thus it affects the thermodynamics, especially at high temperatures, where dissociation into radicals becomes of quantitative importance. The Chapman–Jouguet conditions selected for the figure are those for the reduced chemistry, which differ little from those with detailed chemistry, giving different propagation velocities, for example, but those differences are very small, less than 2 m/s, the value with detailed chemistry being approximately 2000 m/s, as seen in Fig. 27.

In the illustration in Fig. 28, the gas velocity with respect to the shock, at the position immediately behind the leading shock (termed the Neumann state, the high pressure there representing the Neumann spike), is about 360 m/s (at a Mach number around 0.4), and the figure suggests that the average gas properties change very little from this point to the end of the induction zone. The velocity therefore remains practically constant throughout the induction region, enabling the theory of isothermal, isobaric

branched-chain explosions to be employed there with good accuracy, so that Eq. (36), modified as indicated after Eq. (39) for stoichiometric or lean conditions, can be used to estimate the induction time, from which the length of the induction zone is obtained by simply multiplying this induction time by the velocity at the Neumann state. This simplification, replacing the more complicated integration along the Rayleigh line by use of a specific formula, applies quite generally to such detonation-structure problems, while the appreciable property changes that occur after that necessitate use of the Rayleigh-line integration subsequently, if the complete structure is to be obtained. Although simplified approximations can be introduced for the structure of the heat-release region that follows the induction zone, Rayleigh-line integrations are needed in order to obtain accurate results.

There is, however, a significant difficulty in applying the chemistry of Table 1 to the induction zone in the case selected here for illustration. The ratio of the induction length to the Neumann-state velocity for this example is about  $0.3 \mu\text{s}$ , which is of the same order of magnitude as, or shorter than, typical vibrational relaxation times for the leading shock wave. An approximation underlying all classical chemical-kinetic rate expressions is the assumption of translational, rotational, and vibrational equilibrium of the reacting molecules. This assumption ceases to apply for vibrational modes at such short times. For such rapid processes it becomes necessary, in principle, to treat each vibrational state of each molecule as a separate species and to introduce different reaction-rate expressions for each state, as well as adding to the chemical-kinetic description new rate expressions for changes in vibrational states. While this may appear to lead to hopeless complexity, some progress in this direction has, in fact, been made [355–358]. For practical purposes, however, a simpler procedure most likely is more desirable.

One approach would be to calculate vibrational relaxation times and compare them with induction times obtained with the rate parameters from Table 1, and when the vibrational relaxation times are found to be comparable with or shorter than the calculated induction time, employ the relaxation time as the induction time, on the grounds that the chain-branching chemistry is so fast under those conditions that vibrational relaxation is controlling. This simplified approach focuses attention on studying processes of vibrational relaxation, especially for key species, such as hydrogen, oxygen, and nitrogen. An appreciable amount of information is available concerning vibrational relaxation [157], including the classical general Landau–Teller expression for the rate, as well as both experimental and theoretical data on rate parameters for oxygen and nitrogen, that acquisition motivated, for example, by the fact that they are the main components of air and therefore are relevant to problems such as those of hypersonic re-entry.

Relaxation data for hydrogen, however, are largely lacking, and this is of major importance in detonation applications, especially because its presence has been found to accelerate appreciably the relaxation rates of those other species, so that hydrogen may become the slowest to relax. In a first approximation, then, one approach would be to simply employ the vibrational relaxation rate of pure diatomic hydrogen whenever it is shorter than the calculated induction time. For this purpose, the natural logarithm of the product of the hydrogen relaxation time (in s) and pressure (in atm) can be expressed as  $80T^{-1/3} - 20$  [359], with  $T$  in K, derived from measurements [360], based on the Landau–Teller form. It must be emphasized, however, that this suggestion is very speculative and is unlikely to apply with different inerts, not giving correct dependences on mixture composition. In using such a rough approach, all species probably would best be approximated as relaxing in the same way, at the same rate, and, moreover, the lead shock should be considered to be vibrationally frozen, resulting in a

higher temperature at the Neumann state (which, helpfully, would lead to an increased relaxation rate). Since it is entirely unclear how good such an approximation may be, the need for additional measurements of vibrational relaxation rates in hydrogen–oxygen–nitrogen mixtures is strongly underscored by these observations. This effect is mainly important in the more energetic mixtures and with initial pressures being near atmospheric or above; at sufficiently low pressures, or for weak mixtures, the induction times are longer, so that vibrational relaxation probably does not come into play.

#### 8.4. Mechanisms of instability of planar detonations

A further complication is that, except for strongly overdriven detonations, the steady, planar structures are unstable. This has been well known experimentally since the 1960's [349], and continuing research has increasingly clarified the origins of the instability (see, e.g. Ref. [361], and references therein). For example, a perturbation that intensifies the lead shock increases the temperature at the Neumann state, which increases the reaction rate in the induction zone as the gas moves downstream at the local flow velocity (creating what has been called an entropy wave), thereby shortening the induction zone and causing the beginning of the heat release to move upstream. This upstream movement of the onset of heat release acts like a piston, which generates an upstream-propagating acoustic wave that, in turn, strengthens the shock further when it reaches it, thereby intensifying the initial perturbation to the lead shock [362–364]. The consequent feedback is the source of planar oscillations, the period being the transit time of the entropy wave (the induction time) plus the (generally shorter) transit time of the returning acoustic wave. This instability (often called a galloping detonation) occurs when the induction time is sufficiently sensitive to temperature, which it practically always is; simple estimates of the necessary conditions are available in terms of empirical overall rate parameters [66,365]. It is worth mentioning that, for the specific case of hydrogen–air mixtures, theoretical analyses of galloping detonations based on different variants of the Zeldovich chemistry [366,367] are seen to reproduce successfully many of the stability characteristics observed in computations employing detailed chemistry [368], including in particular the existence of two pulsating modes of markedly different frequency.

The instabilities observed experimentally for hydrogen in the 1960's were, however, not of this planar-pulsation type, but instead they were more complex multidimensional instabilities. It was known already from model analytical and computational investigations of Erpenbeck [369–372] that, even when the heat release in a detonation is small compared with the initial thermal enthalpy, and, moreover, even with rates insensitive to temperature, planar detonations are unstable to two-dimensional disturbances by a mechanism involving a third type of wave, a vorticity wave. The vorticity wave, like the entropy wave, travels downstream at the local gas velocity, and its influence on the heat release affects the aforementioned upstream-propagating acoustic wave that interacts with the shock, now in such a way as to amplify the non-planar shape that initially generated the vorticity wave [373–375]. A weakly nonlinear bifurcation analysis of this two-dimensional amplification mechanism with one-step model chemistry [376] has shown that this instability evolves into the diamond patterns illustrated in Fig. 29, where the curved vertical lines represent a sequence of shock shapes traveling to the right, the gray diamond indicating the path of a triple point between an incident and Mach-reflected shock, the weaker third shock that extends towards the left not appearing. Since this instability occurs for detonations that are even too mild to exhibit the pulsating

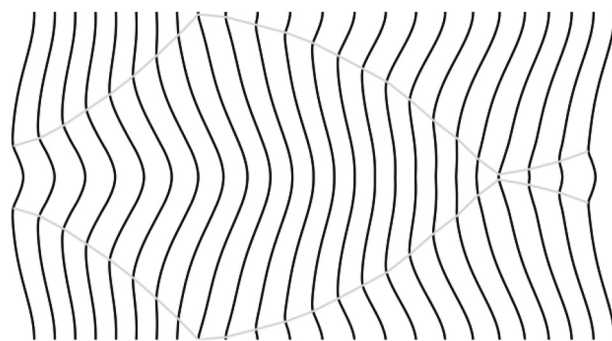


Fig. 29. A sequence of shapes of the lead shock computed from a weakly nonlinear theory [376], with the resulting predicted smoked-foiled diamond pattern outlined.

instability, it is much more prevalent experimentally, leading to what is now called cellular detonation.

We now realize that the vast majority of hydrogen detonations are cellular. This does not mean that the steady, planar hydrogen detonation structure is without interest; on the contrary, that structure must be understood in order to understand in detail the cellular detonation structure. The real-world triple-point interactions clearly exhibit not only effects of the vorticity waves but also influences of the strong sensitivity to temperature for the length of the induction zone. This leads, for example, to differences between the structures of the Mach-reflected shock (the strongest of the three) and the weaker transverse reflected shock trailing behind it, with characteristics of the shear layer between the two and of associated interactions clarified further in more recent detailed experiments [377]. Pressures are highest at the triple point, a result of which is that detonation passage leaves marks on smoked-foil walls that enable cell shapes and sizes to be measured readily. The cellular structures that are observed vary appreciably with conditions. For example, at low pressures and high dilution, with nitrogen replaced by argon as the diluent, the cells are very regular and are shaped very much like the diamonds in Fig. 29. They are less regular with nitrogen and become very irregular at low dilution, approaching purely hydrogen–oxygen mixtures, for example. The reasons underlying these variations are not well understood and are in need of further study. The cell sizes, in general, decrease with increasing pressure, being approximately proportional to the induction length of the planar detonation. Consideration of the oscillation period determined by propagation of the entropy and acoustic waves leads to an estimated longitudinal cell length of about 13 induction lengths, in rough agreement with observations, but this does not help to explain the irregularities.

Most computational studies of multidimensional hydrogen detonation structures have employed simplified chemical kinetics, such as one-step Arrhenius descriptions, with rate parameters adjusted empirically to fit various data, for instance on autoignition times. Only recently have computational capabilities progressed to a point at which detailed chemistry, such as that in Table 1, can be employed numerically. The reduced chemistry that has been presented earlier could profitably be used in these multidimensional computational investigations, but that has not yet been done. Time-dependent, two-dimensional computations with detailed chemistry for stoichiometric mixtures with argon dilution at reduced pressures showed regular cell structures in reasonable agreement with experiment, but corresponding recent computations for air at normal atmospheric pressure produced large disagreements with experiments, resulting in predicted representative cell sizes up to an order of magnitude smaller than observed [378]. The most likely reason for this disagreement was indicated to be that the detailed



chemistry predicted induction lengths that were too short because of the neglect of vibrational relaxation, as discussed above. This further indicates the desirability of improving descriptions of vibrational relaxation. It would be worthwhile to work towards incorporating such improvements in readily manageable reaction-rate tables by extending the available simplified chemical-kinetic descriptions like those given in Table 2 to include these relaxation effects.

## 9. Applications, outstanding problems, and future prospects for hydrogen utilization

The applications of the material that have been reviewed here are to be found wherever gas-phase oxidation of hydrogen occurs. This includes accident scenarios, irrespective of the ultimate intended hydrogen application, whence the information clearly is relevant to hydrogen safety. In addition, there is evident relevance to power-production and propulsion applications involving energy release through hydrogen combustion.

The extensive recent progress that has been summarized demonstrates that, in many respects, the necessary understanding, the knowledge about flammability, and the formulations needed for efficient computation of newly considered situations are now complete. Many areas have, however, been indicated above to be in need of further study, including reaction-rate parameters of certain elementary steps (mostly steps of lesser importance), effects of vibrational relaxation on the chemistry, transport-property descriptions at very high pressures, and a number of high-pressure deflagration and detonation phenomena.

More specifically, concerning the chemistry, while the hydrogen–oxygen branching reactions in the shuffle steps seem now to be in reasonably good shape, more work is needed on elementary rates in the hydroperoxyl chemistry, such as improving descriptions of chaperon efficiencies in different mixtures for its  $\text{H} + \text{O}_2 + \text{M} \rightleftharpoons \text{HO}_2 + \text{M}$  formation step, and better determining the rate of the important step  $\text{HO}_2 + \text{H} \rightleftharpoons \text{OH} + \text{OH}$  as a function of temperature. It would also be prudent to verify that the direct recombination step  $\text{O} + \text{OH} + \text{M} \rightleftharpoons \text{HO}_2 + \text{M}$  is unimportant by measuring its rate. Rates of H-atom attack on hydrogen peroxide, notably  $\text{H}_2\text{O}_2 + \text{H} \rightleftharpoons \text{HO}_2 + \text{H}_2$  at high temperature also require more experiments. Finally, in connection with detonation problems, there is a strong need for clarifying the influences of vibrational relaxation rates; it would be ideal if a relaxation step or two could be added to Table 1 to enable it to be used in calculations of hydrogen–oxygen detonations for systems initially at or above normal atmospheric pressures. Concerning reduced mechanisms, a better skeletal mechanism would be desirable for high-pressure, fuel-rich deflagrations, while further systematic reductions, beyond the skeletal stage, through steady-state approximations, seem now to have been carried about as far as is reasonable for most applications.

A number of difficulties remain at high pressures, of special importance in energy and propulsion applications. Agreements between computed and measured combustion behaviors in premixed systems, as well as high-pressure diffusion-flame extinction conditions, are not very good, and it is not entirely clear where the difficulties lie. These problems may again involve the chemistry, since different chemical mechanisms often tend to give significantly different predictions at high pressures. On the other hand, there are also uncertainties in high-pressure transport properties that deserve attention. Accuracies of procedures for calculating coefficients of viscosity and of thermal conductivity are in question, especially concerning their dependence on hydrogen mixture compositions, and improved experimental and computational methods for determining coefficients of thermal diffusion would be

desirable for hydrogen atoms and molecules. Transitions from deflagration to detonation and possible interactions between vorticity waves and entropy waves in detonations are complex issues that are not well understood. At very high pressures, as in rocket-motor chambers, even fundamental equations of state become of uncertain accuracy, although there is some indication that this may not be of critical importance in predictions of quantities of interest.

A number of specific outstanding hydrogen-combustion problems are now ripe for theoretical and numerical attack. For example, the new results for hydrogen mass consumption rates, as in Eq. (96), are ready to be used in studies of diffusive-thermal instabilities of hydrogen flames and of associated dynamics, as well as in investigating influences of strain and curvature on hydrogen flames, further clarifying cellular-flame phenomena. In addition, for fuel-lean, near-limit hydrogen flames, an accurate one-step chemistry description is now available for use in future analytical and numerical investigations. The opposite limit, fuel-rich hydrogen flames, which tend to support pulsating instabilities, have been given comparatively little analytical study by asymptotic methods, and understanding of their behavior might be improved by further investigations of this kind. In addition, concerning flame stabilization, there is a lack of numerical studies of hydrogen diffusion-flame attachment to orifices and of triple flame propagation in nonuniform environments, which could be based on the mathematical formulations derived earlier for these problems [295,299,314], appropriately buttressed by the updated transport and chemistry descriptions described in this paper. Finally, analyses of acoustic responses and acoustic amplification by diffusion flames, employing asymptotic descriptions of hydrogen chemistry, have not been addressed but are ready to be pursued, with relevance to liquid-propellant rocket instabilities.

Also concerning diffusion-flame attachment, experimental investigations would be worthwhile to test numerical predictions, including measurements of edge-flame propagation rates in strained mixing layers of the type already available for methane and propane [379]. In addition, detailed experimental measurements of deflagration structures would be worthwhile, to test the current predicted results. On-going investigations of ultra-lean hydrogen–oxygen deflagrations in Hele-Shaw cells can be of interest in exploring effects of competing instabilities on flame structure and propagation [380]. Further experiments on hydrogen flame balls would also be quite interesting, for better testing predictions and improving understanding, notably concerning flammability limits, but they would require microgravity platforms, such as the International Space Station. There is a clear lack of good, believable, experimental information on low-temperature ignition times in hydrogen mixtures, although it is currently unclear how such data could be acquired. Additional experimental knowledge of hydrogen–air ignition in supersonic flows would also be worth exploring, in connection with applications to supersonic combustion. There thus are a number of desirable opportunities for important future experimental contributions to our understanding of hydrogen combustion.

With these various future needs and exceptions, then, we now have a good background for addressing the flammability behavior of hydrogen. The question, after observing that, becomes one of ascertaining how important all of the currently available information will be in the future. More generally, will hydrogen play an increasing or decreasing role in society?

In addressing the question of how much attention will be paid to the preceding information in the future, it may be observed that current indications in every sector of the economy point towards the increasing importance of hydrogen. With the increasing emphasis on renewable fuels, consideration of utilization of

hydrogen continually arises in many different ways. For instance, nuclear energy plants are convenient places to produce hydrogen as an energy carrier, so that, if pressures to decrease usage of fossil fuels turn towards nuclear energy (as many environmentalists are beginning to favor), the role of hydrogen is likely to increase. Also, in efforts to reduce greenhouse gases, for example, syngas production from coal is increasingly under consideration, and gas-turbine manufacturers are more and more interested in being able to add hydrogen to natural gas, so that understanding of hydrogen combustion in concert with other fuels is becoming increasingly important. It is true that most of the methods envisioned to increase future use of hydrogen for energy production consider fuel cells and other processes that do not involve combustion, but their growth increases concerns about hydrogen safety, thereby generating associated safety programs, such as those which now exist in Europe and elsewhere. Moreover, in evaluating technologies for hydrogen utilization that do not involve combustion, it is always important to keep in mind the fact that direct combustion is an option and therefore should be compared with the alternative approaches.

The growth of the multidisciplinary International Journal of Hydrogen Energy can be considered to be a measure of the evolution of the world-wide interest in a hydrogen economy. While this journal addresses all aspects of hydrogen energy, combustion of hydrogen occupies perhaps twenty percent of the material published, generally to be found towards the end of each issue, for example in sections identified as engines, combustion, or safety. The journal began in 1976 as about a 400-page quarterly and expanded to monthly in 1985, with about 800 pages per year. In 1995 there still were only about 1000 pages per year, indicating a slow decade of growth, but the interest apparently exploded after that. In 2008, the publication increases to 24 issues per year, and in the year 2012 nearly 20,000 pages in total were published. This surely attests to the favorable future prospects for hydrogen utilization and the associated importance of knowledge and understanding of hydrogen combustion processes.

## Acknowledgments

Much of our understanding of hydrogen combustion has developed over the past twenty years through numerous scientific conversations with Amable Liñán. His insight has guided many of the physical arguments that serve to explain in this paper the features of hydrogen combustion. Our collaborators Priyank Saxena, Eduardo Fernández-Tarrazo, Pierre Boivin, Carmen Jiménez, and Daniel Fernández-Galisteo are also gratefully acknowledged for providing assistance with numerical computations and figures. In particular, some of the new rate parameters in Tables 1 and 2 are due to Priyank. This work was supported by the US AFOSR Grant #FA9550-12-1-0138 and by the Comunidad de Madrid through project #P2009/ENE-1597. Partial support from the Spanish MCINN through project #CSD2010-00011 is also acknowledged.

## References

- [1] Hinshelwood CN, Williamson AT. The reaction between hydrogen and oxygen. Oxford: Clarendon Press; 1934.
- [2] Semenov NN. Chemical kinetics and chain reactions. Oxford: Clarendon Press; 1935.
- [3] Li J, Zhao Z, Kazakov A, Dryer FL. An updated comprehensive kinetic model of hydrogen combustion. *Int J Chem Kinet* 2004;36:566–75.
- [4] Conaire MÓ, Curran HJ, Simmie JM, Pitz WJ, Westbrook CK. A comprehensive modeling study of hydrogen oxidation. *Int J Chem Kinet* 2004;36:603–22.
- [5] Konnov AA. Remaining uncertainties in the kinetic mechanism of hydrogen combustion. *Combust Flame* 2008;152:507–28.
- [6] Shimizu K, Hibi A, Koshi M, Morii Y, Tsuboi N. Updated kinetic mechanism for high-pressure hydrogen combustion. *J Propuls Power* 2011;27:383–95.
- [7] Hong Z, Davidson DF, Hanson RK. An improved  $H_2/O_2$  mechanism based on recent shock tube/laser absorption measurements. *Combust Flame* 2011;158:633–44.
- [8] Burke MP, Chaos M, Ju Y, Dryer FL, Klippenstein SJ. Comprehensive  $H_2/O_2$  kinetic model for high-pressure combustion. *Int J Chem Kinet* 2012;44:444–74.
- [9] Davis SG, Joshi AV, Wang H, Egolfopoulos F. An optimized kinetic model of  $H_2/CO$  combustion. *Proc Combust Inst* 2005;30:1283–92.
- [10] Saxena P, Williams FA. Testing a small detailed chemical-kinetic mechanism for the combustion of hydrogen and carbon monoxide. *Combust Flame* 2006;145:316–23. accessible online from: <http://web.eng.ucsd.edu/mae/groups/combustion/mechanism.html>.
- [11] Sun H, Yang SI, Jomaas G, Law CK. High-pressure laminar flame speeds and kinetic modeling of carbon monoxide/hydrogen combustion. *Proc Combust Inst* 2007;31:439–46.
- [12] Kéromnès A, Metcalfe WK, Heufer KA, Donohoe N, Das AK, Sung C-J, et al. An experimental and detailed chemical kinetic modeling study of hydrogen and syngas mixture oxidation at elevated pressures. *Combust Flame* 2013;160:995–1011.
- [13] Ströhle J, Myhrvold T. An evaluation of detailed mechanisms for hydrogen combustion under gas turbine conditions. *Int J Hydrog Energy* 2007;32:125–35.
- [14] Weydahl T, Poyyapakkam M, Seljeskog M, Haugen NEL. Assessment of existing  $H_2/O_2$  chemical reaction mechanisms at reheat gas turbine conditions. *Int J Hydrog Energy* 2011;36:12025–34.
- [15] Stanković I, Merci B. Analysis of auto-ignition of heated hydrogen-air mixtures with different detailed mechanisms. *Combust Theor Model* 2011;15:409–36.
- [16] Baulch DL, Bowman CT, Cobos CJ, Cox RA, Just Th, Kerr JA, et al. Evaluated kinetic data for combustion modeling: supplement II. *J Phys Chem Ref Data* 2005;34:757–1397.
- [17] Niemann U, Seshadri K, Williams FA. Effect of pressure on structure and extinction of near-limit hydrogen counterflow flames. *Proc Combust Inst* 2013;34:881–6.
- [18] Seshadri K, Peters N, Williams FA. Asymptotic analyses of stoichiometric and lean hydrogen-air flames. *Combust Flame* 1994;96:407–27.
- [19] Fernández-Galisteo D, Sánchez AL, Liñán A, Williams FA. One-step reduced kinetics for lean hydrogen-air deflagration. *Combust Flame* 2009;156:985–96.
- [20] Masten DA, Hanson RK, Bowman CT. Shock tube study of the reaction  $H + O_2 \rightarrow OH + O$  using laser absorption. *J Phys Chem* 1990;94:7119–28.
- [21] Hong Z, Davidson DF, Barbour EA, Hanson RK. A new shock tube study of the  $H + O_2 \rightarrow OH + O$  reaction rate using tunable diode laser absorption of  $H_2O$  near 2.5  $\mu m$ . *Proc Combust Inst* 2011;33:309–16.
- [22] Hwang SM, Ryu Si-Ok, De Witt KJ, Rabinowitz MJ. High temperature rate coefficient measurements of  $H + O_2$  chain-branching and chain-terminating reaction. *Chem Phys Lett* 2005;408:107–11.
- [23] Pirraglia AN, Michael JV, Sutherland JW, Klemm RB. A flash photolysis-shock tube kinetic study of the H atom reaction with  $O_2$ :  $H + O_2 \rightleftharpoons OH + O$  ( $962 K \leq T \leq 1705 K$ ) and  $H + O_2 + Ar \rightarrow HO_2 + Ar$  ( $746 K \leq T \leq 987 K$ ). *J Phys Chem* 1989;93:282–91.
- [24] Yetter RA, Dryer FL, Rabitz H. A comprehensive reaction mechanism for carbon monoxide/hydrogen/oxygen kinetics. *Combust Sci Technol* 1991;79:97–128.
- [25] Smooke MD, Giovangigli V. Formulation of the premixed and nonpremixed test problems. In: Smooke M, editor. *Reduced kinetic mechanisms and asymptotic approximations for methane-air flames*. Berlin: Springer-Verlag; 1991. pp. 1–28.
- [26] Fernández-Galisteo D, Sánchez AL, Liñán A, Williams FA. The hydrogen-air burning rate near the lean flammability limit. *Combust Theor Model* 2009;13:741–61.
- [27] Sánchez AL, Liñán A, Williams FA. A generalized Burke-Schumann formulation for hydrogen-oxygen diffusion flames maintaining partial equilibrium of the shuffle reactions. *Combust Sci Technol* 1997;123:317–45.
- [28] Troe J. Detailed modeling of the temperature and pressure dependence of the reaction  $H + O_2 (+M) \rightarrow HO_2 (+M)$ . *Proc Combust Inst* 2000;28:1463–9.
- [29] Bates RW, Golden DM, Hanson RK, Bowman CT. Experimental study and modeling of the reaction  $H + O_2 + M \rightarrow HO_2 + M$  ( $M = Ar, N_2, H_2O$ ) at elevated pressures and temperatures between 1050 and 1250 K. *Phys Chem Chem Phys* 2001;3:2337–42.
- [30] Michael JV, Su M-C, Sutherland JW, Carrol JJ, Wagner AF. Rate constant for  $H + O_2 + M \rightarrow HO_2 + M$  in seven bath gases. *J Phys Chem A* 2002;106:5297–313.
- [31] Baulch DL, Cobos CJ, Cox RA, Esser C, Frank P, Just Th, et al. Evaluated kinetic data for combustion modelling. *J Phys Chem Ref Data* 1992;21:411–734.
- [32] Mueller MA, Kim TJ, Yetter RA, Dryer FL. Flow reactor studies and kinetic modeling of the  $H_2/O_2$  reaction. *Int J Chem Kinet* 1999;31:113–25.
- [33] Michael JV, Sutherland JW, Harding LB, Wagner AF. Initiation in  $H_2/O_2$ : rate constants for  $H_2 + O_2 \rightarrow H + H_2O$  at high temperature. *Proc Combust Inst* 2000;28:1471–8.
- [34] del Álamo G, Williams FA, Sánchez AL. Hydrogen-oxygen induction times at temperatures above crossover. *Combust Sci Technol* 2004;176:1599–626.
- [35] Warnatz J. Survey of rate coefficients in the C/H/O system. In: Gardiner WC, editor. *Combustion chemistry*. Berlin: Springer-Verlag; 1984. pp. 197–360.
- [36] Hippler H, Neubauer H, Troe J. Shock wave studies of the reactions  $HO + H_2O_2 \rightarrow H_2O + HO_2$  and  $HO + HO_2 \rightarrow H_2O + O_2$  between 930 and 1680 K. *J Chem Phys* 1995;103:3510–6.
- [37] Kappel Ch, Luther K, Troe J. Shock wave study of the unimolecular dissociation of  $H_2O_2$  in its falloff range and of its secondary reactions. *Phys Chem Chem Phys* 2002;4:4392–8.

- [38] Hong Z, Vasu SS, Davidson DF, Hanson RK. Experimental study of the rate of  $\text{OH} + \text{HO}_2 \rightarrow \text{H}_2\text{O} + \text{O}_2$  at high temperatures using the reverse reaction. *J Phys Chem* 2010;114:5520–5.
- [39] Hong Z, Lam KY, Sur R, Wang S, Davidson DF, Hanson RK. On the rate constants of  $\text{OH} + \text{HO}_2 \rightarrow \text{H}_2\text{O} + \text{O}_2$ : a comprehensive study of  $\text{H}_2\text{O}_2$  thermal decomposition using multi-species laser absorption. *Proc Combust Inst* 2013;34:565–71.
- [40] Sivaramakrishnan R, Comandini A, Tranter RS, Brezinsky K, Davis SG, Wang H. Combustion of  $\text{CO}/\text{H}_2$  mixtures at elevated pressures. *Proc Combust Inst* 2007;31:429–37.
- [41] Burke MP, Klippenstein SJ, Harding LB. A quantitative explanation for the apparent anomalous temperature dependence of  $\text{OH} + \text{HO}_2 \rightarrow \text{H}_2\text{O} + \text{O}_2$  through multi-scale modeling. *Proc Combust Inst* 2013;34:547–55.
- [42] Srinivasan NK, Michael JV. The thermal decomposition of water. *Int J Chem Kinet* 2006;38:211–9.
- [43] Troe J, Ushakov VG. SACM/CT study of the dissociation/recombination dynamics of hydrogen peroxide on an *ab initio* potential energy surface Part II. Specific rate constants  $k(E_f)$ , thermal rate constants  $k_\infty(T)$ , and lifetime distributions. *Phys Chem Chem Phys* 2008;10:3915–24.
- [44] Troe J. The thermal dissociation/recombination reaction of hydrogen peroxide  $\text{H}_2\text{O}_2(+\text{M}) \rightleftharpoons 2\text{OH}(+\text{M})$  III. Analysis and representation of the temperature and pressure dependence over wide ranges. *Combust Flame* 2011;158:594–601.
- [45] Hippler H, Troe J, Willner J. Shock wave study of the reaction  $\text{HO}_2 + \text{HO}_2 \rightarrow \text{H}_2\text{O}_2 + \text{O}_2$ : confirmation of a rate constant minimum near 700 K. *J Chem Phys* 1990;93:1755–60.
- [46] Lee D, Hochgreb S. Hydrogen autoignition at pressures above the second explosion limit (0.6–4.0 MPa). *Int J Chem Kinet* 1998;30:385–406.
- [47] Tsang W, Hampson RF. Chemical kinetic data base for combustion chemistry. Part 1. Methane and related compounds. *J Phys Chem Ref Data* 1986;15:1087–279.
- [48] Baldwin RR, Brattan D, Tunncliffe B, Walker RW, Webster SJ. The hydrogen-sensitized decomposition of hydrogen peroxyde. *Combust Flame* 1970;15:133–42.
- [49] Hong Z, Cook RD, Davidson DF, Hanson RK. A shock tube study of the  $\text{OH} + \text{H}_2\text{O}_2 \rightarrow \text{H}_2\text{O} + \text{HO}_2$  and  $\text{H}_2\text{O}_2 + \text{M} \rightarrow 2\text{OH} + \text{M}$  using laser absorption of  $\text{H}_2\text{O}$  and  $\text{OH}$ . *J Phys Chem* 2010;114:5718–27.
- [50] Boivin P, Sánchez AL, Williams FA. Four-step and three-step systematically reduced chemistry for wide-range  $\text{H}_2$ -air combustion problems. *Combust Flame* 2013;160:76–82.
- [51] Boivin P, Jiménez C, Sánchez AL, Williams FA. An explicit reduced mechanism for  $\text{H}_2$ -air combustion. *Proc Combust Inst* 2011;33:517–23.
- [52] Boivin P, Sánchez AL, Williams FA. Explicit analytic prediction for hydrogen-oxygen ignition times at temperatures below crossover. *Combust Flame* 2012;159:748–52.
- [53] Strföle J, Myhrvold T. Reduction of a detailed reaction mechanism for hydrogen combustion under gas turbine conditions. *Combust Flame* 2006;144:545–57.
- [54] Griffiths JF. Reduced kinetic models and their application to practical combustion systems. *Prog Energy Combust Sci* 1995;21:25–107.
- [55] Lu T, Law CK. Toward accommodating realistic fuel chemistry in large-scale computations. *Prog Energy Combust Sci* 2009;35:192–215.
- [56] Pope S. Computationally efficient implementation of combustion chemistry using in situ adaptive tabulation. *Combust Theor Model* 1997;1:41–63.
- [57] Cicquel O, Darabiha N, Thévenin D. Laminar premixed hydrogen/air counterflow flame simulations using flame prolongation of ILDM with differential diffusion. *Proc Combust Inst* 2000;28:1901–8.
- [58] Oijen JV, Goey LD. Modelling of premixed laminar flames using flamelet-generated manifolds. *Combust Sci Technol* 2000;161:113–37.
- [59] Lam SH, Goussis D. Understanding complex chemical kinetics with computational singular perturbation. *Proc Combust Inst* 1989;22:931–41.
- [60] Lam SH, Goussis D. Conventional asymptotics and computational singular perturbation for simplified kinetics modeling. In: Smooke M, editor. *Reduced kinetic mechanisms and asymptotic approximations for methane-air flames*. Berlin: Springer-Verlag; 1991. pp. 227–42.
- [61] Lam SH, Goussis D. The CSP method for simplifying kinetics. *Int J Chem Kinet* 1994;26:461–86.
- [62] Maas U, Pope S. Simplifying chemical kinetics: intrinsic low-dimensional manifolds in composition space. *Combust Flame* 1992;88:239–64.
- [63] Keck JC. Rate-controlled constrained-equilibrium theory of chemical reactions in complex systems. *Prog Energy Combust Sci* 1990;16:125–54.
- [64] Keck JC, Gillespie D. Rate-controlled partial-equilibrium method for treating reacting gas mixtures. *Combust Flame* 1971;17:237–41.
- [65] Jones W, Rigopoulos S. Rate-controlled constrained equilibrium: formulation and application to nonpremixed laminar flames. *Combust Flame* 2005;142:223–34.
- [66] Williams FA. *Combustion theory*. 2nd ed. Menlo Park, CA: Benjamin Cummings; 1985.
- [67] Janicka J, Kollmann W. A two-variables formalism for the treatment of chemical reactions in turbulent  $\text{H}_2$ -air diffusion flames. *Proc Combust Inst* 1979;1979(17):421–30.
- [68] Mauss F, Peters N, Rogg B, Williams FA. Reduced kinetic mechanisms for premixed hydrogen flames. In: Peters N, Rogg B, editors. *Reduced kinetic mechanisms for applications in combustion systems*. Heidelberg: Springer-Verlag; 1993. pp. 29–43.
- [69] He L, Clavin P. Premixed hydrogen-oxygen flames. Part I: flame structure near the flammability limits. *Combust Flame* 1993;93:391–407.
- [70] Fernández-Tarrazo E, Sánchez AL, Liñán A, Williams FA. The structure of lean hydrogen-air flame balls. *Proc Combust Inst* 2011;33:1203–10.
- [71] Fernández-Tarrazo E, Sánchez AL, Liñán A, Williams FA. Flammability conditions for ultra-lean hydrogen premixed combustion based on flame-ball analyses. *Int J Hydrog Energy* 2012;37:1813–25.
- [72] Treviño C. Ignition phenomena in  $\text{H}_2$ - $\text{O}_2$  mixtures. *Prog Astronaut Aeronaut* 1991;131:19–43.
- [73] Gutheil E, Balakrishnan G, Williams FA. Structure and extinction of hydrogen-air diffusion flames. In: Peters N, Rogg B, editors. *Reduced kinetic mechanisms for applications in combustion systems*. Heidelberg: Springer-Verlag; 1993. pp. 177–95.
- [74] Lee SR, Chung SH. On the structure of hydrogen diffusion flames with reduced kinetic mechanisms. *Combust Sci Technol* 1994;96:247–77.
- [75] Balakrishnan G, Smooke M, Williams FA. A numerical investigation of extinction and ignition limits in laminar nonpremixed counterflowing hydrogen-air streams for both elementary and reduced chemistry. *Combust Flame* 1995;102:329–40.
- [76] Thaker AA, Cheliah HK. Numerical prediction of oblique detonation wave structures using detailed and reduced mechanisms. *Combust Theor Model* 1997;1:347–76.
- [77] Williams FA. Detailed and reduced chemistry for hydrogen autoignition. *J Loss Prev Process Ind* 2008;21:131–5.
- [78] Brown NJ, Revzan KL. Comparative sensitivity analysis of transport properties and reaction rate coefficients. *Int J Chem Kinet* 2005;37:538–53.
- [79] Brown NJ, Bastien LAJ, Price PN. Transport properties for combustion modeling. *Prog Energy Combust Sci* 2011;37:565–82.
- [80] Hirschfelder JO, Curtis CF, Bird RB. *Molecular theory of gases and liquids*. New York: John Wiley & Sons; 1954.
- [81] Palle S, Nolan C, Miller RS. On molecular transport effects in real gas laminar diffusion flames at large pressure. *Phys Fluids* 2005;17:103601.
- [82] Palle S, Miller RS. Analysis of high-pressure hydrogen, methane, and heptane laminar diffusion flames: thermal diffusion factor modeling. *Combust Flame* 2007;151:581–600.
- [83] Ribert G, Zong N, Yang V, Pons L, Darabiha N, Candel S. Counterflow diffusion flames of general fluids: oxygen/hydrogen mixtures. *Combust Flame* 2008;154:319–30.
- [84] Calcote HF. Ion and electron profiles in flames. *Proc Combust Inst* 1963;9:622–37.
- [85] Lawton J, Weinberg FJ. *Electrical aspects of combustion*. Oxford: Clarendon Press; 1969.
- [86] Kee RJ, Dixon-Lewis G, Warnatz J, Coltrin ME, Miller JA. A Fortran computer code package for the evaluation of gas-phase, multi-component transport properties. Technical Report SAND86-8246. Sandia National Laboratories; 1986.
- [87] Paul PH. DRMF: a new package for the evaluation of gas-phase transport properties. Technical Report SAND98-8203. Sandia National Laboratories; 1997.
- [88] Dixon-Lewis G. Flame structure and flame reaction kinetics II. Transport phenomena in multicomponent systems. *Proc R Soc A* 1968;307:111–35.
- [89] Ern A, Giovangigli V. Multicomponent transport algorithms. In: *Lecture notes in physics*, vol. n24. Heidelberg, Germany: Springer; 1994.
- [90] Ern A, Giovangigli V. A multicomponent transport software for fast and accurate evaluation algorithms. Available from: <http://www.cmap.polytechnique.fr/www.eglib/>; 2004.
- [91] Waldmann L, Trübenbacher E. Formale kinetische theorie von gagemischen aus anregbaren molekülen. *Zeitschrift für Naturforschung A* 1962;17:363–76.
- [92] Ern A, Giovangigli V. Fast and accurate multicomponent transport property evaluation. *J Comput Phys* 1995;120:105–16.
- [93] Wangard III W, Dandy DS, Miller BJ. A numerically stable method for integration of the multicomponent species diffusion equations. *J Comput Phys* 2001;174:460–72.
- [94] Oran ES, Boris JP. Detailed modeling of combustion systems. *Prog Energy Combust Sci* 1981;7:1–71.
- [95] Fristrom RM, Monchick L. Two simple approximations to the thermal diffusion factor and their applications to flame studies. *Combust Flame* 1988;71:89–99.
- [96] Rosner DE, Israel RS, La Mantia B. “Heavy” species Ludwig-Soret transport effects in air-breathing combustion. *Combust Flame* 2000;123:547–60.
- [97] Ern A, Giovangigli V. Thermal diffusion effects in hydrogen-air and methane-air flames. *Combust Theor Model* 1998;2:349–72.
- [98] Smooke MD. The computation of laminar flames. *Proc Combust Inst* 2013;34:65–98.
- [99] Williams BA. Sensitivity of calculated extinction strain rate to molecular transport formulation in nonpremixed counterflow flames. *Combust Flame* 2001;124:330–3.
- [100] Dong Y, Holley AT, Andac MG, Egolfopoulos FN, Davis SG, Middha P, et al. Extinction of premixed  $\text{H}_2$ /air flames: chemical kinetics and molecular diffusion effects. *Combust Flame* 2005;142:374–87.
- [101] Bongers H, de Goey LPH. The effect of simplified transport modeling on the burning velocity of laminar premixed flames. *Combust Sci Technol* 2003;175:1915–28.
- [102] Sánchez AL, Balakrishnan G, Liñán A, Williams FA. Relationships between bifurcation and numerical analyses for ignition of hydrogen-air diffusion flames. *Combust Flame* 1996;105:569–90.



- [103] Fernández-Tarrazo E, Sánchez AL, Williams FA. Hydrogen-air mixing-layer ignition at temperatures below crossover. *Combust Flame* 2013;160:1981–9.
- [104] Lewis B, von Elbe G. Combustion, flames, and explosions of gases. 2nd ed. New York: Academic Press; 1961.
- [105] Middha P, Yang B, Wang H. A first-principle calculation of the binary diffusion coefficients pertinent to kinetic modeling of hydrogen/oxygen/helium flames. *Proc Combust Inst* 2002;29:1361–9.
- [106] Middha P, Wang H. First-principle calculation for the high-temperature diffusion coefficients of binary pairs: the H-Ar case. *Combust Theor Model* 2005;9:353–63.
- [107] Qiao L, Gu Y, Dahm WJA, Oran ES, Faeth GM. A study of the effects of diluents on near-limit H<sub>2</sub>-air flames in microgravity at normal and reduced pressures. *Combust Flame* 2007;151:196–208.
- [108] Andac MG, Egolfopoulos FN. Diffusion and kinetic effects on the ignition of premixed and non-premixed flames. *Proc Combust Inst* 2007;31:1165–72.
- [109] Esposito G, Sarnacki BG, Chelliah HK. Uncertainty propagation of chemical kinetics parameters and binary diffusion coefficients in predicting extinction limits of hydrogen/oxygen/nitrogen non-premixed flames. *Combust Theor Model* 2012;16:1029–52.
- [110] Assael MJ, Mixafendi S, Wakeham WA. The viscosity and thermal conductivity of normal hydrogen in the limit of zero density. *J Phys Chem Ref Data* 1986;15:1315–22.
- [111] Boushehri A, Bzowzski J, Kestin J, Mason EA. Equilibrium and transport properties of 11 polyatomic gases at low density. *J Phys Chem Ref Data* 1987;16:445–66.
- [112] Paul P, Warnatz J. A re-evaluation of the means used to calculate transport properties of reacting flows. *Proc Combust Inst* 1998;27:495–504.
- [113] Stallcop JR, Partidge H, Walch SP, Levin E. H–N<sub>2</sub> interaction energies, transport cross sections, and collision integrals. *J Chem Phys* 1992;97:3431–6.
- [114] Stallcop JR, Partidge H, Levin E. Effective potential energies and transport cross sections for interactions of hydrogen and nitrogen. *Phys Rev A* 2000;62:062709.
- [115] Dixon-Lewis G. Kinetic mechanism, structure and properties of premixed flames in hydrogen-oxygen-nitrogen mixtures. *Philos Trans R Soc Lond A* 1979;292:45–99.
- [116] Greenberg JB. On the prediction of thermal diffusion effects in laminar one-dimensional flames. *Combust Sci Technol* 1980;24:83–8.
- [117] García-Ybarra P, Clavin P. Cross-transport effects in nonadiabatic premixed flames. In: *Progress in astronautics and astronautics*, vol. 76. New York: American Institute of Aeronautics and Astronautics; 1981. pp. 463–81.
- [118] García-Ybarra P, Nicoli C, Clavin P. Soret and dilution effects on premixed flames. *Combust Sci Technol* 1984;42:87–109.
- [119] Ern A, Giovangigli V. Impact of detailed multicomponent transport on planar and counterflow hydrogen/air and methane/air flames. *Combust Sci Technol* 1999;149:157–81.
- [120] Libby P, Liñán A, Williams FA. Strained premixed laminar flames with non-unity Lewis numbers. *Combust Sci Technol* 1983;34:257–93.
- [121] Libby P, Williams FA. Strained premixed laminar flames with two reaction zones. *Combust Sci Technol* 1984;37:221–52.
- [122] Yang F, Law CK, Sung CJ, Zhang HQ. A mechanistic study of Soret diffusion in hydrogen-air flames. *Combust Flame* 2010;157:192–200.
- [123] Grcar JF, Bell JB, Day MS. The Soret effect in naturally propagating, premixed, lean, hydrogen-air flames. *Proc Combust Inst* 2009;32:1173–80.
- [124] García-Ybarra P, Treviño C. Analysis of the thermal diffusion effects on the ignition of hydrogen-air mixtures in the boundary layer of a hot flat plate. *Combust Flame* 1994;96:293–303.
- [125] Figueira da Silva LF, Deshaies B, Champion M. Boundary layer ignition of hydrogen-air mixtures in supersonic flows. *J Therm Sci* 1994;3:43–8.
- [126] Figueira da Silva LF, Deshaies B. The influence of equivalence ratio and Soret effect on the ignition of hydrogen-air mixtures in supersonic boundary layers. *Proc Combust Inst* 1994;25:29–36.
- [127] Kurdyumov V, Blasco J, Sánchez AL, Liñán A. On the calculation of the minimum ignition energy. *Combust Flame* 2004;136:394–7.
- [128] Hancock RD, Schauer FR, Lucht RP, Katta VR, Hsu KY. Thermal diffusion effects and vortex-flame interactions in hydrogen jet diffusion flames. *Proc Combust Inst* 1996;26:1087–93.
- [129] Arias-Zugasti M, Rosner DE. Soret transport, unequal diffusivity, and dilution effects on laminar diffusion flame temperatures and positions. *Combust Flame* 2008;153:33–44.
- [130] Briones A, Puri IK, Aggarwal SK. Effect of pressure on counterflow H<sub>2</sub>-air partially premixed flames. *Combust Flame* 2005;140:46–59.
- [131] Billet G, Giovangigli V, de Gassowski G. Impact of volume viscosity on a shock-hydrogen-bubble interaction. *Combust Theor Model* 2008;12:221–48.
- [132] Fru G, Janiga G, Thévenin D. Impact of volume viscosity on the structure of turbulent premixed flames in the thin reaction zone regime. *Flow Turbul Combust* 2012;88:451–78.
- [133] Ern A, Giovangigli V. Volume viscosity of dilute polyatomic gas mixtures. *Eur J Mech B Fluids* 1995;14:653–69.
- [134] Wilke CR. A viscosity equation for gas mixtures. *J Chem Phys* 1950;18:517–9.
- [135] Hirschfelder JO. Heat conductivity in polyatomic, electronically excited, or chemically reacting mixtures. III. *Proc Combust Inst* 1957;6:351–66.
- [136] Eric L, Petersen EL, Kalitan DM, Barrett AB, Reehal SC, Mertens JD, et al. New syngas/air ignition data at lower temperature and elevated pressure and comparison to current kinetics models. *Combust Flame* 2007;149:244–7.
- [137] Dryer FL, Chaos M. Ignition of syngas/air and hydrogen/air mixtures at low temperatures and high pressures: experimental data interpretation and kinetic modeling implications. *Combust Flame* 2008;152:293–9.
- [138] Medvedev SP, Agafonov GL, Khomik SV, Gelfand BE. Ignition delay in hydrogen-air and syngas-air mixtures: experimental data interpretation via flame propagation. *Combust Flame* 2010;157:1436–8.
- [139] von Elbe G, Lewis B. The reaction between hydrogen and oxygen above the upper explosion limit. *J Am Chem Soc* 1937;59:656–62.
- [140] Urzay J, Kseib N, Davidson DF, Iaccarino G, Hanson RK. Uncertainty-quantification analysis of the effects of residual impurities on hydrogen-oxygen ignition in shock tubes. *Combust Flame*. <http://dx.doi.org/10.1016/j.combustflame.2013.08.012>; 2013.
- [141] Boivin P, Dauptain A, Jiménez C, Cuenot B. Simulation of a supersonic hydrogen-air autoignition-stabilized flame using reduced chemistry. *Combust Flame* 2012;159:1779–90.
- [142] Sánchez AL, Fernández-Tarrazo E, Boivin P, Liñán A, Williams FA. Ignition time of hydrogen-air diffusion flames. *C R Mec* 2012;340:882–93.
- [143] Mellado JD, Sánchez AL, Kim JS, Liñán A. Branched-chain ignition in strained mixing layers. *Combust Theor Model* 2000;4:265–88.
- [144] Treviño C, Méndez F. Asymptotic analysis of the ignition of hydrogen by a hot plate in boundary layer flow. *Combust Sci Technol* 1991;78:197–216.
- [145] von Elbe G, Lewis B. Mechanism of the thermal reaction between hydrogen and oxygen. *J Chem Phys* 1942;10:366–93.
- [146] Willbourn AH, Phil D, Hinshelwood CN. The mechanism of the hydrogen-oxygen reaction I. The third explosion limit. *Proc R Soc Lond A* 1946;185:353–69.
- [147] Wang X, Law CK. An analysis of the explosion limits of hydrogen-oxygen mixtures. *J Chem Phys* 2013;138:134305.
- [148] Seshadri K, Peters N, Paczko G. Rate-ratio asymptotic analysis of autoignition of *n*-heptane in laminar nonpremixed flows. *Combust Flame* 2006;146:131–41.
- [149] Saxena P, Peters N, Williams FA. An analytical approximation for high-temperature autoignition times of higher alkanes. *Combust Flame* 2007;149:79–90.
- [150] Oldenberg O, Sommers Jr HS. Explosion limits of the hydrogen-oxygen mixture. *J Chem Phys* 1939;7:279.
- [151] Oldenberg O, Sommers Jr HS. *J Chem Phys* 1941;9:114–7.
- [152] Heiple HR, Lewis B. The reaction between hydrogen and oxygen: kinetics of the third explosion limit. *J Chem Phys* 1941;9:584–90.
- [153] Maas U, Warnatz J. Ignition processes in hydrogen-oxygen mixtures. *Combust Flame* 1988;74:53–69.
- [154] Zel'dovich YaB, Barenblatt GI, Librovich VB, Makhviladze GM. The mathematical theory of combustion and explosions. New York: Consultants Bureau; 1985.
- [155] Sánchez AL, Fernández-Tarrazo E, Williams FA. The chemistry involved in the third explosion limit of H<sub>2</sub>–O<sub>2</sub> mixtures. *Combust Flame* 2014;161:111–7.
- [156] Kassel LW, Storch HH. Chemical kinetics of the reaction of oxygen with hydrogen and with deuterium. *J Am Chem Soc* 1935;57:672–8.
- [157] Vincenti WG, Kruger CH. Introduction to physical gas dynamics. Huntington, NY: Robert E Krieger Publishing Company; 1965. p. 47.
- [158] Echehki T, Chen JH. Direct numerical simulation of autoignition in non-homogeneous hydrogen-air mixtures. *Combust Flame* 2003;134:169–91.
- [159] Mastorakos E. Ignition of turbulent non-premixed flames. *Prog Energy Combust Sci* 2009;35:57–97.
- [160] Peters N. Turbulent combustion. Cambridge: Cambridge University Press; 2000.
- [161] Darabiha N, Candel S. The influence of the temperature on the extinction and ignition limits of strained hydrogen-air diffusion flames. *Combust Sci Technol* 1992;86:67–85.
- [162] Sánchez AL, Liñán A, Williams FA. A bifurcation analysis of high-temperature ignition of H<sub>2</sub>–O<sub>2</sub> diffusion flames. *Proc Combust Inst* 1994;25:1529–37.
- [163] Lee SR, Law CK. Asymptotic analysis of ignition in nonpremixed counterflowing hydrogen versus heated air. *Combust Sci Technol* 1994;97:337–89.
- [164] Kreutz TG, Nishioka M, Law CK. The role of kinetic versus thermal feedback in nonpremixed ignition of hydrogen versus heated air. *Combust Flame* 1994;99:758–66.
- [165] Kreutz TG, Law CK. Ignition in nonpremixed counterflowing hydrogen versus heated air: computational study with detailed chemistry. *Combust Flame* 1996;104:157–75.
- [166] Helenbrook BT, Im HG, Law CK. Theory of radical-induced ignition of counterflowing hydrogen versus oxygen at high temperatures. *Combust Flame* 1998;112:242–52.
- [167] Kreutz TG, Law CK. Ignition in nonpremixed counterflowing hydrogen versus heated air: computational study with skeletal and reduced chemistry. *Combust Flame* 1998;114:436–56.
- [168] Fotache CG, Kreutz TG, Zhu DL, Law CK. An experimental study of ignition in nonpremixed counterflowing hydrogen versus heated air. *Combust Sci Technol* 1995;109:373–93.
- [169] Seiser R, Seshadri K. The influence of water on extinction and ignition of hydrogen and methane flames. *Proc Combust Inst* 2005;30:407–14.
- [170] Sung CJ, Law CK. Ignition of oscillatory counterflowing nonpremixed hydrogen against heated air. *Combust Sci Technol* 1997;129:347–70.
- [171] Mason SD, Chen JH, Im HG. Effects of unsteady scalar dissipation rate on ignition of non-premixed hydrogen/air mixtures in counterflow. *Proc Combust Inst* 2002;29:1629–36.



- [172] Bansal G, Im HG, Lee SR. Effects of scalar dissipation rate fluctuations on autoignition of hydrogen/air mixture. *AIAA J* 2009;47:468–72.
- [173] Seiser R, Frank JH, Liu S, Chen JH, Sigurdsson RJ, Seshadri K. Ignition of hydrogen in unsteady nonpremixed flows. *Proc Combust Inst* 2005;30:423–30.
- [174] Figueira da Silva LF, Deshaies B, Champion M, Rene-Corail M. Some specific aspects of combustion in supersonic  $H_2$ -air laminar mixing layers. *Combust Sci Technol* 1993;89:317–33.
- [175] Ju Y, Nioka T. Reduced mechanism of ignition for nonpremixed hydrogen/air in a supersonic mixing layer. *Combust Flame* 1994;99:240–6.
- [176] Treviño C, Liñán A. Mixing layer ignition of hydrogen. *Combust Flame* 1995;103:129–41.
- [177] Nishioka M, Law CK. A numerical study of ignition in the supersonic hydrogen/air laminar mixing layer. *Combust Flame* 1995;108:199–219.
- [178] Im HG, Helenbrook BT, Lee SR, Law CK. Ignition in the supersonic hydrogen/air mixing layer with reduced reaction mechanisms. *J Fluid Mech* 1996;322:275–96.
- [179] Sánchez AL, Liñán A, Williams FA. A WKB analysis of radical growth in the hydrogen-air mixing layer. *J Eng Math* 1997;31:119–30.
- [180] Sánchez AL, Liñán A, Williams FA. Chain-branching explosions in mixing layers. *SIAM J Appl Math* 1999;59:1335–55.
- [181] Han B, Sung CJ, Nishioka M. Effects of vitiated air on hydrogen ignition in a high-speed laminar mixing layer. *Combust Sci Technol* 2004;176:305–30.
- [182] Burrows M, Kurkov AP. Analytical and experimental study of supersonic combustion of hydrogen; 1973. NASA TM-2808.
- [183] Li JG, Yu G, Zhang Y, Li Y, Qian DX. Experimental studies on self-ignition of hydrogen/air supersonic combustion. *J Propuls Power* 1997;13:538–42.
- [184] Sung CJ, Li JG, Yu G, Law CK. Chemical kinetics and self-ignition in a model supersonic hydrogen-air combustor. *AIAA J* 1999;37:208–14.
- [185] Liñán A. The asymptotic structure of counterflow diffusion flames for large activation energies. *Acta Astronaut* 1974;1:1007–39.
- [186] Liñán A, Crespo A. An asymptotic analysis of unsteady diffusion flames for large activation energies. *Combust Sci Technol* 1976;14:95–117.
- [187] Figueira da Silva LF, Deshaies B, Champion M. Numerical study of ignition within hydrogen-air supersonic boundary layers. *AIAA J* 1993;31:884–90.
- [188] Zheng XL, Blouch JD, Zhu DL, Kreutz TG, Law CK. Ignition of premixed hydrogen/air by heated counterflow. *Proc Combust Inst* 2002;29:1637–43.
- [189] Zheng XL, Law CK. Ignition of premixed hydrogen/air by heated counterflow under reduced and elevated pressures. *Combust Flame* 2004;136:168–79.
- [190] Sánchez AL, Iglesias I, Liñán A. An asymptotic analysis of chain-branching ignition in the laminar wake of a splitter plate separating streams of hydrogen and oxygen. *Combust Theor Model* 1998;2:259–71.
- [191] Peters N. On the stability of Liñán's "Premixed Flame Regime". *Combust Flame* 1978;33:315–8.
- [192] Yamada E, Watanabe S, Hayashi K, Tsuboi N. Numerical analysis on auto-ignition of a high pressure hydrogen jet spouting from a tube. *Proc Combust Inst* 2009;32:2363–9.
- [193] Yamada E, Kitabayashi N, Hayashi K, Tsuboi N. Mechanism of high-pressure hydrogen auto-ignition when spouting into air. *Int J Hydrog Energy* 2011;36:2560–6.
- [194] Thévenin D, Candel S. Ignition dynamics of a diffusion flame rolled up in a vortex. *Phys Fluids* 1995;7:434–45.
- [195] Zheng XL, Yuan J, Law CK. Nonpremixed ignition of  $H_2$ /air in a mixing layer with a vortex. *Proc Combust Inst* 2004;30:415–21.
- [196] Cheng TS, Wehrmeyer JA, Pitz RW, Jarret Jr O, Northam GB. Raman measurement of mixing and finite-rate chemistry in a supersonic hydrogen-air diffusion flame. *Combust Flame* 1994;99:157–73.
- [197] Williams FA. Turbulent combustion. In: Buckmaster JD, editor. *The mathematics of combustion*. Philadelphia: SIAM; 1985. pp. 97–132.
- [198] Clavin P. Dynamic behavior of premixed flame fronts in laminar and turbulent flows. *Prog Energy Combust Sci* 1985;11:1–59.
- [199] Liu DDS, MacFarlane R. Laminar burning velocities of hydrogen-air and hydrogen-air-steam flames. *Combust Flame* 1983;49:59–71.
- [200] Dowdy DR, Smith DB, Taylor SC, Williams A. The use of expanding spherical flames to determine burning velocities and stretch effects in hydrogen/air mixtures. *Proc Combust Inst* 1990;23:325–32.
- [201] Egolopoulos FN, Law CK. An experimental and computational study of the burning rate of ultra-lean to moderately-rich  $H_2/O_2/N_2$  laminar flames with pressure variations. *Proc Combust Inst* 1990;23:333–40.
- [202] Vagelopoulos CM, Egolopoulos FN, Law CK. Further considerations on the determination of laminar flame speeds with the counterflow twin-flame technique. *Proc Combust Inst* 1994;25:1341–7.
- [203] Aung KT, Hassan MI, Faeth GM. Flame stretch interactions of laminar premixed hydrogen/air flames at normal temperature and pressure. *Combust Flame* 1997;109:1–24.
- [204] Karpov VP, Lipatnikov AN, Wolanski P. Finding the Markstein number using the measurements of expanding spherical laminar flames. *Combust Flame* 1997;109:436–48.
- [205] Aung KT, Hassan MI, Faeth GM. Effects of pressure and nitrogen dilution on flame/stretch interactions of laminar premixed  $H_2/O_2/N_2$  flames. *Combust Flame* 1998;112:1–15.
- [206] Tse SD, Zhu DL, Law CK. Morphology and burning rates of expanding spherical flames in  $H_2/O_2$ /inert mixtures up to 60 atmospheres. *Proc Combust Inst* 2000;28:1793–800.
- [207] Kwon OC, Faeth GM. Flame/stretch interactions of premixed hydrogen-fueled flames: measurements and predictions. *Combust and Flame* 2001;124:590–610.
- [208] Lamoureux N, Djebaïli-Chameix N, Paillar C-E. Laminar flame velocity determination for  $H_2$ -air-He- $CO_2$  mixtures using the spherical bomb method. *Exp Therm Fluid Sci* 2003;27:385–93.
- [209] Verhelst S, Woolley R, Lawes M, Sierens R. Laminar and unstable burning velocities and Markstein lengths of hydrogen-air mixtures at engine-like conditions. *Proc Combust Inst* 2005;30:209–16.
- [210] Bradley D, Lawes M, Liu K, Verhelst S, Woolley R. Laminar burning velocities of lean hydrogen-air mixtures at pressures up to 1.0 MPa. *Combust Flame* 2007;149:162–72.
- [211] Hu E, Hu Z, He J, Miao H. Experimental and numerical study on laminar burning velocities and flame instabilities of hydrogen-air mixtures at elevated pressures and temperatures. *Int J Hydrog Energy* 2009;34:8741–55.
- [212] Burke MP, Chen Z, Ju Y, Dryer FL. Effect of cylindrical confinement on the determination of laminar flame speeds using outwardly propagating flames. *Combust Flame* 2009;156:771–9.
- [213] Kuznetsov M, Kobelt S, Grune J, Jordan T. Flammability limits and laminar flame speeds of hydrogen-air mixtures at sub-atmospheric pressures. *Int J Hydrog Energy* 2012;37:17580–8.
- [214] Krejci MC, Mathieu O, Vissotski AJ, Ravi S, Sikes TG, Petersen EL, et al. Laminar flame speed and ignition delay time data for the kinetic modeling of hydrogen and syngas fuel blends. *J Eng Gas Turbines Power* 2013;135:021503.
- [215] Koroll GW, Kumar RK, Bowles EM. Burning velocities of hydrogen-air mixtures. *Combust Flame* 1993;94:330–40.
- [216] Qin X, Kobayashi H, Nioka T. Laminar burning velocity of hydrogen-air premixed flames at elevated pressure. *Exp Therm Fluid Sci* 2000;21:58–63.
- [217] Pareja J, Burbano HJ, Ogami Y. Measurements of the laminar burning velocity of hydrogen-air premixed flames. *Int J Hydrog Energy* 2010;35:1812–8.
- [218] Dahoe AE. Laminar burning velocities of hydrogen-air mixtures from closed vessel gas explosions. *J Loss Prev Process Ind* 2005;18:152–66.
- [219] Hermanns RTE, Konnov AA, Bastiaans RJM, de Goeij LPH. Laminar burning velocities of diluted hydrogen-oxygen-nitrogen mixtures. *Energy Fuels* 2007;21:1977–81.
- [220] Pareja J, Burbano HJ, Amell A, Carvajal J. Laminar burning velocities and flame stability analysis of hydrogen/air premixed flames at low pressure. *Int J Hydrog Energy* 2011;36:6317–24.
- [221] Qiao L, Gu Y, Dahm WJA, Oran ES, Faeth GM. Near-limit laminar burning velocities of microgravity premixed hydrogen flames with chemically-passive fire suppressants. *Proc Combust Inst* 2007;31:2701–9.
- [222] Williams FA. Progress in knowledge of flamelet structure and extinction. *Prog Energy Combust Sci* 2000;26:657–82.
- [223] Herbon JT, Hanson RK, Golden DM, Bowman CT. A shock tube study of the enthalpy of formation of OH. *Proc Combust Inst* 2002;29:1201–8.
- [224] Kelley AP, Law CK. Nonlinear effects in the extraction of laminar flame speeds from expanding spherical flames. *Combust Flame* 2009;156:1844–51.
- [225] Bascombe KN. Hydrogen-atom concentrations in hydrogen/oxygen/nitrogen flames. *Proc Combust Inst* 1965;10:55–64.
- [226] Dixon-Lewis G, Sutton MM, Williams A. Some reactions of hydrogen atoms and simple radicals at high temperature. *Proc Combust Inst* 1965;10:495–502.
- [227] Eberius KH, Hoyermann K, Wagner GG. Experimental and mathematical study of a hydrogen-oxygen flame. *Proc Combust Inst* 1971;13:713–21.
- [228] Dixon-Lewis G, Sutton MM, Williams A. Flame structure and flame reaction kinetics IV. Experimental investigations of a fuel-rich hydrogen-oxygen+nitrogen flame at atmospheric pressure. *Proc R Soc Lond A* 1970;317:227–34.
- [229] Brown NJ, Eberius KH, Fristrom RM, Hoyermann K, Wagner GG. Low-pressure hydrogen/oxygen flame studies. *Combust Flame* 1978;33:151–60.
- [230] Kohse-Höinghaus K, Koczar P, Just Th. Absolute concentration measurements of OH in low-pressure hydrogen-oxygen, methane-oxygen, and acetylene-oxygen flames. *Proc Combust Inst* 1986;21:1719–27.
- [231] Vandooren J, Bian J. Validation of  $H_2/O_2$  reaction mechanism by comparison with the experimental structure of a rich hydrogen-oxygen flame. *Proc Combust Inst* 1990;23:341–6.
- [232] Paletskii AA, Kuibida LV, Bolshova TA, Korobeinichev OP, Fristrom RM. Study of the structure of a ten-atmosphere  $H_2-O_2-Ar$  flame using molecular-beam inlet mass-spectrometric probing. *Combust Explos Shock Waves* 1996;32:245–50.
- [233] Korobeinichev OP, Shvartsberg VM, Il'in SB, Chernov AA, Bol'shova TA. Laminar flame structure in a low-pressure premixed  $H_2/O_2/Ar$  mixture. *Combust Explos Shock Waves* 1999;35:239–44.
- [234] Korobeinichev OP, Shmakov AG, Rybitskaya IV, Bol'shova TA, Chernov AA, Knyaz'kov DA, et al. Kinetics and mechanism of chemical reactions in the  $H_2/O_2/N_2$  flame at atmospheric pressure. *Kinet Catal* 2009;50:156–61.
- [235] Zel'dovich YaB. Chain reactions in hot flames – an approximate theory for flame velocity. *Kinetika i Kataliz* 1961;2:308–18.
- [236] Joulin G, Liñán A, Ludford GSS, Peters N, Schmidt-Lainé C. Flames with chain-branching chain-breaking kinetics. *SIAM J Appl Math* 1985;45:420–34.
- [237] Dold JW. Premixed flames modelled with thermally sensitive intermediate branching kinetics. *Combust Theor Model* 2007;11:909–48.
- [238] Korobeinichev OP, Bolshova TA. Applicability of Zel'dovich's theory of chain propagation of flames to combustion of hydrogen-oxygen mixtures. *Combust Explos Shock Waves* 2009;45:507–10.

- [239] Clavin P, Graña-Otero JC. Curved and stretched flames: the two Markstein numbers. *J Fluid Mech* 2011;686:187–217.
- [240] Kurdyumov VN, Fernández-Galisteo D. Asymptotic structure of premixed flames for a simple chain-branching chemistry model with finite activation energy near the flammability limit. *Combust Flame* 2012;159:3110–8.
- [241] Gubernov VV, Kolobov AV, Polezhaev AA, Sidhu HS. Analysing the stability of premixed rich hydrogen-air flame with the use of two-step models. *Combust Flame* 2013;160:1060–9.
- [242] Fernández-Galisteo D, del Alamo G, Sánchez AL, Liñán A. Zeldovich analysis of hydrogen-air premixed flames. In: Third European combustion Meeting, Crete, Greece 2007.
- [243] Liñán A, Williams FA. Fundamental aspects of combustion. New York: Oxford University Press; 1993.
- [244] Gray P, Holland S, Smith DB. The effect of isotopic substitution on the flame speeds of hydrogen-oxygen and hydrogen-nitrous oxide flames. *Combust Flame* 1970;14:361–74.
- [245] Sun CJ, Sung CJ, He L, Law CK. Dynamics of weakly stretched flames: quantitative description and extraction of global flame parameters. *Combust Flame* 1999;118:108–28.
- [246] Davis SG, Searby G. The use of counterflow flames for the evaluation of burning velocities and stretch effects in hydrogen/air mixtures. *Combust Sci Technol* 2002;174(11–12):93–110.
- [247] Bradley D, Gaskell PH, Gu XJ. Burning velocities, Markstein lengths, and flame quenching for spherical methane-air flames: a computational study. *Combust Flame* 1996;104:176–98.
- [248] Karpov VP. Cellular flame structure under conditions of constant volume bomb and its relationship with vibratory combustion. *Combust Explos Shock Waves* 1965;1:39–42.
- [249] Bregeon B, Gordon AS, Williams FA. Near-limit downward propagation of hydrogen and methane flames in oxygen-nitrogen mixtures. *Combust Flame* 1978;33:33–45.
- [250] Mitani T, Williams FA. Studies of cellular flames in hydrogen-oxygen-nitrogen mixtures. *Combust Flame* 1980;39:169–90.
- [251] Sivashinsky GI. Diffusional-thermal theory of cellular flames. *Combust Sci Technol* 1977;15:137–46.
- [252] Joulin G, Mitani T. Linear stability analysis of two-reactant flames. *Combust Flame* 1981;40:235–46.
- [253] Denet B, Haldenwang P. Numerical study of thermal-diffusive instability of premixed flames. *Combust Sci Technol* 1992;86:199–221.
- [254] Patnaik G, Kailasanath K, Oran ES, Laskey KJ. Detailed numerical simulations of cellular flames. *Proc Combust Inst* 1988;22:1517–26.
- [255] Altantzis C, Frouzakis CE, Tomboulides AG, Kerkemeier SG, Boulouchos K. Detailed numerical simulations of intrinsically unstable two-dimensional planar lean premixed hydrogen/air flames. *Proc Combust Inst* 2011;33:1261–8.
- [256] Shkadinskii KG, Khaikin BI, Merzhanov AG. Propagation of a pulsating exothermic reaction front in the condensed phase. *Combust Explos Shock Waves* 1973;7:15–22 [translated from *Fizika Goreniya i Vzryva* 1971;1:19–28].
- [257] Joulin G, Clavin P. Linear stability analysis of nonadiabatic flames: diffusional-thermal model. *Combust Flame* 1979;35:139–53.
- [258] He L, Clavin P. Premixed hydrogen-oxygen flames. Part II: quasi-isobaric ignition near the flammability limits. *Combust Flame* 1993;93:408–20.
- [259] Kailasanath K, Ganguly K, Patnaik G. Dynamics of flames near the rich-flammability limit of hydrogen-air mixtures. *Prog Astronaut Aeronaut* 1993;151:38–48.
- [260] Goyal G, Maas U, Warnatz J. Simulation of the behavior of rich hydrogen-air flames near the flammability limit. *Combust Sci Technol* 1995;105:183–93.
- [261] Christiansen EW, Sung CJ, Law CK. Pulsating instability in near-limit propagation of rich hydrogen/air flames. *Proc Combust Inst* 1998;27:555–62.
- [262] Christiansen EW, Law CK, Sung CJ. Steady and pulsating propagation and extinction of rich hydrogen/air flames at elevated pressures. *Combust Flame* 2001;124:35–49.
- [263] Sung CJ, Makino A, Law CK. On stretch-affected pulsating instability in rich hydrogen/air flames: asymptotic analysis and computation. *Combust Flame* 2002;128:422–34.
- [264] Jomaas G, Bechtold JK, Law CK. Spiral waves in expanding hydrogen-air flames: experiment and theory. *Proc Combust Inst* 2007;31:1039–46.
- [265] Jomaas G, Law CK. Observation and regime classification of pulsation patterns in expanding spherical flames. *Phys Fluids* 2010;22:124102.
- [266] Zel'vovich YaB. Theory of combustion and detonation of gases. Moscow: Izdvo. Akad. Nauk (Academy of Sciences, USSR); 1944.
- [267] Ronney PD. Near-limit flame structures at low Lewis number. *Combust Flame* 1990;82:1–14.
- [268] Ronney PD, Whaling KN, Abbud-Madrid A, Gatto JL, Pisowicz VL. Stationary premixed flames in spherical and cylindrical geometries. *AIAA J* 1994;32:569–77.
- [269] Ronney PD, Wu MS, Weiland KJ, Pearlman HG. Flame ball experiments in space: preliminary results from STS-83. *AIAA J* 1998;36:1361–8.
- [270] Ronney PD. Understanding combustion processes through microgravity research. *Proc Combust Inst* 1998;27:2485–506.
- [271] Shoshin YL, van Oijen JA, Sepman AV, de Goey LPH. Experimental and computational study of the transition to the flame ball regime at normal gravity. *Proc Combust Inst* 2011;33:1211–8.
- [272] Williams FA, Grcar JF. A hypothesized burning-velocity formula for very lean hydrogen-air mixtures. *Proc Combust Inst* 2009;32:1351–7.
- [273] Buckmaster J, Joulin G, Ronney PD. Effects of heat loss on the structure and stability of flame balls. *Combust Flame* 1990;79:381–92.
- [274] Buckmaster J, Joulin G, Ronney PD. Structure and stability of non-adiabatic flame balls: II. Effects of far-field losses. *Combust Flame* 1991;84:411–22.
- [275] Buckmaster J, Smooke M, Giovangigli V. Analytical and numerical modeling of flame-balls in hydrogen-air mixtures. *Combust Flame* 1993;94:113–24.
- [276] Wu MS, Liu JB, Ronney PD. Numerical simulation of diluent effects in flame ball structure and dynamics. *Proc Combust Inst* 1998;27:2543–50.
- [277] Wu MS, Ronney PD, Colantonio RO, VanZandt DM. Detailed numerical simulation of flame ball structure and dynamics. *Combust Flame* 1999;116:387–97.
- [278] Kwon OC, Abid M, Ronney PD, Wu MS, Ju Y. Numerical modeling of flame balls with radiative reabsorption effects. In: 3rd Joint US Sections Meeting of the Combustion Institute, Chicago, IL March 21–23, 2003.
- [279] Ronney PD. Studies of premixed laminar and turbulent flames at micro-gravity; 2005. NASA Final Report, Grant No. NAG3–2887.
- [280] Barlow RS, Karpets AN, Frank JH, Chen JY. Scalar profiles and NO formation in laminar opposed-flow partially premixed methane/air flames. *Combust Flame* 2001;127:2102–18.
- [281] Joulin G. Preferential diffusion and the initiation of lean flames of light fuels. *SIAM J Appl Math* 1987;47:998–1016.
- [282] Joulin G. Personal communication; 2013.
- [283] Clusius K, Gutschmidt H. Die untere explosionsgrenze der gemische von schwerem wasserstoff mit luft. *Naturwissenschaften* 1934;22:693.
- [284] Payman W, Titman H. Limits of inflammability of hydrogen and deuterium in oxygen and in air. *Nature* 1936;137:190.
- [285] Clusius K, Faber G. Zur Isotopentrennung in aufsteigenden H<sub>2</sub>-D<sub>2</sub>-flammen. *Zeitschrift Naturforschung Teil A* 1947;2:97.
- [286] Gray P, Smith DB. Isotope effects on flame speeds for hydrogen and deuterium. *Chem Commun* 1967;4:146–8.
- [287] Grcar JF. A new type of steady and stable, laminar, premixed flame in ultra-lean, hydrogen-air combustion. *Proc Combust Inst* 2009;32:1011–8.
- [288] Minaev S, Kagan L, Joulin G, Sivashinsky G. On self-drifting flame balls. *Combust Theor Model* 2001;5:609–22.
- [289] Kagan L, Minaev S, Sivashinsky G. On self-drifting flame balls. *Math Comput Simul* 2004;65:511–20.
- [290] Gerlinger W, Schneider K, Bockhorn H. Numerical simulation of three-dimensional instabilities of spherical flame structures. *Proc Combust Inst* 2000;28:793–9.
- [291] Gerlinger W, Schneider K, Fröhlich J, Bockhorn H. Numerical simulations on the stability of spherical flame structures. *Combust Flame* 2003;132:247–71.
- [292] Cheng TS, Chao Y-C, Wu C-Y, Li Y-H, Nakamura Y, Lee K-Y, et al. Experimental and numerical investigation of microscale hydrogen diffusion flames. *Proc Combust Inst* 2005;30:2489–97.
- [293] Lyons KM, Watson KA, Carter CD, Donbar JM. On flame holes and local extinction in lifted-jet diffusion flames. *Combust Flame* 2005;142:308–13.
- [294] Buckmaster J. Edge-flames. *Prog Energy Combust Sci* 2002;28:435–75.
- [295] Daou J, Liñán A. Ignition and extinction fronts in counterflowing premixed reactive gases. *Combust Flame* 1999;118:479–88.
- [296] Pantano C, Pullin DI. On the dynamics of the collapse of a diffusion-flame hole. *J Fluid Mech* 2003;480:311–32.
- [297] Hermanns M, Vera M, Liñán A. On the dynamics of flame edges in diffusion flame/vortex interactions. *Combust Flame* 2007;149:32–48.
- [298] Chung SH. Stabilization, propagation and instability of tribrachial triple flames. *Proc Combust Inst* 2007;31:877–92.
- [299] Fernández E, Kurdyumov V, Liñán A. Diffusion flame attachment and lift-off in the near wake of a fuel injector. *Proc Combust Inst* 2000;28:2125–31.
- [300] Lee BJ, Chung SH. Stabilization of lifted tribrachial flames in a laminar nonpremixed jet. *Combust Flame* 1997;109:163–72.
- [301] Weiland NT, Strakey PA. Stability characteristics of turbulent hydrogen dilute diffusion flames. *Combust Sci Technol* 2009;181:756–81.
- [302] Takahashi F, Schmoll WJ, Katta VR. Attachment mechanism of diffusion flames. *Proc Combust Inst* 1998;27:675–84.
- [303] Cheng TS, Wehrmeyer JA, Pitz RW. Simultaneous temperature and multi-species measurement in a lifted hydrogen diffusion flame. *Combust Flame* 1992;91:323–45.
- [304] Cabra R, Myhrvold T, Chen JY, Dibble RW, Karpets AN, Barlow RS. Simultaneous laser raman-rayleigh-lif measurements and numerical modeling results of a lifted turbulent H<sub>2</sub>/N<sub>2</sub> jet flame in a vitiated coflow. *Proc Combust Inst* 2002;29:1881–8.
- [305] Michobuchi Y, Tachibana S, Shinio J, Ogawa S, Takeno T. A numerical analysis of the structure of a turbulent hydrogen jet lifted flame. *Proc Combust Inst* 2002;29:2009–15.
- [306] Michobuchi Y, Shinio J, Ogawa S, Takeno T. A numerical study on the formation of diffusion flame islands in a turbulent hydrogen jet lifted flame. *Proc Combust Inst* 2005;30:611–9.
- [307] Yoo CS, Sankaran R, Chen JH. Three-dimensional direct numerical simulation of a turbulent lifted hydrogen jet flame in heated coflow: flame stabilization and structure. *J Fluid Mech* 2009;640:453–81.
- [308] Luo K, Wang H, Yi F, Fan J. Direct numerical simulation study of an experimental lifted H<sub>2</sub>/N<sub>2</sub> flame. Part 1: validation and flame structure. *Energy Fuels* 2012;26:6118–27.
- [309] Ruetsch GR, Vervish L, Liñán A. Effects of heat release on triple flames. *Phys Fluids* 1995;7:1447–54.
- [310] Im HG, Chen JH. Structure and propagation of triple flames in partially premixed hydrogen-air mixtures. *Combust Flame* 1999;119:436–54.

- [311] Im HG, Chen JH. Effects of flow strain on triple flame propagation. *Combust Flame* 2001;126:1384–92.
- [312] Takagi T, Nakajima I, Kinoshita S. Structure and propagation of strain-controlled  $H_2/N_2$ /air diffusion edge flames. *Proc Combust Inst* 2002;29:1573–9.
- [313] Revuelta A, Sánchez AL, Liñán A. Laminar mixing in diluted and undiluted fuel jets upstream from lifted flames. *Combust Flame* 2002;128:199–210.
- [314] Liñán A, Fernández-Tarrazo E, Vera M, Sánchez AL. Lifted laminar jet diffusion flames. *Combust Sci Technol* 2005;177:933–53.
- [315] Savaş Ö, Gollahalli SR. Stability of lifted laminar round gas-jet flame. *J Fluid Mech* 1986;165:297–318.
- [316] Williams FA. Recent advances in theoretical descriptions of turbulent diffusion flames. In: Murthy SNB, editor. *Turbulent mixing in non-reactive and reactive flows*. New York: Plenum; 1975. pp. 189–208.
- [317] Dixon-Lewis G, Missaghi M. Structure and extinction limits of counterflow diffusion flames of hydrogen-nitrogen mixtures in air. *Proc Combust Inst* 1988;22:1461–70.
- [318] Pellet GL, Northam GB, Wilson LG. Counterflow diffusion flames of hydrogen, and hydrogen plus methane, ethylene, propane, and silane, vs. air: strain rates at extinction; 1991. AIAA Paper 91–0370.
- [319] Pellet GL, Northam GB, Wilson LG. Strain-induced extinction of hydrogen-air counterflow diffusion flames: effects of steam,  $CO_2$ ,  $N_2$ , and  $O_2$  additives to air; 1992. AIAA Paper 92–0877.
- [320] Balakrishnan G, Trees D, Williams FA. An experimental investigation of strain-induced extinction of diluted hydrogen-air counterflow diffusion flames. *Combust Flame* 1994;98:123–6.
- [321] Trees D, Brown TM, Seshadri K, Smooke MD, Balakrishnan G, Pitz RW, et al. The structure of nonpremixed hydrogen-air flames. *Combust Sci Technol* 1995;104:427–39.
- [322] Brown TM, Tanoff MA, Osborne RJ, Pitz RW, Smooke MD. Experimental and numerical investigation of laminar hydrogen-air counterflow diffusion flames. *Combust Sci Technol* 1997;129:71–88.
- [323] Wehrmeyer OA, Yeralan S, Tecu KS. Influence of strain rate and fuel dilution on laminar nonpremixed hydrogen-air flame structure: an experimental investigation. *Combust Flame* 1996;107:125–40.
- [324] Pellett GL, Isaac KM, Humphreys Jr WM, Gartrell LR, Roberts WL, Dancy CL, et al. Velocity and thermal structure, and strain-induced extinction of 14 to 100 % hydrogen-air counterflow diffusion flames. *Combust Flame* 1998;112:575–92.
- [325] Kim Y-M, Kim H-J. Multidimensional effects on structure and extinction process of counterflow nonpremixed hydrogen-air flames. *Combust Sci Technol* 1998;137:51–80.
- [326] Frouzakis CE, Lee J, Tomboulides AG, Boulouchos K. Two-dimensional direct numerical simulation of opposed-jet hydrogen-air diffusion flame. *Proc Combust Inst* 1998;27:571–7.
- [327] Finke H, Grünfold G. An experimental investigation of extinction of curved laminar hydrogen diffusion flames. *Proc Combust Inst* 2000;28:2133–40.
- [328] Sohn CH, Chung SH. Effect of pressure on the extinction, acoustic pressure response, and NO formation in diluted hydrogen-air diffusion flames. *Combust Flame* 2000;121:288–300.
- [329] Jiménez C. Personal communication; 2013.
- [330] Sánchez AL, Liñán A, Williams FA, Balakrishnan G. Theory of structures of hydrogen-oxygen diffusion flames. *Combust Sci Technol* 1995;110–111:277–301.
- [331] Gutheil E, Williams FA. A numerical and asymptotic investigation of structures and extinction of hydrogen-air diffusion flames at pressures and temperatures of high-speed combustion. *Proc Combust Inst* 1990;23:513–21.
- [332] Balakrishnan G, Treviño C, Mauss F. The asymptotic structure of hydrogen-air diffusion flames. *Combust Flame* 1992;91:246–56.
- [333] Sohn CH, Chung SH, Lee SR, Kim JS. Structure and acoustic-pressure response of hydrogen-oxygen diffusion flames at high pressure. *Combust Flame* 1998;115:299–312.
- [334] Lafon P, Prud'homme R. Modèles de combustion d'une goutte avec condensation des produits brûlés. *La Recherche Aérospatiale* 1994;1:67–82.
- [335] Yang V, Lin NN, Shuen JS. Vaporization of liquid oxygen (LOX) droplets in supercritical hydrogen environments. *Combust Sci Technol* 1994;97:247–70.
- [336] Daou J, Haldenwang P, Nicoli C. Supercritical burning of liquid oxygen (LOX) droplet with detailed chemistry. *Combust Flame* 1995;101:153–69.
- [337] Nicoli C, Haldenwang P, Daou J. Substitute mixtures for LOX droplet vaporization study. *Combust Sci Technol* 1996;112:55–74.
- [338] Harstad K, Bellan J. Isolated fluid oxygen drop behavior in fluid hydrogen at rocket chamber pressures. *Int J Heat Mass Transf* 1998;41:3537–50.
- [339] Kim HJ, Sohn CH, Chung SH, Kim JS. Nonlinear acoustic-pressure responses of oxygen droplet flames burning in gaseous hydrogen. *KSME Int J* 2001;15:510–21.
- [340] Sohn CH, Chung CH, Kim JS, Williams FA. Acoustic response of droplet flames to pressure oscillations. *AIAA J* 1996;34:1847–54.
- [341] Kim JS, Williams FA. Contribution of strained diffusion flames to acoustic pressure response. *Combust Flame* 1994;98:279–99.
- [342] Kim JS, Williams FA. Acoustic-instability boundaries in liquid-propellant rockets – theoretical explanation of empirical correlation. *J Propuls Power* 1996;12:621–4.
- [343] Mayer W, Tamura H. Propellant injection in a liquid oxygen/gaseous hydrogen rocket engine. *J Propuls Power* 1996;12:1137–47.
- [344] Mayer W, Schik A, Schäffer M, Tamura H. Injection and mixing processes in high-pressure liquid oxygen/gaseous hydrogen rocket combustors. *J Propuls Power* 2000;16:823–8.
- [345] Dorofeev SB, Sidorov VP, Dvoishnikov AE, Breitung W. Deflagration to detonation transition in large confined volume of lean hydrogen-air mixtures. *Combust Flame* 1996;104:95–110.
- [346] Dorofeev SB, Kuznetsov MS, Alekseev VI, Efimenko AA, Breitung W. Evaluation of limits for effective flame acceleration in hydrogen mixtures. *J Loss Prev Process Ind* 2001;14:583–9.
- [347] Vesper A, Breitung W, Dorofeev SB. Run-up distances to supersonic flames in obstacle-laden tubes. *J Phys IV France* 2002;12:333–40.
- [348] Breitung W, Dorofeev S, Kotchourko A, Redlinger R, Scholtyssek W, Bentaib A, et al. Integral large scale experiments on hydrogen combustion for severe accident code validation-HYCOM. *Nucl Eng Des* 2005;235:253–70.
- [349] Ciccarelli G, Dorofeev S. Flame acceleration and transition to detonation in ducts. *Prog Energy Combust Sci* 2008;34:499–550.
- [350] Brailovsky I, Sivashinsky GL. Hydraulic resistance as a mechanism for deflagration-to-detonation transition. *Combust Flame* 2000;122:492–9.
- [351] Sivashinsky GL. Some developments in premixed combustion modeling. *Proc Combust Inst* 2002;29:1737–61.
- [352] Gelfand BE, Silnikov MV, Medvedev SP, Khomik SV. *Thermo-gas dynamics of hydrogen combustion and explosion*. Heidelberg, Germany: Springer-Verlag; 2012.
- [353] Glassman I, Yetter RA. *Combustion*. 4th ed. New York: Academic Press; 2008. pp. 282–93.
- [354] McBride BJ, Zehe MJ, Gordon S. NASA Glenn coefficients for calculating thermodynamic properties of individual species. Technical Report NASA/TP–2002–211556. NASA, Glenn Research Center; 2002.
- [355] Starik AM, Titova NS. Kinetics of detonation initiation in the supersonic flow of the  $H_2 + O_2$  (air) mixture in  $O_2$  molecule excitation by resonance laser radiation. *Kinet Catal* 2003;44:28–39.
- [356] Skrebkov OV, Karkach SP. Vibrational nonequilibrium and electronic excitation in the reaction of hydrogen with oxygen behind a shock wave. *Kinet Catal* 2007;48:367–75.
- [357] Starik AM, Loukhovitski BI, Sharipov AS, Titova NS. Intensification of shock-induced combustion by electric-discharge-excited oxygen molecules: numerical study. *Combust Theor Model* 2010;14:653–79.
- [358] Starik A, Sharipov A. Theoretical analysis of reaction kinetics with singlet oxygen molecules. *Phys Chem Chem Phys* 2011;13:16424–36.
- [359] Taylor B. Personal communication; 2013.
- [360] Dove JE, Teitelbaum HJ. The vibrational relaxation of  $H_2$ . I. Experimental measurements of the rate of relaxation by  $H_2$ , He, Ne, Ar, and Kr. *Chem Phys* 1974;6:431–44.
- [361] Clavin P, Williams FA. Analytical studies of the dynamics of gaseous detonations. *Philos Trans R Soc A* 2012;370:597–624.
- [362] Clavin P, He L. Stability and nonlinear dynamics of one-dimensional overdriven detonations in gases. *J Fluid Mech* 1996;306:353–78.
- [363] Clavin P, He L. Acoustic effects in the nonlinear oscillations of planar detonations. *Phys Rev E* 1996;53:4778–84.
- [364] Clavin P, Williams FA. Dynamics of planar gaseous detonations near Chapman–Jouguet conditions for small heat release. *Combust Theor Model* 2002;6:127–39.
- [365] Strehlow RA. *Combustion fundamentals*. New York: McGraw-Hill; 1984.
- [366] Short M, Quirk JJ. On the nonlinear stability and detonability limit of a detonation wave for a model three-step chain-branching reaction. *J Fluid Mech* 1997;339:89–119.
- [367] Sánchez AL, Carretero M, Clavin P, Williams FA. One-dimensional overdriven detonations with branched-chain kinetics. *Phys Fluids* 2001;13:776–92.
- [368] Yungster S, Radhakrishnan K. Pulsating one-dimensional detonations in hydrogen-air mixtures. *Combust Theor Model* 2004;8:745–70.
- [369] Erpenbeck JJ. Stability of steady-state equilibrium detonations. *Phys Fluids* 1962;5:604–14.
- [370] Erpenbeck JJ. Stability of idealized one-reaction detonation. *Phys Fluids* 1964;7:684–96.
- [371] Erpenbeck JJ. Stability of idealized one-reaction detonation: zero activation energy. *Phys Fluids* 1965;8:1192–3.
- [372] Erpenbeck JJ. Detonation stability for disturbances of small transverse wavelength. *Phys Fluids* 1966;9:1293–306.
- [373] Clavin P, He L, Williams FA. Multidimensional stability analysis of overdriven gaseous detonations. *Phys Fluids* 1997;9:3764–85.
- [374] Clavin P, He L. Theory of cellular detonations in gases. Part 1: stability limits at strong overdrive. *C R Académie de Sci Paris* 2001;329:463–71.
- [375] Clavin P, Williams FA. Multidimensional stability analysis of gaseous detonations near Chapman–Jouguet conditions for small heat release. *J Fluid Mech* 2009;324:125–50.
- [376] Clavin P, Denet B. Diamond patterns in the cellular front of an overdriven detonation. *Phys Rev Lett* 2002;88:044502.
- [377] Austin JM, Pintgen F, Shepherd JE. Reaction zones in highly unstable detonations. *Proc Combust Inst* 2005;30:1849–57.
- [378] Taylor BD, Kessler DA, Gamezo VN, Oran ES. Numerical simulations of hydrogen detonations with detailed chemical kinetics. *Proc Combust Inst* 2013;34:2009–16.
- [379] Cha MS, Ronney PD. Propagation rates of nonpremixed edge flames. *Combust Flame* 2006;146:312–28.
- [380] Ronney PD. Personal communication; 2013.

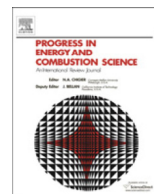
## **Update**

# **Progress in Energy and Combustion Science**

Volume 54, Issue , May 2016, Page 93–94

DOI: <https://doi.org/10.1016/j.pecs.2016.04.001>





## Corrigendum

## Corrigendum to “Recent advances in understanding of flammability characteristics of hydrogen” [Prog Energ Combust Sci 41 (2014) 1–55]

Antonio L. Sánchez<sup>a</sup>, Forman A. Williams<sup>b,\*</sup><sup>a</sup> Dept. Ingeniería Térmica y de Fluidos, Universidad Carlos III de Madrid, Leganés 28911, Spain<sup>b</sup> Dept. of Mechanical and Aerospace Engineering, University of California San Diego, La Jolla, CA 92093-0411, USA

The authors would like to notify readers of errors pertaining to Table 2 and Fig. 14 of the above referenced article. Specifically, the preexponential factor for the backward reaction 1b in Table 2 was mistakenly given the value  $3.03 \times 10^4$ , instead of the correct value  $7.04 \times 10^{13}$ , and the reference numbers appearing in the legends of Fig. 14 were all offset by one, so that “Dowdy et al. [199]” should be “Dowdy et al. [200]”, “Egolfopoulos & Law [200]” should be “Egolfopoulos & Law [201]”, and so on. Please find reprinted here corrected versions for both the table and the figure. For the table, rather than just correcting the typo, we have chosen to take this opportunity to improve the accuracy of the rate constants for all six backward reactions, so that the new values are obtained from fits that minimize errors in equilibrium constants over wider temperature ranges than those used in the previous fits.

The authors would like to apologise for any inconvenience caused.

**Table 2**Rate coefficients in Arrhenius form  $k = BT^n \exp(-T_a/T)$  for the skeletal mechanism with rate parameters in mol, s, cm<sup>3</sup>, kJ, and K.

	Reaction	B	n	T <sub>a</sub>
1f	H + O <sub>2</sub> → OH + O	$3.52 \times 10^{16}$	−0.7	8590
1b	OH + O → H + O <sub>2</sub>	$1.05 \times 10^{14}$	−0.313	132
2f	H <sub>2</sub> + O → OH + H	$5.06 \times 10^4$	2.67	3165
2b	OH + H → H <sub>2</sub> + O	$2.94 \times 10^4$	2.64	2430
3f	H <sub>2</sub> + OH → H <sub>2</sub> O + H	$1.17 \times 10^9$	1.3	1825
3b	H <sub>2</sub> O + H → H <sub>2</sub> + OH	$1.42 \times 10^{10}$	1.18	9379
4f	H + O <sub>2</sub> + M → HO <sub>2</sub> + M <sup>a</sup>	k <sub>0</sub> $5.75 \times 10^{19}$	−1.4	0.0
		k <sub>∞</sub> $4.65 \times 10^{12}$	0.44	0.0
5f	HO <sub>2</sub> + H → OH + OH	$7.08 \times 10^{13}$	0.0	148
6f	HO <sub>2</sub> + H → H <sub>2</sub> + O <sub>2</sub>	$1.66 \times 10^{13}$	0.0	414
6b	H <sub>2</sub> + O <sub>2</sub> → HO <sub>2</sub> + H	$2.93 \times 10^{12}$	0.356	27929
7f	HO <sub>2</sub> + OH → H <sub>2</sub> O + O <sub>2</sub>	$2.89 \times 10^{13}$	0.0	−250
		$4.50 \times 10^{14}$	0.0	5500
8f	H + OH + M → H <sub>2</sub> O + M <sup>b</sup>	$4.00 \times 10^{22}$	−2.0	0.0
8b	H <sub>2</sub> O + M → H + OH + M <sup>b</sup>	$2.02 \times 10^{23}$	−1.85	59682
9f	H + H + M → H <sub>2</sub> + M <sup>c</sup>	$1.30 \times 10^{18}$	−1.0	0.0
9b	H <sub>2</sub> + M → H + H + M <sup>c</sup>	$5.41 \times 10^{17}$	−0.727	52129
10f	H <sub>2</sub> O <sub>2</sub> + M → OH + OH + M <sup>d</sup>	k <sub>0</sub> $7.60 \times 10^{30}$	−4.20	25703
		k <sub>∞</sub> $2.63 \times 10^{19}$	−1.27	25703
11f	HO <sub>2</sub> + HO <sub>2</sub> → H <sub>2</sub> O <sub>2</sub> + O <sub>2</sub>	$1.03 \times 10^{14}$	0.0	5556
		$1.94 \times 10^{11}$	0.0	−709
12f	HO <sub>2</sub> + H <sub>2</sub> → H <sub>2</sub> O <sub>2</sub> + H	$7.80 \times 10^{10}$	0.61	12045

<sup>a</sup> Chaperon efficiencies: H<sub>2</sub> (2.5), H<sub>2</sub>O (16.0), CO (1.2), CO<sub>2</sub> (2.4), Ar and He (0.7), and 1.0 for all other species; Troe falloff with  $F_c = 0.5$ .

<sup>b</sup> Chaperon efficiencies: H<sub>2</sub> (2.5), H<sub>2</sub>O (12.0), CO (1.9), CO<sub>2</sub> (3.8), Ar and He (0.4), and 1.0 for all other species.

<sup>c</sup> Chaperon efficiencies: H<sub>2</sub> (2.5), H<sub>2</sub>O (12.0), CO (1.9), CO<sub>2</sub> (3.8), Ar and He (0.5), and 1.0 for all other species.

<sup>d</sup> Chaperon efficiencies: H<sub>2</sub> (2.5), H<sub>2</sub>O (6.0), H<sub>2</sub>O<sub>2</sub> (6.0), CO (1.5), CO<sub>2</sub> (2.0), Ar (0.7), and He (0.4), and 1.0 for all other species; Troe falloff with  $F_c = 0.43$ .

\* Corresponding author. Forman A. Williams, Dept. of Mechanical and Aerospace Engineering, University of California San Diego, La Jolla, CA 92093-0411, USA.  
E-mail address: [faw@ucsd.edu](mailto:faw@ucsd.edu) (F.A. Williams).

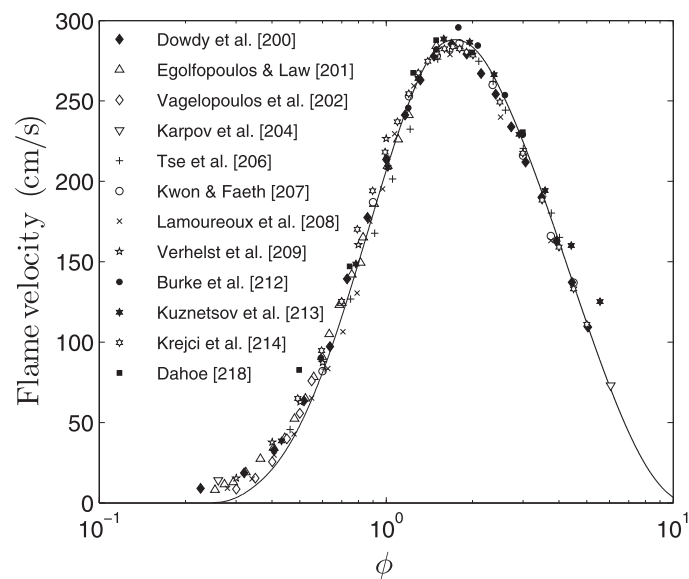


**Fig. 14.** The variation with equivalence ratio of the laminar propagation velocity of hydrogen–air planar deflagrations at normal atmospheric conditions as obtained from experimental measurements (symbols) and from numerical integrations with the detailed chemistry of Table 1 (solid curve).